Effects of magnesium, polyaspartic acid, carbonate accumulation rate and temperature on the crystallization, morphology, elemental incorporation and isotopic fractionation of calcium carbonate phases

Mag. Mag.rer.nat. Andrea Niedermayr

Assessors:

Univ.-Prof. Dipl.-Min. Dr.rer.nat. Martin Dietzel

Univ.-Doz. Dipl.-Geoökol. PhD Stephan Jürgen Köhler

Acknowledgments

Statutory declaration

I declare that I have authored this thesis independently, that I have not used other than the declared sources / resources, and that I have explicitly marked all material which has been quoted either literally or by content from the used sources.

………………………………   …………………………………………………..
                date   (signature)

Abstract

Calcium carbonates ($CaCO_3$) are widespread in sediments and organisms and highly relevant materials for industrial applications. $CaCO_3$ precipitates may also clog drainage tubes, oil producer pipes and heat exchangers. The formation of calcium carbonate is strongly affected by dissolved magnesium (Mg) and polyaspartic acid (Pasp) e.g. in environments related to seawater and biomineralization, respectively. In the present study the formation of the anhydrous $CaCO_3$ polymorphs calcite, aragonite and vaterite were investigated at various temperatures ($6 < T < 40°C$), carbonate accumulation rates ($0.15 < R_{CO_3} < 320$ µmol h^{-1}), concentrations of Mg (≤ 55 mmol l^{-1}) and Pasp (≤ 3.4 mg l^{-1}). Focus is given on individual morphologies and fractionation of isotopes and cation incorporation during $CaCO_3$ crystallization Precipitation of $CaCO_3$ was induced by CO_2 diffusion through a membrane into a solution containing Ca, traces of Sr and Mg and/or Pasp.

The pH was kept constant at 8.3 by adding a diluted NaOH solution which allows quantifying precise R_{CO_3} values, nucleation times and precipitation rates. The $CaCO_3$ precipitation rates and saturation degrees are mainly controlled by the parameters R_{CO_3} and T. Calcium carbonate formation was retarded from few minutes up to several hours at $T \leq 10°C$, and up to several hundreds of hours at elevated [Mg] and [Pasp]. Distinct $CaCO_3$ polymorph formation is mainly controlled by [Mg], [Pasp], T and R_{CO_3}. [Mg]/[Ca] > 0.2 (40°C) to [Mg]/[Ca] > 2 (6°C) promote the formation of aragonite and suppress the formation of vaterite. Pasp inhibits aragonite formation and favours vaterite formation, whereas combining both Pasp and Mg causes calcite formation. In the presence of Pasp, $CaCO_3$ is formed only in case of supersaturation with respect to monohydrocalcite. Mg stabilizes the $\{01\bar{1}1\}$ faces of calcite and changes its morphology from $\{10\bar{1}4\}$ rhombohedral to dodecahedral or elongated shapes. The presence of Pasp causes round edges, steps and a rough surface. The morphologies of aragonite and vaterite are highly influenced by the level of saturation degree and T. The cell size parameter c for aragonite (Pmcn) is (i) positively correlated with $[Sr]_{Ar}$, and (ii) negatively correlated with T due to the rise in Sr uptake at lower T. Calcite and vaterite have also an inverse correlation between Sr incorporation in $CaCO_3$ and T, and a positive correlation between Sr incorporation and precipitation rate, [Mg] and [Pasp]. The $^{44/40}Ca$ isotopic fractionation between vaterite and dissolved Ca^{2+} ($\Delta^{44/40}Ca_{CaCO_3-aq} = -0.10$ to -0.55 ‰) is much lower than that for calcite (-0.69 to -2.04 ‰) and aragonite (-0.91 to -1.55 ‰). Individual $CaCO_3$ polymorphs can be distinguished by Sr incorporation vs. $^{44/40}Ca$ isotopic fractionation.

The present study provides conditions to synthesize tailored $CaCO_3$ polymorphs concerning distinct structure, shape and composition. Moreover, the results can be used for an advanced understanding for the mechanisms of $CaCO_3$ biomineralization, to improve and validate environmental multiproxy approaches, and to evaluate $CaCO_3$ scaling mechanisms with special regard on inhibition and monitoring. Respective results are discussed and compared to data from field studies where $CaCO_3$ sinter is formed.

Kurzfassung

Kalziumkarbonat (CaCO₃) weist eine Vielzahl von industriellen Anwendungen und eine weite Verbreitung in Sedimenten und Lebewesen auf. Die Ausfällung von CaCO₃ kann ferner zur Blockade von Tunneldrainagen, Ölförderleitungen und Wärmetauschern führen. Die Bildung von CaCO₃ wird durch gelöstes Magnesium (Mg) und Polyasparaginsäure (Pasp) stark beeinflusst z.B. im Meerwasser und bei der Biomineralisation. Die vorliegende Studie befasst sich mit der Bildung der wasserfreien CaCO₃-Polymorphe Kalzit, Aragonit und Vaterit bei unterschiedlichen Temperaturen (6 < T < 40°C), Karbonat-Akkumulationsraten (0.15 < R_{CO_3} < 320 µmol h^{-1}), Mg- (≤ 55 mmol l^{-1}) and Pasp-Konzentrationen (≤ 3.4 mg l^{-1}). Der Fokus wird auf die Morphologie, Isotopenfraktionierung und Elementeinbau während der CaCO₃ Kristallisation gelegt. Die Ausfällung von CaCO₃ erfolgte über die Diffusion von CO_2 in eine Ca, Sr und Inhibitor (Mg, Pasp) haltige Lösung. Der pH-Wert wurde durch die Zugabe von verdünnter NaOH Lösung auf 8.3 konstant gehalten. Die NaOH Zugabe ermöglichte eine präzise Ermittlung des R_{CO_3} Wertes, des Zeitpunktes der CaCO₃-Nukleation und der Präzipitationskinetik. Die Karbonatepräzipitationsrate und der Sättigungsgrad werden vorwiegend über die Parameter R_{CO_3} und T kontrolliert. Die CaCO₃-Ausfällung wird bei T ≤ 10°C um einige Minuten bis Stunden und durch erhöhte [Mg] und [Pasp] um bis zu mehreren hunderte Stunden verzögert. Die Bildung der einzelnen CaCO₃ Polymorphe wird über [Mg], [Pasp], T und R_{CO_3} gesteuert. [Mg]/[Ca] > 0.2 (40°C) bis [Mg]/[Ca] > 2 (6°C) in der Lösung fördern die Aragonitbildung und unterdrücken die Vateritbildung. Pasp inhibiert die Aragonitbildung und begünstigt die Vateritbildung, während die Kombination von Pasp und Mg zur Kalzitbildung führt. In Anwesenheit von Pasp wird eine CaCO₃ Bildung erst ab einer Übersättigung von Monohydrokalzit beobachtet. Mg stabilisiert die {01$\overline{1}$1} Flächen von Kalzit und ändert dadurch die Morphologie von einer rhomboedrischen zu einer dodekahedralen Tracht oder länglichem Habitus. Pasp verursacht die Abrundung von Kanten, Stufenbildung und eine höhere Oberflächenrauhigkeit. Die Morphologie von Aragonit und Vaterit wird vorwiegend über den Sättigungsgrad und T bestimmt. Der Gitterparameter c von Aragonit (Pmcn) besitzt eine (i) positive Korrelation mit $[Sr]_{Ar}$ und (ii) eine negative Korrelation mit T aufgrund eines erhöhten Sr-Einbaues bei geringen T. Kalzit und Vaterit zeigen ebenfalls eine negative Korrelation zwischen dem Sr-Einbau im CaCO₃ und T sowie eine positive Korrelation zwischen dem Sr-Einbau und Präzipitationsrate, [Mg] and [Pasp]. Die $^{44/40}$Ca-Isotopenfraktionierung zwischen Vaterit und gelöstem Ca^{2+} ($\Delta^{44/40}Ca_{CaCO_3-aq}$ =-0.10 to -0.55 ‰) ist viel geringer als jene für Kalzit (-0.69 to -2.04 ‰) und Aragonit (-0.91 to -1.55 ‰). Die Auftragung der Verteilungskoeffizienten von Sr im CaCO₃ Festkörper (D_{Sr}) gegen die $^{44/40}$Ca-Isotopenfraktionierung ermöglicht die Unterscheidung der CaCO₃ Polymorphe.

Die Ergebnisse der vorliegenden Studie liefern die Bedingungen für die in Bezug auf Struktur, Form und Zusammensetzung maßgeschneiderte Bildung von CaCO₃ Polymorphen. Weiters können die Ergebnisse für ein verbessertes Verständnis der CaCO₃-Biomineralisation, von Umweltproxyansätze und zur Evaluierung der Sinterbildungsmechanismen, im speziellen zur Inhibition und zum Monitoring, herangezogen werden. Entsprechende Ergebnisse werden diskutiert und den Resultaten aus den durchgeführten Feldstudien zur Bildung von Kalksinter gegenübergestellt.

Table of content

1   Introduction

1.1 Motivation

The formation of calcium carbonate has been extensively studied during the last centuries due to its significance in natural and man-made environments. Organisms precipitate calcium carbonates to built up shells, skeletons and spines (e.g. Politi et al., 2004). About 30 wt.% of Phanerozoic sediments are referred to carbonates, mainly calcium carbonate (Veizer and Mackenzie, 2003). Technical applications of calcium carbonates comprise e.g. the usage as fillers (e.g. in rubber, paints, plastics, tooth paste) and coating materials in the paper industry (e.g. Gopinath et al., 2002). Therefore calcium carbonate with special morphologies and surface properties are crystallized. On the other hand, calcium carbonate precipitation may clog drainages, oil production wells, and heat exchangers (e.g. Zhang et al., 2001; Gamisch and Girmscheid, 2007).

In natural and man made environments the calcium carbonate polymorphs calcite, aragonite and vaterite occur in the sequence of their abundance and thermodynamic stability at Earth surface conditions (5 to 50°C and 1 atm; e.g. Plummer and Busenberg, 1982). Distinct calcium carbonate polymorphs are formed under different temperature, precipitation conditions and under the influence of additives like Mg or organics. Further three hydrous calcium carbonate phases occur in rather special environments and as precursor: monohydrocalcite, ikaite and amorphous calcium carbonate.

Distinct calcium carbonate phases incorporate different amounts of (trace) elements and isotopes. These (trace) element incorporation and isotopic fractionation behaviour during calcium carbonate formation may provide fundamental insights into their growth mechanism and environment. Trace element incorporation and isotope signals can be used for monitoring aspects to evaluate ongoing sinter formation and inhibition effects in man made environments, e.g. sinter formation in tunnel drainage systems.

Trace element distributions and isotopic signatures from calcium carbonate archives are widely used for reconstruction of paleo-environments since centuries. These carbonate records play an important role for the documentation of the climate and Earth's history because of the widespread appearance of marine and terrestrial carbonates. E.g. Sr and Mg signatures from speleothem records, foraminifers, corals and ostracodes can be applied for temperature reconstruction (paleothermometry) (e.g. Mucci, 1987; Oomori et al., 1987). In several cases the occurrences of metastabile calcium carbonate phases have to be considered as primary precipitates. Primary elemental signatures can persist although solid $CaCO_3$ is transformed (Frisia et al., 2002). Furthermore small amounts of "impurities" of another calcium carbonate phase may have a large impact on the bulk elemental composition or isotopic signature. E.g. a small amount of calcite would change the Mg concentration in aragonite samples significantly as Mg incorporation into aragonite is up to about three orders of magnitude lower compared to calcite (e.g. Zhong and Mucci, 1989; Gabitov et al., 2008) and as Mg incorporation into calcite increases with increasing temperature

(Oomori et al., 1987), while Mg incorporation into aragonite decreases with increasing temperature (Gaetani and Cohen, 2006).

The temperature dependency of oxygen isotope incorporation ($\delta^{18}O$) is widely used for paleothermometry since Urey has proposed this paleothermometer in 1947 (Faure and Mensing, 2005; Urey, 1947). Due to more accurate measurements new isotope systems are available. For instance, calcium isotopes were studied for paleo-environmental reconstructions of e.g precipitation rates and temperatures (e.g. Gussone et al., 2004; Gussone et al., 2007; Fantle and Depaolo, 2007b; Fantle and Depaolo, 2007a; Farkaš et al., 2007a; Farkaš et al., 2007b; Tang et. al., 2008). However, any element or isotope record has its own accuracy and uncertainty, like variability of the initial Mg and Sr concentrations or isotopic composition ($\delta^{18}O$, $\delta^{13}C$, $\delta^{44/40}Ca$ value), kinetic effects or alteration impact. In the case of calcium carbonate a multiproxy approach consisting e.g. of Sr, Mg and isotopic signatures can improve accuracy and reveal further insight into environmental conditions during $CaCO_3$ formation. But the proxies may depend on each other like incorporation of Sr on Mg content of $CaCO_3$.

Magnesium (e.g. in the ocean) and organic macromolecules like (poly)aspartic acid can influence the formation of these calcium carbonates, their chemical and isotopic composition. Polyaspartic acid is a polyamino acid with free carboxylic groups and its derivates occur in organisms (e.g. shells, asparagus) and is further applied as an inhibitor for calcium carbonate formation.

1.2 Aims and accomplishment

The effect of Mg and polyaspartic acid on calcium carbonate formation is a main goal of this study. This comprises the inhibition effect, variation in the polymorph composition and change in the morphology and surface by these additives and under the influence of temperature and carbonate accumulation rate. The experimental approach aims in a profound understanding of the kinetics and mechanisms of calcium carbonate formation. The goal of this study is the formation of all three polymorphs calcite, aragonite and vaterite under well controlled conditions to study afterwards their individual properties. Further focus is given on the distinct incorporation of Mg and Sr and on Ca isotopic fractionation during calcium carbonate formation. The individual effects of the calcium accumulation rate, temperature and additives on the polymorph formation, solid phase morphology, and elemental distribution and isotopic fractionation between $CaCO_3$ and the solution are discussed. For the investigation of the nucleation stage as well as the crystal growth stage all experiments were carried out without seeds. The results from the laboratory experiments were compared with those of the field studies. In the field studies the mechanisms and kinetics of $CaCO_3$ formation and the evolution of the carbon and oxygen isotopic composition were further topics of this research.

2   Theoretical Background

2.1   Species distribution in water

Electrostatic forces cause attraction between oppositely charged ions in water, if they are close enough to each other. As consequence these oppositely charged ions can be bound together and form different kinds of species mainly ions. The hydration spheres of the ions result in reduced electrostatic forces between the dissolved species. Diffusion of ions and water molecules and the collisions can weaken this bounding.

The concentrations of each species can be calculated by the equilibrium constants, if the system is in equilibrium and the amount of molecules is large enough to obey a Gaussian distribution of all species. These equilibrium constants are usually determined by experiments and are given as functions of temperature at constant pressure. The temperature dependency of the equilibrium constants K can also be calculated from the reaction enthalpy ΔH_r, temperature T and ideal gas constant R (8.3145 kJ K^{-1} mol^{-1}) by the van't Hoff equation (e.g. Appelo and Postma, 2006)

$$\frac{dlnK}{dT} = \frac{\Delta H_r}{RT^2}$$

(2-1)

The values of the equilibrium constants are usually considered in geochemical modelling programs like PhreeqC and they are given in databases.

CO$_2$-H$_2$O System

As soon as water is in contact with the atmosphere it can degas or dissolve CO_2 until the equilibrium with the respective CO_2 content in the atmosphere is reached. The ongoing process depends on the CO_2 partial pressure difference and its direction. CO_2 degasses, if the internal partial pressure of CO_2 in the solution is higher than in the atmosphere. Otherwise CO_2 uptake occurs, if the partial pressure has the opposite direction. Finally the activity of the dissolved carbon dioxide (CO_2) or ($H_2CO_3^*$) is in equilibrium proportional to the CO_2 partial pressure in the gaseous phase according to Henry law (e.g. Drever, 2002):

$$(CO_2) = (H_2CO_3^*) = K_{CO_2}p_{CO_2}$$

(2-2)

The Henry constant K_{CO_2} can be calculated according to the equation in Tab. 2-1. $H_2CO_3^*$ denotes the aqueous $CO_{2(aq)}$ and the carbonic acid H_2CO_3

$$H_2CO_3^* \rightleftharpoons CO_{2(aq)} + H_2CO_3$$

(2-3)

where H_2CO_3 is formed when CO_2 reacts with H_2O molecules according to equation

$$CO_{2(aq)} + H_2O \rightleftharpoons H_2CO_3$$

(2-4)

H_2CO_3 accounts for only 1 to 2 ‰ of the dissolved $H_2CO_3^*$. However $H_2CO_3^*$ deprotonates partly to HCO_3^- and CO_3^{2-} according to following equations:

$$H_2CO_3 \overset{K_1}{\rightleftharpoons} H^+ + HCO_3^- \qquad (2\text{-}5)$$

$$HCO_3^- \overset{K_2}{\rightleftharpoons} H^+ + CO_3^{2-} \qquad (2\text{-}6)$$

The equilibrium constants K_1 and K_2 can be calculated by the equations in Tab. 2-1 according to Plummer and Busenberg (1982).

Tab. 2-1: Factors for the temperature dependent equilibrium constants in the CO_2-H_2O system (Plummer and Busenberg, 1982) : log K = a+bT+c/T+d log T+e/T² with T in Kelvin

Phase	a	b	c	d	e
K_{CO2}	108.3865	0.0198508	-6919.53	-40.45154	669365
K_1	-356.3094	-0.0609196	21834.37	126.8339	-1684915
K_2	-107.8871	-0.0325285	5151.79	38.9256	-563713.9

The mol fraction of each species can be calculated according to the equations

$$x_{H_2CO_3} = \frac{[H_2CO_3^*]}{[DIC]} = \left[1 + \frac{K_1}{[H^+]} + \frac{K_1 K_2}{[H^+]^2}\right]^{-1} \qquad (2\text{-}7)$$

$$x_{HCO_3^-} = \frac{[HCO_3^-]}{[DIC]} = \left[1 + \frac{[H^+]}{K_1} + \frac{K_2}{[H^+]}\right]^{-1} \qquad (2\text{-}8)$$

$$x_{CO_3^{2-}} = \frac{[CO_3^{2-}]}{[DIC]} = \left[1 + \frac{[H^+]}{K_2} + \frac{[H^+]^2}{K_1 K_2}\right]^{-1} \qquad (2\text{-}9)$$

(Dietzel and Kirchhoff, 2003). DIC is the total dissolved inorganic carbon. $H_2CO_3^*$ dominates at low pH (<6.35 at 25°C), whereas HCO_3^- dominates at moderate pH and CO_3^{2-} at high pH (>10.3 at 25°C). The pH values where two DIC species are equal in value decrease with temperature. This means that the DIC species distribution is shifted to higher relativ CO_3^{2-} content at elevated temperature (see also Fig. 2-1).
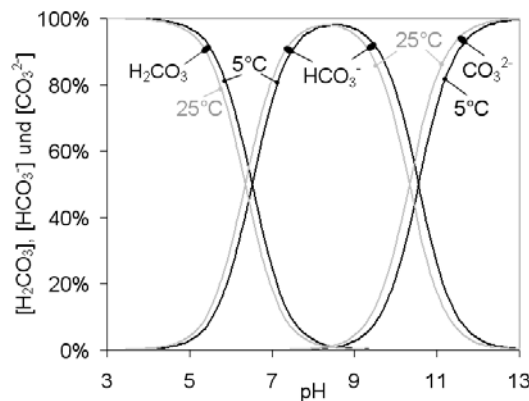
Fig. 2-1: Calculated percentage of H_2CO_3, HCO_3^- and CO_3^{2-} with respect to DIC as a function of the pH estimated from the equations in Tab. 2-1 and equation (2-7) to (2-9) at 5°C and 25°C.

2.2 Calcium carbonate precipitation

The following processes can induce calcium carbonate precipitation:

- CO_2 degassing
- CO_2 uptake
- Warming
- Evaporation
- Mixing
- Ion transport (e.g. biomineralisation)

All six processes have in common, that the saturation degree of the solution increases either by the rise of the carbonate activity (CO_3^{2-}), of the calcium activity (Ca^{2+}) or by the decrease of the solubility K_{sp} of the respective mineral.

$$SI = \log \frac{(Ca^{2+})(CO_3^{2-})}{K_{sp}}$$ (2-10)

Considering caves and springs, calcium carbonate precipitation typically occurs when calcium and DIC containing solutions get into contact with the atmosphere and CO_2 degasses. The degassing of the CO_2 causes an increase in pH, which results into higher carbonate concentration although the DIC decreases slightly. However, the saturation with respect to the calcium carbonate phases increases and at a certain supersaturation calcium carbonate can precipitate. The formation of calcium carbonate is given by the overal reaction

$$Ca^{2+} + 2\ HCO_3^- \rightleftharpoons\ CaCO_{3(s)} + CO_{2(g)} + H_2O$$ (2-11)
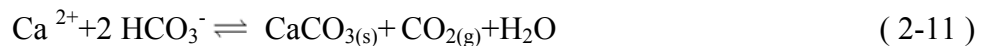
Calcium carbonates can also precipitate by CO_2 uptake at very high alkaline solutions. In this case the adsorbed $CO_{2(aq)}$ reacts with the OH^- of the solution and is transformed to the carbonate ion. In this case the $CaCO_3$ precipitation is caused by the rise of the DIC concentration and in consequence by the rise of the carbonate and saturation with respect to the calcium carbonate. Following simplified overall reaction describes this process:

$$Ca^{2+} + 2\ OH^- + CO_{2(g)} \rightleftharpoons CaCO_{3(s)} + H_2O$$ (2-12)
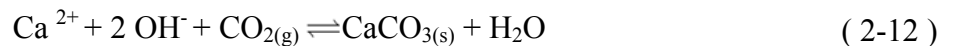
This process is valid e.g. in highly alkaline lakes or drainage solution. In the latter case portlandite ($Ca(OH)_2$) dissolution causes high pH and Ca concentrations (Dietzel et al., 1992). $CaCO_3$ formation occurs then according to equation (2-12) and can cause clogging of drainage tubes.

Warming causes a slight decrease of the solubility of anhydrous calcium carbonate phases (see section 2.4.3), but the effect of the rise in carbonate CO_3^{2-} is much larger. The DIC distribution is shifted from bicarbonate to carbonate ions at elevated temperatures. This can result in $CaCO_3$ precipitation by heating calcium and DIC containing water, like e.g. in heat exchangers and water boilers.

Calcium carbonate precipitates after the rise of calcium and carbonate activities through evaporation. In the main sequence of precipitation solids by evaporation $CaCO_3$ is the first precipitate in the evaporation circle.

Moreover the mixture of a Ca^{2+}- and HCO_3^-- containing solution at moderate pH with a highly alkaline solution can result in $CaCO_3$ formation (e.g. in tunnel systems). The mixing of a calcium-rich solution with a carbonate-rich solution may also cause $CaCO_3$ precipitation although this process is relatively rare in nature due to the low carbonate concentration in natural water.

In many cases also the combination of these processes causes $CaCO_3$ precipitation in natural and man-made systems.

Concerning biomineralization organism can form solid $CaCO_3$ by active control of Ca^{2+}, DIC and H^+ concentration in their cells. Corals produce their $CaCO_3$ skeleton e.g. by actively adding Ca^{2+} ions and removing H^+ from the calcifying fluid with Ca^{2+}-ATPase enzymes (Al-Horani et al., 2003). CO_2 diffuses as consequence of the high pH to the calcification space and reacts with OH^- to form CO_3^{2-} ions. Furthermore seawater is transported through the vacuoles and may reach the calcifying fluid by penetration through the porous skeleton and peri-cellular channels. Finally, Ca^{2+} and CO_3^{2-} enriched solution results into $CaCO_3$ precipitation (Cohen and McConnaughey, 2003 and references therein). The vacuoles of foraminifers can take up seawater, various pumps and channels may increase the pH, the Ca^{2+} and the DIC in this fluid, respectively. The vacuoles are transported to the delimited biomineralization space on the surface of the shell where Ca^{2+} and CO_3^{2-} ions are released (exocytose) and in consequence $CaCO_3$ precipitates (Erez, 2003).

2.3 Nucleation

Nucleation causes the formation of a new phase from a solution, melt or vapour ("old phase") via formation of small embryos. Nucleation occurs if the free energy of the phase is higher than the free energy of the new phase. In this case the "old phase" becomes metastabile. For the nucleation a free energy barrier must be exceeded, because the nuclei have a larger surface to volume ratio and the surface molecules contribute much more to the free energy than the molecules inside the phase. Latter is caused by the weaker bonds of the surface molecules to their neighbours compared to bulk molecules (Deyoreo and Vekilov, 2003 and references therein).

Nucleation can occur e.g. by a temperature change. Calcium carbonate solutions nucleate e.g. with increasing temperature like in heat exchangers. In a natural aquatic solution the rise of supersaturation is usually the driving force for nucleation.

Nucleation occurs spontaneously or it can be induced by seed crystals. The term "secondary nucleation" is used in systems where crystalline matter is present and its surface act as substrate for nucleation (nomenclature from Mullin, 2001). "Primary nucleation" occurs in systems without any solids. It can occur spontaneously by aggregation of ions and molecules so called cluster formation. In this case no interaction with any surface or particle occures ("homogenous nucleation"). Contrary,

foreign (particle) surfaces are present before the nucleation process and act as nuclei for the new phase at heterogeneous nucleation. This nucleation type includes also nucleation on walls of vessels used for experiments (Mullin, 2001).

2.3.1 Classical nucleation theory – Gibbs approach

Initially a homogenous multi-component system of ions, atoms and molecules within a single phase exists. These ions, atoms and molecules can coalesce and nuclei are formed. The stability of these nuclei depends mainly on their sizes and the composition of the surrounding solution. The stability of the nuclei is given by the Gibbs free energy, which aims always for a minimum. Smaller particles have a tendency to disintegrate because of their large free energy which is caused by the large surface to volume ratio (see above). The Gibbs free energy for a nuclei with a radius r can be calculated according to the following equation from the Gibbs free energy of the surface (subscribe s) and the free energy of the volume/bulk (subscribe v) (Mullin, 2001):

$$\Delta G = \Delta G_s + \Delta G_v = 4\pi r^2 \gamma + \frac{4}{3}\pi r^3 \Delta g_v = 4\pi r^2 \gamma + \frac{4\pi r^3}{3\nu} kT \ln(1+S) \qquad (2\text{-}13)$$

γ is the surface tension between the nuclei and the surrounding phase (aqueous solution) and Δg_v is the difference between the free energies per unit volume of the nucleus and the surrounding phase. Δg_v can be expressed by the specific volume of the nuclei (growth unit) ν, by the Boltzmann constant k, temperature T and the relative supersaturation $S = c/c_{crit}$ (Mullin, 2001). The free energy increases at very small radii through growing; the nuclei are unstable and will in average disintegrate. However, some nuclei reach the critical radius r^* at which both dissolution and growing result into a lower free energy. For larger radii the contribution of surface free energy becomes unimportant and the free energy is determined by the volume free energy. As a consequence the nuclei become stable and grow, when this critical radius is exceeded.

The critical radius results from the derivation of equation (2-13), which is set to zero, and is given in equation

$$r^* = \frac{-2\gamma}{\Delta g_v} = \frac{2\nu\gamma}{kT \ln(1+S)} \qquad (2\text{-}14)$$

The maximum free energy for nucleation ΔG^* which has to be exceeded to form stable nuclei depends on the structure of the nuclei (Zhang and Liu, 2009). It is given by equation (2-15) and was calculated by inserting the critical radius of equation (2-14) into equation (2-13):

$$\Delta G^* = \frac{16\pi\Omega^2\gamma^3}{3(kT \ln(1+S))^2} \qquad (2\text{-}15)$$

This critical free energy for nucleation determines also the nucleation rate J. The number of nuclei which are formed per unit time and unit volume can be calculated by driving the critical free energy with k and T (Deyoreo and Vekilov, 2003) according to equation

$$J = Ae^{-\frac{\Delta G^*}{kT}}$$

(2-16)

This approach contains A, the frequency of the molecular processes, ΔG^*, the critical Gibbs free energy, k, the Bolzmann constant and T, the temperature in Kelvin (Horn and Rieger, 2001). The nucleation rate J depends strongly on the surface energy γ and on the supersaturation σ (Deyoreo and Vekilov, 2003):

$$J = Ae^{-\frac{B\gamma^3}{\sigma^2}}$$

(2-17)

The coefficient B contains all other parameters (Ω, T) and constants (k, π, 16, 3) from equations (2-15) and (2-16).

2.3.2 Nucleation of metastable phases

The ratio of the nucleation of a stable to a metastable phase is given by the equation

$$\frac{J_m}{J_s} = \left(\frac{\rho_m}{\rho_s}\right)^2 \left(\frac{\sigma_m}{\sigma_s}\right)^3 \left(\frac{\ln(S_m)}{\ln(S_s)}\right)^2$$

(2-18)

Where ρ, σ and S are the density, surface energy and the supersaturation ratio with subscribes s and m for stable and metastable phases (Noguera et al., 2006). The free energy of formation of a nucleus, ΔG_j, consists of the energy gained from forming bonds ΔG_{bulk} and of energy required to create a surface ΔG_{surf} according to

$$\Delta G_j = \Delta G_{bulk} + \Delta G_{surf} = -jkT \ln\frac{a}{a_0} + A\bar{\gamma}$$

(2-19)

where j is the number of molecular units in the nucleus, a is the actual concentration (activity) and a_0 the concentration at solubility equilibrium of the solutes, γ is the interfacial energy and A the surface area of the nuclei.

Ostwald (1897) found in saturated solutions and during crystallisation of under cooled melts that first an intermediate phase is formed and not the most stabile one. Ostwald formulated the rule, that the transformation of an unstable state into a stable one does not occur directly, but passes intermediate stages, which have the closest free energy difference from the initial stage. This is called "Ostwald's rule of stages" (Billinge, 2009) and would result in the following general precipitation sequence for calcium carbonate at ambient temperature (25°C): first amorphous

calcium carbonate (ACC), than monohydrocalcite, followed by vaterite, aragonite and calcite. This sequence is due to the nucleation rate for the at least stable phase versus the most stable phase. The least stable phase is kinetically favoured because its solid solution interfacial energy is lower (Stumm and Morgan, 1996). The interfacial mineral-aqueous solution free energy γ increases with decreasing solubility (Stumm and Morgan, 1996 and references therein):

$$\frac{4\bar{r}^2\bar{\gamma}}{kT} = 4.7 - 0.272\ln c_{sat}$$ (2-20)

This is in accordance with experimental findings at high supersaturation. Gebauer et al. (2008) found e.g. the formation of clusters and nucleation of ACC I (calcite short range order) in solutions with lower pH of 9 to 9.5 (and therefore lower supersaturation) compared ACC II (vaterite short range order) in solution with a higher pH of 9.75 to 10 (and therefore higher supersaturation). ACC I has a higher binding energy and is transformed to calcite, whereas ACC II has a lower binding energy and is transformed to vaterite (Gebauer et al., 2008).

2.3.3 Non classical nucleation theory

The classical nucleation theory assumes the presence of the components in a molecularly dispersed state (Horn and Rieger, 2001) and neglects hydration and solvation phenomena, volume work, entropy effects, molecular interactions and collective phenomena like fluctuation of concentration. Two conceptes will be discussed in the following sections which consider these phenomens partly.

- Cluster formation concept
  This concept is based on the formation of clusters, which have a different structure than the final macroscopic phase (Schmelzer et al., 2000). The formation of clusters is in good agreement with several experiments (Gebauer et al., 2008; Pouget et al., 2009; Zhang and Liu, 2009; Zhong and Chu, 2009). Numerous experiments indicate precursors with sizes not exceeding the critical radius (Gebauer et al., 2008 and references therein). Stable prenucleation ion clusters are also formed in undersaturated state. The amount of the calcium-carbonate bonds increase with increasing pH because of the larger carbonate ion fraction at higher pH. Clusters with 2 nm hydrodynamic diameter (approximately 70 calcium and carbonate ion) are found in the supersaturated stage close to nucleation. In the early post nucleation stage this cluster size disappeared, whereas the clusters have then a hydrodynamic diameter from ~5 to 6 nm. It might be a hint for the nucleation by cluster aggregation (Gebauer et al., 2008), although this issue is still in discussion.
  Fig. 2-2 indicates the different stages of the crystal formation. First the ions form clusters, so called protonuclei and then they are ordered to nuclei with the final or intermediate phase and finally they grow. The intermediate phase reorders and forms a more stable phase.

Colloid experiments from Zang and Liu (2009) indicate the transformation from metastable liquid-like structure to final crystal-like structure during the nucleation process (under influence of an alternating electric field). The ordering starts in the centre of the nuclei and proceeds continuously to the marigin. Generally the crystallinity of nuclei increases with increasing sizes of the nuclei (Zhang and Liu, 2009). Particles >200 nm develop crystalline domains within the amorphous matrix (Pouget et al, 2010).
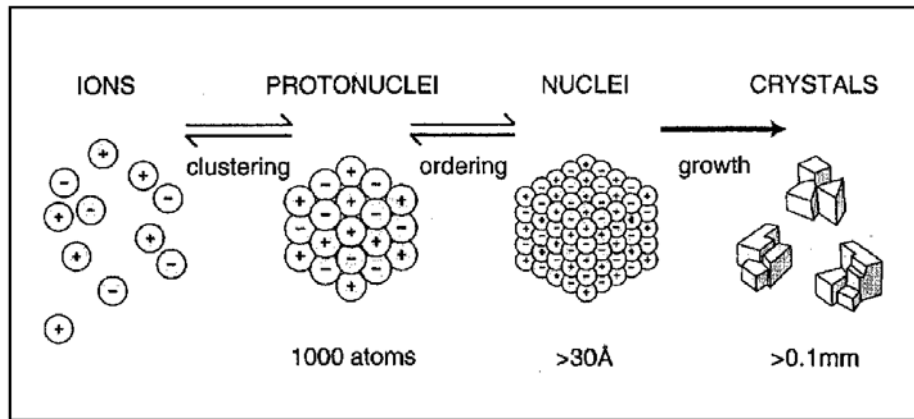
Fig. 2-2: Crystal formation process (Dudley and Baker, 2007)

- Density function theory
  The density function theory (DFT) is nowadays used for computational modelling, e.g. by Tommaso and Leeuw (2008). This statistical method is a reformulation of the Van der Waals approach. The Van der Waals approach considers besides to the thermodynamic parameter like temperature, pressure and composition the local changes of the compositions and density (Schmelzer et al., 2000). DFT is based on the assumption that the molecule number density in the solution undergoes continuous changes, or in other words statistical fluctuations. These statistical fluctuations are considered in the free energy of Helmholz f_H. The Gibbs free energy change for the density fluctuation can be calculated according to equation

$$\Delta G = \int_V ([f_H(\bar{r}) - \mu_{old}]\rho(\bar{r}) + p)d\bar{r} \qquad (\,2\text{-}21\,)$$

$\bar{r}$ is the position vector, μ_{old} the chemical potential of the previous phase (solution), p the pressure of the solution and $\rho(\bar{r})$ is the molecule number density at the position vector $\bar{r}$ (Gebauer, 2008 and references therein).

2.4   Crystal growth

Crystal growth occurs after a nucleus has exceeded the critical radius or on mineral surfaces which are exposed to a supersaturated solution. The critical supersaturation for crystal growth is less than that for nucleation (Nielsen and Toft, 1984), because the surface to volume ratio is smaller during crystal growth than during nucleation. It results into a lower free energy of the newly formed crystal compared to the nucleus and therefore a lower energy barrier for crystal growth (Appelo and Postma, 2006). Lower reactant concentrations are sufficient to get in average a net growth. On atomic scale new atoms incorporate on the crystal surface and atoms release from the surface. However, in oversaturated solutions much more atoms are newly bound to the surface than released and a net precipitation and crystal growth take place (Stumm and Morgan, 1996).

The crystal growth comprises following steps (Bethke, 2008):
1. Diffusion of the reactant from solution to the surface
2a. Adsorption of the reactant at active reaction sites or
2b. Adsorption of the reactant on the surface and diffusion to the active reaction site
2. chemical reaction: formation of bonds, partial dehydration
3. desorption of reaction products
4. diffusion of the product from the mineral surface to the solution

Active reaction sites are usually kinks, followed by edges. Adsorption (2) and desorption (4) are fast processes; therefore either the diffusion (1 and 5) or the chemical reaction (3) are the step limiting processes (Lasaga, 1984). The system is transport-controlled, if diffusion is the slowest process. Otherwise, it is called "surface-reaction-controlled", if the chemical reaction on the surface is the slowest process (Bethke, 2008).
The precipitation includes both nucleation and crystal growth. The precipitation rate depends mainly on the saturation degree Ω according to the empiric rate equation

$$R = k'(\Omega - 1)^n$$ (2-22)

(e.g. Nancollas and Reddy, 1971; Morse, 1978; Arvidson and Mackenzie, 2000).
The exponent n contains information about the precipitation mechanism and k' is the apparent rate constant. More precisely the following equation is valid

$$R = k \frac{A_0}{V} \left(\frac{m}{m_0} \right)^{n_1} (\Omega - 1)^n g(c)$$ (2-23)

where k is the specific rate constant, A_0 is the initial surface area of the solid in the solution, V is the volume of the solution, m_0 is the initial amount of solid (moles) and m is the amount (in moles) at a given time, g(c) contains effects of catalysis and inhibition. The apparent specific rate constant depends therefore on the specific rate constant of the phase, the surface area of the solid to solution

volume ratio, the initial amount and the amount at a time t and on effects of catalysis and inhibition (Arvidson and Mackenzie, 2000; Appelo and Postma, 2006).

The empirical parameters n and k in equation (2-23) depend on the ionic strength (Zuddas and Mucci, 1998), availability of seeds (Spanos and Koutsoukos, 1998), temperature, $(CO_3^{2-})/(Ca^{2+})$ ratio (Nilsson and Sternbeck, 1999) and the precipitation mechanism itself. Thus a wide variability of n and k values are found in literature (e.g. Burton and Walter, 1987; Spanos and Koutsoukos, 1998; Zuddas and Mucci, 1998; Nilsson and Sternbeck, 1999).

Different growth mechanisms occur due to the different saturation degrees or chemical potential μ as driving force (Fig. 2-3), which results into a different exponent n in equation (2-22) and (2-23).
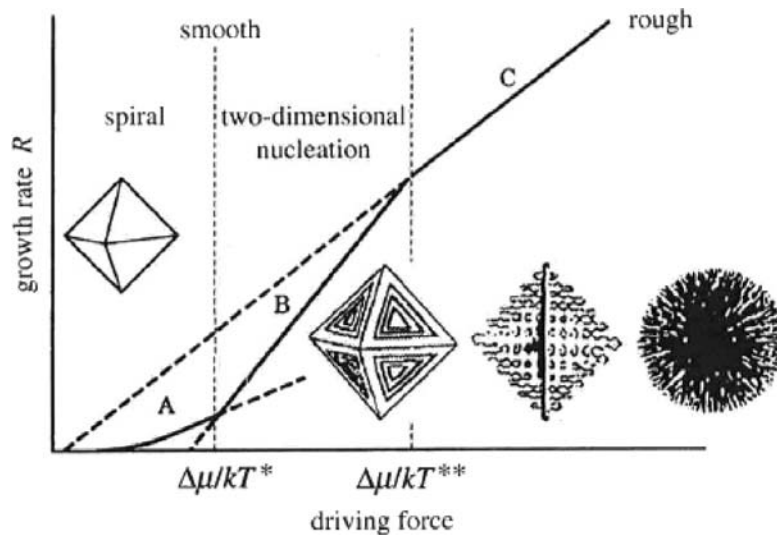
Fig. 2-3: Dependence of the growth mechanism and morphology on the driving force like e.g. supersaturation (Sunagawa, 2005).

The saturation degree determines, which growth mechanism occurs at the surface, beginning at low supersaturation (Sunagawa, 2005; Sethmann et al., 2010) :

- Spiral growth occurs on screw dislocations. These screw dislocations are kink sides for the new layer. In consequence no surface nucleation is necessary for the crystal growth and the crystal growth can occur also at very low supersaturation of the solution (see Fig. 3-2) (Mullin, 2001).

- Mononuclear growth: Only one nucleation takes place at the surface. All further added units are added to this nucleated unit. The surface growth until it is totally covered and further nucleation takes place.

- Layer by layer growth is described by the birth and spread model or Frank-van der Merwe growth mode: one growth layer nucleates and growth within a distinct time period on one surface

- Polynuclear growth: Surface nucleation or Three-dimensional growth of multilayer islands (Volmer-Weber growth mode). Islands are formed on the surface and growth takes place at these islands and also on the top of these islands.

Several concepts describe the growth process (Kossel, 1934; Mullin, 2001):

1.) Continuums theory or **surface energy theory**

Systems aim a minimum of the total free energy for a given volume unit according to the surface energy theory. This principle was first introduced by Gibbs in 1878. Wulff suggested in 1901 that crystal faces grow proportional to their respective surface energies. Surfaces with high free energies grow therefore fast and disappear, while the other surfaces grow slowly and determine in consequence the habit of the crystal. This theory assumes that the whole plane growth at one time step. Atoms and energies have to be homogeneous distributed over the surface (Kossel, 1934). No preferential growth sides like kinks are considered by this theory.

2.) Molecular theory or **adsorption layer theory**

The adsorption layer theory was introduced by Volmer in 1939 and is based on the incorporation of the new building unit (molecule/atom or ion) into the crystal. Thereby incorporation happens not immediately when the new building unit reaches the surface. The building unit can still migrate freely on the surface (surface diffusion) in a loosely bound adsorption layer to the positions with the largest attractive forces. This adsorption layer is in a steady state with the bulk solution and has probably a thickness of less than 10 nm and maybe even less than 1 nm (Mullin, 2001). According to Kossel (1934) following growth units can be found on the growing crystal faces: flat surfaces, steps, kinks, surface-adsorbed growth units, edge vacancies and surface vacancies. The building units move on the crystal surface to kinks and edges, where they are preferentially incorporated. New layers are created by surface nucleation, preferentially at corners (Mullin, 2001).

3.) **Kinematic theory**

The theory of Burton, Cabrera and Frank (BCF) results into the step velocity and growth rate. It describes the movement of the boundaries by a continuous adsorption of molecules on the terraces, diffusion and incorporation of them at step edges. The proximity of the other steps is thereby considered, whereas it assumes equilibrium concentrations at the steps, no effect of the moving boundary and no reaction or interaction between the atoms (Myers-Beaghton and Vvedensky, 1991).

4.) **Diffusion reaction theory**

This concept was originally developed by Noyes and Whitney (1897). The difference between the bulk solution concentration and the concentration on the solid surface causes a diffusion process. The diffusion law is thereby applied for the dissolution/precipitation rate. The latter is proportional to the concentration difference between the concentration of the saturated solution and concentration in the solution at the crystal surface (Noyes and Whitney, 1897). Nernst (1904) has introduced a diffusion layer and Berthoud and Valeton have furthermore suggested to consider also the chemical reaction process. A effectiveness factor was introduced by Gardside (see Mullin, 2001 and references therein). The entrapment model of Watson (1996) uses a similar approach.

2.5   Calcium carbonate phases

Calcium carbonate has three crystalline polymorphs: calcite, aragonite and vaterite, ordered according to their thermodynamic stability at earth surface conditions (5 to 50°C and 1 atm; e.g. Plummer and Busenberg (1982) and pure solutions. Besides to these anhydrous $CaCO_3$ polymorphs, the two hydrous minerals: ikaite ($CaCO_3 \cdot 6H_2O$), monohydrocalcite ($CaCO_3 \cdot H_2O$) and amorphous calcium carbonate (ACC) may be formed.

2.5.1 Occurrence of the calcium carbonate phases

Biogenic induced calcite is preferentially formed by coccoliths, foraminifers, rugose corals, brachiopods, calcareous sponges, octacorals, echinoids, crinoids, asteroids, ophiuroids, bryozoans, archaeocyaths, trilobites, ostracodes, annelid worms, pelecypods, gastropods, crustaceans, calcareous algaes and sponges (Morse and Mackenzie, 1990; Porter, 2007). Biogenic aragonite is formed e.g. by recent (scleractinian) corals, bryozoans, annelid worms, pelecypods, gastropods, crustaceans, molluscs and sponges (Morse and Mackenzie, 1990; Porter, 2007). Biogenic induced vaterite was found in otoliths of several fish species (Gauldie, 1993), gastropod egg shells (Hall et al., 1970), freshwater pearls and spicules from tropical marine organisms. Gastropods use vaterite to repair tissues of fractured shells (Lippmann, 1973; Soldati et al., 2008 and references therein).

Inorganic calcite is the dominant mineral in sinter from springs, cave and hydrothermal solutions as well as in marine and terrestrial evaporates, oolites, and carbonate cements of sediments (Morse and Mackenzie, 1990). Inorganic aragonite precipitation is stimulated by elevated [Mg]/[Ca] ratio in highly saline lakes e.g. in the Dead Sea or Great Salt Lake (Lippmann, 1973, and references therein). Moreover, speleothems may consist of aragonite (e.g. Frisia et al., 2002). Inorganic precipitated vaterite occurs rarely in nature, e.g. in some metamorphic rocks (Strasser, 1989) and sediments (Rowlands and Webster, 1971 and references therein), but it can be involved at the early stage of $CaCO_3$ precipitation (e.g.Rieger et al., 2007). Furthermore vaterite formation is involved in clogging human veins (Kanakis et al., 2001) and in gallstone formation (Palchik and Moroz, 2005) and is found in ooids of fishes like sturgeon, bichir and bowfin (Carlström, 1963).

Monohydrocalcite was discovered in natural calcareous encrustations in Lake Issyk-Kul (Kyrgyzstan) by Tsvetkov in 1959 (Taylor, 1975). It occurs in beach rock surrounding the lakes Fellmongery and Butler in the south-east of South Australia (Taylor, 1975) and as speleothems in small caves of the Frankish Schweiz in Germany (Fischbeck and Müller, 1971). Aerosol transport of small droplets due to thermal gradient may be responsible for the formation of monohydrocalcite (Fischbeck and Müller, 1971). Monohydrocalcite does only occur under dry conditions. Furthermore biochemical genesis by microorganisms (Broughton, 1972 and references therein) may be responsible for monohydrocalcite formation in caves. Fellmongery is a saline lake with a high [Mg]/[Ca] and high pH, where monohydrocalcite was found in the surrounding sediments. Otoliths of tiger shark are composed of monohydrocalcite and aragonite according to Carlström (1963).

Monohydrocalcite occurs also in air conditioner systems or as moonmilk inside caves (Swainson, 2008 and references therein).

Ikaite occurs in deeper ocean basins and in sediments of cold climate shelves and estuaries. Ikaite is formed at temperatures mainly below 4°C, at alkaline conditions and favoured by phosphate (Selleck et al., 2007 and references therein).

Amorphous calcium carbonate (ACC) can be formed by organisms as intermediate storage of calcium (Becker et al., 2003) or as precursor material e.g. for stings of sea urchin or eye lenses of brittle stars and shells of brachiopods (Griesshaber et al., 2009). ACC is a highly metastable phase, which occurs at the very early stage (at the first seconds to minutes) of the calcium-carbonate formation with particle sizes up to 120 nm (Pouget et al., 2009). Magnesium (e.g. Loste et al., 2003), phosphates (Clarkson et al., 1992), negatively charged polymers (Bentov et al., 2010 and references therein) and organic substances like amino acids, glutamate and polysaccharides (e.g. Aizenberg et al., 1996), phosphate rich organic matrix and phosphoamino acids (Bentov et al., 2010) stabilize ACC.

Although the skeleton $CaCO_3$ polymorphs are not directly influenced by the modern seawater chemistry, it seems to be influenced by the ancient chemistry which occurred during the first appearance of the taxon skeleton. This can be explained by the larger difficulty to establish the skeleton polymorph which is not favoured by the seawater chemistry (PORTER, 2007). On the other hand the animals seem to change not their $CaCO_3$ skeleton, if it is optimized once, although the sea water chemistry changes.

2.5.2 Physical properties and structure of the $CaCO_3$ phases

The mineralogical, physical and isotopic properties of these $CaCO_3$ phases are summarized in Tab. 2-2. ACC has a density ρ_{ACC} of 1.48 g cm^{-3} (Cölfen and Völkel, 2006). It is obvious that the density becomes smaller with increasing solubility, except of aragonite. Calcite and monohydrocalcite crystallize in the trigonal system, vaterite in the hexagonal system. However the structure of vaterite is still in discussion (see e.g. Wang and Becker, 2009) as an orthorhombic structure is also considered. This might be caused by the disordered structure of the randomly distributed carbonate ions parallel to c-axis. The carbonate positions are statistically and incompletely occupied (see Kamhi, 1963, Meyer, 1969, Wang and Becker, 2009). The cell size of vaterite has increased over the years from a ≈ 4.1Å, c ≈ 8.5 Å (Olshausen, 1925 as written in Meyer, 1969) over a = 7.16 Å, c = 16.98 Å (Kamhi, 1963) to a = 7.29 Å, c = 25.302 Å (Wang and Becker, 2009). However vaterite has despites to its large coordination number of 8 the lowest density because of its awkwardly structure (Meyer, 1969). Aragonite has an orthorhombic structure and ikaite is monoclinic.

The different symmetries are caused by different arrangements of the atoms. The carbonate group is orthogonally arranged to the optical axis c in calcite and aragonite. In calcite all carbonate groups are aligned in the same direction within one plane, which alternates between the planes. Contrary, the carbonate groups in the two planes between two Ca planes of aragonite have two different directions. The carbonate groups between to calcium ions in aragonite are also slightly shifted, whereas in

calcite all carbonate groups are in the same plane. In vaterite the carbonate groups are ordered in the direction of the optical axis c and they have several directions (Wang and Becker, 2009). Respective XRD pattern are shown and discussed in chapter 5.1.

Tab. 2-2: Mineralogical data of calcite (Maslen et al., 1993), aragonite (Devilliers, 1971), vaterite (Kamhi, 1963), monohydrocalcite (Swainson, 2008) and ikaite (Hesse et al., 1983). Densities of these solid phases are from Morse and Mackenzie (1990). * Different structure and coordination number occur for vaterite (e.g. Meyer, 1969). The given coordination number is related to the given structure.

Mineral	Calcite	Aragonite	Vaterite	Mono-hydrocalcite	Ikaite
Chemical Formula	$CaCO_3$	$CaCO_3$	$CaCO_3$	$CaCO_3 \cdot H_2O$	$CaCO_3 \cdot 6H_2O$
Crystal class	Ditrigonal – Scaleno-hedral	Ortho-rhombic-Dipyramidal	Dihexagonal–Dipyramidal	Trigonal-Pyramidal	Monoclinic-Prismatic
Symmetry elements	3 2/m	2/m 2/m 2/m	6/m 2/m 2/m	3	2/m
Space group	$R\bar{3}c$	P m c n	P 63/mmc	$P3_1$	C 2/c
Unit cell: a in Å	4.99	4.96	7.16	10.55	8.79
b in Å	4.99	7.97	7.16	10.55	8.31
c in Å	17.06	5.74	16.98	7.56	11.02
α in °	90	90	90	90	90
β in °	90	90	90	90	110.5
γ in °	120	90	120	120	90
Density ρ in g cm^{-3}	2.71	2.93	2.54	2.43	1.77
V_{cell} in Å^3	368	227	749	730	745
Ca coordination	[6]	[9]	[8] *	[8]	[8]

The in-plane bending peak is a double peak in FTIR pattern for aragonite (see Tab. 2-3), which has for aragonite also the smallest wave number of all peaks. This indicates the smaller bonding energy between some carbon and oxygen ions in aragonite. The double peak is related to a smaller symmetry for the carbonation of aragonite. It is caused by two slightly different C-O distances and the non-polar carbonate, where the oxygen is 0.03 to 0.02 Å out of the plane of the oxygen atoms (De Villiers, 1971; Ungaretti, 1971; Antao and Hassan, 2009). Calcite and vaterite have a double generated peak, which indicates an undistorted and planar carbonate-ion. Vaterite has the largest in-plane carbonate vibration frequencies and wave number ν_4 and therefore a stronger bounding between oxygen and carbon in directions within the plane. Aragonite has also the smallest out of plane bending wavenumber ν_2 compared to vaterite and calcite, both latter polymorphs have similar wavenumbers (see Tab. 2-3). Contrary, the asymmetric stretching wave number/ frequency/ energy is higher for aragonite compared to vaterite and calcite. Latter minerals have very similar asymmetric stretching frequencies of the carbonate ions; the stretching frequency of the carbonate ions in vaterite is slightly higher than the stretching frequency of the carbonate group in calcite. The symmetric stretching ν_1 has a higher frequency and energy for vaterite than for aragonite. ν_1 streching should not exist for calcites due to the symmetric charge distribution of the carbonate

group and the missing change in the dipole momentum during vibration, which results in an IR-inactivity. However, a small peak is also visible, especially for Mg-calcite with higher Mg content. Ikaite and monohydrocalcite have both an eight fold coordination of the calcium atoms with their neighbour oxygen atoms. Ikaite has six independent bonds to O atoms of the water molecules and two bonds to two different O atoms at one carbonate group. The Ca atom of monohydrocalcite has bonds to two water molecules and four neighbour carbonate molecules, two carbonate molecules are bond with two O atoms to one Ca and the other two carbonate groups are bound by one oxygen atom (Swainson, 2008). Respective wavenumber in the FTIR spectra of the hydrated $CaCO_3$ phases are also given in Tab. 2-3.

Tab. 2-3: Wavenumbers in cm^{-1} for different $CaCO_3$ phases, ν_1: symmetric stretching mode, ν_2: out-of-plane bending, ν_3: asymmetric stretching and ν_4: in-plane bending mode of C-O in carbonate group.

	Ref.	ν_1	ν_2	ν_{3a}	ν_{3b}	ν_{4a}	ν_{4b}	$\nu_{HOH}(A_1)$	$\nu_{OH}(A_1)$	$\nu_{OH}(B_2)$	$\nu_{OH}(B_2)$
Calcite	1	-	877	1420	-	711	-				
Aragonite	1	1083	854	1488	1440	713	700				
Vaterite	1	1089	877,873	1487	1445	746	738				
Monohydro-calcite	2	1063	872	1492	1401	762	698	1700	3236	3327	3400
Ikaite	2	1085	876	1425	1411	743	720	1673	3216	3119, 3361, 3404	3468, 3502, 3543
ACC	1	1067	864	1490	1425	725	690				

1: Andersen and Breceivic (1991)

2: Coleyshaw et al. (2003)

2.5.3 Thermodynamic stability of the calcium carbonate phases

Plummer and Busenberg (1982) determined the values of the following constants for calcite, aragonite and vaterite in the temperature range between 0 and 90°C. The solubility products for ACC and ikaite were determined by Clarkson et al. (1992). A least square fit with the data of Kralj and Brecevic (1995) was carried out to calculate a corresponding formula for monohydrocalcite (Tab. 2-4).

Tab. 2-4: Solubility product for hydrous and anhydrous $CaCO_3$ phases (K_{sp}) as a function of temperature (T in K) According to the expression $\log (K_{sp}) = a - b \cdot T + c \cdot T^{-1} + d \cdot \log(T)$.

Phase	Ref.	a	b	c	d	T (°C)
Calcite	1	-171.9065	-0.077993	2839.319	71.595	0 - 90
Aragonite	1	-171.9773	-0.077993	2903.293	71.595	0 - 90
Vaterite	1	-172.1295	-0.077996	3074.688	71.595	0 - 90
ACC	2	-10.224	-	1247	-	16 - 60
Monohydrocalcite	3*	-149.0744	-0.011493	-260	71.558	15 – 50
Ikaite	2	-0.9336	-	-1696	-	4 – 39

1: Plummer and Busenberg (1982)

2: Clarkson et al. (1992)

3*: coefficients were calculated from data of Kralj and Brecevic (1995) by least square method

Calcite is the most stabile phase at Earth surface conditions (25°C, 1 atm), followed by aragonite, vaterite, monohydrocalcite and ACC. The solubility of these phases decreases with increasing temperature. Ikaite occurs at low temperature and is more soluble than vaterite. In contrast to the other phases the solubility of ikaite increases with increasing temperature. The Gibb's free energy of formation ΔG_r^0, enthalpy ΔH_r^0, heat capacity ΔC_{pr}^0 and entropy ΔS_r^0 at standard conditions can be calculated from the solubility coefficient by the equations (2-24) to (2-27) (see also Plummer and Busenberg, 1982).

$$\Delta G_r^0 = -RT\ln K = -\alpha R(aT + bT^2 + c + \frac{dT\ln T}{\alpha})$$ (2-24)

$$\Delta H_r^0 = RT^2\frac{d\ln K}{dT} = \alpha R(bT^2 - c + \frac{dT}{\alpha})$$ (2-25)

$$\Delta c_{pr}^0 = \frac{\partial \Delta H_r^0}{\partial T} = \alpha R(2bT + \frac{d}{\alpha})$$ (2-26)

$$\Delta S_r^0 = -\frac{\partial \Delta G_r^0}{\partial T} = \alpha R(aT + 2bT + \frac{d}{\alpha}(1 + \ln T))$$ (2-27)

The conversion factor α is 2.3026 and R is the gas constant (8.3145 J K^{-1} mol^{-1}), T is the temperature in K and the factors a,b,c and d are given in Tab. 2-4 (Plummer and Busenberg, 1982). The observed entropy change for the transformation of aragonite to calcite at 25°C and 1 atm is 3.7 J mol^{-1} K^{-1} (Stumm and Morgan, 1996).

2.5.4 Surface and lattice characteristics of CaCO$_3$ polymorphs

Ca-O bond in CaCO$_3$ has mainly an ionic character (I.C. is 79%; covalent contribution is 21%) and can be calculated according to following equation (Donald, 2004):

$$\text{I.C.} = (1\text{-e}^{-0.25(\Delta X)^2})100 \qquad \text{given in } \%$$ (2-28)

where ΔX is the difference in the electro-negativities of the components. The Ca-O bond is four times weaker than the C-O bond (Reeder, 1983; Gussone et al., 2005). Ca-O bonds are about 60% stronger in the calcite structure than in the aragonite structure (Zheng, 1999; Gussone et al., 2005). Photoemission spectra indicate that aragonite has bond energies of 347.4, 289.8 and 531.7 eV for Ca 2p, C 1s and O 1s, respectively. The bond energies are 347.1, 289.6 and 531.6 eV for calcite and 346.9, 289.5 and 531.4 eV for vaterite. These differences in the bonding energies can be explained by the different arrangement of the atoms. According to the lattice energy, aragonite would be the most stable phase for large crystals (at T=0 K). In fact calcite is more stable due to its higher entropy

content at elevated temperatures (e.g. T=273 K). The high bond energy for Ca 2p in aragonite indicates that the surface is dominated by carbonate, while calcite and vaterite contain also OH⁻ species at the surface. The lower bond energy of calcite compared to aragonite is attributed to the calcium which is linked to OH⁻ at the surface. Gopinath et. al. (2002) suggested that this hydroxyl species at the surface of rhombohedra $CaCO_3$ might be a further reason for calcite's high stability. The surface of aragonite has the lowest Ca content of all $CaCO_3$ polymporphs, but the highest oxygen content. Calcite has the highest Ca but lowest C content at the surface, while vaterite has the highest carbon and lowest oxygen content on its surface (Gopinath et al., 2002) .

Besides to the bond energy, the formation energies of crystals depend also on the surface energy γ especially at small crystal sizes in the nucleation stage. The surface energy γ for calcite surface is the lowest (0.59 J m^{-2}) according to Abdel-Aal et al. (2002) and therefore calcite is the most stable phase (De Leeuw and Parker, 1998). DeLeeuw and Parker (1998) have listed different surface energies and hydration energies.) The charge density at the two homo charged calcium planes of vaterite: (001) and (100) is with 6.7 calcium ions/nm² larger than the (001) calcium plane of calcite with a charge density of 4.5 calcium ions/nm² (Tong et al., 2004 and references therein).

$CaCO_{3(aq)}$ may be directly adsorbed on the calcium carbonate due to its ~ 20 times higher water exchange rate compared to $Ca^{2+}_{(aq)}$ (Nilsson and Sternbeck, 1999). Several studies are related to surface speciation of calcite (e.g. Nilsson and Sternbeck, 1999; Pokrovsky et al., 1999b; Pokrovsky et al., 1999a; Pokrovsky et al., 2000; Villegas-Jimenez et al., 2009; Heberling et al., 2011) and respective proton/calcium exchange behaviour (Villegas-Jimenez et al., 2009). The distribution of surface species depends mainly on the pH as indicated by high-resolution X-ray reflectivety (Fenter et al., 2000). Stipp and Hochella (1991) found spectral evidence by X-ray photoelectron spectroscopy (XPS) for two surface sides, $>CaOH^0$ and $>CO_3H^0$, at the hydrated calcite surface. The following surface complexes can be formed: $>CO_3H^0$, $>CO_3^-$, $>CO_3Me^+$, $>MeOH_2^+$, $>MeOH^0$, $>MeO^-$, $>MeHCO_3^0$ and $>MeCO_3^-$, where respective reactions and stability constants for different metal ions Me (Ca, Mg, Sr, Ba, Mn, Be, Co, Ni, Zn, Cd and Pb) are given by VanCappellen (1993), Pokrovsky et al. (1999a), Pokrovsky et al. (1999b), and Pokrovsky and Schott (2002). A Basic-Stern SCM model was developed by Heberling et al. (2011) for modelling of zetapotential data. Two ordered H_2O layers were found considering a small tilt of about 4° of the surface carbonate ions toward the calcite surface.

2.5.5 Amorphous calcium carbonate

Amorphous calcium carbonate (ACC) was found to be involved in the first stages of calcium carbonate formation (Pouget et al., 2009). It has a local order at the Å scale according to Rodriguez-Blanco (2008) and Michel (2008). The latter found a structural coherence of shorter than 15 Å. ACC with different short range orders can be distinguished. This short range orders are related to the crystallisation product. Gebauer (2008) found in his experiments two different types, ACC 1 and ACC II, which differ in their bonding strength (Gebauer et al., 2008). The more stable ACC I and less stable ACC II have a short range order comparable to calcite and vaterite, respectively. ACC I and ACC II were therefore called proto-calcite ACC (pc-ACC) and proto-vaterite ACC (pv-ACC) determined by TEM and Small-angle X-ray scattering (SAXS) (Gebauer et al., 2010). Furthermore Lam et al. (2007) found different short-range order (coordination number, Ca-O, Ca-Ca interatomic distances) of ACC by X-Ray Adsorption Spectroscopy (EXAFS and XANES), which are related to additives in the solution. Mg-ACC showed thereby a short range order similar to aragonite and monohydrocalcite, while Pasp-ACC displays a short range order of vaterite (Lam et al., 2007). This is slightly controversial to Michel et al. (2008), who pointed out that the short and intermediate-range structure does not fit to any calcium carbonate phases. However these authors found by NMR measurements also that most of hydrogen is present as structural H_2O and a minority (7±3%) as OH^-. Furthermore most of the carbonate in ACC is monodentate (Michel et al., 2008).

The stabilisation of ACC by Mg is well known. It is caused by high dehydration energy of Mg. Magnesium has to be partly dehydrated to be incorporated into hydrous calcium carbonate like ACC, whereas Mg has to be completely dehydrated to be incorporated in anhydrous calcium carbonate (e.g. calcite) (Loste E. et al., 2003). In consequence ACC is longer stable in presence of Mg, because more energy is necessary for the dehydration of Mg compared to Ca and the transformation from ACC to other $CaCO_3$ phases.

2.6 Inhibition of calcium carbonate

Inhibitiors are substances which avoid or retard processes like e.g. precipitation of calcium carbonate. They are either used consciously or they are present in nature and act unwittingly.

Inhibitors act as crystal modifier, dispersant and/or threshold inhibitor. As crystal modifier the inhibitor is incorporated or adsorbed on the solid surface and causes distortion or does not admit formation of a regular crystalline lattice. If the inhibitor charges the surface, it may prevent agglomeration due to electrostatic charge repulsion. A threshold inhibitor blocks active crystal growth sites and therefore crystal growth (Chen, 2005).

Inhibitors can influence the crystallisation by following processes (Chen, 2005 and references therein):

- Ion pairing and complex formation
  The added inhibitor forms aqueous complexes with the reacting ions in the solution. This changes the activity coefficients of the solutes (carbonate and calcium species) and the saturation state of the solid phases in the solution (Morse, 1983).

- Influencing the pre-nucleation cluster formation
- Influencing the homogeneous or heterogeneous nucleation and crystal growth
- Incorporation
  The inhibitor substance can be incorporated into the calcium carbonate crystal and modify the crystal properties by defects. The defects may decrease the stability of these crystals.

- Adsorption of inhibitor on nuclei
  The inhibitor substance can adsorb on the reacting nuclei or crystal surface. This can cause a concurrent increase in carbonate concentration at the surface, if the inhibitor is positively charged, or an increase in the calcium concentration at the surface, if the inhibitor is negatively charged. Adsorption of the inhibitor is preferred at sites with higher energy, where usually also the crystal growth takes place (Morse, 1983). In case of a positively charged inhibitor I^+ the surface coverage θ_{Ca} of adsorbed Ca^{2+} cations is given by the expression

$$\theta_{Ca} = \frac{K_{Ca}[Ca^{2+}]_0}{1 + K_{Ca}[Ca^{2+}]_0 + K_I[I^+]_0} \qquad (\,2\text{-}29\,)$$

  K_{Ca} and K_I imply the adsorption equilibrium constants for Ca and the inhibitor, respectively. $[Ca^{2+}]_0$ and $[I^+]_0$ are the concentration of Ca and inhibitor in the layer above the surface (Compton and Brown, 1994).

- Agglomeration of crystals

Two dominant models describe the dependence of the concentration of impurities (Davis et al., 2000):

1. According to the impurity adsorption or step pinning theory, the inhibitor is adsorbed to step-edges or accumulates on terraces. A higher supersaturation is necessary to *break through the chain of adsorbed impurities* (Davis et al., 2000). The value of this threshold supersaturation depends on the amount and kind of impurities. The step velocity of a pure system is reached soon when the supersaturation threshold is exceeded (Davis et al., 2000).

2. The impurity incorporation theory is based on the capture of impurities by growing steps or the incorporation of the impurity molecules at a kink site along a step edge. In consequence the internal free energy and the crystal solubility increase. Higher solubility results in a rise of the equilibrium activity and in consequence the step velocity v_s decreases according to the following equation:

$$v_s = \beta\omega(a - a_e) \qquad (\,2\text{-}30)$$

where β is the kinetic coefficient, ω the specific molecular volume (6.13 10^{-23} cm³ per molecule for calcite), a is the activity of the solid forming ion in the solution and a_e the equilibrium activity of them (Davis et al., 2000).

The following inhibitors for calcium carbonate formation are known (Wada et al., 1995; Gutjahr et al., 1996; Lebron and Suarez, 1998; Hoch et al., 2000 and references therein)

- Mg, Fe, Cu, Zn ions
- Phosphates (especially pyrophosphate and triphosphate)
- Phosphorus compounds (Phosphino polycarboxylic acid)
- Chelates like EDTA
- (Poly)carboxyl acids (e.g. acetic acid, citric acid, malic acid)
- Polyaspartate, polyaspartic acid, polysuccinimide
- Polyglutamic acid, polycerylic acid (biomin.)
- Polysaccharide (inulin)
- Humic acids and amino acids
- Dissolved organic mater (e.g. fulvic acid)

2.6.1 Inhibition effect of polyaspartic acid

Pasp is a macromolecule and belongs to the polyanionic polyamino acid which has several free carboxylic groups (Fig. 2-4).
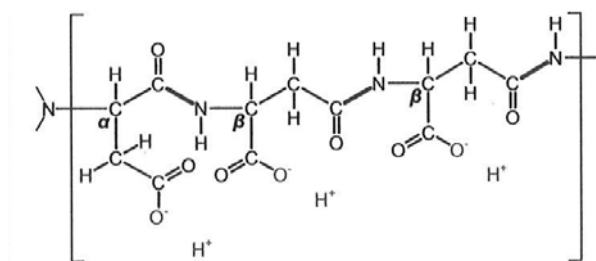
Fig. 2-4: **Completely dissociated poly α,β-DL-aspartic acid (pH $\geq$ 7) (Gamisch and Girmscheid, 2007).**

Pasp has been reported as a structural and functional analogue of sub domains of proteins which control biomineralisation (Joentgen et al., 2002). Aspartic acid containing proteins are used by crustacean and corals to avoid calcification in sea water and aspartic acid is found in human dentin. Furthermore L-aspartic acid occurs e.g. in potatoes, eggs, beef, cow milk, rice and wheat with decreasing amount from 16 to 5 wt. % (Knapp, 2010) and asparagus tips (68 μmol g^{-1} dry weight; Lill et al., 1990). It is a non essential amino acid, because the plants, animals and human body can produce it by themselves (Knapp, 2010). It is used as potassium and magnesium aspartate for infusions, as precursor for Aspartam (=artificial sweetener or against bitterness in medicine), for special diets (Wagenknecht and Knapp, 2010) and for Mg-therapy (Schmidbaur et al., 1990). This natural aspartic acid consists only of α moieties, while the artificial Pasp (DS100) used in this study has α and β linked moieties in ratio of approx. 30:70 with a molar weight of 2000-3000 mol%. Artificial Pasp is formed by *thermal polymerization from aspartic acid followed by alkaline*

hydrolysis (Gamisch and Girmscheid, 2007). Aspartic acid itself can be obtained by e.g. a multistep reaction from maleic acid anhydride (Gamisch and Girmscheid, 2007 and references therein).

Polycarboxylic acids are known to complex strongly Ca. On the other hand the rigidity of the peptide backbone of Pasp makes it difficult to complex a calcium ion with two carboxyl groups of the same Pasp molecules (Aschauer et al., 2010) which leads to weaker aqueous complexes. Pasp forms only outer sphere complexes with Ca^{2+} ions, which results in shorter relaxation times and the carboxylic groups remain reactive. The bonding strength between Pasp and Ca of a crystal lattice increases when the ionic distances in the crystal structure are similar to the distances of the carboxyl-groups of the polyaspartic acid (Gamisch and Girmscheid, 2007 and references therein). Generally amino acids adsorb preferentially on surface-step edges which offers the best geometric and chemical fit to them (Orme et al., 2001). This occurs e.g. at the (0001) and $(1\bar{1}00)$ surface of calcite. The calculated adsorption energy of Pasp to a calcite surface is -13.04 eV (-1.3 eV per carboxyl group). Free carboxyl groups of Pasp react at calcite surface with its terminal end and its backbone remains upright (Aschauer et al., 2010).

Pasp acts as inhibitor by adsorption on the calcium carbonate surface, preferentially on active kinks and edges, where also $CaCO_3$ growth takes place. Therefore only small amounts of Pasp are necessary for inhibition of nucleation and crystal growth. The crystal nuclei remain small and dissolve easier (Sikes et al., 1994).

Obtuse sides of calcites are energetically favoured for adsorption of large Pasp macromolecules. According to computational calculations, less energy is necessary for the dehydration of surface bond water at the obtuse side, because the footprint of Pasp molecules is smaller at the obtuse side than at the acute side (Elhadj et al., 2005; Gamisch and Girmscheid, 2007). Adsorbed polyaspartic acid inhibits the adsorption of new lattice atoms and causes negatively charged surfaces which repel each other. This can result into a dispersion of the calcium carbonates. Calcium-polyaspartate complexes are thermodynamically less stabile. Pasp is completely dissociated at pH of 8 (Fig. 2-5).

n	Linie	Dissoziationsgrad α_n	Dissoziationskonstanten [1]
1	— — —	$\alpha_1 = [H_4L] / [PASP]$	$pK_1 = 2,27$
2	- - - - -	$\alpha_2 = [H_3L^-] / [PASP]$	$pK_2 = 3,60$
3	··········	$\alpha_3 = [H_2L^{2-}] / [PASP]$	$pK_3 = 4,09$
4	—·—··—··—	$\alpha_4 = [HL^{3-}] / [PASP]$	$pK_4 = 5,17$
5	——	$\alpha_5 = [L^{4-}] / [PASP]$	$[PASP] = [H_4L] + [H_3L^-] + [H_2L^{2-}] + [HL^{3-}] + [L^{4-}]$
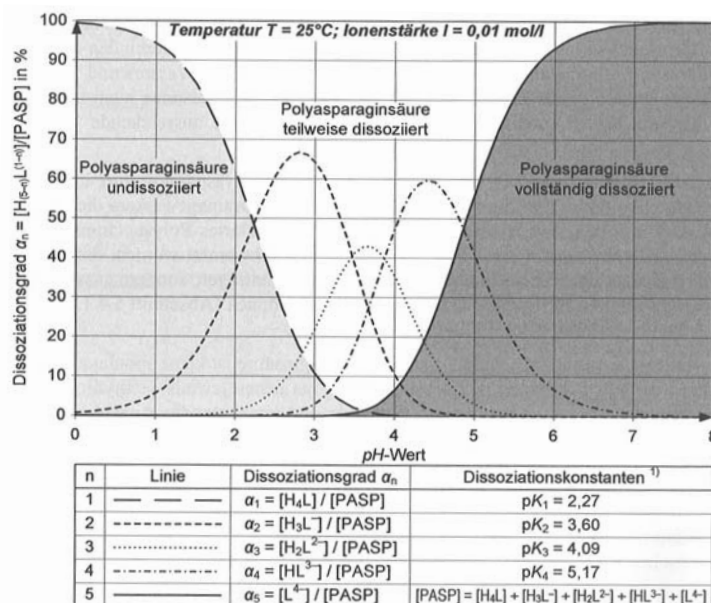
Fig. 2-5: Dissociation of polyaspartic acid (Wu and Grant, 2002; Gamisch and Girmscheid, 2007)

2.6.2 Inhibition effect of magnesium

Magnesium impurities can affect the $CaCO_3$ properties by slow dehydration, by adsorption of Mg at the $CaCO_3$ surface resulting in step blocking and by Mg incorporation, which enhances the solubility.

1. The surface charge density of Mg^{2+} is larger than that for Ca^{2+}, due to the smaller ionic radius and similar charge of Mg^{2+} compared to Ca^{2+}. The water dipoles are bound in consequence approximately 20% stronger to Mg^{2+} than to Ca^{2+} and the (de)hydration energy for Mg^{2+} is higher. The hydration energy of calcium and magnesium is 102 and 120 kJ mol^{-1}, respectively. The rate of calcite formation decreases with increasing Mg concentration (Lippmann, 1973) due to the higher hydration energy, which has to exceed by Mg incorporation.

2. Mg adsorb on the mineral surface in competition with Ca (Compton and Brown, 1994). The dissolution rate D_{net} can be calculated by the equation

$$D_{net} = k_f(1-\theta_{Ca})(1-\theta_{CO_3}) - k_b\theta_{Ca}\theta_{CO_3} \qquad (\,2\text{-}31\,)$$

with the surface coverage of adsorbed ion A θ_A

$$\theta_A = \frac{K_A[A]_0}{1+K_A[A]_0} \qquad (\,2\text{-}32\,)$$

In case of a positively charged inhibitor the surface coverage of adsorbed Ca^{2+} cations is given by the equation

$$\theta_{Ca} = \frac{K_{Ca}[Ca^{2+}]_0}{1+K_{Ca}[Ca^{2+}]_0 + K_{Mg}[Mg^{2+}]_0} \qquad (\,2\text{-}33\,)$$

$K_{Mg}[Mg^{2+}]_0$ indicate the influence of magnesium. Compton and Brown (1994) found the following parameters for the equation (2-33): $K_{Ca}=10^6$ cm³ mol^{-1} and $K_{Mg}=2.3\ 10^5$ cm³ mol^{-1}. For instance for a solution with 50 mM Mg^{2+} and 10 mM Ca^{2+} the surface coverage would be 53% Mg^{2+} and 47% Ca^{2+} (Compton and Brown, 1994).

3. Magnesium incorporates easily into calcite, due to the divalent charge and smaller but similar ionic radius of Mg^{2+} (0.72 Å) in comparison to Ca^{2+} (1.0 Å; Shannon, 1976). The 6 fold coordination of Ca^{2+} in the structure of calcite allows the incorporation of smaller divalent metal ions. Aragonite incorporates less Mg^{2+}, because this small ion does not fit into its 9 fold coordinated orthorhombic structure. Vaterite has 8 fold coordination, but a lower density and may allow Mg^{2+} incorporation.

The Mg concentration in Mg-calcite determines its solubility (Busenberg and Plummer, 1989; Davis et al., 2000). The Mg incorporation increases with increasing temperature, because the substitution of Ca^{2+} with Mg^{2+} is endothermic and more favoured at higher temperature. Davis et al. (2000) demonstrated by AFM measurements an increase in the solubility of Mg calcite from $10^{-8.48}$ to $10^{-8.2}$ when Mg increases to 3.5 mol% in the solid. Macroscopic measurements show a change in the solubility from $10^{-8.48}$ to $10^{-8.28}$ by an increase of Mg of 15 mol% (Busenberg and Plummer, 1989). Nevertheless the decrease in the solubility is due to the strain in the solid lattice, which is caused by incorporation of Mg. This results into an increasing use of the internal free energy of the crystal. AFM measurements of Davis (2000) confirm the second model for the impurity effect of Mg.

2.7   Incorporation of magnesium and strontium

Strontium and magnesium signatures of carbonate achieve like marine and limnic sediments, speleothems and travertine are widely used for the reconstruction of paleo-environments. The temperature, salinity, precipitation rate dependency of the Mg and Sr incorporation and effects of different compositions were verified by several studies (e.g. Clarke and Wheeler, 1922; Kinsman and Holland, 1969; Veizer et al., 1971; Engstrom and Nelson, 1991; Lea et al., 1999; Elderfield et al., 2006; Gagnon et al., 2007; Fairchild and Treble, 2009; Elderfield, 2010). Different $CaCO_3$ polymorphs show thereby different incorporation behaviour.
Mg^{2+} (0.72 Å, M=24.31 g mol^{-1}) and Sr^{2+} (1.12Å, M=87.62 g mol^{-1}) can substitute for Ca^{2+} (1.0 Å; M=40.08 g mol^{-1}) in calcium carbonate phases. This radii and molar masses are given in Shannon (1976) and Schwister et al. (1999), respectively.
The isomorphic substitution of Ca^{2+} in $CaCO_3$ by divalent metal ions Me^{2+} (e.g. Mg^{2+} and Sr^{2+}) can be followed by the equation

$$(1-n)Ca^{2+} + nMe^{2+} + CO_3^{2-} = Ca_{1-n}Me_nCO_3 \qquad (\text{ 2-34 })$$

The value of n depends on distinct $CaCO_3$ polymorph and environmental conditions during formation.
The distribution coefficient of specific elements between the solid and aqueous phase contains both adsorption and incorporation of the ion on/into the solid phase (surface). The distribution or partitioning coefficient of a metal Me between the solution and the calcium carbonate polymorph can be followed by the Nernst distribution law

$$D_{Me} = \frac{\left(\dfrac{[Me]}{[Ca]}\right)_s}{\left(\dfrac{[Me]}{[Ca]}\right)_{aq}} \qquad (\text{ 2-35 })$$

(e.g. Henderson and Kracek, 1927; Usdowski, 1975). The ratio of Me to Ca concentrations of the solid (index s) is divided by the ratio of the molar Me to Ca concentration in the solution (index aq).

This approach is valid if the molar concentration ratios are similar within the error to the activity ratios.

Equation (2-35) is only valid in open systems with respect to the aqueous solution. In closed systems the evolution of the individual concentrations over the time has to be considered according to the equation

$$\left(\frac{[Me]}{[Ca]}\right)_s = \left(\frac{[Me]_0}{[Ca]_0}\right)_{aq} \frac{1 - \left(\frac{[Ca]}{[Ca]_0}\right)_{aq}^{D_{Me}}}{1 - \left(\frac{[Ca]}{[Ca]_0}\right)_{aq}} \qquad (\ 2\text{-}36\ )$$

(Usdowski, 1975; Böttcher and Dietzel, 2010). This equation considers the overall bulk solid ([Me]/[Ca])$_s$ after a certain crystallisation interval, the initial Me to Ca ratio in the solution ([Me]$_0$/[Ca]$_0$)$_{aq}$ and the evolution of Ca concentration, which is expressed as ratio of the Ca concentration in the solution after a certain crystallisation interval to the initial calcium concentration in the solution ([Ca]/[Ca]$_0$)$_{aq}$. The explicite equation for D$_{Me}$ is given by:

$$D_{Me} = \frac{\log\left\{1 - \frac{\left(\frac{[Me]}{[Ca]}\right)_s}{\left(\frac{[Me]_0}{[Ca]_0}\right)_{aq}}\left[1 - \left(\frac{[Ca]}{[Ca]_0}\right)_{aq}\right]\right\}}{\log\left[\left(\frac{[Ca]}{[Ca]_0}\right)_{aq}\right]} \qquad (\ 2\text{-}37\ )$$

Generally, the tendency for the incorporation of a metal into carbonate precipitates is higher assuming the same structure, if the solubility of the end member of the metal carbonate is lower (Astilleros et al., 2006).

Magnesium is preferentially incorporated into calcite (e.g. D$_{Mg^{2+}\ Cc} \approx 0.015$ to 0.03, Morse and Bender, 1990), because of the small size of Mg^{2+} ion which matches quite well to the 6-fold coordination of Ca^{2+} in the calcite structure. Magnesium incorporation increases with increasing temperature (e.g. Mucci, 1987; Oomori et al., 1987; Lea et al., 1999). Furthermore more Mg is incorporated at higher supersaturation of fictive MgCO$_3$ of the solution (Pokrovsky, 1998). Elderfield (2006) found also a positive correlation between incorporated Mg in benthic foraminifers and carbonate concentration of surrounding ocean water.

Typical D$_{Sr}$ values for calcite are about 0.2 (0.06 to 0.4) (Lorens, 1981; Zhong and Mucci, 1989). Generally more Sr incorporates at higher precipitation rates (Lorens, 1981; Tesoriero and Pankow, 1996; Tang et al., 2008b). The temperature dependency is affected by the precipitation rate. At high precipitation rates D$_{Sr}$ between calcite and aqueous solution is negatively correlated with temperatures (Tang et al., 2008), but this temperature dependency is reverse at lower precipitation rates close to equilibrium, where the Sr uptake increases with increasing temperature (Tang et al., 2008). The positive temperature correlation was also found in coccoliths (e.g. Stoll et al., 2002) and foraminifers (Lea et al., 1999). Tang et al. (2008) have interpreted this behaviour by the higher diffusivity of Sr at elevated temperatures in the surface entrapment model of Watson (2004). Higher Mg concentrations in the solution cause also a higher Sr incorporation, but lower D$_{Mg}$ value in seeded experiments (Mucci and Morse, 1983; Morse and Bender, 1990). Furthermore carboxylate

molecules like aspartic acid, glutamic acid, malonic, citric, oxydiacetic and D-tartaric acid increase the Mg^{2+} incorporation into e.g. ACC (Wang et al., 2009). The larger Sr ion incorporates mainly at the obtuse side of calcite crystals, while Mg incorporates at the acute side (Paquette and Reeder, 1995; Davis et al., 2004). The lattice of calcite becomes significantly smaller in case of the incorporation of Mg (e.g. Goldsmith et al., 1958; Goldsmith et al., 1961; Bischoff et al., 1983), due to the smaller bond length (Mg-O about 2.12 Å) compared to Ca (Ca-O about 2.35 Å) (Finch and Allison, 2008). This peak shift, determined in powder X-ray diffraction (XRD) patter can be used for the analyses of the amount of incorporated Mg into the calcite lattice (Goldsmith et al., 1958, Goldsmith et al., 1961).

Aragonite incorporates less Mg ($D_{Mg^{2+} Ar} = 10^{-3}$ to 10^{-4}; Zhong and Mucci, 1989; Gabitov et al., 2008), because the small Mg ion does not fit into the orthorhombic structure with the 9 fold coordinated metal ion. Experiments from Gabitov et al. (2008) indicate an increase of the Mg incorporation with increasing precipitation rate. In contrast Sr fits very well into the aragonite structure and is incorporated into aragonite with the same concentration, like it occurs in the solution or even higher ($D_{Sr} \geq 1$, e.g. Dietzel et al., 2004). Strontium incorporation into aragonite decreases with increasing temperature (e.g. Kinsman and Holland, 1969; Cohen et al., 2002; Dietzel et al., 2004). D_{Mg} between vaterite and aqueous solution is about 0.04 to 0.1 (Sawada et al., 1990, Brečević et al., 1996). Magnesium ion (1.7 mol%) has not perturbed the vaterite structure in the experiments of Brecevic et al. (1996).

2.8   Stabile isotopes

Stable isotopes have a broad application in geochemistry and environmental studis. Their application comprises process identification, geothermometry, determination of the provenience and flow path evolution, e.g. identification of biological cycles (e.g. Kendall and Doctor, 2004).

Isotopes are atoms with equal proton numbers, but different neutron numbers. The mass number of isotopes changes, while the element remains the same. The different masses cause a change in their physical and chemical properties. For instance Raman and IR-spectra are shifted by the replacement of one isotope by another isotope of the same element. Chemical reaction rates are related to isotope composition. Melting and boiling point increase for $D_2^{16}O$ and $H_2^{18}O$ (Hoefs, 2009). Light isotopes form weaker bonds with their neighbars, as it can be shown by quantum mechanical calculation (see Bigeleisen and Mayer, 1947; Schauble, 2009; Hoefs, 2009 and references therein).

The isotopic ratio is the concentration of the rare isotope [x_A] to the more frequent isotope [x_B] (Appelo and Postma, 2006):

$$R_s = \frac{[x_A]}{[x_B]} \qquad\qquad (2\text{-}38)$$

e.g. $R_s = [^{13}C]/[^{12}C]$.

This ratio of a sample R_s is divided by the ratio of a standard material, R_{std}, multiplied by 1000 and given in ‰ according to expression

$$\delta_s = \frac{R_s - R_{Std.}}{R_{Std.}} 1000 = \left(\frac{R_s}{R_{Std.}} - 1 \right) 1000 \qquad (2\text{-}39)$$

Negative δ-values mean a depletion of the rare isotope versus the standard.

2.8.1 Isotopic fractionation

Isotopic fraction is the *partition of isotopes between two substances or two phases of the same substance with different isotope ratios* (Hoefs, 2009). It can be caused by chemical, physical and biological processes, where the isotopes react slightly different because of their masses.

Isotopic exchange reactions, kinetic and physical processes like crystallization, adsorption, desorption and diffusion of molecules due to concentration and temperature gradients can cause isotopic fractionation (Hoefs, 2009). The kinetic fractionation is thereby caused by the mass dependent velocity.

Isotopic exchange reaction comprise no phase transformation, instead of it a change of the isotopic distribution between different chemical substances, between different phases or between individual molecules takes place. The fractionation factor $\alpha_{A\text{-}B}$ is used for the description of the distribution of isotopes between the two phases A and B. It is calculated from the isotopic ratios R_A and R_B of the phases A and B, respectively.

$$\alpha_{A-B} = \frac{R_A}{R_B} \qquad (2\text{-}40)$$

$$\alpha_{A-B} = \frac{\delta_B + 1000}{\delta_A + 1000} \qquad (2\text{-}41)$$

The enrichment factor $\Delta_{A\text{-}B}$ can be calculated from the fractionation factor or δ-values according to following equation:

$$\Delta_{A-B} = \delta_A - \delta_B \approx 1000(\alpha_{A-B} - 1) \approx 1000 \ln \alpha_{A-B} \qquad (2\text{-}42)$$

Kinetic fractionation is caused by incomplete and unidirectional processes, where different isotopes have different reaction rates. Diffusion, dissolution, precipitation, evaporation, dissociation, redox and enzymatic reactions can induce kinetic fractionation.

Different isotopes of an element have different zero point energy in a molecule of the same chemical composition according to the quantum theory (Todt, 2000). The bond strength depends strongly on the mass dependent vibration energy of atoms or molecules. Lighter isotopes have a higher vibration frequency in the lattice and their chemical bonds are in consequence less stable. Therefore lighter isotopes are more easily released. Heavier isotopes have more stable bonds. In consequence heavy

water D_2O has for instance a higher melting and freezing point, higher viscosity and higher temperature of maximal density compared to usual water.

Lighter isotopes diffuse faster than heavier isotopes and accumulate therefore preferentially in the reaction product (kinetic fractionation). In the case of CO_2 diffusion the isotopic fractionation is defined by the ratio of the diffusion rates $D_{^{12}CO_2}/D_{^{13}CO_2}$ of individual isotopes, which is proportional to the square root of the mass ratios μ.

$$\alpha = \frac{D_{^{12}CO_2}}{D_{^{13}CO_2}} = \sqrt{\frac{\mu_{^{13}CO_2}}{\mu_{^{12}CO_2}}}$$

$$(2\text{-}43)$$

The Rayleigh fractionation process describes the fractionation between two phases in a system with constant fractionation factors, where the product is removed from the reactant and is not available for back reaction. Furthermore evaporation of molecules, from water which consist of heavier isotopes ($D_2^{16}O$, $H_2^{18}O$, $D_2^{18}O$), is less favoured than evaporation of lighter isotopes ($H_2^{16}O$). The water reservoir is depleted in lighter isotopes ($H_2^{16}O$), whereas the gaseous phase is enriched in lighter isotopes. In this case, the instantaneous isotopic ratio in the remaining reservoir (cloud) R_{remain} can be calculated according to the following equation:

$$R_{remain} = R_0 f^{\alpha-1}$$

$$(2\text{-}44)$$

R is the instantaneous isotopic ratio of the remaining reservoir, R_0 is the initial isotopic ratio of the reservoir R, f is the part of the remaining substance and α is the fractionation factor. The instantaneous isotopic composition in the removed phase (water droplets in rain) R_{remove} can be calculated according to following equation:

$$R_{remove} = \alpha R_0 f^{\alpha-1}$$

$$(2\text{-}45)$$

The average isotopic composition ratio of the remaining and the removed phase can be calculated according to following equations:

$$R_{av\_remove} = R_0 \frac{1-f^{\alpha-1}}{1-f}$$

$$(2\text{-}46)$$

$$R_{av\_remain} = R_0 \frac{1-f^{1/\alpha}}{1-f}$$

$$(2\text{-}47)$$

The value of the fractionation factor depends on the temperature. This results into the application of isotopes like e.g. oxygen for the reconstruction of temperature. The isotopic composition in solids depends to a high degree upon the nature of the chemical bonds within the mineral. Short bond with high ionic potential tends to high vibration energies and therefore preferentially into the incorporation of heavy isotopes (Hoefs, 2009).

2.8.2 Oxygen isotopes

Oxygen has three stable isotopes, ^{16}O, [17]O and [18]O with an abundance of 99.757, 0.038 and 0.205%, respectively. The ^{18}O/^{16}O ratio is usually measured due to the higher abundance of these isotopes. The marine Pee Dee Belemnite (VPDB) calcium carbonate from South Carolina (USA) and Vienna Standard Mean Ocean Water (VSMOW) are used as reference material. V stands for Vienna, where this standard is distributed. The following equations can be applied for the conversation between $\delta^{18}O$ (VSMOW) and $\delta^{18}O$(VPDB):

$$\delta^{18}O(VSMOW) = 1.0309 \ \delta^{18}O(VPDB) + 30.91 \qquad (2\text{-}48)$$

$$\delta^{18}O(VPDB) = 0.97002 \ \delta^{18}O(VSMOW) - 29.98 \qquad (2\text{-}49)$$

The oxygen isotopic fractionation of natural samples range usually from about -40 to 40‰ and are displayed in Fig. 2-6.
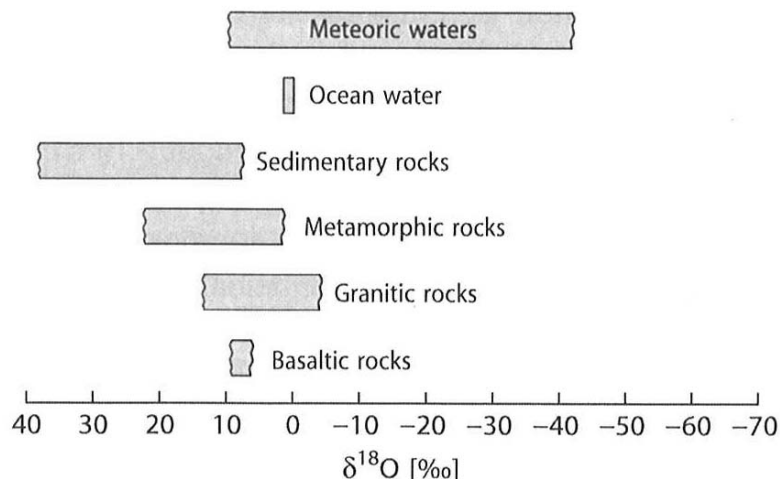
Fig. 2-6: Typical $\delta^{18}O_{SMOW}$ values of important natural reservoirs (Hoefs, 2009)

The temperature dependency of oxygen isotopic signature in minerals and especially in carbonates (Epstein et al., 1953) has widely been applied for reconstruction of paleo-climate in marine and terrestrial systems (Lea et al., 2000; Spötl and Mangini, 2002; Fleitmann et al., 2003). Foraminifers, corals and ostracodes are typically used for the reconstruction of sea water temperature (paleothermometry). Besides to the temperature the oxygen isotopes are influenced by salinity (e.g. Epstein and Mayeda, 1953), CO_3^{2-} -concentration (Spero et al., 1997) and kinetic effects, which have to be considered (Gonfiantini et al., 1968; Usdowski et al., 1979; Dietzel et al., 2009), especially if the precipitation is caused by fast loss of CO_2 or by evaporation (Hendy, 1971). The isotopic fractionation factor of oxygen between aragonite and solution is about 0.6 to 1.2 ‰ higher than that for calcite (Kim and O'neil, 1997). The oxygen isotopic fractionation between vaterite and solution is even higher at isotopic equilibrium than that between aragonite or calcite and solution according to modelling of Chacko and Deines (2008) and experimental results of Kim and O'Neil (1997).

Latter authors found an ^{18}O enrichment of 0.6 ‰ in vaterite compared to calcite and confirmed thereby the earlier measured value of 0.5 ‰ from Taruntani et al. (1969).

Chacko and Deines (2008) have used the measured internal Raman and FTIR vibration to estimate the isotopic fractionation factors of oxygen isotopes in various carbonates. These authors have used polynom equations of 6th order, where the individual temperature dependency of the oxygen isotopic fractionation of various carbonates is given. Furthermore the dependency of the oxygen isotopic fractionation on Mg is given by the following equations:

$$1000 \ln \beta_{Mg-Cc} = 1000 \ln \beta_{Cc} + X_{Mg} (1000 \ln \beta_{magnesite} - 1000 \ln \beta_{Cc}) \qquad (2\text{-}50)$$

X_{Mg} is the mol%-fraction of Mg: [Mg]/([Ca]+[Mg]). β is the individual oxygen isotope value of the phases (Mg-Cc magnesium calcite, Cc calcite, magnesite and water) and is related to the internal vibrations, which depend on the cation radius, cation mass and cation- anion bond strength (Chacko and Deines, 2008).

2.8.3 Carbon isotopes

Carbon has two stable isotopes, ^{12}C and ^{13}C, with an abundance of 99.89 and 1.11 %, respectively. A marine Pee Dee Belemnite (VPDB) calcium carbonate standard from South Carolina is used as reference material ($^{13}R = 11237.2 \; 10^{-6}$). Pure carbonates have typical values of 0±5 ‰ VPBD (Drever, 2004). Further ranges are plotted in Fig. 2-7.
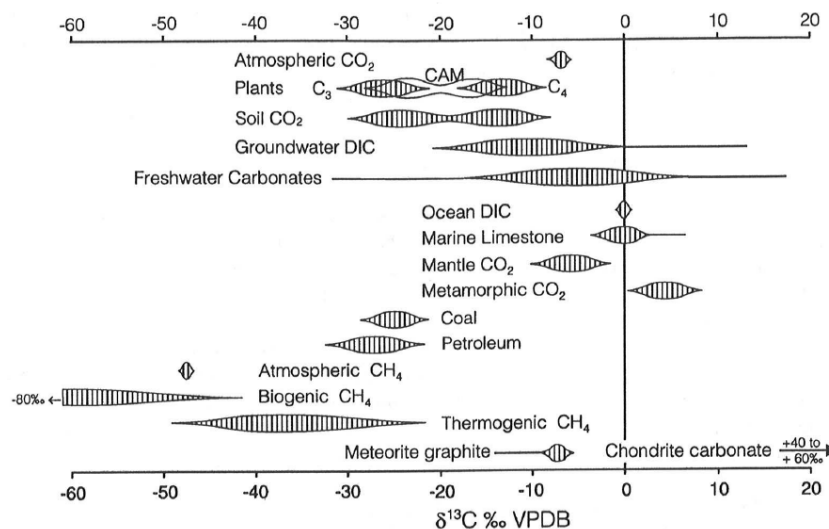
Fig. 2-7: Typical $\delta^{13}C_{VPDB}$ values of important reservoirs (Clark and Fritz, 1997)

C isotopes are 0.9 ‰ enriched in calcite and 2.7 ‰ enriched in aragonite compared to HCO_3^-.

Typical $\delta^{13}C$-value for $CO_{2(g)}$ of the Earths surface is about -7‰. Slighter isotopes are faster transferred to aqeous CO_2. This results into a $\delta^{13}C$-value of -8‰ for $CO_{2(aq)}$. Subsequent hydration promotes the heavier C isotopes and results into $\delta^{13}C$-value of 2‰ for HCO_3^-. Further dissociation of $H^{13}CO_3^-$ is slightly lower than of $H^{12}CO_3^-$ and the $\delta^{13}C$-value of CO_3^{2-} therefore lower. Last but

not least the heavier $\delta^{13}C$ has a stronger bound in the $CaCO_3$-lattice and remains therefore in the $CaCO_3$, which results into $\delta^{13}C$ values of approx. 4‰ (Appelo and Postma, 2006 and references therein). The fraction between the species depends on the temperature (T in Kelvin, θ in °C).

$$\alpha_{CO_{2(g)}-H_2CO_3^*} = (0.0041 \quad \theta - 1.18)10^{-3} + 1 \qquad \text{for } 0 \le T \le 60°C \quad (2\text{-}51)$$

$$\varepsilon_{CO_{2(g)}-HCO_3^-} \approx 10^3 \ln \alpha_{CO_{2(g)}-HCO_3^-} = \frac{9.52}{T}10^3 - 24.1 \qquad \text{for } 5 \le T \le 125°C \quad (2\text{-}52)$$

$$\varepsilon_{CO_{2(g)}-CaCO_{3(S)}} \approx 10^3 \ln \alpha_{CO_{2(g)}-CaCO_{3(S)}} = \frac{-9.1496}{T}10^3 - 20.545 \qquad \text{for } 0 \le T \le 100°C \quad (2\text{-}53)$$

$$\varepsilon_{CO_{2(g)}-CO_3^{2-}} \approx 10^3 \ln \alpha_{CO_{2(g)}-CO_3^{2-}} = \frac{8.81}{T}10^3 - 22.014 \qquad \text{for } 0 \le T \le 100°C \quad (2\text{-}54)$$

Equations (2-51) to (2-54) are given in Dietzel and Kirchhoff (2003) and originates from Vogel et al. (1970), Mook et al. (1974), Thode et al. (Heinemann et al., 2008), Bottinga et al. (1968), respectively. Romanek et al. (1992) found in their seeded experiments e.g. following temperature calcite-CO_2(g) and aragonite-CO_2 enrichment factors for ^{13}C

$$\Delta^{13}C_{Cc-CO_{2(g)}} = 11.98 - 0.12T \qquad\qquad (2\text{-}55)$$

$$\Delta^{13}C_{Ar-CO_{2(g)}} = 13.88 - 0.13T \qquad\qquad (2\text{-}56)$$

where T is the temperature in °C.

2.8.4 Calcium isotopes

Six stable calcium isotopic composition occurs in nature: 96.94% ^{40}Ca, 0.647% ^{42}Ca, 0.135 % ^{43}Ca, 2.08 % ^{44}Ca, 0.004 % ^{46}Ca and 0.187% ^{48}Ca (Hoefs, 2009). The decay of ^{40}K to radiogenic ^{40}Ca influences the Ca isotopic composition, if the rock contains high amounts of K (Faure and Mensing, 2005).

Following notation for the calcium isotopic fractionation between precipitated $CaCO_3$ and aqeous Ca is used

$$\Delta^{44/40}Ca_{CaCO_3\text{-}aq} = \delta^{44/40}Ca_{CaCO_3} - \delta^{44/40}Ca_{aq} \qquad\qquad (2\text{-}57)$$

$$\Delta^{44/40}Ca_{CaCO_3\text{-}aq} \approx 1000 \ln \alpha_{CaCO_3\text{-}aq} \qquad\qquad (2\text{-}58)$$

SRM 915a from NIST consists of highly purified calcium carbonate and is used as Ca isotope reference material (Gills, 1995; Heuser et al., 2002). Most values of calcium isotopic fractionation, $\Delta^{44/40}Ca_{CaCO_3\text{-}aq}$ are within a narrow range of -0.6 to -1.4 ‰ (Fig. 2.8).

The Ca isotopic fractionation between precipitated $CaCO_3$ and aqueous Ca decreases with increasing temperature. The effect of precipitation rate is still under discussion and has an opposite correlation by Tang et al. (2008a) vs. Lemarchand (2004). The calcium isotopic fractionation and its different temperature influence depend furthermore on the species, e.g. the foraminifera Globigerinoids

universa has a lower temperature dependency of Ca isotopic fractionation compared to foraminifera Globigerinoids sacculifer (Marriott et al., 2004).
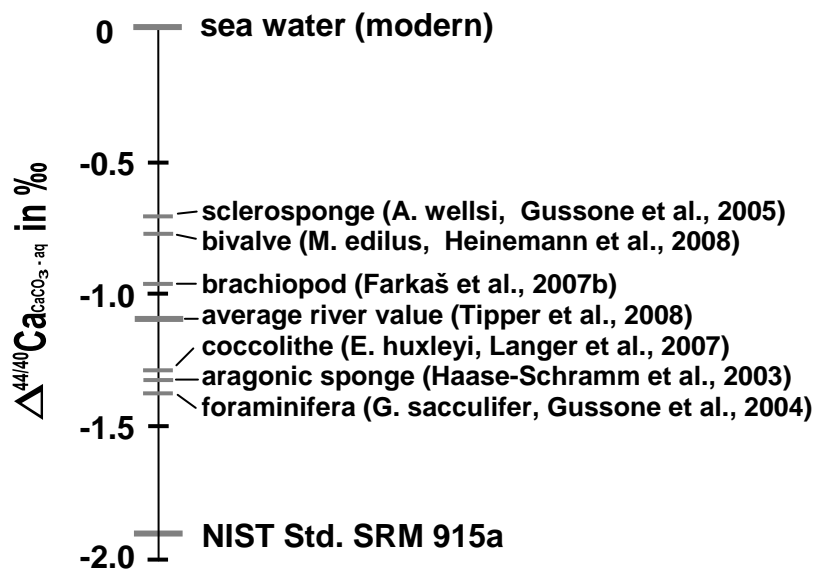
Fig. 2-8: Compilation of average values of calcium isotopic fractionation of different CaCO₃ precipitating organism and reference materials

The observed Ca-isotopic fractionation was interpreted by following models:

1. Equilibrium fractionation model

   The heavier Ca remains in the solution. Because these Ca isotopes prefer energetically the stronger bonds, which are found in the Ca-aquocomplex compared to carbonate minerals (Marriott et al., 2004).

2. Kinetic diffusion model

   A Ca-aquacomplex (with about 25 water molecules) diffuses through a thin boundary layer at the fluid- crystal interface. No significant energetic advantages of ^{44}Ca-O bonds in the Ca-aquocomplex versus carbonate minerals are considered (Gussone et al., 2003; Gussone et al., 2005).

3. Diffusion controlled entrapment model

   During crystal growth a depletion of the ^{44}Ca in a thin surface layer occurs. This is due to the faster reaction of the lighter ^{40}Ca isotope. The isotopic bulk composition in the crystal is similar to the surrounding solution. An ion diffusion process balances this concentration difference between the surface and solution. At fast rates the diffusion process is too slow for re-equilibration and the ^{44}Ca becomes more depleted. Elevated temperature results into a higher diffusion rate which decreases the isotopic fractionation (Tang et al., 2008a).

4. <u>Rate controlled model</u>

   The model from Lemarchand (2004) assumes an isotopic fractionation $\Delta^{44/40}Ca_{CaCO_3\text{-}aq}$ of about -1.5 ‰ at equilibrium. The isotopic signature depends on the rate of Ca precipitation and on the stirring strength. No stirring cause a larger Ca isotopic fractionation. In case of a small isotopic exchange rate compared to a fast precipitation rate the fractionation will be small, far away from equilibrium. A larger fraction is obtained at low precipitation rates and large isotopic exchange rates the equilibrium value will be aimed and a larger fractionation occurs (Lemarchand, 2004). This model is in contrast to the previous model 3.

5. <u>Adsorption steady state calcite growth model</u>

   This steady state box model has four regions (boxes) which are differently involved in the crystal growth process: (1) bulk calcite crystal, (2) crystal surface, (3) bulk solution and an (4) interface region. Exchange between bulk solution and interface region and transport of the adsorpted Ca to the surface takes place (Fantle and Depaolo, 2007a).

6. <u>Kinetic surface reaction model</u>

   This model is based on the relation between the gross forward (R_f gross precipititation), backward (R_b dissolution) and netto precipitation rate (R_p). The isotopic fractionation and trace element incorporation are kinetically controlled in case of high net precipitation rate vs. backward reaction rate. Lighter isotopes are favoured due to their larger mobility. Most experiments were conducted at the transition region between kinetic and equilibrium model, where the netto precipitation rate is in the same range than the backward reaction rate of the isotopes/ions. In this case both the kinetic and equilibrium model have to be considered in a combined equation of both isotopic fractionations. The crossover for the dominance of kinetic and the equilbrium fractionation is referred to $R_p \approx R_b$ (Depaolo, 2011).

Gussone et al. (2005) found a 0.6 ‰ lower calcium isotopic fractionation for calcite against aqueous Ca compared to aragonite against aqueous Ca. These authors have suggested therefore a mineralogical control of Ca isotope fractionation in different $CaCO_3$ polymorphs (Cc and Ar). This can be either by the different vibration behaviour of Ca in aragonite and calcite (Marriott et al., 2004) or by the difference in the surface chemistry of the two polymorphs. The Ca isotopic fractionation of vaterite was not investigated until now.

3   Sampling, Experimental and Analytical Procedure

3.1   Sampling and in situ measurements in the field

Temperature, pH and electric conductivity were measured in situ directly in the water by a WTW Multi 350i device and WTW Tetra Con 325 conductivity electrode, Pt 1000 temperature sensor and a pH electrode (Blueline 28 pH). Latter was calibrated with temperated standards at 4, 7 and 10. Furthermore the alkalinity was measured directly in the field. Therefore about 50 ml water samples were taken and 5 droplets of the Methlyorange-Bromcrysol-indicator mixture were added. 0.05 M HCl was used for the titration. Alcalinitiy was obtained by

$$Alcalinity = 1000 \frac{V_{HCl} \cdot M}{V_{samp}} \qquad (3\text{-}1)$$

V_{HCl} is the added amount of a M molar HCl in ml and V_{samp} is the sample amount in ml.
20 ml water samples were taken by syringes, filtered through 0.45 µm filter and acidified with 400 µl HNO_3 for cation analyses. Another 20 ml were taken and filtered for anion analyses. 50 ml water samples were stored in a gas tight glass bottle for alkalinity determination in the laboratory.
1 ml water samples were also gathered by a small syringe and stored in prepared He fluted boron-silicate vials for O- and C-isotopes, respectively.

3.2 Laboratory experiments

3.2.1 Experimental background

Unseeded calcium carbonate precipitation experiments were carried out by using an advanced CO_2 diffusion technique as displayed in Fig. 3-1 (see also Tang et al., 2008b). This technique is based on the transfer of CO_2 from an inner solution to an outer solution through a membrane. As the CO_2 enters the outer solution, it reacts with H_2O molecules to form carbonic acid according to equation

$$CO_{2(aq)} + H_2O \ = \ H_2CO_3 \qquad (3\text{-}2)$$

The carbonic acid partly dissociates to HCO_3^- and CO_3^{2-} according to equations

$$H_2CO_3 \ = \ H^+ + HCO_3^- \qquad (3\text{-}3)$$

$$HCO_3^- \ = \ H^+ + CO_3^{2-} \qquad (3\text{-}4)$$

As dissociation reactions are fast, hydration of CO_2 is the rate limiting step for transformation of CO_2 to CO_3^{2-} ions. However, concentrations of individual species are determined by pH, dissolved

inorganic carbon (DIC) concentration, ionic strength and temperature. The pH of the outer solution is kept constant during the experimental run by adding a diluted NaOH solution to compensate the H^+, which is produced according to equations (3-3) and (3-4).
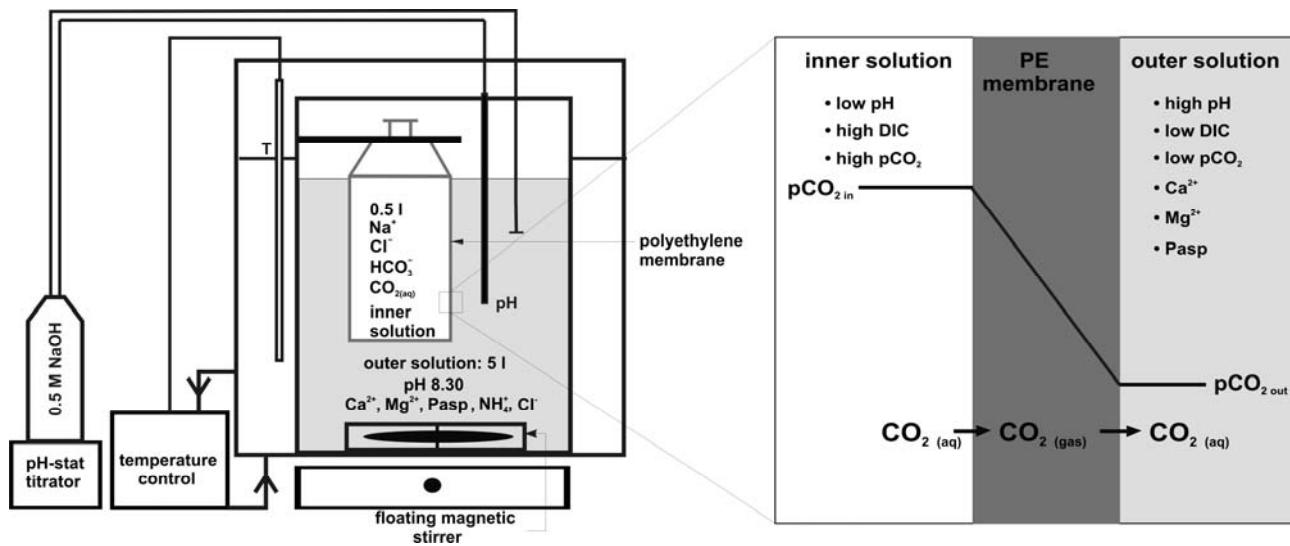
Fig. 3-1 : Experimental setup for the crystallization of CaCO$_3$ in the homogeneous outer solution by CO$_2$ diffusion technique.

CO_2 is continuously transferred from the DIC containing inner solution to the metal chloride containing outer solution and DIC accumulates in the outer solution. At a certain CO_3^{2-} activity nucleation and crystallization of calcium carbonate occurs according to equation

$$Ca^{2+} + CO_3^{2-} = CaCO_3 \qquad\qquad K_{sp}^{-1} \qquad\qquad (3\text{-}5)$$

(K_{sp}: solubility product of respective solid, see Tab. 2-4). During ongoing calcium carbonate formation additional H^+ is produced as the chemical bounded CO_3^{2-} has to be replaced by the dissociation of H_2CO_3 and HCO_3^- (equations (3-3) to (3-4)). Therefore elevated amounts of NaOH have to be added to keep the pH constant as soon as formation of CaCO$_3$ occurs besides diffusion of CO_2. The rise of the OH$^-$ addition as a function of experimental time - caused by CaCO$_3$ formation - reflects the individual precipitation behaviour, like nucleation, solid growth and precipitation rate.

In the presence of Mg^{2+}, isomorphic substitution of Ca^{2+} ions in CaCO$_3$ during formation according to equation

$$(1-n)Ca^{2+} + nMg^{2+} + CO_3^{2-} = Ca_{1-n}Mg_nCO_3 \qquad\qquad (3\text{-}6)$$

has to be considered. The value of n depends on distinct polymorph formation and environmental conditions during formation.

3.2.2 Starting materials and experimental conditions

The experiments were conducted at temperatures of 6, 10, 25 and 40°C (±1.5 °C) using a thermostatic water bath (Julabo HC E07 F18 or Huber ministat 230 CCC2). The temperature variation within one experimental run is less than ± 0.4 °C. The pH of the outer solution is kept constant at 8.30 ± 0.03 (pH stat.) by titration with freshly prepared 0.5 M NaOH solution using Schott Titroline alpha plus titrators with a minimum NaOH addition of 10 µl. The titration unit was equipped with a Schott Blueline 28 pH combination electrode and micro-burette. The pH standard solutions (pH = 4, 7 and 10) were used for the calibration at the given temperature of the experiments. All solutions were prepared by using deionised water (18.2 MΩcm^{-1}, Purelab Maxima ELGA or Millipore Integral 3 using 0.01 µm filter membranes) and pro analysis grade chemicals (Merck$^{®}$).

The inner solution (0.5 l) contains 35 or 40 g $NaHCO_3$ and various amounts of diluted NaOH (0.5 M) or HCl solution (1 M) to adjust the level of CO_2 partial pressure (see add and $pCO_{2\ in}$ values in Tab. A4, see appendix). The outer solution (5 l) consists of 10 mM $CaCl_2·2H_2O$ and 5 mM NH_4Cl for all experimental runs, except of marked experiments in Tab. A4 which contains more Ca. In several experiments various amounts of $MgCl_2·6H_2O$ and polyaspartic acid (Pasp) from a 40 wt.% stock solution (Bayerpure$^{®}$ DS 100: 1:100 or 1:300 pre-diluted before addition; final concentration see Tab. A4 see appendix) were added. The used Pasp $(C_4H_4NO_3Na)_x$ has a molecular weight between 2000 and 3000 g mol^{-1}. Volumes between 60 and 4000 µl of the pre-diluted Pasp stock solution were added to the outer solution before starting the experiments. Up to 0.08 mM strontium $(SrCl_2·6H_2O)$ were added to study the Sr incorporation during polymorph formation. As soon as the above ingredients were added, the experimental solution was stirred for one hour before starting the experiments.

The outer solution was protected against the laboratory atmosphere by an airtight cap. A Teflon$^{®}$ coated floating magnetic stirring bar in Tefzel$^{®}$ mountain brackets (NALGENE$^{®}$ DS6630-4000) was used for stirring the outer solution at 200 rpm during the whole experimental run to yield a homogeneous outer solution. A floating bar stirrer was applied to avoid grinding of the precipitates.

The inner and outer solutions were separated by a polyethylene membrane with a thickness of 0.2 or 2 mm (see Tab. A4). The adjusted CO_2 partial pressure gradient between the inner and outer solution in combination with the respective membrane thickness results in distinct CO_2 fluxes from the inner solution to the outer solution as the experiments proceed (Fig. 3-1).

During individual runs aliquots of the outer solution were sampled using syringes and 0.2 µm filters to follow the chemical composition during an experiment. At the end of the experiment the precipitates that occurred on both the vessel wall and the PE membrane were carefully removed from the surfaces using a plastic wiper. Subsequently the entire outer solution was filtered through a 0.2 µm cellulose acetate filter using a vacuum filtration device. The recovered solids were washed with ethanol, dried and stored at 40°C. A part of the precipitated solids was dissolved in 2% HNO_3 for chemical analyses.

To obtain more detailed information about the evolution of the calcium carbonate formation, $CaCO_3$ precipitates were also collected during several individual experimental runs after $CaCO_3$ nucleation was detected by NaOH titration. The evolution of the solids was followed in selected experiments by two different approaches: (i) Sampling of solution by syringes and separation of solids by membrane filtration (experiments 79 and 30; Tab. A4 see appendix). (ii) Decreasing the volume of the outer solution and collecting precipitates at the PE membrane (experiments 33, 56 and 96; Tab. A4 see appendix). Sampling of precipitates starts between 1 and 19 hours after first precipitation of $CaCO_3$ was detected, where the time periods depend on the individual experimental conditions.

3.2.3 Hydrochemical modelling

Hydrochemical modelling was carried out by using the computer code PHREEQC and wateq4f database (Ball and Nordstrom, 2001) considering the Truesdell-Jones equation for the activity coefficient calculation (Appelo and Postma, 2006) and thermodynamic constants from Plummer and Busenberg (1982), Clarkson (1992) and Kralj and Brecevic (1995). In Tab. 2-4 the individual equations for the solubility products of solid $CaCO_3$ phases used for modelling in the present study are given as a function of temperature. The expression for the solubility of monohydrocalcite as a function of temperature was re-calculated by the least square method from the data of Kralj and Brecevic (1995).

The saturation degree of respective $CaCO_3$ modification Ω is defined by the equation

$$\Omega = \frac{IAP}{K_{sp}} = \frac{\left(Ca^{2+}\right)\left(CO_3^{2-}\right)}{K_{sp}} \qquad (3-7)$$

where IAP is the ion activity product of the solution and K_{sp} is the individual solubility product from Tab. 2-4. At $\Omega = 1$ thermodynamic equilibrium between solid calcium carbonate and aqueous solution is reached. Parenthesis (i) denotes the activity of the aqueous species i. Activities are calculated by multiplying concentrations, [i], with individual ion activity coefficient, γ_i, according to

$$(i) = \gamma_i [i] \qquad (3-8)$$

Internal CO_2 partial pressure $pCO_2{}_{in}$ of the inner solution were calculated by PHREEQC using Henry`s constant, pH and alkalinity.

3.2.4 Analyses of titration curves

In Fig. 3-2 typical NaOH titration curves are given for 2 and 0.2 mm thick membranes, respectively. From the evolution of a titration curve the individual parameters like time of first precipitation, precipitation time as well as CO_2 diffusion and $CaCO_3$ precipitation rate can be calculated as discussed below.

The time of first precipitation of $CaCO_3$, t_{fp}, is given by the starting time of experiment and the time at the first inflection point of the titration curve (see t_{fp} in Fig. 3.3). In principle the formation of $CaCO_3$ comprise the reaction of Ca^{2+} and CO_3^{2-} ions to yield aqueous species, nuclei, and growth of $CaCO_3$. The value of t_{fp} includes the time to achieve a certain critical supersaturation, t_{crit}, and the induction time, t_{ind}, according to the equation

$$t_{fp} = t_{crit} + t_{ind}$$
(3-9)

Accordingly, t_{ind} is the time period between the critical supersaturation is achieved and the experimental time of first $CaCO_3$ formation. The induction time t_{ind} depends on the environmental conditions and decreases with increasing supersaturation (Pokrovsky, 1998). The value of t_{ind} is determined by the relaxation time, the time for the formation of a stable nucleus, and the time which a nucleus needs for growth to be detected (Mullin, 2001).
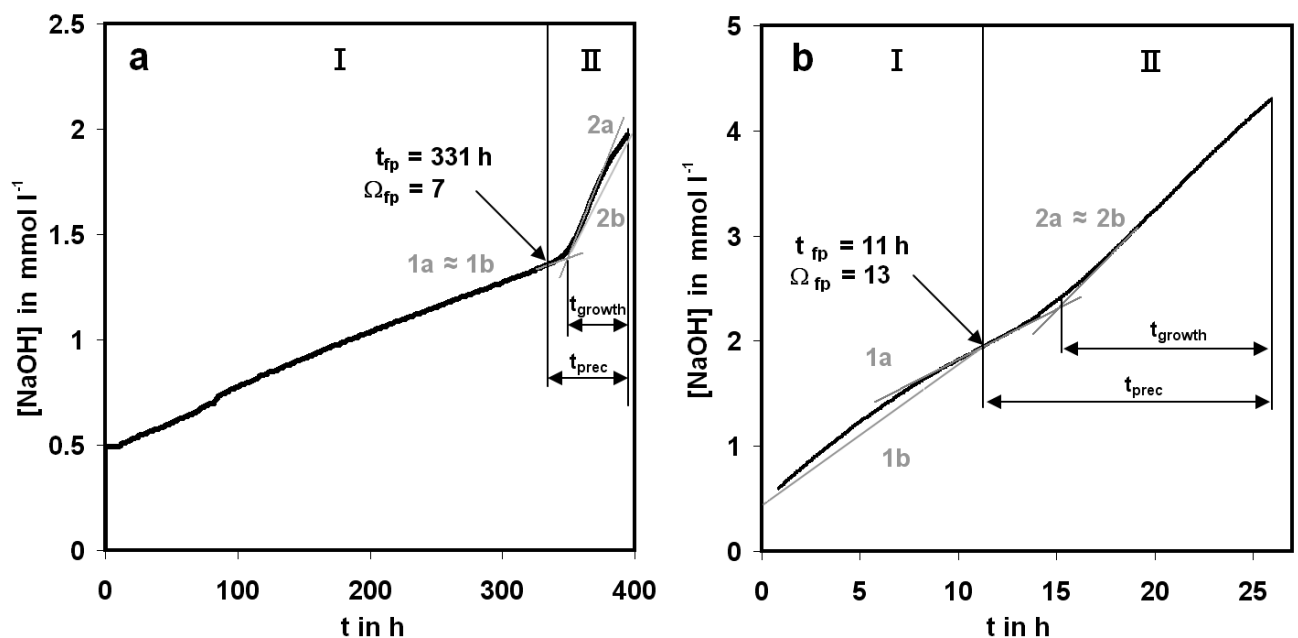
Fig. 3-2: NaOH addition over experimental time t for (a) experiment 49 with a 2 mm PE membrane and (b) experiment 54 with a 0.2 mm PE membrane (see Fig. 3-1 and Tab. A4 see appendix). CO_2 diffuses through the PE membrane from the inner to the outer solution at stage I, whereas at stage II diffusion of CO_2 and precipitation of $CaCO_3$ occur. t_{fp} and t_{prec} denote the time of first precipitation, the duration of $CaCO_3$ precipitation in hours, respectively. t_{growth} is the growth time in accordance with Tang et al. (2008). The slopes of lines 1a and 1b reflect the CO_2 diffusion rate at t_{fp}, D_{CO_2fp}, and the average CO_2 diffusion rate, D_{CO_2av}, respectively (equations (3-11) and 3-10). The $CaCO_3$ precipitation rate (R) is displayed by the slope of lines 2a in comparison with the average $CaCO_3$ precipitation rate in line 2b which was used by Tang et al. (2008), Ω_{fp}: degree of saturation with respect to calcite at t_{fp}.
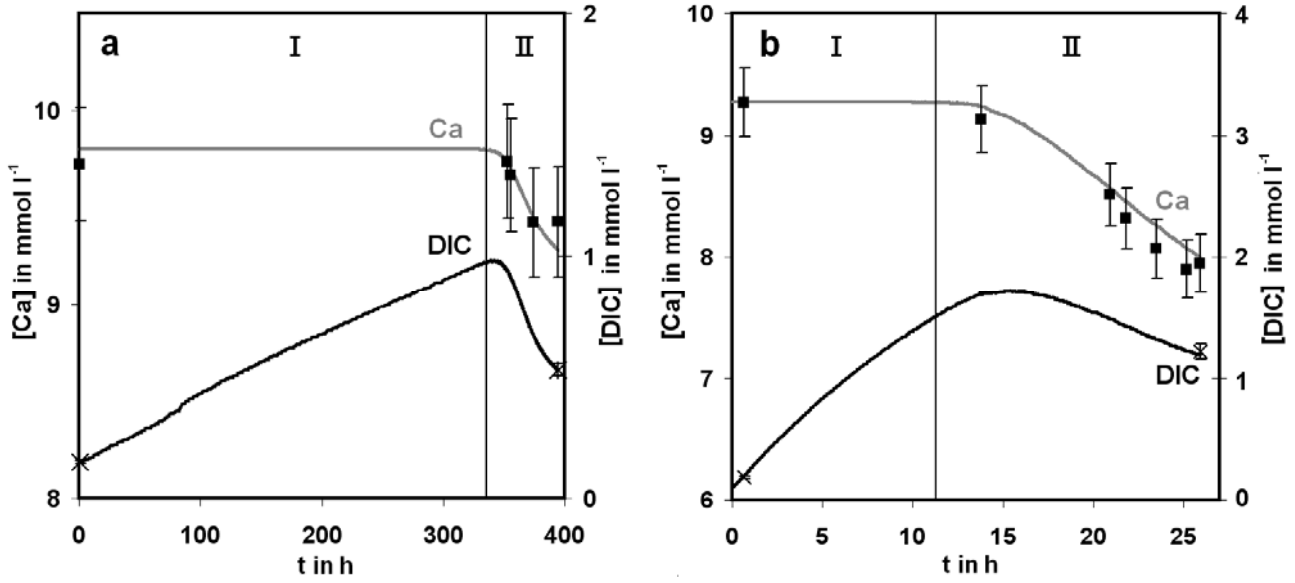
Fig. 3-3: Dissolved Ca and inorganic carbonate (DIC) concentrations over experimental time t for (a) experiment 49 and (b) experiment 54 (see Fig. 3-2 and Tab. A4 see appendix). Solid lines were calculated from the NaOH titration considering the CO₂ diffusion and CaCO₃ precipitation. ■: measured Ca concentration. x: measured DIC concentration.

For the present experimental approach the diffusion rate of CO_2, D_{CO_2}, in $\mu mol\ h^{-1}$ through the PE membrane is an essential parameter to control $CaCO_3$ formation conditions (see Fig. 3-1). The value of D_{CO_2} describes the flux of DIC into the Ca containing outer solution for $CaCO_3$ precipitation. The average CO_2 diffusion rate, D_{CO_2av}, was obtained by the total amount of added sodium hydroxide ($NaOH_{fp}$) until first precipitation of $CaCO_3$ occurred according to equation

$$D_{CO_2av} = f_1(T,pH,Mg)\frac{NaOH_{fp}}{t_{fp}}$$ (3-10)

without considering the initial time needed to adjust pH 8.30 (see Figs. 3-2a and b; slope of regression line 1b). In contrast, the CO_2 diffusion rate at first precipitation of $CaCO_3$, D_{CO_2fp}, was determined by the slope of the regression line 1a ($\Delta NaOH_1 / \Delta t_1$) just before the formation of $CaCO_3$ was detected according to equation

$$D_{CO_2fp} = f_1(T,pH,Mg)\frac{\Delta NaOH_1}{\Delta t_1}$$ (3-11)

(see Fig. 3-2a and b; slope of regression line 1a). For experiments with low CO_2 fluxes the values of D_{CO_2av} and D_{CO_2fp} are almost identical (see Fig. 3-2a), whereas high CO_2 fluxes induce slightly lower D_{CO_2fp} versus D_{CO_2av} values. This is due to a slight decrease of the CO_2 gradient between the inner and outer solution during an experimental run (see values in Tab. A4 see appendix). The conversion factor f_1 in equations (3-10) and (3-11) varies from 0.974 to 0.904 between 6 and 40°C, respectively (pH = 8.3 without Mg addition). Individual values of f_1 were calculated by the DIC species distribution at pH 8.3 and the given temperature using PHREEQC. The following aqueous species

are considered: $CaCO_3^0$, $MgCO_3^0$, $SrCO_3^0$, $NaCO_3^-$, $CaHCO_3^+$, $MgHCO_3^+$, $SrHCO_3^+$, $NaHCO_3^0$, $CaOH^+$, $MgOH^+$, $SrOH^+$, NH_4^+, NH_3, Ca^{2+}, Mg^{2+}, Sr^{2+}, Na^+, H^+, OH^-, $CO_{2(aq)}$, H_2CO_3, HCO_3^- and CO_3^{2-}. Values of f_1 are close to, but below 1 as the CO_2 liberated into the outer solution is mainly converted to HCO_3^- (overall reaction: $CO_2 + H_2O = H^+ + HCO_3^-$), but significantly dissociated also to CO_3^{2-} (overall reaction: $CO_2 + H_2O = 2H^+ + CO_3^{2-}$) and CO_3^{2-} containing aquocomplexes (e.g. $CaCO_3^0$ and $MgCO_3^0$) are formed at pH 8.3. The conversion to H_2CO_3 is less important (overall reaction: $CO_2 + H_2O = H_2CO_3$). For the reaction of CO_2 to CO_3^{2-} 2 mol OH^- per 1 mol CO_3^{2-} are required to balance pH change during CO_2 uptake. Thus, CO_2 flux is correlated to NaOH addition by $f_1 < 1$. In the presence of Mg the factor is even lower, as additionally the aqueous complexes $MgCO_3^0$ and $MgOH^+$ are formed.

The carbonate accumulation rate R_{CO_3} (see Tab. A4 see appendix) was calculated from the D_{CO_2av} value by the equation

$$R_{CO_3} = \frac{[CO_3^{2-}] + [CaCO_3^0] + [MgCO_3^0]}{[DIC]} D_{CO_2av} \qquad (3\text{-}12)$$

The concentrations of CO_3^{2-}, $CaCO_3^0$, and $MgCO_3^0$ were calculated by PHREEQC for each experiment by considering the initial chemistry and the NaOH concentration at the time of first precipitation. $NaCO_3^-$ and $SrCO_3^0$ formation can be neglected in equation (3-12), because their concentrations are more than 2 orders of magnitude lower than $[CaCO_3^0]$.

In the case of nucleation and ongoing precipitation of $CaCO_3$, both, CO_2 diffusion and $CaCO_3$ formation, have to be balanced by NaOH addition to keep the pH constant (see Figs. 3-2a and b; stage II). The precipitation rate of $CaCO_3$ (R in $\mu mol\ h^{-1}$) can be obtained by the slope of the titration curve at the second inflection point ($\Delta NaOH_2 / \Delta t_2$) by using the expression

$$R = f_2(T, pH, Mg) \frac{\Delta NaOH_2}{\Delta t_2} - D_{CO_2fp} \qquad (3\text{-}13)$$

(see line 2a in Fig. 4-2a and Fig. 4-2b). The conversion factor f_2 ranges from 1.027 to 1.134 between 6 and 40°C, respectively (pH = 8.3 without Mg addition). In analogy to f_1, individual values of f_2 were calculated by DIC species distribution at the given temperature using PHREEQC. The factor f_2 is above 1 as the CO_3^{2-} that is required for the formation of $CaCO_3$ is originated not only from the deprotonation of bicarbonate (equation (3-4)) but also from other aqueous carbonate species like CO_3^{2-}, $CaCO_3^0$ or $MgCO_3^0$.

The carbonate activity, $(CO_3^{2-})_{fp}$, and degree of saturation with respect to individual $CaCO_3$ modifications, Ω_{fp}, at the time of first formation of $CaCO_3$ were calculated by the values of $NaOH_{fp}$ and the initial metal chloride concentration of the outer solution using PHREEQC.

3.3   Analytical methods

3.3.1 Chemical composition of solutions and dissolved solids

Cation concentrations were determined with Inductively Coupled Plasma Optical Emission Spectrometry (ICP-OES) Optima 4300DV from Perkin Elmer. Ca was measured at a wavelengths of 317.9 nm, Mg at 279.6 nm, Na at 589.0 nm (or 589.6 nm) and Sr at 407.8 nm (421.6 nm or 460.8). A mixture of single element standards (1000 to 10000 ppm) was used for the calibration. This standard mixture contained 10 ppm Ca, K, Mg, Na, P, Si; 1 ppm Ag, Al, As, B, Ba, Bi, Cd, Co, Cr, Cu, Fe, Li, Mn, Ni, Pb, Se, Sr, Zn and 0.1 ppm Be and Y. A recalibration was performed every 10th measurement. The measurements were carried out with 3 to 5 repetitions, in the radial mode, where each repetition consists itself of 10 measurements. The standard deviation of these repeated measurements was about 1 % and up to 3 % were also accepted. Additionally an internal control sample was used to examine the constancy of the measurements indicating a precision of 3 % for [Mg]/[Ca] and 5% for [Sr]/[Ca] in the used concentration range.

A Dionex 600 ion chromatograph (IC) with an analytic column AS17 was used for the determination of the anion concentration. KOH was used as eluent and the gradient procedure was performed by establishing automatically different KOH concentrations within the device. A multi element standard with 15 ppm sulfate, 10 ppm nitrate, 15 ppm phosphate, 10 ppm nitrite, 2 ppm fluoride and 3 ppm chloride was used for the calibration before the measurements. The solutions were diluted to fit into the calibration range. The standard deviation of the ion chromatographic measurements is about 3%.

The titrator Titrino 702 SM alpha plus was used for the determination of the alkalinities in the laboratory. Step size for titration was 0.025 ml of a 0.01 M HCl for samples from the CO_2 diffusion technique experiments and 0.02 ml of a 0.05 M HCl for all other samples (determination of the alkalinity of NaOH and field samples). The standard deviation of the automatic titration is smaller than 3%, which was confirmed by replication measurements. 250 ml of Titrisol 1M HCl were used for the production of 5 liter 0.05 M HCl. The titer determination was carried out with Trizma® (Tri(hydroxymethyl) - $C_4H_{11}O_2$).

3.3.2 Solid phase characterization

The solids were filtered from the solution or directly taken at different sample locations in the field and dried at 40°C. The PANalytic X-ray powder diffractometer X'Pert Pro was used for the

quantification of calcite, aragonite and vaterite concentrations. The samples were analysed in a 2θ range from 18° to 124° with a step size of 0.004° by using a Co K$_\alpha$ X-ray radiation source (40mA, 45kV) and a X'Celerator Detector. Unit cell parameters were determined by Rietveld analyses from the XRD spectra. The structure of Maslen (1993), DeVilliers (1971) and Kamhi (1963) were used at the beginning of the Rietveld analyses for calcite, aragonite and vaterite, respectively. For error estimation Rietveld analysis were repeated several times for several samples with different starting conditions and the error of the cell size determination was calculated. The profil parameter R$_p$ and weighted profile parameter R$_{wp}$ indicate consistence of between the XRD spectra (y$_{oi}$) and the calculated spectra using the Rietveld method (y$_{ci}$). R$_p$ gives the relative deviation between the calculated and the measured intensity, while R$_{wp}$ is the weighted squared deviation between the calculated and measured intensity and is related to the weighted measured intensity (Allmann, 2003).

$$R_p = \frac{\sum_i |y_{oi} - y_{ci}|}{\sum_i y_{oi}}$$
(3-14)

$$R_{wp} = \sqrt{\frac{\sum_i (w_i(y_{oi} - y_{ci})^2)}{\sum_i (w_i y_{oi}^2)}}$$
(3-15)

R$_p$ and R$_{wp}$ were used for the evaluation of the fitting progress and the final results.

Furthermore the Fourier transform infrared (FTIR) spectrometer (Spektrum 100 from Perkin Elmer) was used for the identification and quantification of the amount of the phases calcite, aragonite and vaterite. The samples were measured mainly with the ATR- unit (attenuated total reflection) in the range from 650 to 4000 cm^{-1} (wave number). Several samples were analysed by using 200 mg KBr pellets containing 0.5 wt-% of the solid sample in transmission mode from 400 to 4000 cm^{-1}. The pellets were pressed at 9.2 kg cm^{-2} and immediately analyzed. For identification mainly the ν_4 peak was used, which is 699 and 713 cm^{-1} for aragonite, 712 cm^{-1} for calcite and 743 cm^{-1} for vaterite. The intensity ratios of these peaks were used for the quantification. Aragonite and calcite have an overlapping peak. Therefore the ratio between the intensity of the 713 peak to the intensity of the 699 peak was determined to be 1.6 in calcite free samples. In the case of calcite containing samples this ratio increases proportional to the amount of the calcite.

The mineralogy of single crystals was determined by using a Jobin Yvon Labram HR 800 micro-Raman spectroscope with the green laser (532 nm). The spot diameter is of about 2 μm (objective: 100 times). The green laser beam was weakened to 20 % by a focal to avoid beam damage of the carbonate samples. Data acquisition time was 5 sec. Aragonite was again characterized by a double peak at 705 and 706 cm^{-1}. Vaterite has a characteristic peaks in translation mode at 0 to 400 cm^{-1}, whereas calcite has only two peaks in this wave number range. Furthermore the peak of vaterite is

located at 758 cm^{-1} similar like in FTIR. The characteristic Raman peak of calcite is located at about 711 cm^{-1}. This value varies in dependence of the incorporated Mg concentration between 711 and 716 cm^{-1} ([Mg] = 3.1 mol%). The symmetric stretching vibration is also Raman active and correlates very well with the incorporated Mg concentration into the calcite crystals. Therefore this peak shift was used to map the Mg concentration in samples.

For analysis of the chemical composition of single crystals, the JEOL JXA 8200 micro-probe was used for selected samples. Before the measurement the samples were empeded in resin grinded and polished (1 μm) manually and were coated with carbon. The beam voltage and current were 15 kV and 5 nA (75 μW) or 7.5 kV and 15 nA (113 μW). The $L_{\alpha 1}$ peak of Ca was determined with the Pentaerythriol (PETJ) analyzing crystal at channel 1 during a measurement time of 20 sec. The background was determined 10 sec before and after each sample analysis. The $L_{\alpha 1}$ peak of Sr was determined at two channels (4 and 5) with Pentaerythrio (PETH) analyzing crystal. The $L_{\alpha 1}$ peak of Mg was determined at two channels (1 and 2) with a Thallium acid phtalate (TAP) analyzing crystal. The usage of two channels per element causes slightly better measurement statistics and therefore more accurate results. Collection times for Mg and Sr were 100 sec + twice 50 sec background. Only one channel was used for each element (Mg and Sr) in case of the determination of additionally iron and silicon. Calcite, dolomite and strontianite were used as standard materials. Cathodoluminescence (CL) images were taken at beam currents of up to 20 nA with a contrast of about 8.5 and a brightness of 9.3 to see also very small distortions of the lattice.

The morphology and surface of the crystals were displayed by the scanning electron microscope (SEM) ZEISS DSM 982 Gemini. The electrons were accelerated with 10 kV and a sample current of about 13.2 μA was adjusted, for imaging a secondary electron (SE) detector was used at a working distance of 14 to 17 mm. This range was used to adjust the optimal depth of focus by optimal resolution. Gold was used for sample coating by the Edwards Scan coat six sputter device for 300 sec.

Selected samples were analyzed by atomic force microscopy (AFM) at the Center for Nanoporous Materials in Manchester by Pablo Cubillias. Nanowizard II atomic force microscope from JPK Instruments was used in the contact mode. Contact mode tips (DNP-10) with a nominal tip radius of 20 nm from Veeco probes were applied. These tips were mounted on a cantilever with a spring constant of 0.2 N m^{-1}. Eighter (i) the deflection of the cantilever and therefore the force between tip and sample surface is measured or (ii) the height position of the translation stage which is hold at a constant force between tip and sample. Mode i result in a vertical deflection image, which displays the topology of the sample in case of plotting the deflection against the cantilever position. Mode ii results directly in imaging the surface morphology from the height position of the tip at a constant force between the tip and the mineral surface. Vertical dimensions of the surface can be measured by applying a voltage to a piezoelectric translater to keep the force between the tip and the surface constant (Butt et al., 2005 and personal communication with Cubillas P.).

The specific surface area of the precipitates, S_{BET}, was measured by Brunauer Emmett Teller (BET) gas adsorption method. A Helium-nitrogen gas mixture with a ratio of 70:30 was used in a

Micromeritics Flowsorb II 2300 device. This method is based on the adsorption of a gas on the solid surface, when the sample is cooled with liquid nitrogen (see Brunauer et al., 1938). The dried samples were weighed before and after the measurement to identify weight loss due to further drying at 60°C, which was carried out directly before the measurement. The small amount of precipitated solids limits the sample amount to 0.1 to 1 g. Therefore the error was estimated to be up to 20%. If the amount of calcite was insufficient for BET analyses, a specific surface area, S_{GEO}, was estimated from particle size distribution (PSD) analyses with the SA-CP2 Shimadzu device by the geometrical approach according to Tang et al. (2008). Previous to the measurements the calcite crystals were dispersed in a calcite saturated NAPP solution containing 0.004 M sodium pyrophosphate ($Na_4P_2O_7$ $\cdot 10H_2O$), stirred and dispersed in an ultrasonic water bath to avoid agglomeration of crystals which influence the sedimentation rate and therefore the result. The sedimentation mode and the centrifuge mode at 1000 rpm were combined to cover a particle size measurement in the diameter range from 0.2 μm to 40 μm. However, BET measurement is always the preferred method if applicable, because the determined surface area is closer to the reactive surface area than the geometric surface estimated from the PSD method. For several vaterite precipitates both S_{BET} and S_{GEO} values were obtained to the degree of surface roughness SR = S_{BET}/S_{GEO}.

3.3.3 Isotopic composition

$\delta^{13/12}C$ and $\delta^{18/16}O$ isotope value were determined by the continuous flow stable isotope ratio mass spectrometer (CF-IRMS) Finnigan Delta^{plus} (at Joanneum Research Graz). For isotopic analysis of the DIC of solid $CaCO_3$ 350 to 600 mg solid samples were therefore prepared in a boron silicate vial, which was cleaned before with heated 5% phosphoric acid and several times with MilliQ water. The international IAEA reference materials NBS 18 and NBS 19 as well as the internal standard CO18 served as reference material. The samples and reference materials were treated according to the IUPAC recommendations and each sample was analysed twice.

For $\delta^{13/12}C$ and $\delta^{18/16}O$ isotope measurements in water 1 ml water samples were injected into a fluted vial by a syringe and the samples were equilibrated at 20°C. For $\delta^{18/16}O$ isotope analysis the international reference materials: VSMOW, GISP and VSLAP were taken.

The determination of $\Delta^{44/40}Ca$ isotope fractionation was performed at the Finnigan Triton T1 thermal ionization mass spectrometer (TIMS) MAT 262 RPQ+ at IFM-GEOMAR in Kiel. SRM915a was used as standard. The double spike technique was used for the correction of isotope fractionation during the data acquisition in the mass spectrometer. Thereby ^{43}Ca-^{48}Ca double spike was mixed with the dissolved sample (Heuser et al., 2002). This dissolved sample was prepared by dissolving 300 to 400 ng Ca of the sample in ultrapure 2.5 N HNO_3 acid. After the addition of the spike the sample was purified (e.g. from carbonate) by repeated evaporation and dissolution in phosphoric acid. Finally a $TaCl_5$ activator was added, the droplet of this sample mixture was pipetted on a Re filament and the filament was heated. The acceleration voltage at the TIMS is 10 kV and the Faraday

cups have resistors of 10^{11} Ω (Heuser et al., 2002, Böhm et al., 2006). The faraday cups are moved to measure in the first sequence the masses 40, 41, 42 and 43 simultaneously and in the second sequence the masses 44 and 48. The whole range can not be covered by a single sequence. At the beginning of the measurement the sample is heated up by increasing the current with a rate of 200–240 mA min^{-1} to 2800 mA (1450°C). The signal was focused and the peak was centered before the current was increased to about 3100 mA (1500 to 1600°C). Data acquisition was started when a certain ion beam at mass 40 was reached. The measurement was repeated in total 172 times. Between the measurements the background was determined by closed beam (Heuser et al., 2002). Further details of the measurement are described in Heuser et al (2002). The standard deviation of replicates (n=2 to 6) is between 0.02 and 0.3 ‰ and is given in the Tab. A7 see appendix.

4   Field Studies

The field study comprises three sites for calcium carbonate precipitation in natural and man-made environments. The sites are situated along an NE-SW Profile through western Styria and Eastern Carinthia (see Fig. 4-1).
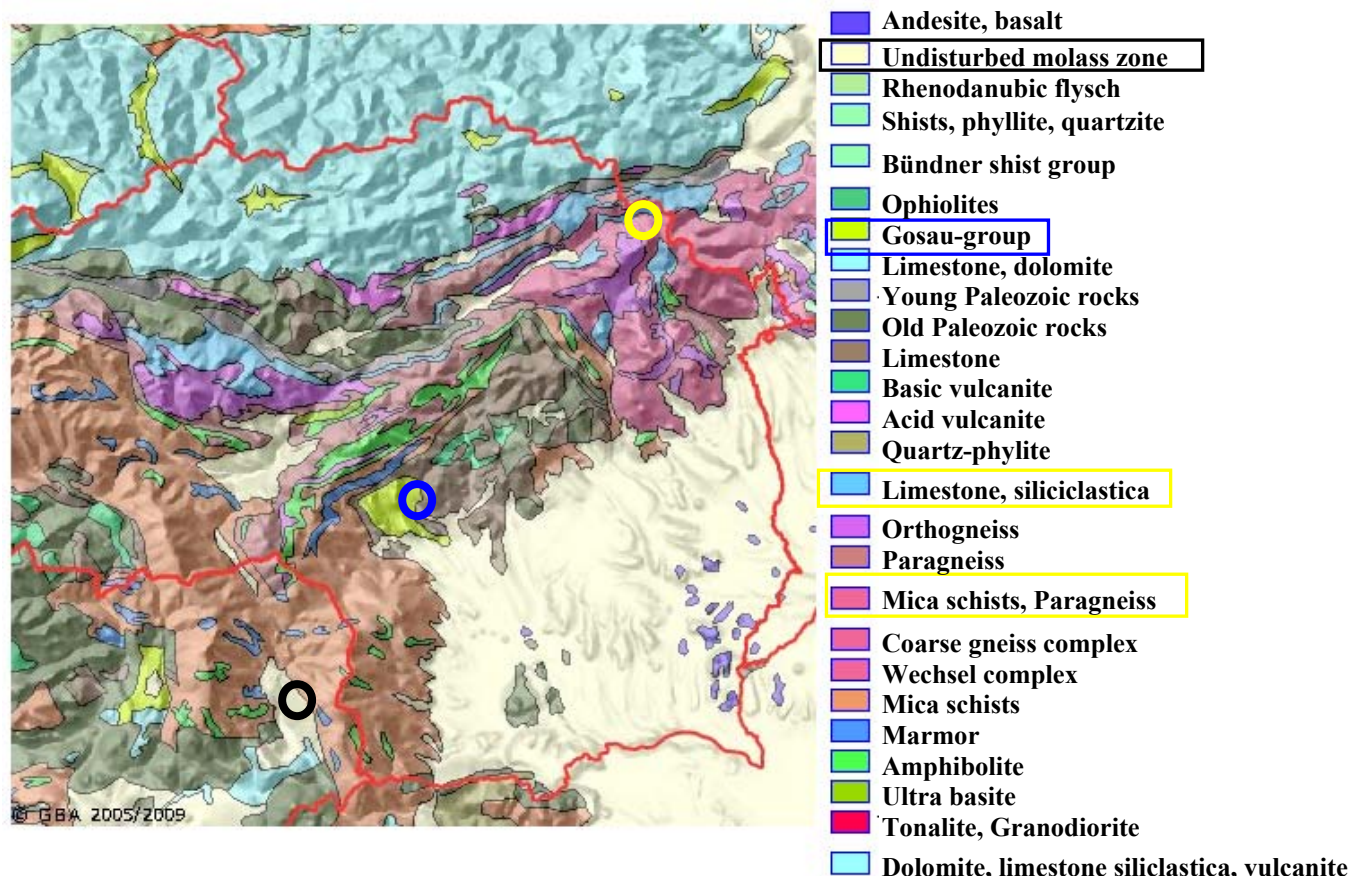
Fig. 4-1: Sampling sites in Styria (Geologische Bundesanstalt, 2009). Yellow circle: Spital tunnel at Semmering, blue circle: spring in Wolfsgraben, black circle: Koralm tunnel Mitterpichling.

The Spital tunnel is located in the Semmering area about 70 km north-east of Graz (yellow circle in Fig. 4-1) with a shales, gneis and limestone (see Mandl et al., 2001) from the Paleozoic of Graz. The investigated $CaCO_3$ precipitating spring is located in the "Wolfsgraben" close to St. Pankrazen 25 km north-west of Graz (blue circle in Fig. 4-1) at the border of the old Paleozoic rocks (Silurian to Carboniferous) to the Gosau group (Cretaceous to Paleogene). Besides to the Spital tunnel the sampling site Mitterpichling in Koralm tunnel (under construction) is selected as calcium carbonate is precipitated in the respective drainage systems and inhibitors shall be tested in further studies (not shown). This sampling site is situated 50 km south-west of Graz (black circle in Fig. 4-1) within an undisturbed molasse horizon, close to the shale of the Koralm outcrops (see Beck-Mannagetta, 1980).

4.1   Wolfsgraben spring

The Wolfsgraben spring is conspicuous due to its tendency of recent carbonate precipitation at a high [Mg]/[Ca] ratio. It is situated in a trench (Fig. 4-2a) in the Flösserkogel Formation (lower to middle Devonian) of the hilly Paleozoic area of Graz. The Flösserkogel Formation is characterised by dolomites, partly silt-sandstones and volcano-clastica and belongs to a flat subtidal unit with intertidal sedimentary deposition areas (Hubmann et al., 2008). The catchment area of the spring is dominated by a forest mainly with deciduous trees. The discharge of the spring was about 0.15 and 0.28 l s^{-1} at 11.Sept.2007 and 27.Aug.2008, respectively.

Fig. 4-2: (a) The landscape above the Wolfsgraben spring indicates a trench, (b) precipitates are found after the spring water reaches the Earth`s surface, (c, d) Precipitates are covered by moss, which slow down the water flow.

The following processes cause the formation of calcium carbonate at the "Wolfsgraben" spring. Initially, meteoric solutions infiltrate into the local soil horizons, where biogenic CO_2 is absorbed and the pH decreases. The low pH results in enhanced weathering of the carbonates (mainly dolomite).

The chemistry of the water indicated the uptake of soil CO_2 and dolomite dissolution by a calcium concentration of 1.6 mmol l^{-1}, magnesium concentration of 1.2 mmol l^{-1}, DIC concentration of 6.54 mmol l^{-1} and pH of 7.8 (see Tab. A1, 11.Sept. 2007). Similar values were obtained at 27. Aug. 2008: [Ca] = 1.7 mmol l^{-1}, [Mg] = 1.3 mmol l^{-1} and [DIC] = 6.53 mmol l^{-1} at a pH of 7.47, although the discharge was nearly double (0.28 l s^{-1}) compared to sampling at 11.Sept. 2007.

The carbonate sources were also affirmed by the isotopic composition of carbon. A $\delta^{13}C_{DIC}$ isotope value of -13.3 ‰ was obtained e.g. at 27.08.2008. This isotopic value is in accordance with the $\delta^{13}C_{DIC}$ isotope value of similar natural systems (e.g. Wiegand et al., 2004). It can be obtained for dissolution of marine carbonates at closed system conditions from isotopic composition of biogenic soil CO_2 ($\delta^{13}C_{CO_{2(g)}\,soil}$ = -25±5 ‰ VPDB in areas with C_3 plants; see Fig. 2-8 and Kendall and Doctor, 2004) and marine carbonate ($\delta^{13}C_{limestone}$=0±5 ‰ VPDB, Drever, 2004) by the equation (e.g. Dietzel and Kirchhoff, 2003):

$$\delta^{13}C_{DIC} = x_{CO_{2(g)}\,soil}\delta^{13}C_{CO_{2(g)}\,soil} + x_{limestone}\,\delta^{13}C_{limestone} = 0.5\,(\delta^{13}C_{CO_{2(g)}\,soil} + \delta^{13}C_{limestone}) \qquad (4\text{-}1)$$

, where $x_{CO_{2(g)\,soil}}$ and $x_{limestone}$ denote the fraction of biogenic soil CO_2 and limestone content on the total DIC and $x_{CO_{2(g)\,soil}} + x_{limestone} = 1$. At pH close to 8, where HCO_3^- dominates about carbonate ion and $H_2CO_3^*$, $x_{CO_{2(g)\,soil}}$ and $x_{limestone}$ are nearly 0.5 according to the overall expression

$$Ca^{2+} + 2\,HCO_3^- \rightleftharpoons CaCO_3 + H_2CO_3^* \qquad\qquad (\,4\text{-}2\,)$$

As the spring water get into contact with the Earth`s atmosphere, it degasses and consequently the pH increases from 7.8 to 8.6 (Fig. 4-3a) along the flow path. Moreover, the temperature rises from 8.6°C to 9.6°C (Tab. 4-1; 11.Sept. 2007). As a result the carbonate concentration increases from about 0.04 to 0.19 mmol l^{-1} (Fig. 4-3b) and the saturation index with respect to calcite increases from 0.46 to 1.16 (Fig. 4-3c), whereas the alkalinity and the total dissolved inorganic carbon concentration [DIC] decreases (Tab. 4-1). The largest CO_2 drop occurred in the first 12 m compared to the next 30m (Fig. 4-3c). The rise of the saturation index causes finally calcium carbonate precipitation at a distance of about 13 m from the spring (Fig. 4-3d, Fig. 4-3b) as it can be followed by the drop of the calcium concentration (Fig. 4-4a).

Tab. 4-1: Field parameters from (a) 11.09.2007 and (b) 27.08.2008, dist. denotes the distance from the spring in meter, T is the temperature, and Alk the alkalinity, DIC is dissolved inorganic carbonate, [ ] denotes total concentration of the given species, Ω_{Cc} is the saturation degree in respect to calcite and $\delta^{13}C_{DIC}$ the carbon isotopic composition of the dissolved inorganic carbon (DIC) in the solution.

date	dist.	pH	T	Alk	[DIC]	[HCO$_3$]	[CO$_3^{2-}$]	[Ca]	[Mg]	Ω_{Cc}	$\delta^{13}C_{DIC}$
	m		°C			mmol l^{-1}					‰
a	0	7.80	8.6	6.32	6.54	6.24	0.037	1.53	1.27	2.9	
a	13	8.58	9.0	5.57	5.42	5.19	0.190	1.47	1.22	14.5	
a	25	8.59	9.6	5.20	5.05	4.84	0.180	1.58	1.21	13.2	
a	42	8.57	9.6	5.02	4.88	4.67	0.170	1.58	1.16	12.8	
b	0	7.47	8.5	6.00	6.53	5.85	0.007	1.70	1.32	1.4	-13.31
b	1.5	7.52	8.6	5.89	6.35	5.73	0.008	1.74	1.34	1.6	-13.33
b	7	7.74	8.8	5.92	6.17	5.73	0.013	1.74	1.35	2.6	-12.80
b	15	8.05	9.1	5.88	5.95	5.64	0.027	1.63	1.28	5.1	-12.38
b	20	8.14	9.4	5.81	5.84	5.54	0.032	1.59	1.28	6.0	-12.21
b	27	8.17	9.6	5.66	5.68	5.39	0.034	1.58	1.32	6.3	-12.16
b	36	8.06	9.9	5.58	5.64	5.35	0.026	1.56	1.29	4.9	-11.96
b	39	8.09	9.8	5.56	5.61	5.32	0.028	1.55	1.30	5.1	-11.91
b	50	8.14	10.1	5.41	5.43	5.17	0.031	1.43	1.23	5.3	-11.68
b	53	8.17	10.2	5.41	5.42	5.15	0.032	1.49	1.29	5.7	-11.60
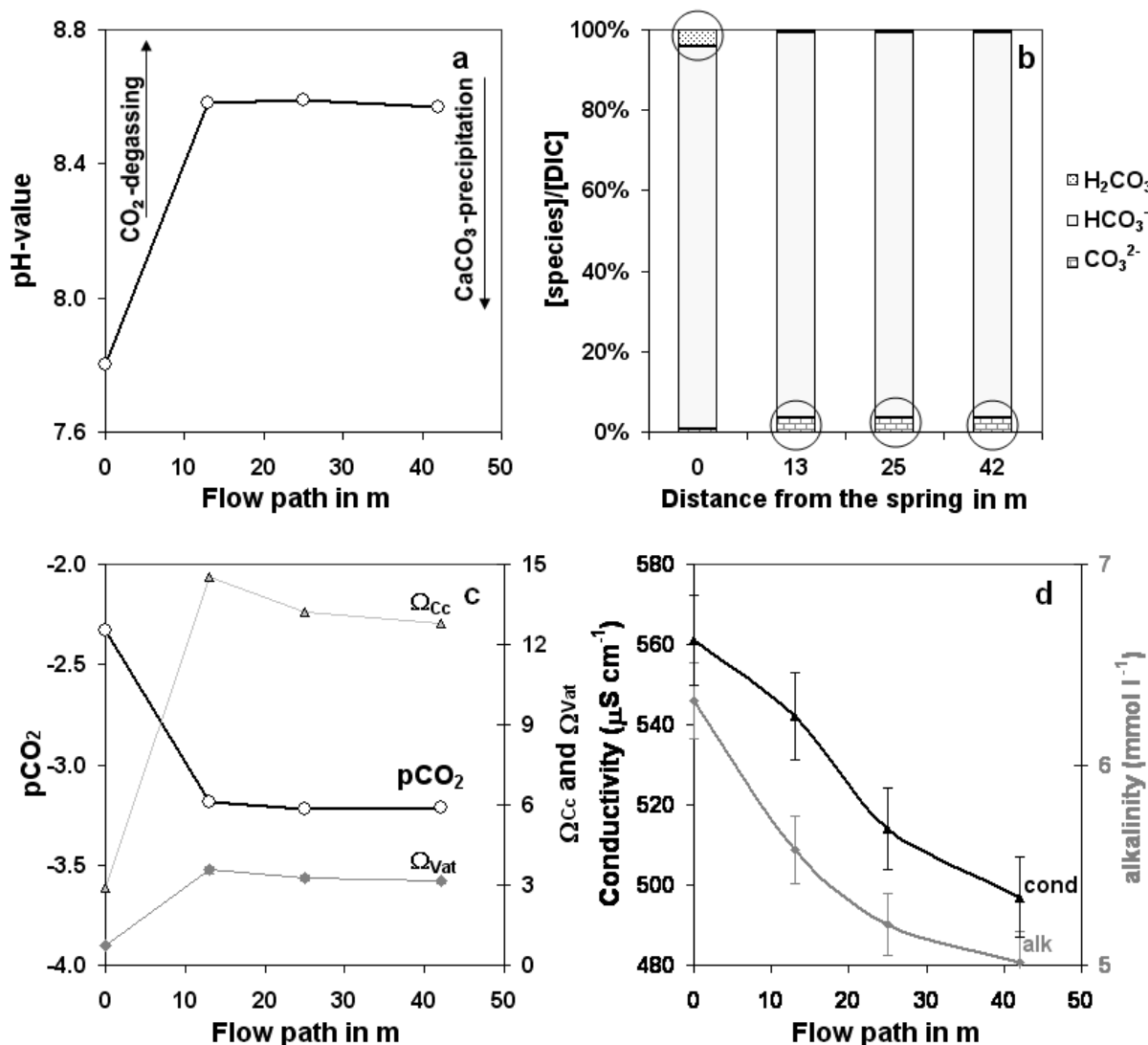
Fig. 4-3: (a) pH increases along the flow path due to CO_2 degassing (sampling: 11.Sept. 2007). The CO_2 degassing rate decreases along the flow path and additionally $CaCO_3$ precipitation occurs. After 25 m the $CaCO_3$ precipitation determines the pH. **(b)** At the spring H_2CO_3 occurs as second abundant species after bicarbonate, while at 15m distance from the spring the carbonate ion becomes dominant compared to H_2CO_3 due to the increase in pH by CO_2 degassing. **(c)** Internal partial pressure of CO_2 (pCO_2) and the saturation degree with respect to calcite (Ω_{Cc}) and vaterite (Ω_{vat}). **(d)** The conductivity and the alkalinity decrease both because of CO_2 degassing and $CaCO_3$ precipitation.
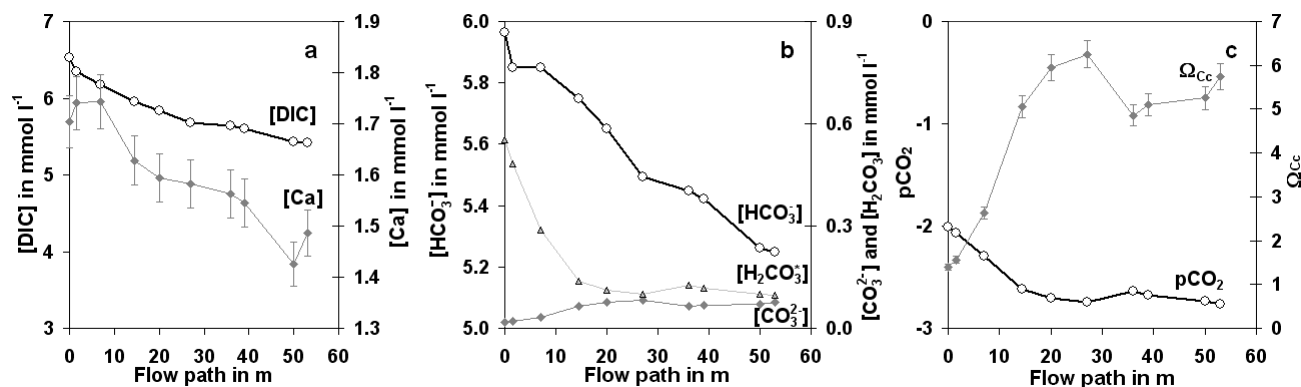
Fig. 4-4: (a) Decrease of Ca concentration, [Ca], due to $CaCO_3$ precipitation and decrease of the concentration of the dissolved inorganic carbon [DIC] due to CO_2 degassing and $CaCO_3$ precipitation (sampling: 27. Aug. 2008). **(b)** Change in the carbonate, bicarbonate and carbonic acid (+CO_2) concentration along the flow path. **(c)** Decrease of pCO_2 and rise of the saturation index with respect to calcite Ω_{Cc} along the flow path.

The degassing rate of CO_2 was slightly lower at 27 Aug. 2008 (from 5.9 to 0.83 µmol m^{-1} s^{-1}). However, the DIC decreases from 6.53 (0 m) over 6.35 mmol l^{-1} (1.5 m) and 6.17 mmol l^{-1} (7 m) to 5.91 (14.5 m) (Fig. 4-4a), while the pH rise from 7.47 over 7.52 and 7.74 to 8.05, respectively. This leads to a rise of the carbonate concentration from 17.5 over 19.5 and 32.9 to 65.1 µmol l^{-1} (Fig. 4-4b) and a rise of the saturation degree with respect to calcite from 1.4 over 1.6 and 2.6 to 5.1 at the same distances (Fig. 4-4c). Precipitation of $CaCO_3$ starts between 7 and 14.5 m at a saturation degree of 2.6 to 5.1 according to the change of [Ca] (Fig. 4-4a, Tab. 4-1).

CO_2 degassing was also verified by the change in the isotopic composition of carbon in the water samples $\delta^{13}C_{DIC}$.

$^{12}CO_2$ degassed faster than $^{13}CO_2$. Thus, in the remaining DIC the heavier ^{13}C isotope accumulates and the $\delta^{13}C_{DIC}$ became nearly 2 ‰ heavier at a distance of 53 m (Fig. 4-5a). This rise is similar to that observed by Wiegand et al. (2004) at the spring in Köttmansdorf. The rise in $\delta^{13}C_{DIC}$ is proportional to the drop in DIC (Fig. 4-5b) according to following equation

$$\delta^{13}C_{DIC} = -1.607 \,[DIC] - 2.9118 \;(R^2 = 0.97, n=10)\qquad(4\text{-}3)$$

The increase in $\delta^{13}C_{DIC}$ is larger at the beginning due to the higher CO_2 degassing rate. The effective partitioning coefficient χ is 1.0096 according to the equation of Michaelis et al. (1985):

$$\delta^{13}C - \delta^{13}C_0 = (\chi - 1)10^3 \ln \frac{[DIC]}{[DIC_0]}\qquad(4\text{-}4)$$

The degassing rate of CO_2 is about 2 times faster than that of the $CaCO_3$ precipitate (Fig. 4-5c) as it was verified by the slope of ΔDIC vs. ΔCa plot along the flow path. A slope of 1 means pure $CaCO_3$ formation (I in Fig. 4-5c), because a similar amounts of (hydrogen-) carbonate and calcium are removed. A slope of above 1 means additionally CO_2 degassing and a slope below 1 means CO_2 adsorption or a further Ca source. The degassing/uptake rate of CO_2 can therefore directly be calculated from the difference in the slopes II and I under the assumption that no other Ca source or sink exist.
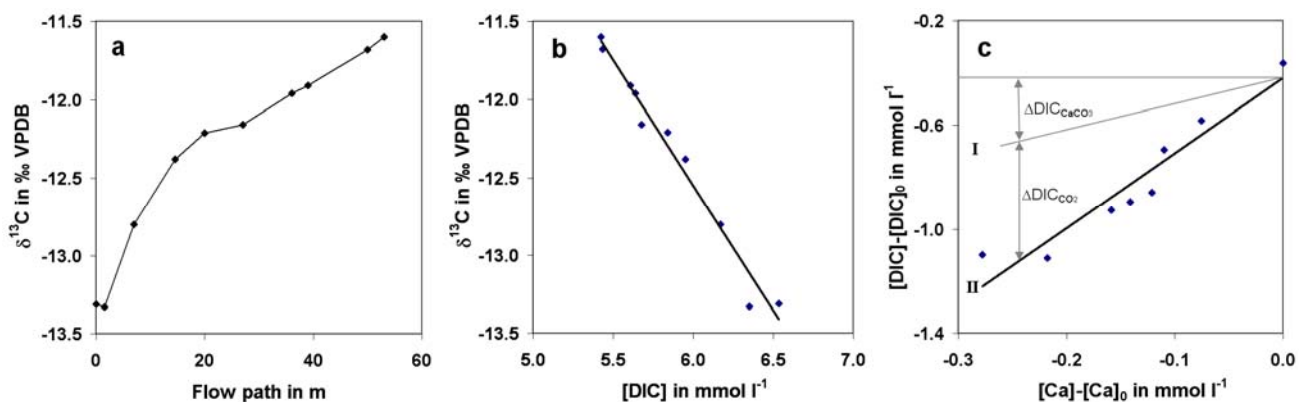
Fig. 4-5: (a) Development of the carbon isotopes along the flow path. (b) Carbon isotopes vs. dissolved inorganic carbon concentration [DIC] and (c) change in [DIC] vs. change in [Ca].

The degassing causes a rise in the pH and therefore a slight change in the species distribution.

Both FTIR spectra and XRD patterns indicate that the precipitates consist mainly of calcite, but small amounts of detrital dolomite are also found in XRD and FTIR pattern. The drop in Mg concentration of the solution is much lower than the drop of [Ca] (Δ[Mg] = 0.28 Δ[Ca]) and Mg becomes therefore enriched, so that [Mg]/[Ca] in the solution increases from 0.78 to 0.87 along the flow path. Magnesium can be incorporated in $CaCO_3$ into calcite, but Ca is more favourable because Mg causes disturtions of the lattice and a larger solublilty. Under consideration of the intial and final Ca concentration the change in the Mg and Ca concentrations a D_{Mg} value of 0.34 was calculated by using equation (2.37).

4.2   Koralm tunnel
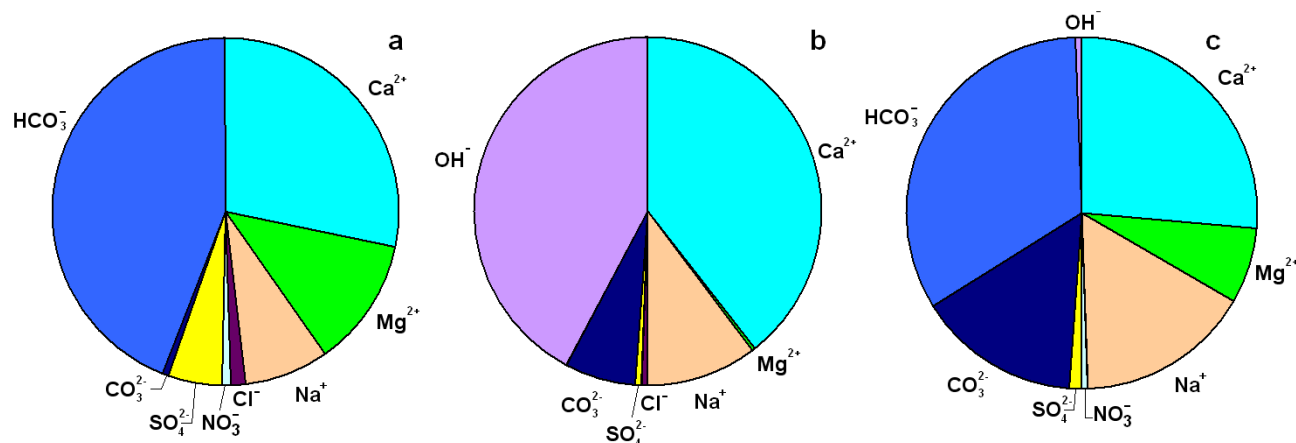
Fig. 4-6: Composition of the Mitterpichling water samples (a) type 1, (b) type 2 and (c) type 3 in meq l⁻¹.

In general, three water types can be distinguished for the sampled drainage solution in the Koralm tunnel at 20 Nov. 2007 and 19 March 2008:

- Type 1 has a pH between 7.0 and 7.8, where bicarbonate is the dominant anion (Fig. 4-6a, samples M1 to M6 Tabs. A1 and A2 in appendix). Calcium concentration reach values up to 0.73 mmol l⁻¹ and Mg concentrations lay between 0.19 and 0.32 mmol l⁻¹. Na^+ up to 0.5 mmol l⁻¹, Si of 0.5 to 0.8 mmol l⁻¹ are measured. The $\delta^{13}C_{DIC}$ (VPDB) values are in the range from -14.6 to -18.8‰.

- Type 2 has a pH of 12.1 to 12.5, where hydroxide is the dominant anion (Fig. 4-6b, samples M7 and M8 Tabs. A1 and A2 in appendix). The Ca concentration accounts for 1.6 to 3.8 mmol l⁻¹. The Mg concentration is one order of magnitude lower than in type 1. The sodium concentration is approximately double of that of type 1. Concentrations of Al, Ba, Li and Sr are more than twice as high in M7 (type 2) compared to type 1, whereas the chloride and nitrate concentrations are lower and sulfate nearly disappears. The $\delta^{13}C_{DIC}$ (VPDB) values are in the range from -20 to -25‰, significantly enriched in ^{12}C compared to type 1 water. The most characteristic feature of

type 2 water is the supersaturation with respect to calcite, aragonite, vaterite and brucite, whereas all type 1 water samples are undersaturated with respect to these phases.

- Type 3 has a pH of about 10 and carbonate is the dominant anion (Fig. 4-6c, sample M9 in Tabs. A1 and A2 in appendix). The Ca and Li concentration are similar to type 1 waters. Concentrations of Mg, Na, Al, Fe, K, Sr and sulfate lay between type 1 and 2.

No precipitation occurred in type 1 water due to the low supersaturation with respect to calcite, whereas supersaturations with respect to calcite (Tab. A3) in type 2 and 3 solution were high enough (SI > 0.6) for calcium carbonate formation (Figs. 4-7a-d) clogging the drainage pipes (Fig. 4-7c). Different shaped precipitates were found at a collecting pond: $CaCO_3$ spheres, plates, stalactites and tubes (Fig. 4-7d). Generally, the $\delta^{18}O$ values of the calcite precipitates display a good correlation (0.92) with $\delta^{13}C$ values. The calcite spheres have the "lightest" stable oxygen ($\delta^{18}O$ = -23.3 ‰) and carbon isotopic signature ($\delta^{13}C$ = -33.1 ‰), followed by tubes with $\delta^{18}O$ = -18.9 to -22.5 ‰ and $\delta^{13}C$ = -27.3 to -33.9 ‰. Platy $CaCO_3$ solids are less depleted in ^{18}O ($\delta^{18}O$ = -17.1 ‰) and ^{13}C ($\delta^{13}C$ = -25.5). Different isotopic composition might be related to the distinct micro-environments where these precipitates were formed. Furthermore kinetic effects can play a significant role in such highly alkaline solutions. $CaCO_3$ plates have a larger surface to volume ratio, which may allow the escape of ^{16}O vs. ^{18}O more easily compared to spheres and tubes.

Generally the ^{13}C and ^{18}O depletion in calcite sinter of high alkaline tunnel drainages vs preciptates at moderate pH are caused by the adsorption of atmospheric CO_2 which can be effected by CO_2 from combustion of fossil fuels (Dietzel et al., 1992).
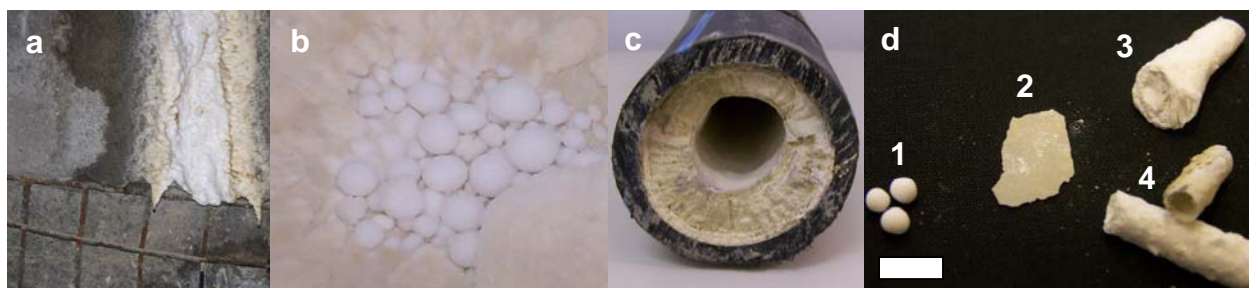
Fig. 4-7: (a) Calcite precipitation at the tunnel wall and (b) within the water collecting pond ($CaCO_3$ sphericals). (c) Calcium carbonate sinter formation in a drainage pipe. (d) Different shaped precipitates (1: sphere, 2: plates, 3: stalactites and 4: tubes) were found in water collecting pond and as stalactites (white scale bar is 10 mm).

4.3 Spital tunnel

The Spital tunnel is located in the Keuper horizon, which was formed about 220 million years ago in Carnian (to Norian) belonging to Semmering unit (Mandl et al., 2001). This area contains sericite mica with dolomite lenses, quartz dikes, and gypsum horizons. Phyllitic mica shists and carbonates (banded limestones and marbles) are located at the top (overlying stratum). Rough gneisses and phyllitic micas are located in the southern part of the Fröschnitz river (Mandl et al., 2001).

Sampling sites are illustrated in Fig. A1 (see appendix) and comprise two tunnel drainage pipes (1 and 11), influx of Holzergraben creek (0), two further influxes (9, 10) and the flowing path to the

receiving stream Fröschnitz creek (1-2 to 6), as well as the water in the Fröschnitz before (7), and after (8) the Holzergraben creek.

Tab. 4-2 In situ determined physical parameters: pH-value, temperature T, specific conductivity (cond.), discharges (Q), measured alkalinity (alk), cation and anion concentrations [].

Nr.	pH	T	cond.	Q	Alk	[Ca]	[K]	[Mg]	[Na]	[Si]	[Sr]	[Cl]	[NO$_3$]	[SO$_4$]
		°C	µS cm^{-1}	l s^{-1}						mmol l^{-1}				
HC 0	8.5	9.1	442		4.3	1.8	0.0	0.7	0.0	0.08	0.0057	0.03	0.07	0.3
HC 1	10.1	8.7	573	3.45	3.6	0.5	0.7	0.8	1.6	0.09	0.0044	1.51	0.05	0.5
HC 1-2	9.5	10	491		2.9	1.2	0.4	0.8	0.9	0.09	0.0059	0.80	0.06	0.4
HC 2	9.6	10.4	484		3.6	1.1	0.4	0.8	0.9	0.09	0.0055	0.77	0.06	0.4
HC 3	9.3	11.2	480		3.6	1.1	0.4	0.9	1.0	0.09	0.0058	0.84	0.07	0.4
HC 4	9.1	11.4	525		4.4	1.4	0.3	0.9	0.9	0.10	0.0063	0.79	0.07	0.5
HC 5	8.7	10.5	558		4.4	1.6	0.2	1.0	0.8	0.10	0.0066	0.71	0.07	0.5
HC 6	8.5	11.4	537		4.3	1.5	0.3	1.0	0.8	0.09	0.0066	0.70	0.07	0.5
HC 7	8.4	12.2	278		2.2	0.9	0.0	0.5	0.3	0.12	0.0025	0.23	0.07	0.3
HC 8	8.6	12.4	301		2.1	0.9	0.0	0.5	0.3	0.12	0.0028	0.27	0.07	0.3
HC 9	8.2	9.6	663	0.05	6.0	2.5	0.1	1.2	0.4	0.11	0.0081	0.36	0.08	0.6
HC 10	8.1	8.9	1756		5.3	2.4	0.1	1.1	9.8	0.13	0.0071	10.59	0.86	0.0
HC 11	10.9	13.4	550	11	1.7	0.6	0.9	0.4	1.9	0.10	0.0040	1.27	0.15	0.4

The investigated tunnel drainage solutions are very alkaline with pH values from about 10 (HC 1) to 11 (HC 11) (see Tab. 4-2). Along the flow path the pH decreases due to calcium carbonate precipitation, CO_2 uptake and mixing with lower pH solution (HC 9 and HC 10) (Fig. 4-8a).
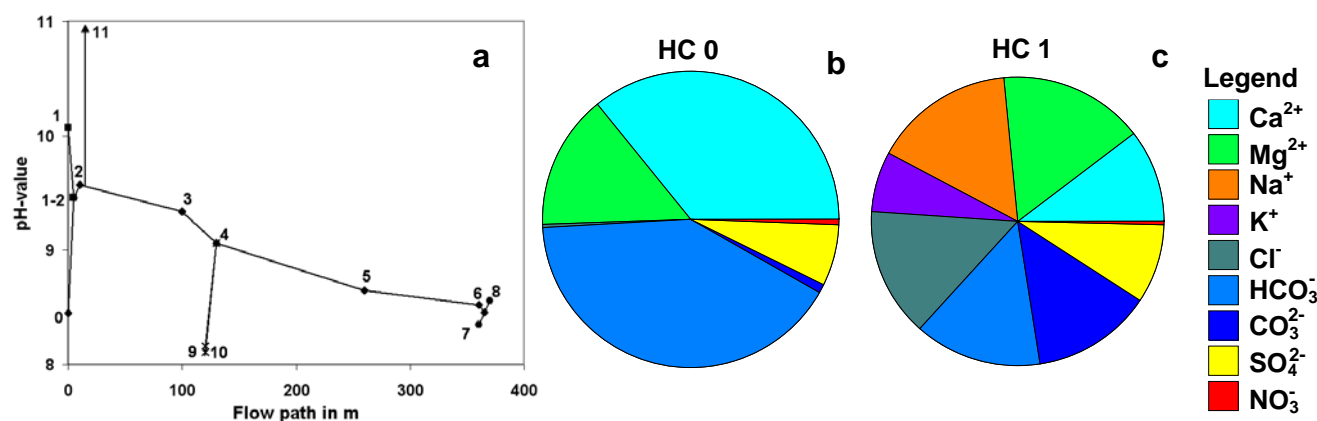
Fig. 4-8: (a) Development of the pH value along the flow path. Comparison of the chemical composition in meq l^{-1}: (b) HC 0 natural water of the Holzgraben creek; (c) HC 1 drainage water

The high pH of the tunnel drainage water (HC 1) results into a bicarbonate to carbonate ratio of 1:1 in the aqueous solution. Besides to calcium and magnesium, high concentrations of potassium, sodium, chloride and sulfate were observed for the drainage water (Fig. 4-8c) which indicates reaction with concrete (e.g. portlandite, $Ca(OH)_2$). HC10 (Tab. 4-2) is influenced by halite dissolution as it was indicated by high concentrations of sodium and chloride. Elevated nitrate

concentration of about 0.86 mmol l^{-1} reflects the agriculture activities in the catchment area. The compositions of all sampled solutions are plotted in the piper plot (Fig. 4-9).
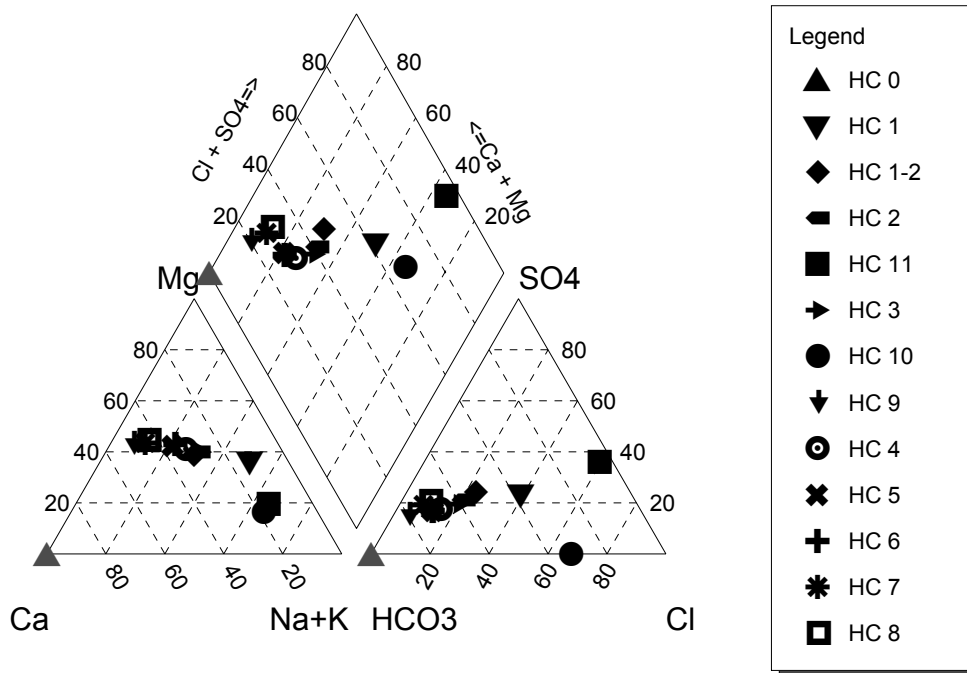
Fig. 4-9: Piperplot for water samples from the tunnel drainage, Holzgraben and Fröschnitz creek.

The conductivity, Ca, Mg and bicarbonate concentration decrease in the first few meters and increase after the solution HC11 was added at the mixing points. The supersaturation with respect to calcite increases by mixing of the Ca-rich natural Holzgraben creek water HC 0 (Fig. 4-8b) with the carbonate-rich drainage water HC1 (Fig. 4-8c). The supersaturation with respect to calcite of the resulting mixture is higher than the individual supersaturation indices of the two incoming solutions. The high pH of the drainage water HC 1 and HC 11 results in an uptake of CO_2 from the surrounding Earth`s atmosphere, which causes a rise of DIC concentration until the sampling points 4. Between the sampling points 4 and 5 the $CO_2$ partial pressure of the Earth`s atmosphere is reached, so that no CO_2 net-uptake occur any longer and DIC drops slightly because of $CaCO_3$ precipitation (Fig. 4-10a). The saturation degree with respect to calcite exceeds 6.3 for all solution, except of the Fröschnitz creek (HC 7, HC 8), where it is between 2.5 and 4.0 (Fig. 4-10b). Solid phase analyses by XRD and FTIR indicate that the sample at the flow path consists mainly of calcite and $\leq$ 20 wt.% of aragonite.

Strontium, magnesium, barium and disolved inorganic carbon (DIC) concentration in the water samples are correlated with calcium concentration (Fig. 4-11) according to following equations:

$$[Sr] = 0.0021\,[Ca] + 0.0032 \tag{4-5}$$

$$[Mg] = 0.36\,[Ca] + 0.42 \tag{4-6}$$

$$[Ba] = 0.00049\,[Ca] + 0.00006 \tag{4-7}$$

$$[DIC] = 1.37\,[Ca] + 2.14 \tag{4-8}$$

The slopes of equations (4-5) to (4-8) correspond to the elemental ratios in the precipitated solid phases according to $([Me]/[Ca])_s = ([\Delta Me]/[\Delta Ca])_{aq}$, if no other source or sink of a single element is found in the investigation area except of homogeneous precipitation or disolution.
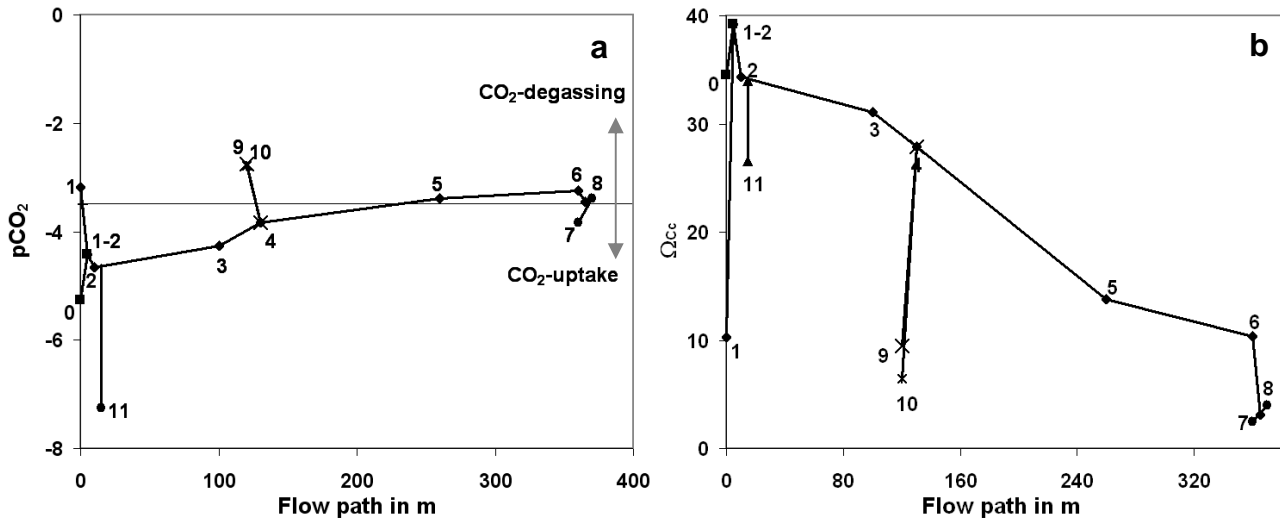
Fig. 4-10: Evolution of the pCO_2 and the saturation degree with respect to calcite, Ω_{Cc}, along the flow path
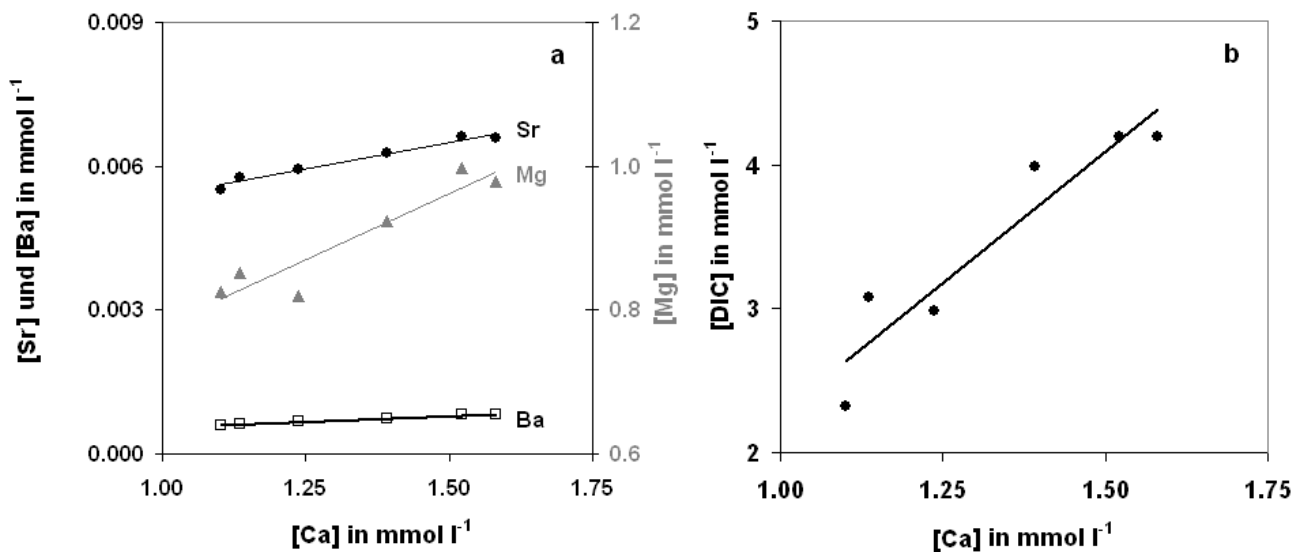
Fig. 4-11: Correlation between (a) [Mg], [Sr], [Ba] and [Ca] and (b) dissolved inorganic carbon (DIC) and Ca concentration, respectively

$D_{Sr}=0.28$, $D_{Mg}=0.28$ and $D_{Ba}=0.024$ were obtained for the slops of log $(([Me]/[Ca])_{aq}]/([Me]/[Ca])_{aq0})$ versus log $([Ca]_{aq}/[Ca]_{aq0})$. These distribution coefficients are comparable with Lorens (1981), Zhong and Mucci (1989) and Morse and Bender (1990) and Tesoriero and Pankow (1996). The values are slightly higher in the tunnel drainage system compared to the published values, especially D_{Ba} is double than that given in Tesoriero and Pankow (1996).

The apparent oxygen isotopic fractionation coefficient $\alpha_{CaCO_3-H_2O}$ becomes smaller along the flow path (Fig. 4-12). A decrease in the oxygen isotopic fractionation at about 0.5 ‰ can be explained by

the increase of the temperature from 10.1 to 8.11 according to the temperature- oxygen isotopic fraction relation of Kim and O'Neil (1997).

The decrease in the pH and precipitation rate along the flow path would result into an increase of the oxygen isotopic fractionation (Dietzel et al., 2009) and can therefore not explain the observed drop in the oxygen isotopic fractionation (Fig. 4-12). In consequence the major drop of the isotopic fractionation between solution and $CaCO_3$ is most probably caused by mixing processes of solutions. Although the total O-isotopic composition of the water is constant over the whole flow path, it ($\delta^{18}O$) might be different for different species. This might explain the observed depletion in ^{18}O as also the CO_3^{2-} species becomes depleted with ^{18}O along the flow path due to the preferential incorporation of CO_3^{2-} with ^{18}O. Sampling the precipitates along the flow path, which are formed under different conditions and may partly contain detritus, would be a further explaination as the layers become most probably thiner along the flow path.
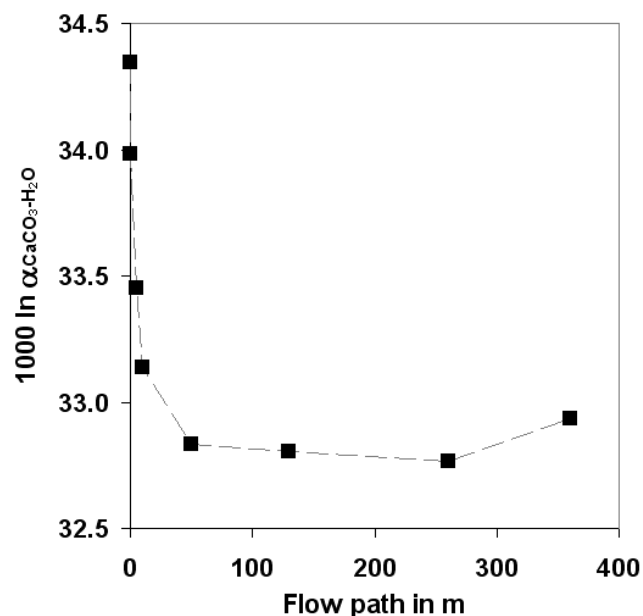
Fig. 4-12: Evolution of $\delta^{18}O$ in $CaCO_3$ and H_2O along the flow path.

The sampled solid does also not reflect directly the current isotopic signatures of the sampling day but rather the average isotopic signatures over a longer periode, and this isotopic signature changes slightly over the time.

The $CaCO_3$ deposits indicate a layered structure with dark and bright horizons. The bright horizons are enriched in ^{18}O versus ^{16}O compared to dark horizons (see Fig. 4-13). From sampling points P9 to P14 both carbon and oxygen isotopic signatures show similar tendencies, which can be caused by kinetic isotopic fractionation. Inverse variations of oxygen and carbon isotops can e.g. be caused by changes in the temperature (Hoefs, 2009). But more detailed observations are required as paramertes like temperature, pH, precipitation, CO_2 uptake and degassing rates may affect the fractionation behaviour.
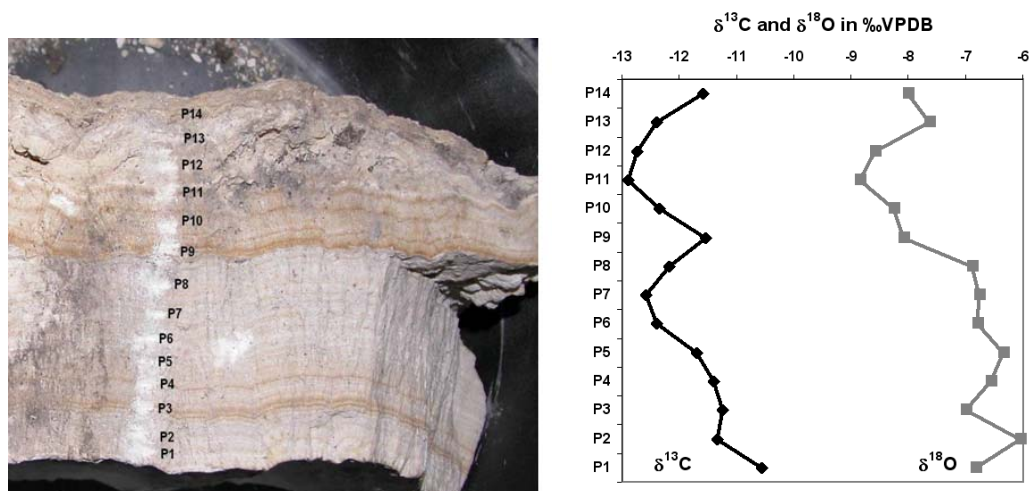
Fig. 4-13: Isotopic signature along the profile of the layered sinter from Holzgraben creek.

Besides to the isotopic composition the Mg distribution varies throught the sample. Darker layers have higher Mg concentration which can be followed from the peak shift of the "forbidden" peak for calcite at wavenumbers between 1086 and 1089 cm^{-1}. Elevated Mg concentrations cause a shift of the peak towards a wave number of 1089 cm^{-1} (Fig. 4-14) as it was found for Mg-calcite by Bischoff et al. (1985), Mg bearing minerals by e.g. Edwards (2005) and in the synthetic Mg-calcite of this study (data not shown) in the Raman spectrum. A similar shift was also found for other peaks (714, 2514 cm^{-1}) in the FTIR spectrum by Böttcher et al. (1997). Furthermore Alia et al. (1997) found an inverse correlation at the 1088 cm^{-1} Raman peak for Sr incorporation. The shift is caused by the stronger Mg-O bond which has a larger effect on the internal vibration of the carbonate ion than the weaker Ca-O bond (Bischoff et al., 1985).
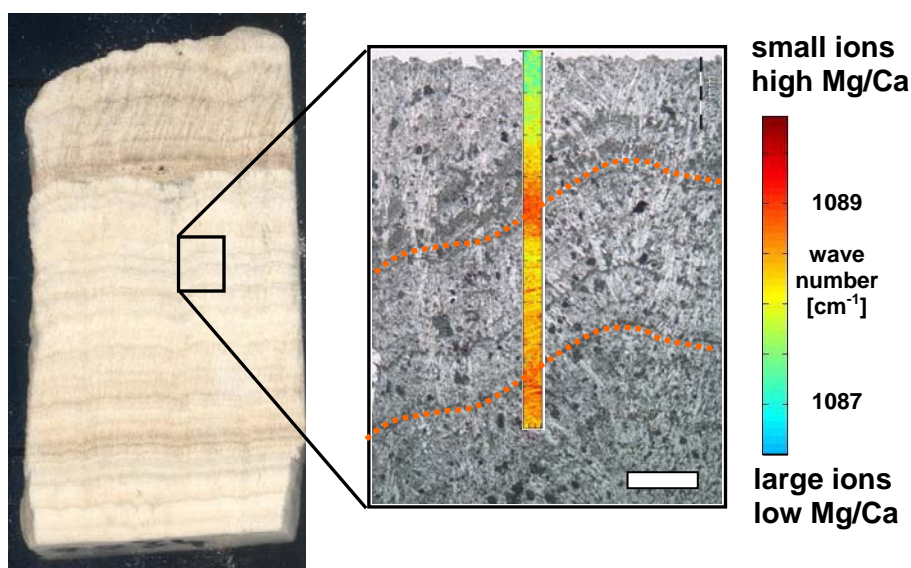
Fig. 4-14: The mapping indicates the position of the Raman peak at symmetric stretching vibration ν_1 peak. The shift of the Raman peak is caused by incorporation of small ions like Mg (increase in wave number). A similar shift was found for Mg-calcite by Bischoff et al. (1985), Mg bearing minerals by e.g. Edwards (2005) and for other peaks (714, 2514 cm^{-1}) in the FTIR spectrum by Böttcher et al. (1997). White scale bar is 2 cm.

Although also other ions like iron might be responsible for the peak shift, as the peakshift indicates only a change in the vibration frequency.

Silicon and iron concentrations correlate also within the dark layers, while Sr and Mg concentrations are partly depleted in the dark area according to the microprobe analyses. The high silicon and iron concentration at the dark areas might indicate the sedimentation of clay particles or other silicate detritus (Fig. 4-15).
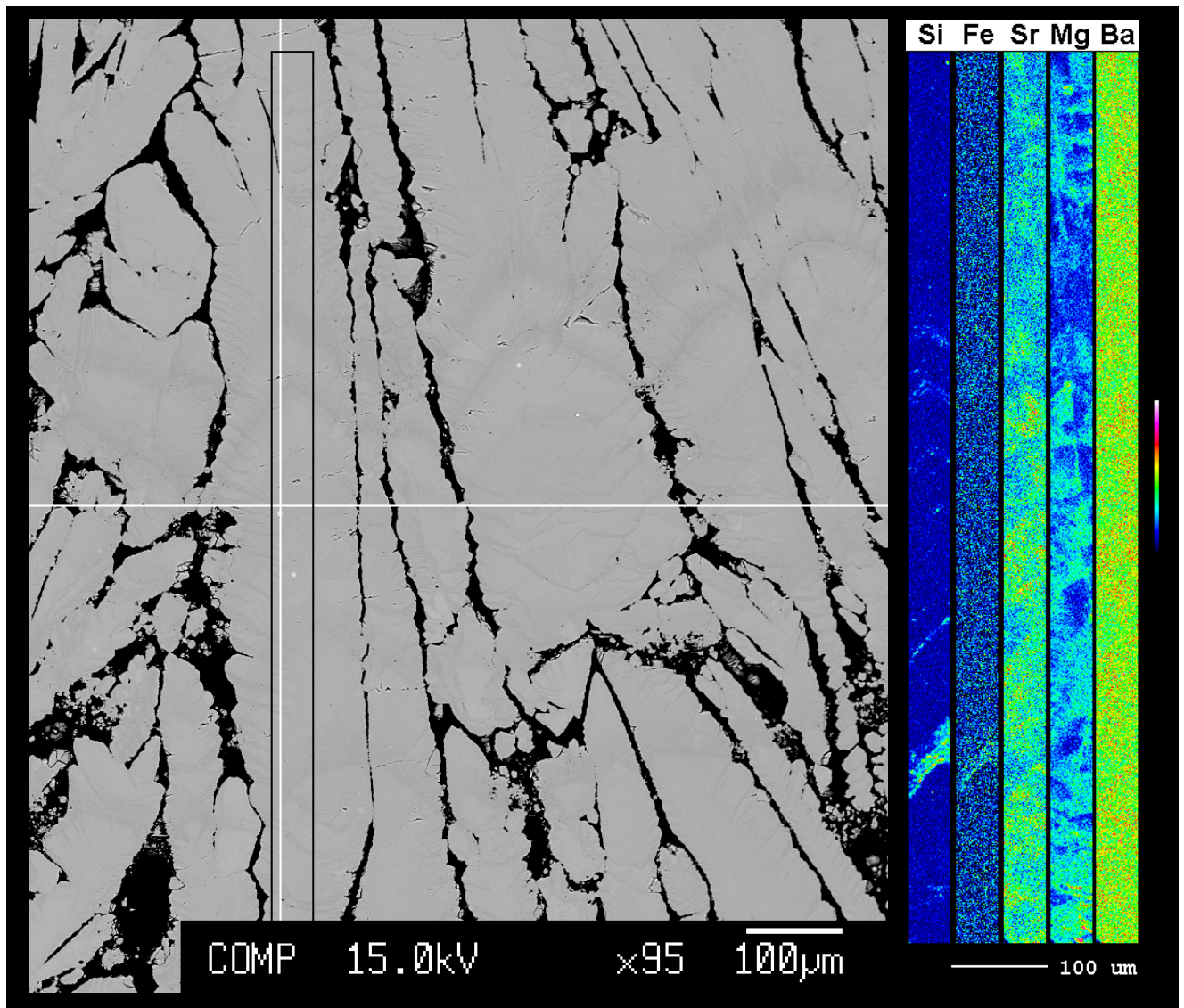
Fig. 4-15: Si, Fe, Sr, Mg and Ba distribution through a calcite crystal analysed by microprobe. Si and Fe correlate both with the appearance of the dark layers. Mg and Sr are inverse related to Si and Fe.

Sr depleted areas have often less Mg, but sometime Sr enriched areas have also less Mg. No unambiguous correlation between Mg and Sr was found as several processes trigger the Mg and Sr incorporation in this complex system. Further microprobe analyses indicate that the silicon distribution has mainly a layered structure, while Mg is mainly referred to the crystal morphology (Fig. 4-16).
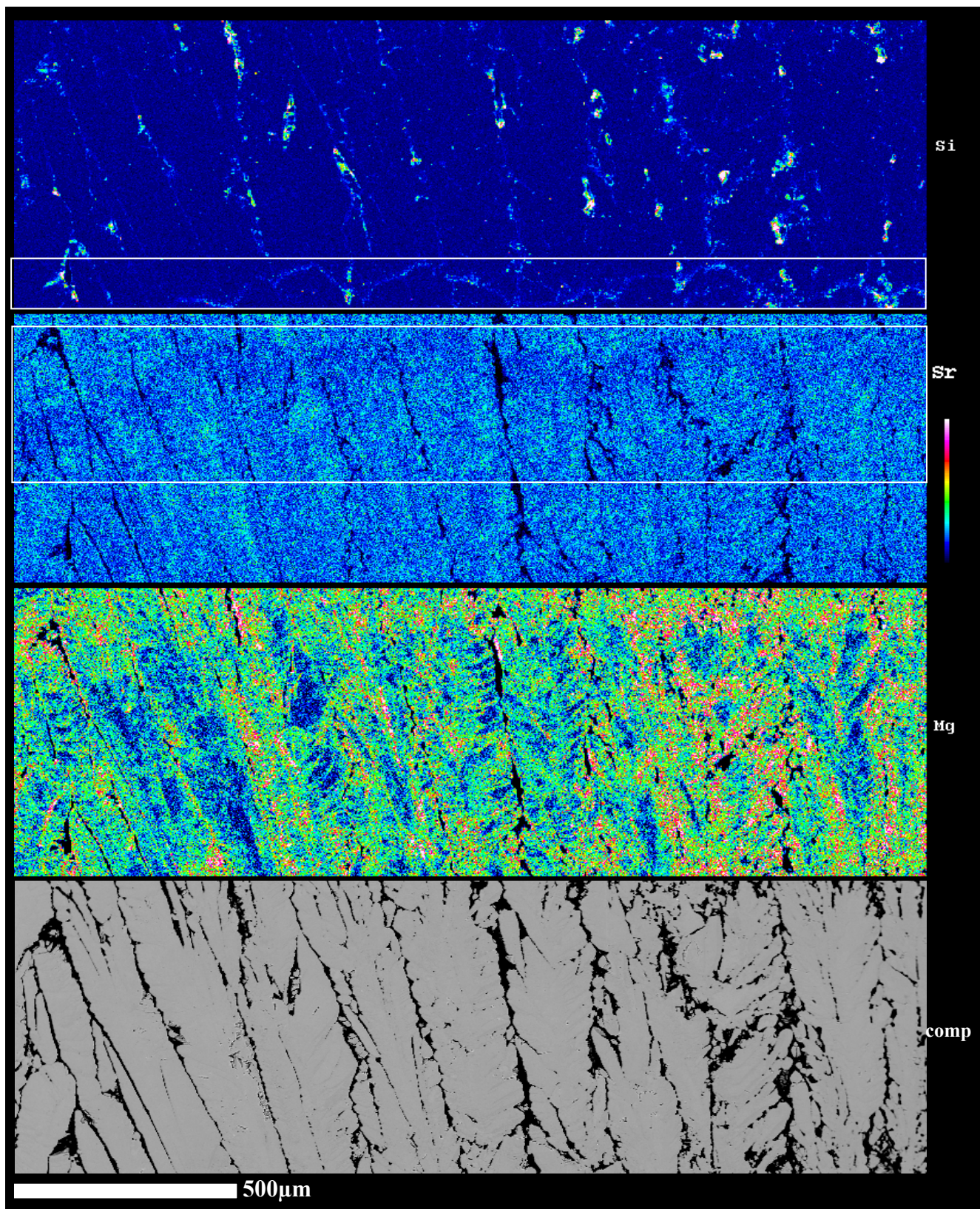
Fig. 4-16: Sr, Si and Mg distribution through a calcite crystal analysed by microprobe. White rectangular indicates Si and Sr distributions, which are bound to layers and go over several crystals, while Mg distribution is mainly bound to the crystal morphology.

5   Experimental Studies

5.1   Polymorph identification

Typical XRD pattern for experiments, where solely calcite, aragonite or vaterite was precipitated, are displayed in Fig. 5-1. In the case of mixtures of $CaCO_3$ polymorphs the areas of the peaks at $d_{104}=3.036$ Å (calcite), $d_{221}=1.978$ Å (aragonite) and $d_{110}=3.56$ Å (vaterite) were used for quantification, where overlap of peaks from distinct polymorphs can be neglected (see Fig. 5-1d).
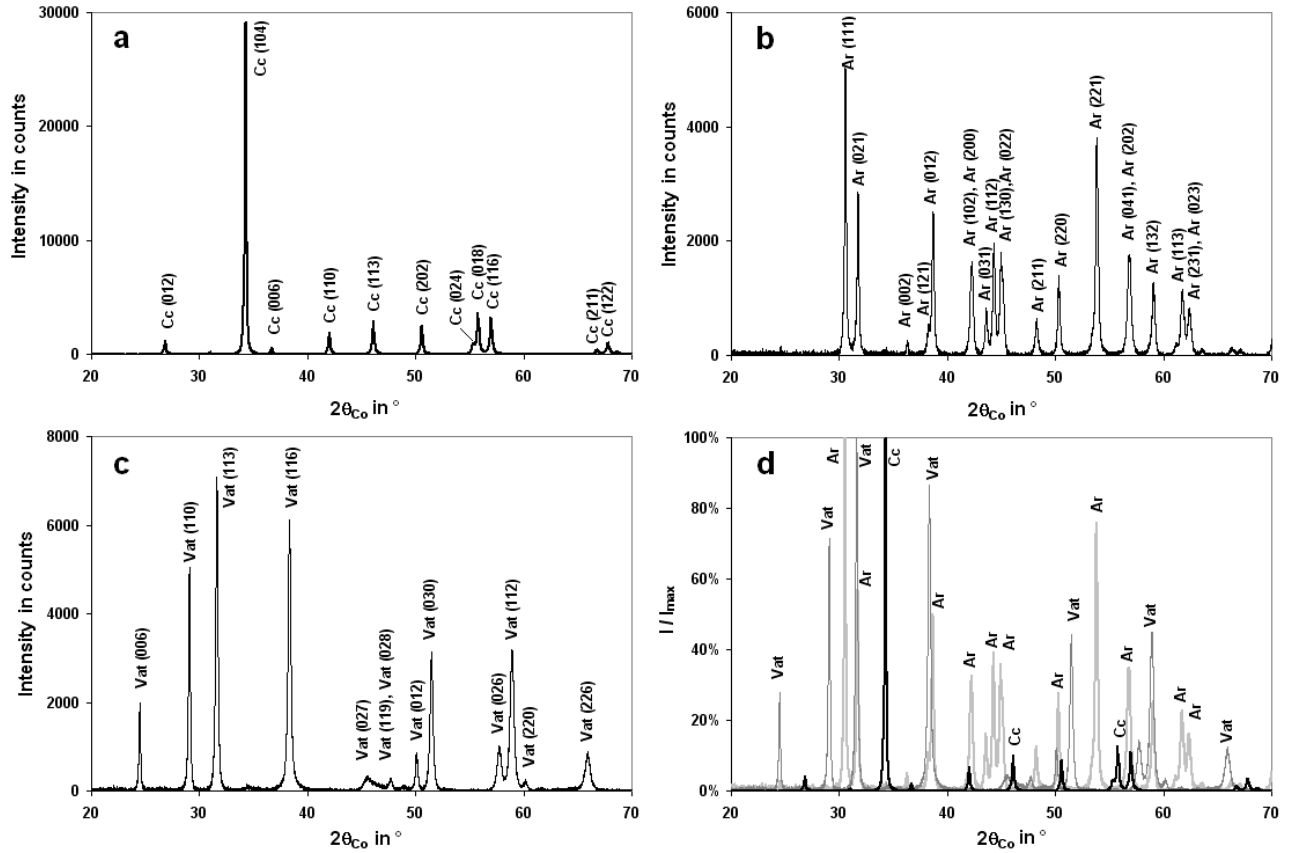
Fig. 5-1: XRD pattern for (a) calcite, (b) aragonite, and (c) vaterite from experiments 24, 62, and 105, respectively (Tab. A4 in appendix). (d) Comparison of XRD pattern for calcite, aragonite, and vaterite. Indices are given according to the space groups R $\bar{3}$ c (a=4.989 Å, c=17.063 Å), Pmcn (a=4.962 Å, b=7.972 Å, c=5.751 Å), and P 6_1 22 (a=7.29 Å, c=25.3 Å) for calcite, aragonite, and vaterite, respectively.

The fraction of calcite (X_{Cc}), aragonite (X_{Ar}) and vaterite (X_{Vat}) were calculated according to the

$$X_{Cc} = \frac{1}{1 + f_a \dfrac{A_{Ar221}}{A_{Cc104}} + f_v \dfrac{A_{Vat110}}{A_{Cc104}}} \qquad (5\text{-}1)$$

$$X_{Ar} = f_a \frac{A_{Ar221}}{A_{Cc104}} X_{Cc} \qquad (5\text{-}2)$$

$$X_{Vat} = 1 - X_{Cc} - X_{Ar} \qquad (5\text{-}3)$$

by the individual peak areas, A_i (see e.g. Kontoyannis and Vagenas, 2000). The values for the coefficients $f_a = 6.4$ and $f_v = 5.7$ were determined by calibration with artificial well known mixtures of $CaCO_3$ polymorphs. The precision of analyses is ± 5 % with a polymorph detection limit of about 1 wt.% (see individual polymorph content in Tab. A4 in appendix). In experiments, where the amount of precipitate was insufficient for XRD analysis, FTIR was applied. Characteristic FTIR spectra for calcite, aragonite, and vaterite are shown in Fig. 5-2. Solids were identified by their in-plane bending vibration ν_4 of the carbonate group with a double peak at 700 and 712-713 cm^{-1} for aragonite and a single peak at 711-712, and 742-743 cm^{-1}, for calcite and vaterite, respectively.
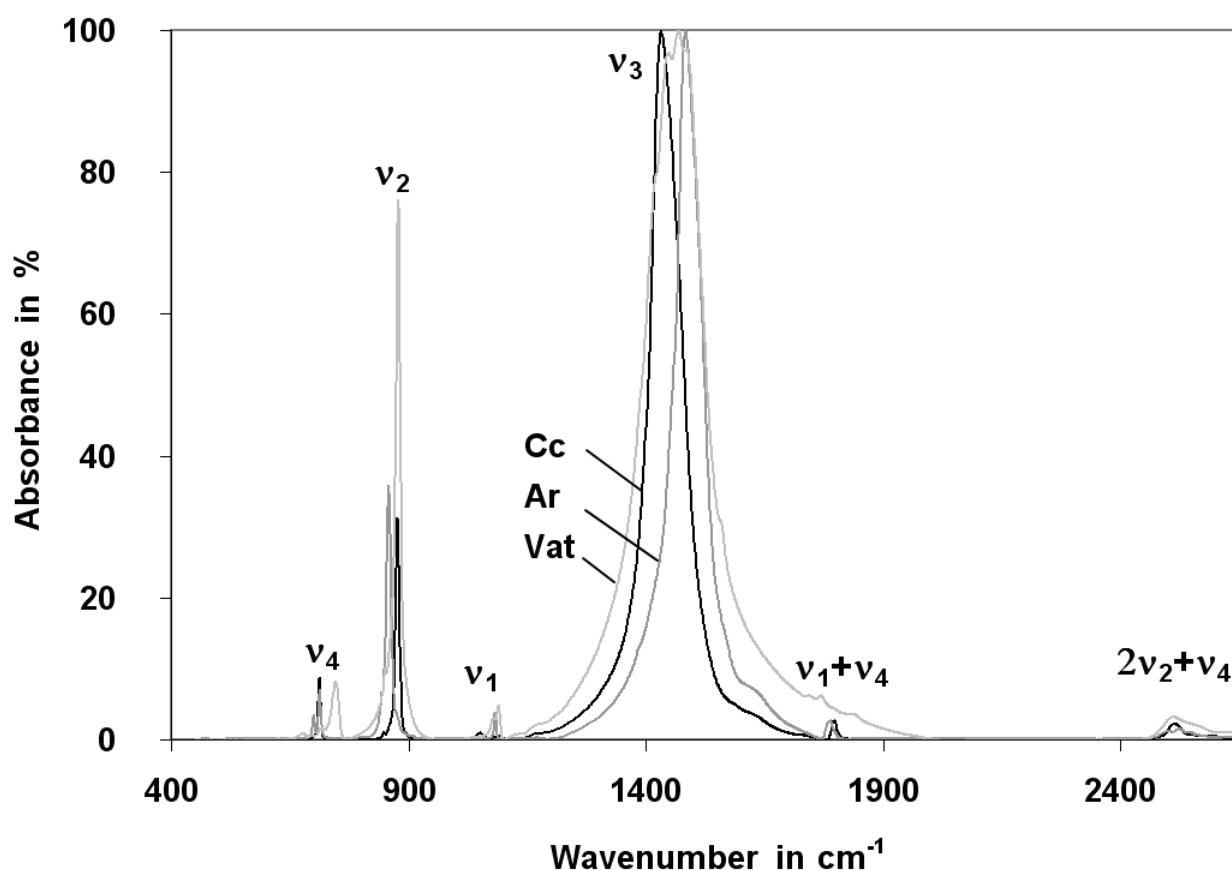
Fig. 5-2: Normalised absorbance in FTIR spectra for calcite, aragonite, and vaterite from experiments 24, 62, and 105, respectively (Tab. A4 see appendix and Fig. 5-1). ν_1: symmetric stretching vibration, ν_2: out-of-plane bending vibration, ν_3: asymmetric stretching vibration, ν_4: in-plane bending vibration of the carbonate group. $\nu_1 + \nu_3$ and $\nu_1 + \nu_4$ are combined modes.

Typical morphologies of the precipitated $CaCO_3$ polymorphs are displayed in Fig. 5-3. Calcite crystals have rhombic shapes (Fig. 5-3a) with typical sizes between 20 and 30 μm. The presence of Mg can modify the shape of the rhombic calcite into steep rhombic or dodecahedron shaped Mg-calcites, but the individual crystal sizes remain the same (Fig. 5-3b). Aragonite crystals are either needle-like (1x10 μm) or dipyramidal shaped (8x30μm; see Fig. 5-3c and Fig. 5-3d). Vaterite appears in hexagonal shaped plates and aggregates of plates or spheres (Fig. 5-3e and Fig. 5-3f). Single vaterite plates are typically sized between 5 to 10 μm in diameter and 1 to 2 μm thick. However, vaterite aggregates reach maximum sizes up to 200 μm in diameter (see also chapter 5.7).
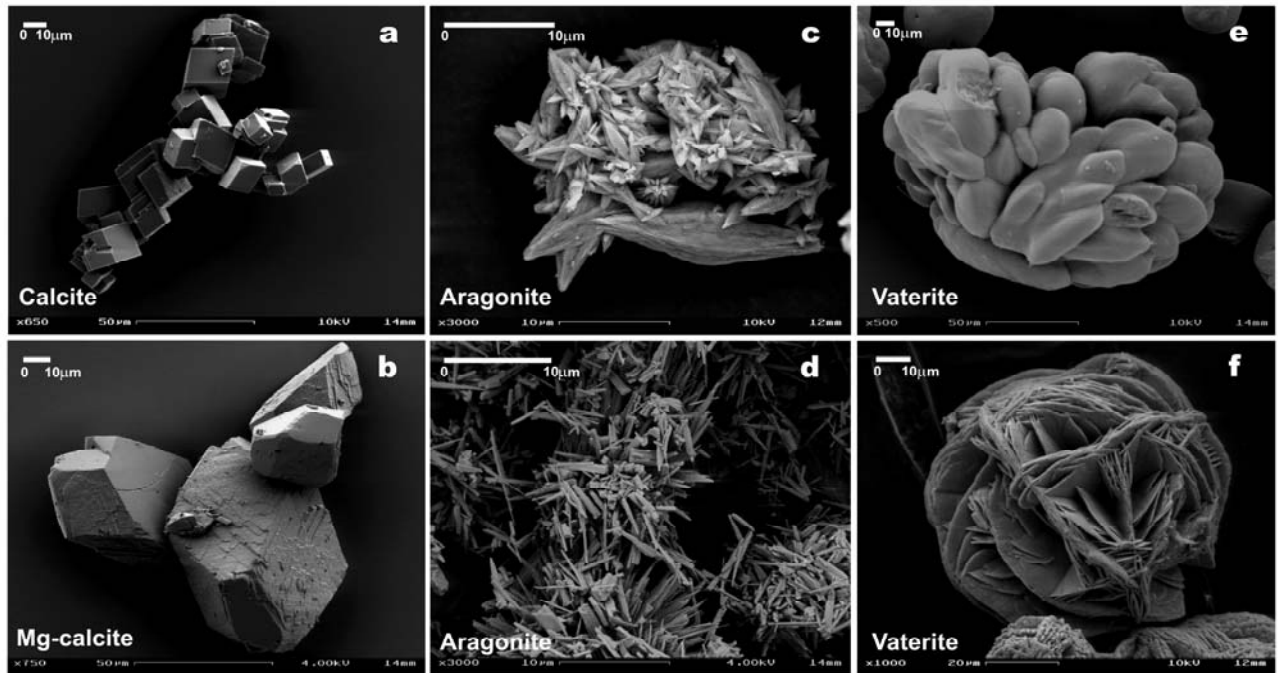
Fig. 5-3: SEM-SE images with typical shapes of the precipitated CaCO$_3$ polymorphs. (a) calcite (experiment 23; Tab. A4 see appendix), (b) Mg-calcite (47), (c) aragonite (62), (d) aragonite (58), (e) vaterite (105), and (f) vaterite (99).

5.2 Polymorph evolution

In most of the experiments the precipitates were separated from the solution at the end of an experimental run and subsequently analysed. However, in several experiments the evolution of polymorph formation was investigated as a function of precipitation time. Fig. 5-4 displays the obtained crystals at the first sampling and at the end of the experiments. Obviously, in all experiments the polymorph content has not changed significantly from the first sampling until the end of the experiments. For instance, calcite crystals with a similar shape were found at t_{prec} = 1.8 and 9.4 h in experiment 33 (Fig. 5-4a and Fig. 5-4b). Mg-calcite and aragonite crystals were identified in experiment 56 at t_{prec} = 1 and 10 h.

During the experiment both, Mg-calcite and aragonite, are growing, but the proportion of aragonite and calcite remains nearly constant (Fig. 5-4d). In experiment 78 aragonite was formed, growing from smaller to bigger needles from t_{prec} = 15 to 41 h (Fig. 5-4f). Vaterite and calcite crystals were deciphered in the experiment 95, growing from t_{prec} = 19 to 26 h with a nearly constant proportion of vaterite and calcite during the experimental run. Thus, the specification and occurrence of individual CaCO$_3$ polymorphs are determined within the time period of nucleation and an initial precipitation period. Ongoing precipitation is referred to the mineralogy and shape of the CaCO$_3$ precipitates fixed within this initial period. If a "transformation time" exists in our experiments, then it is slightly lower than the transformation times which were found by other groups e.g. 4h by Sawada et al. (1990), 5h by Jiménez-López et al. (2001) and 3 to 22 h by Ogino et al. (1987). Schmidt et al. (2010) found transformation duration of 72 hours in their experiments. They verified dissolution and

precipitation processes by using powder X-ray diffraction, scanning electron microscopy and site-selective time-resolved laser fluorescence spectroscopy from EU^{3+} doped solutions.
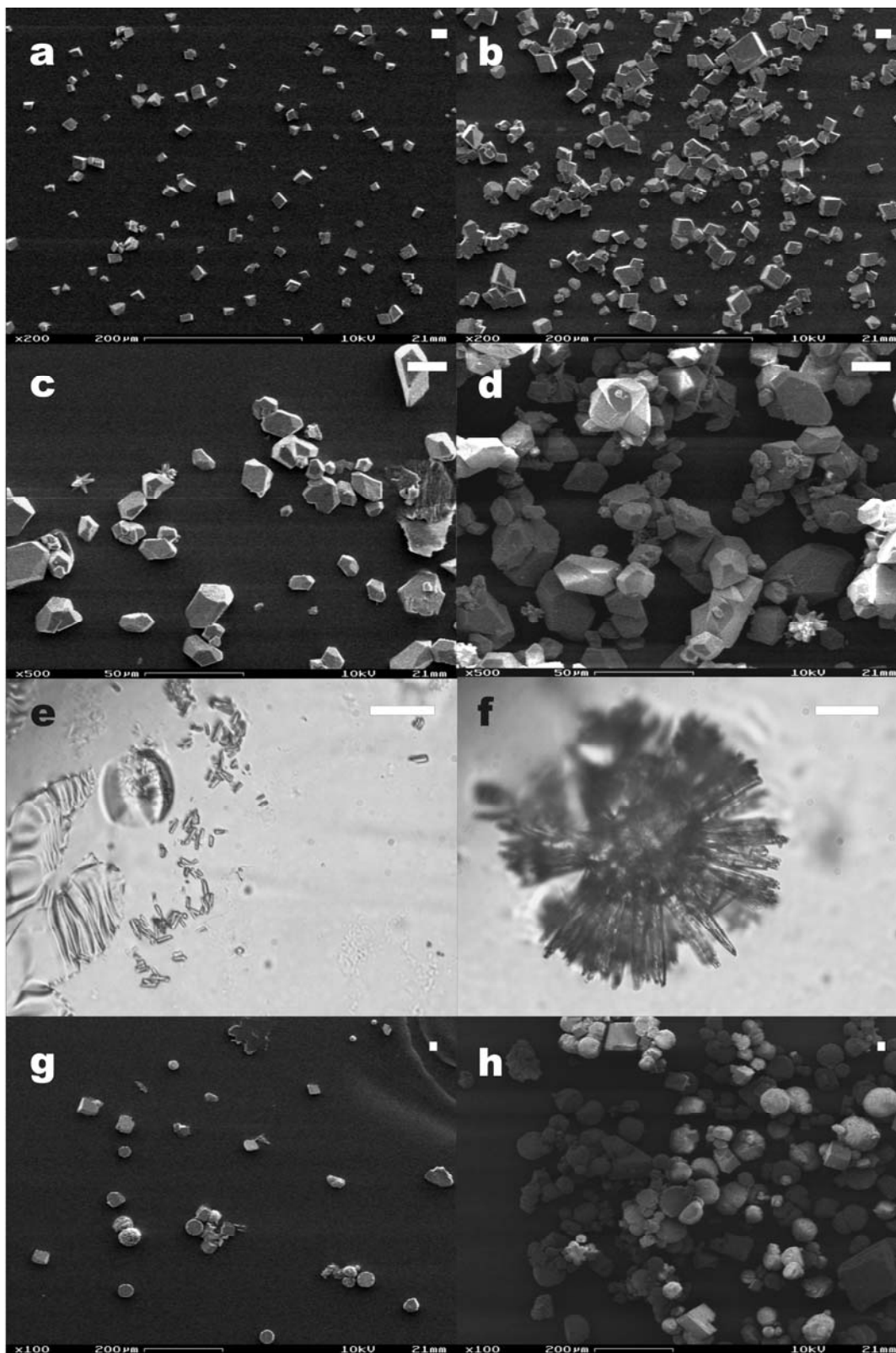
Fig. 5-4: SEM-SE images of calcite crystals in experiment 33 (Tab. A4) at a precipitation time t_{prec} = 1.8 (a) and 9.4 h (b); SEM-SE images Mg-calcites and aragonite in experiment 56 at t_{prec} = 1 (c) and 10 h (d); Optical microscopy image of aragonite crystals in experiment 78 at 15 (e) and 41 h (f). SEM-SE images of vaterite and calcite in experiment 95 at t_{prec} = 19 (g) and 26 h (h).

However, in our experiments ongoing from several hours (1 to 19 h) after $CaCO_3$ nucleation to the final stage of the experiment no transformation of precipitated $CaCO_3$ was detected, which might be caused by keeping the pH constant. A constant pH results in a $CaCO_3$ saturation degree close to the nucleation period of the individual $CaCO_3$ polymorphs. Furthermore continuous carbonate supply during the precipitation stage may additionally prevent the transformation of precipitated $CaCO_3$, whereas in the experiments of e.g. Ogino et al. (1987) the saturation degree of $CaCO_3$ decreases significantly as a function of reaction time. Thus, for the present experimental setup the different precipitation times (t_{prec}; Tab. A4) do not affect the appearance of a distinct $CaCO_3$ polymorph and its shape, and transformation of $CaCO_3$ can be ruled out during ongoing precipitation of $CaCO_3$ after several hours of the $CaCO_3$ nucleation period.

5.3 Nucleation and first precipitation of $CaCO_3$

Formation of $CaCO_3$ was studied without seeds in homogeneous solution, where nucleation and time of first $CaCO_3$ precipitation was observed by pH stat technique through a change in slope of the recorded NaOH titration curve. The slope of the titration curve increases, when the precipition of $CaCO_3$ occurs with an excellent detection limit of down to 10 µmol l^{-1} of $CaCO_3$ formed in the experiment (representing about 1‰ of initially total dissolved Ca). The time of first precipitation of $CaCO_3$, t_{fp}, comprises the time for CO_3^{2-} accumulation and the reaction of Ca^{2+} and CO_3^{2-} ions to yield $CaCO_3$ nuclei (see section 3.2.4). The value of t_{fp} depends on the experimental conditions, such as the R_{CO_3} value (R_{CO_3} is proportional to D_{CO_2av}), the chemical composition (Mg and Pasp concentration), and T of the outer solution.

5.3.1 CO_2 diffusion rate and temperature effect

At a given temperature, the value of D_{CO_2av} was adjusted by the pCO_2 gradient between the inner and outer solution and the thickness of the PE membrane. The average diffusion rate of CO_2 correlates to the t_{fp} value (Fig. 5-5a). A decrease of D_{CO_2av} results in an increase of t_{fp} according to the equations

$$\log(t_{fp}) = -0.70 \log(D_{CO_2av}) + 3.38 \qquad \text{at 6 - 10°C} \qquad (R^2 = 0.98, n=5) \qquad (5\text{-}4)$$

$$\log(t_{fp}) = -0.73 \log(D_{CO_2av}) + 3.05 \qquad \text{at 25 - 40°C} \qquad (R^2 = 0.97, n=12) \qquad (5\text{-}5)$$

for the precipitation of calcite at [Mg]/[Ca] < 0.05. Similar slopes of the regression lines for $\log(t_{fp})$ versus $\log(D_{CO_2av})$ are found for all experiment even at different temperatures, but the intercept differs between 6 - 10°C and 25 - 40°C. Thus, at a given CO_2 diffusion rate an elevated time period is required to obtain the nucleation and initial precipitation of calcite at low (6 - 10°C) compared to high temperatures (25 - 40°C). The delay in nucleation of $CaCO_3$ precipitation at low temperature is due to the about 20% higher solubilities of the $CaCO_3$ polymorphs at low (6°C) versus high temperature (40°C) (see equations in Tab. 2-4). An additional impact is referred to the DIC species

distribution which results in significant lower total CO_3^{2-} concentrations (= $[CO_3^{2-}]$ + $[CaCO_3^0]$ + $[MgCO_3^0]$) at a given DIC concentration at low versus high temperature. E.g. a decrease of total CO_3^{2-} concentration by about 46 mol% from 40 to 6°C is calculated by using PHREEQC at pH 8.30 and a given DIC concentration.
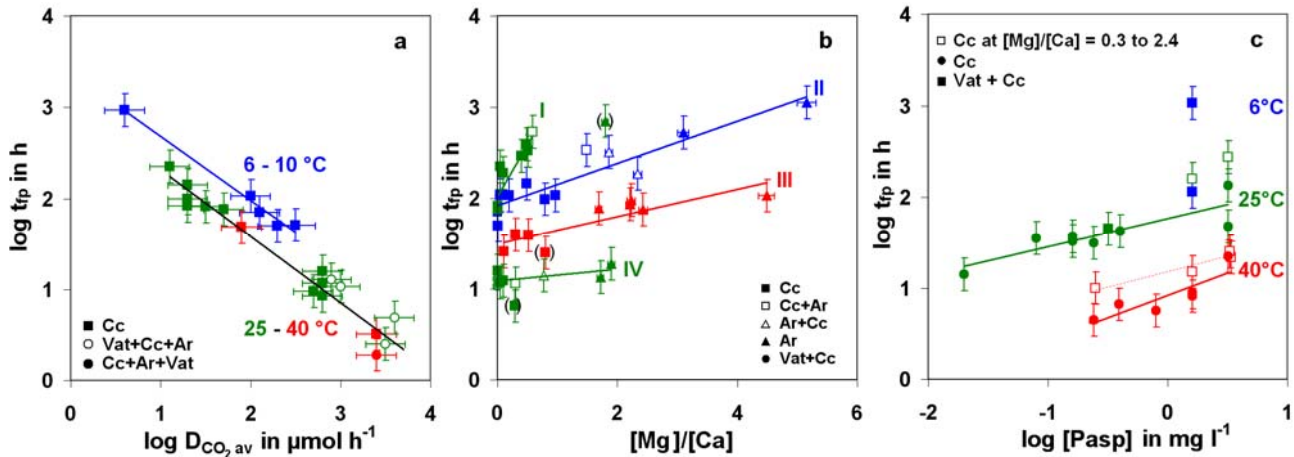
Fig. 5-5: Time of first precipitation of CaCO₃, t$_{fp}$, as a function of (a) average CO$_2$ diffusion rate, D$_{CO_2av}$, (experiments with molar [Mg]/[Ca] ≤ 0.05 and without Pasp), (b) molar [Mg]/[Ca] ratio and (c) Pasp concentration. b: I are experiments at 0.7 < log(D$_{CO_2av}$) < 1.7 and 25°C (green symbols) (equation (5-8)); II at 1.6 < log(D$_{CO_2av}$) < 2.3 and 6°C to 10°C (blue) symbols (equation (5-6)); III at 1.6 < log(D$_{CO_2av}$) < 2 at 40°C (red symbols) (equation (5-9)); and IV at 2.8 < log(D$_{CO_2av}$) < 3 at 25°C (green symbols) (equation (5-7)). I and III: conducted with 2 mm PE membrane. II and IV: conducted with 0.2 mm PE membrane. Given error bars display double standard deviation (2σ) see Tab. A4. Brackets denote experiments which are not considered for the regression analyses due to e.g. high temperature variability.

Only two regression lines for the log(t$_{fp}$) - log(D$_{CO_2av}$) relationship can be found in the temperature range from 6 to 40°C (Fig. 5-5a). No significant difference between 6 and 10°C as well as between 25 and 40°C exists, although the previous considerations would suggest a continuous temperature dependency. It is suggested that the CaCO$_3$ precursor phase at T ≤ 10°C might be different from the respective precursor at T ≥ 25°C, which dominates t$_{fp}$. The value of t$_{fp}$ can be adjusted by changing temperature and CO$_2$ flux into the solution. Interestingly, vaterite is only precipitated at D$_{CO_2av}$ above 800 µmol h^{-1} (log(D$_{CO_2av}$) > 2.9; see Fig. 5-5a).

5.3.2   Effect of Magnesium

The time of first precipitation of CaCO$_3$ depends not only on the CO$_2$ flux into the outer solution, but also on the molar [Mg]/[Ca] ratio of the solution (Fig. 5-5b). For [Mg]/[Ca] > 0.05 the value of t$_{fp}$ (in h) increases significantly according to the expressions

$\log(t_{fp}) = 0.23\ [Mg]/[Ca]+1.92$ at 6 to 10°C, $1.6 < \log(D_{CO_2av}) < 2.3$ µmol h^{-1} (R^2= 0.85, n=12) (5-6)

$\log(t_{fp}) = 0.06\ [Mg]/[Ca]+1.09$ at 25°C, $2.8 < \log(D_{CO_2av}) < 3$ µmol h^{-1} (R^2 = 0.40, n=9)   (5-7)

$\log(t_{fp}) = 1.13\ [Mg]/[Ca]+2.02$ at 25°C, $0.7 < \log(D_{CO_2av}) < 1.3$ µmol h^{-1} (R^2 = 0.90, n=7) (5-8)

$\log(t_{fp}) = 0.14\ [Mg]/[Ca]+1.55$ at 40°C, $1.6 < \log(D_{CO_2av}) < 2$ µmol h^{-1} (R^2 = 0.78, n=8) (5-9)

keeping the temperature constant and within individual D_{CO_2av} ranges (see Fig. 5-5b and Tab. A4 see appendix). The CO_2 diffusion rate ranges are referred to experiments with the same thickness and kind of the PE membrane (0.2 or 2 mm) and chemical composition of the inner solution. Equations (5-6) to (5-9) result in t_{fp} values without Mg addition ([Mg]/[Ca] = 0) which are close to the t_{fp} value at similar diffusion rates obtained by equations (5-4) and (5-5), respectively.

At constant temperature and within the above individual D_{CO_2av} ranges, the value of t_{fp} increases with increasing [Mg]/[Ca] ratios in solution. The impact of the CO_2 diffusion rate on the [Mg]/[Ca] – $\log(t_{fp})$ relationship (see lines I and IV for equations (5-8) and (5-7), respectively; Fig. 5-5b) is stronger at 25°C than the temperature effect in the observed temperature range from 6 to 40°C. The influence of temperature on the slope of the [Mg]/[Ca] – $\log(t_{fp})$ relationship is very small at a constant CO_2-diffusion rate (see lines II and III for equations (5-6) and (5-9), respectively; Fig. 5-5b), but the intercept is shifted to higher t_{fp} values at lower temperature. The retardation of $CaCO_3$ formation in the presence of Mg is in accordance with e.g. Fernández-Díaz (1996).

This retardation is caused by

(i) dissolved Mg^{2+} ions reacting with CO_3^{2-} ions to aqueous complexes and thus reducing the activity of the CO_3^{2-} (for instance, the activity of Mg^{2+} can be reduced by about 36% at [Mg]/[Ca] = 5 and 6°C according to our calculations).

(ii) Mg inhibiting $CaCO_3$ formation by covering and poisoning the $CaCO_3$ surface especially at active surface sites (Berner, 1975).

(iii) increasing the solubility of the so-called Mg-calcite by defects due to incorporation of Mg (Mucci and Morse, 1984).

(iv) Mg inhibiting calcium carbonate growth as the dehydration energy is 18% higher (Lippmann, 1973) for the small sized Mg^{2+} ions ($^{VI}Mg^{2+}$: 0.72 Å) compared to the large Ca^{2+} ions ($^{VI}Ca^{2+}$: 1.0 Å - radii from Shannon, 1976). Thus, co-precipitated or adsorbed Mg^{2+} ions can slow down calcite growth (Lippmann, 1973).

Similar processes may occur during vaterite formation, because vaterite also incorporates Mg within the same order of magnitude as calcite (Noethig-Laslo and Brečević, 1998).

In principle, the inhibition of nucleation of $CaCO_3$ by Mg^{2+} ions causes a higher $(CO_3^{2-})_{fp}/(Ca^{2+})$ ratio and IAP_{fp} in our experiments. But elevated CO_2 diffusion rates can reduce this impact. This explains the strong dependency of the Mg-caused retardation of first precipitation on the CO_2 diffusion rate.

5.3.3   Effect of Polyaspartic acid

In the case of Pasp addition, the value of t_{fp} strongly increases. At a constant temperature (25 and 40°C) and within a given range of CO_2 diffusion rate the following relationships are obtained:

$$\log(t_{fp})=0.31 \log([Pasp]) + 1.76 \text{ at } 25°C, 2.4 < \log(D_{CO_2av}) < 2.8 \text{ μmol h}^{-1} (R^2 = 0.74, n=9) \quad (5-10)$$
$$\log(t_{fp})=0.50 \log([Pasp]) + 0.92 \text{ at } 40°C, 3.0 < \log(D_{CO_2av}) < 3.3 \text{ μmol h}^{-1} (R^2 = 0.74, n=6) \quad (5-11)$$

(see Fig. 5-5c). The time of first $CaCO_3$ precipitation as well as the saturation degree with respect to the calcium carbonate phases at t_{fp} increase significantly with increasing Pasp concentration in the solution, even at low Pasp concentration down to 0.1 mg l^{-1} (Fig. 5-5c).

It has been suggested that the inhibition effect of Pasp is mainly caused by the reaction of Pasp with the reactive surface sites of the $CaCO_3$ nuclei or crystals (e.g. Sikes et al., 1994). This is in accordance with the fact that formation of aqueous Ca-Pasp complexes cannot significantly influence the calcium concentration (10 mmol l^{-1}) in our experiments as Pasp concentrations reach only up to about 2 μmol l^{-1}.

5.3.4   Effect of polyaspartic acid in combination with magnesium

In the presence of both, Pasp and Mg, the time of first precipitation is higher than in the case of either the presence of Pasp or Mg. This can be followed by the equation:

$$\log(t_{fp}) = 0.34 \log([Pasp]) + 1.18 \qquad (R^2 = 0.92, n=3) \qquad (5-12)$$

(at $3.1 < \log(D_{CO_2av}) < 3.2$ μmol h^{-1}, [Mg]/[Ca] $\approx$ 1) in comparison to equation (5-11) at 40°C (see equation (5-12) as dotted line in Fig. 5-5c).

In the case of aspartic acid ($C_4H_7O_4N$) the values of the aquo complex formation constants for Mg^{2+} and Ca^{2+} are $\log(K_{Mg-Asp}) = 2.4$ and $\log(K_{Ca-Asp}) = 1.6$, respectively (Wang et al., 2009). Assuming that Mg^{2+} ions interact stronger than Ca^{2+} ions also with Pasp, elevated Mg concentration may reduce the available Pasp concentration and thus reduce the impact of Pasp on t_{fp}. As this is not valid, the impact of Pasp on nucleation behaviour by interacting with nuclei of solid surfaces is most likely.

5.3.5 Effect of $CaCO_3$ polymorphisms

Obviously, the value of time of first precipitation depends less on the formation of distinct $CaCO_3$ polymorph, than on the [Mg]/[Ca] ratio, Pasp concentration in the solution, and CO_2 diffusion rate (Fig. 5-5a to Fig. 5-5c). The value of t_{fp} seems to be independent of the formed $CaCO_3$ polymorph. The same $\log(t_{fp}) - \log(D_{CO_2av})$ relationship is valid for all $CaCO_3$ polymorphs (Fig. 5-5a), although, e.g. vaterite is only formed at D_{CO_2av} values above $10^{2.9}$ μmol h^{-1}. $CaCO_3$ polymorph formation behave also similar in the $\log(t_{fp})$ - [Mg]/[Ca] diagram (Fig. 5-5b).

5.4 Supersaturation and ion activity product

Once supersaturation with respect to a $CaCO_3$ phase is reached in the experiments, nucleation and first precipitation of $CaCO_3$ occur not immediately. The delay (i) between a critical saturation degree is established and (ii) $CaCO_3$ nucleation is called the induction time. The induction time depends on the given saturation degree (Koutsoukos and Kontoyannis, 1984; Pokrovsky, 1998). In our experiments the saturation degree with respect to $CaCO_3$ polymorphs is not constant during an individual run. The saturation degree increases as fast as carbonate is delivered from the ongoing CO_2 diffusion. At elevated CO_2 diffusion rates higher saturation degrees for first $CaCO_3$ precipitation (e.g. $D_{CO_2av} = 10^{3.6}$ μmol h^{-1} results in $\Omega_{Cc\ fp} = 37$ at experiment 28 in Tab. A4) are obtained during the "induction time".

As discussed above, the presence of Mg and/or Pasp causes a significant retardation of $CaCO_3$ nucleation by several hours and thus elevated saturation degree with respect to $CaCO_3$ polymorphs. Consequently higher saturation degrees for $CaCO_3$ polymorphs can be reached at high Mg and Pasp concentration and by rapid accumulation of a CO_3^{2-} (e.g. $\Omega_{Cc\ fp} = 75$ for experiments 107 and 108).

In the absence of Pasp nearly all experimental solutions are supersaturated with respect to vaterite ($\Omega_{Vat} > 1$) at the time of first $CaCO_3$ precipitation and undersaturated with respect to monohydrocalcite ($\Omega_{Mhc} < 1$) (see Fig. 5-6a, Tab. A4a and b). In the presence of Pasp the saturation degree with respect to monohydrocalcite (Fig. 5-6b and Tab. A4c) was exceeded in all experiments.
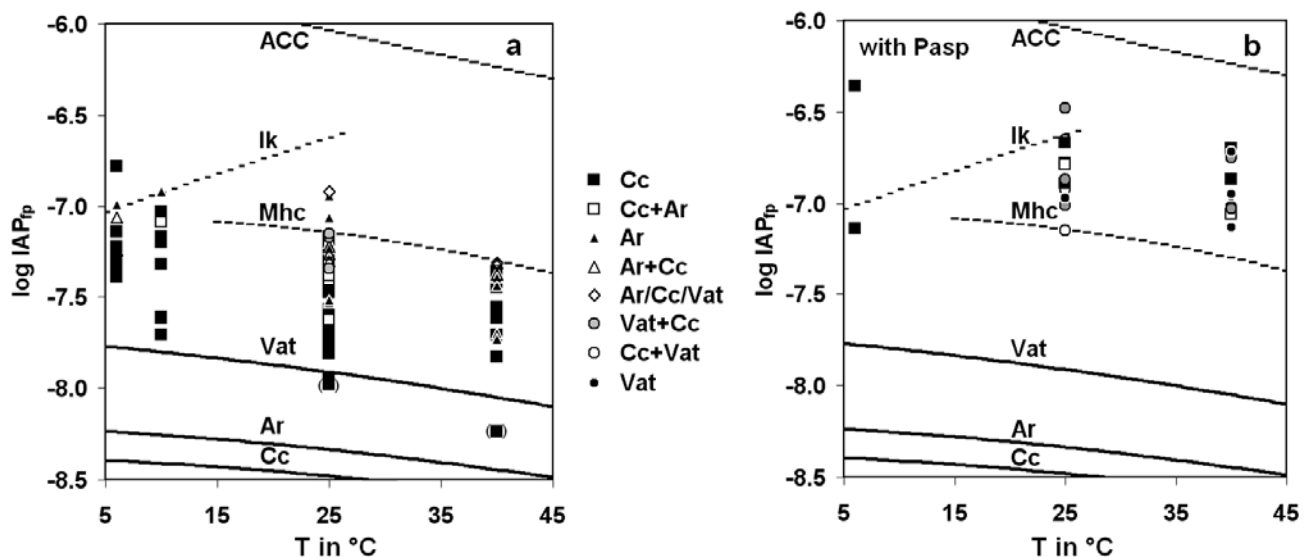
Fig. 5-6: Ion activity product at the time of first $CaCO_3$ precipitation, $IAP_{fp} = (Ca^{2+})\ (CO_3^{2-})$, as a function of temperature (a) without and (b) with Pasp. Individual lines are obtained by the solubility product of calcite (Cc), aragonite (Ar), vaterite (Vat), monohydrocalcite (Mhc), ikaite (Ik), and amorphous calcium carbonate (ACC) (see Tab. 2-4). a: Brackets denote experiments (77 and 29 in Tab. A4) with elevated temperature variation of ±0.5°C and ±0.2°C, respectively.

Considering our experimental results, the above IAP_{fp} limits for $CaCO_3$ formation, vaterite and monohydrocalcite saturation with and without Pasp, respectively, are valid independently of the temperature, carbonate accumulation rate, and Mg concentration.

The IAP_{fp} limits for $CaCO_3$ formation may indicate individual $CaCO_3$ precursors. Interestingly, the formation of vaterite requires $\Omega_{vat\ fp} \geq 4$ (Tab. A4), which is similar to the required value for calcite ($\Omega_{Cc\ fp} \geq 4$) and aragonite formation ($\Omega_{Ar\ fp} \geq 5$). The solubility line of ACC is not reached in any experimental run, even if uncertainties with respect to ACC solubility data were taken into account (e.g. Clarkson et al., 1992).

5.5 Precipitation rate of calcium carbonate

The precipitation rate of calcium carbonate (R' values in Tab. A4) is adjusted by the accumulation rate of carbonate (R_{CO_3} proportional to D_{CO_2av}), the temperature and the concentration of Mg and Pasp in the outer solution. Obviously, without Mg and Pasp the value of R for calcite increases as the D_{CO_2av} value rises for temperatures between 6 and 40°C (Fig. 5-7) and is not limited by the CO_2 diffusion rate ($R \geq D_{CO_2av}$).

Elevated precipitation rates of $CaCO_3$ (e.g. log (R') = 3.6 compared to 1.6; R' in μmol h^{-1}) are caused by elevated Ω_{fp} values (e.g. $\Omega_{Cc\ fp}$ = 37 compared to 6, respectively), which are obtained by higher carbonate accumulation rate. This behaviour is in accordance with equation (2-22) as discussed in section 2.4.
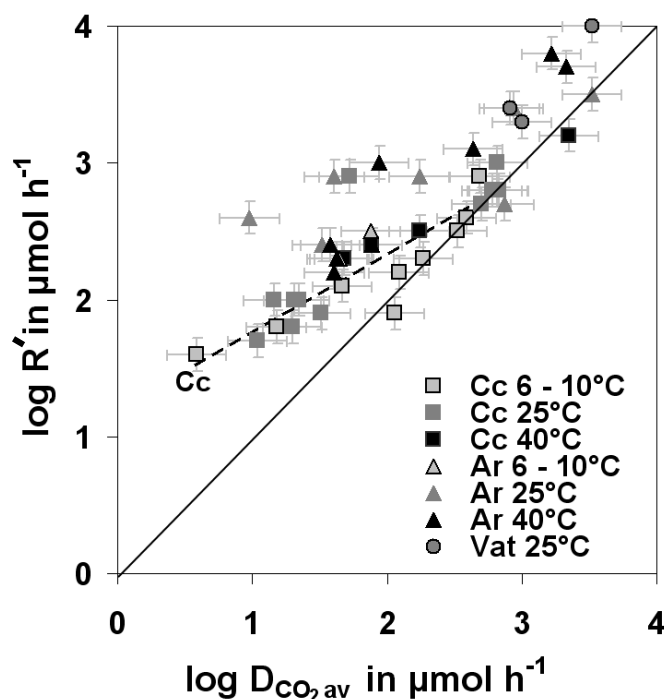
Fig. 5-7: Precipitation rate of $CaCO_3$ (R' in μmol h^{-1}) vs. average CO_2 diffusion rate (D_{CO_2av}) during the formation of calcite (Cc), vaterite (Vat) and aragonite (Ar) in absence of Pasp. Only vaterite and calcite samples with aqueous molar [Mg]/[Ca] ratio < 0.05 are plotted. Solid line: R = D_{CO_2av}; dashed line: regression line for the formation of calcite.

Keeping Ω_{fp} of individual $CaCO_3$ phase's constant, the observed precipitation rate of $CaCO_3$ increases in the order of calcite, aragonite, and vaterite (see Fig. 5-8a and Fig. 5-8b). In the case of aragonite an increase in temperature results in a significant higher precipitation rate at constant saturation degree (Fig. 5-8b).
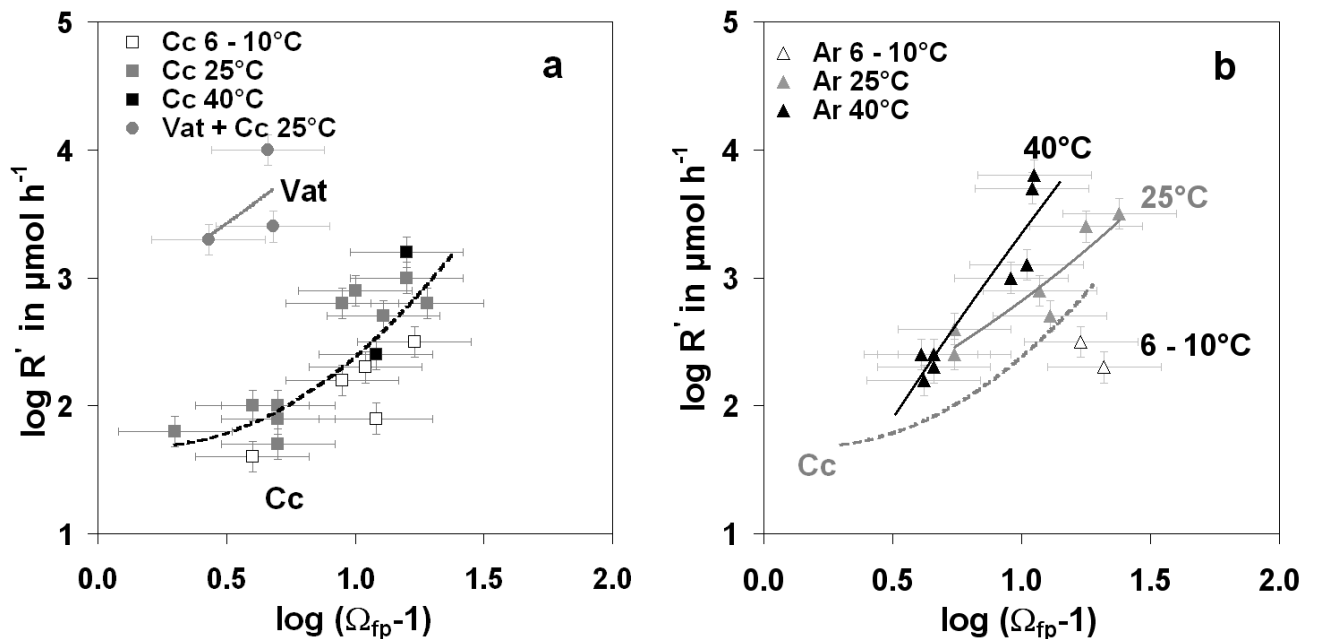
Fig. 5-8: Precipitation rate of $CaCO_3$ (R' in µmol h^{-1}) versus saturation degree at the time of first $CaCO_3$ precipitation (Ω_{fp}) for experiments without Pasp. (a) Precipitation of calcite ([Mg]/[Ca] ≤ 0.05) and vaterite. (b) Precipitation of aragonite. b: The dashed line indicates the relationship for calcite (Cc) as given in a. Given error bars display double standard deviation (2σ) see Tab. A4.

Interestingly, all log (R') values for calcite and aragonite fall into the same line if the ion activity product at first $CaCO_3$ precipitation, IAP_{fp}, is used instead of individual saturation degrees (Fig. 5-9). This let us suggest that first precipitation of $CaCO_3$ is related to similar mechanisms of $CaCO_3$ nucleation for both calcite and aragonite, where individual solubilities of the individual polymorph are not relevant. It is a further indicator for the formation of a similar $CaCO_3$ precursor for all polymorphs, besides to the polymorph independent t_{fp}-D_{CO_2av} and t_{fp}-[Mg]/[Ca] relations.

Elevated temperatures together with high IAP_{fp} values result in most rapid precipitation of calcium carbonates in our experiments according to Fig. 5-9. The log (R') – log (IAP_{fp}) correlation for aragonite and calcite formation at 40°C is strongly nonlinear which is indicative of a change in the reaction mechanisms at a log (IAP)$_{fp}$ of about -7.45.

The precipitation rate of $CaCO_3$ is controlled by the CO_3^{2-} accumulation rate or CO_2 diffusion rate (see Fig. 5-7) and additives (Tab. A4). The higher precipitation rate of aragonite compared to calcite at constant D_{CO_2av} is caused by the retardation of the precipitation in presence of Mg. This results in elevated accumulation of CO_3^{2-} ions and therefore higher saturation degrees and precipitation rates of $CaCO_3$.
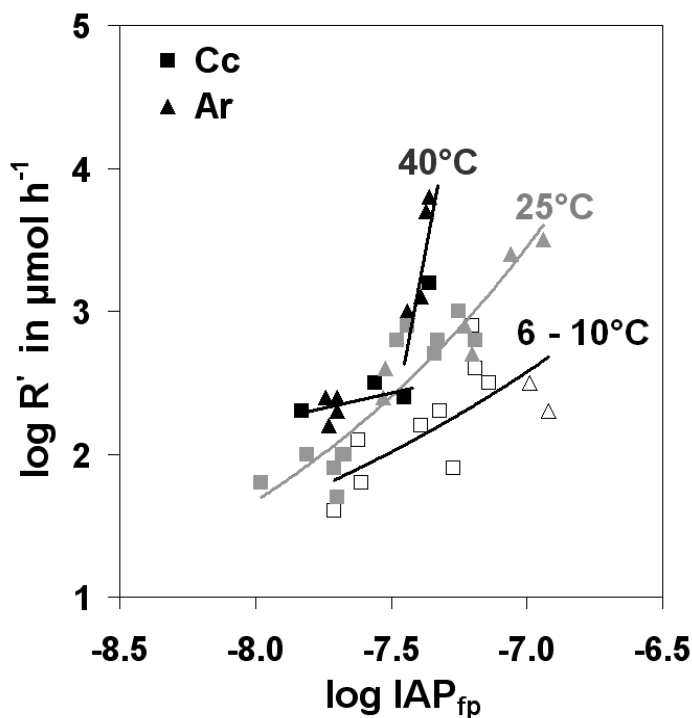
Fig. 5-9: **Precipitation rate of CaCO₃ (R' in µmol h⁻¹) versus ion activity product at the time of first CaCO₃ precipitation, IAP$_{fp}$ = (Ca^{2+}) (CO$_3^{2-}$)$_{fp}$. Different precipitation rates of CaCO₃ are obtained for different temperatures at a given ion activity product. Calcite ([Mg]/[Ca] ≤ 0.11) (squares) and aragonite (triangles) samples plot on the same line.**

The relative precipitation rates of the individual CaCO₃ polymorph influence the polymorph formed (e.g. Berner, 1975), mainly by inhibition of the other two polymorphs (e.g. through Mg and Pasp) or by kinetic effects which are related to the CO_3^{2-} accumulation rate. These conditions for the polymorph formation are discussed in the following part.

5.6 Conditions of CaCO₃ polymorph formation

In general, the CO_3^{2-} accumulation rate is proportional to the saturation degree of individual CaCO₃ polymorphs at the time of first CaCO₃ precipitation, the $(CO_3^{2-})_{fp}/(Ca^{2+})$ ratio and the CO_2 diffusion rate for nearly all experiments at constant pH and constant Ca concentration (see Tab. A4). However, the CaCO₃ nucleation and precipitation is determined by the CO_3^{2-} accumulation rate, which adjusts a certain $(CO_3^{2-})_{fp}/(Ca^{2+})$ ratio at a distinct reaction time (t$_{fp}$). In the following, the $(CO_3^{2-})_{fp}/(Ca^{2+})$ ratio is used to compare our results with other studies and to point out the potential significance of $(CO_3^{2-})_{fp}/(Ca^{2+})$ ratios for CaCO₃ polymorph formation.

Experiments 17 to 19, 31, 59 and 96 (Tab. A4) contain 1.4 to 4.2 fold higher Ca concentration than all other experiments ([Ca] = 10 mmol l⁻¹). Thus, lower $(CO_3^{2-})_{fp}/(Ca^{2+})$ ratios are obtained at

elevated Ca concentrations compared to all other experiments. All experiments indicate no difference e.g. in the aragonite-calcite composition at a given $(CO_3^{2-})_{fp}/(Ca^{2+})$ ratio or CO_3^{2-} accumulation rate (Tab. A4). Moreover, at a given CO_3^{2-} accumulation rate (distinct D_{CO_2av} values; e.g. experiments 92 and 96 in Tab. A4) the vaterite-calcite composition remains nearly constant, even if the Ca concentration is more than 4 times higher.
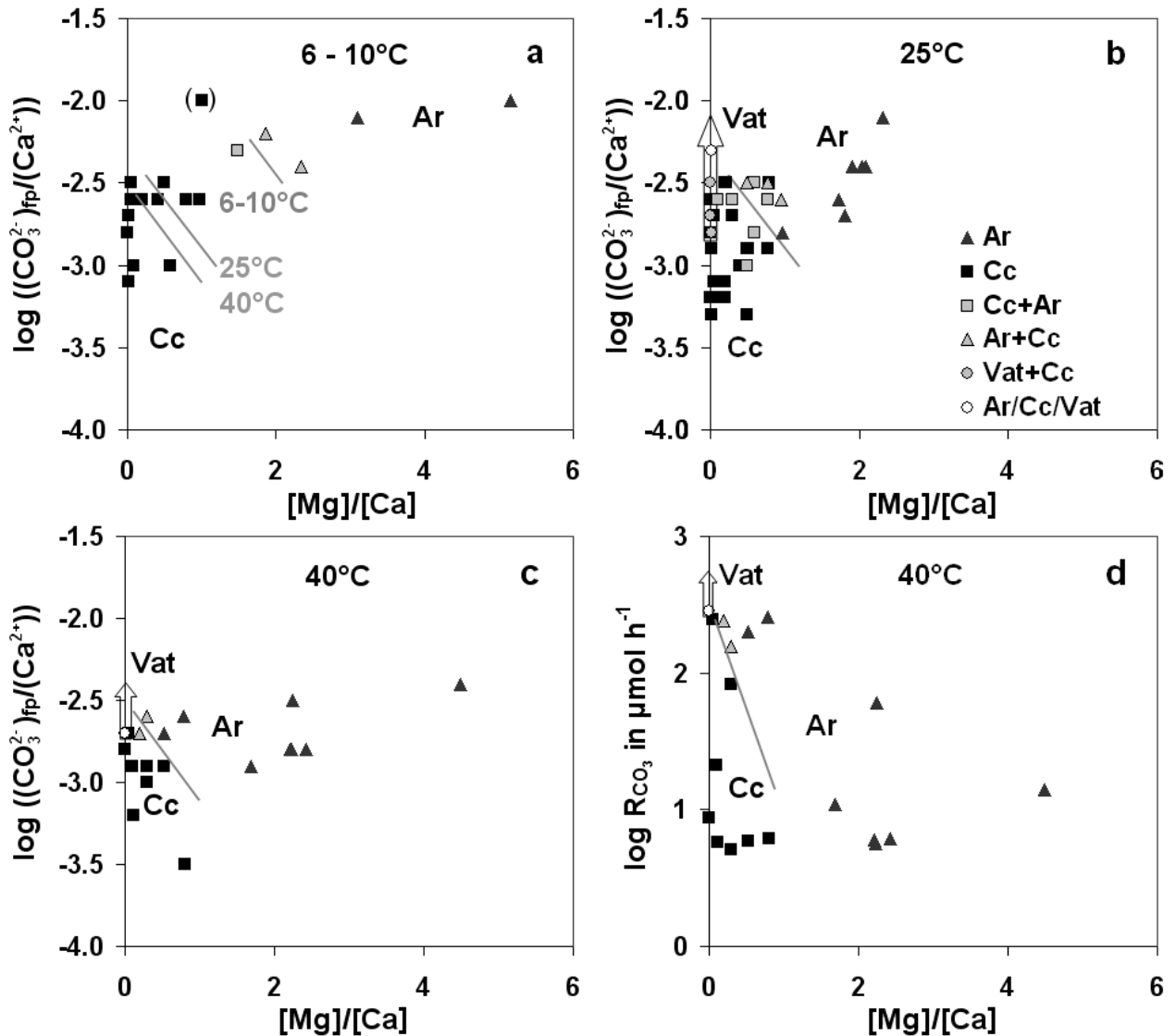
Fig. 5-10: **Mineralogical composition of the precipitated CaCO$_3$ as function of $(CO_3^{2-})_{fp}/(Ca)$ and [Mg]/[Ca] ratio at (a) 6 to 10°C; sample 8 (Tab. A4) is given in parenthesis due to poor titration data, (b) 25°C, and (c) 40°C and (d) as a function of carbonate accumulation rate R$_{CO_3}$ and [Mg]/[Ca] at 40°C. Cc: > 95 wt.% calcite; Ar: > 95 wt.% aragonite; Cc+Ar: > 50 wt.% calcite and < 50 wt.% aragonite; Ar+Cc: > 50 wt.% aragonite and < 50 wt.% calcite; Vat+Cc: > 50 wt.% vaterite and < 50 wt.% calcite ; Ar/Cc/Vat: Mixture of all three polymorphs.**

5.6.1 Aragonite versus calcite and vaterite formation

The amount of aragonite in the precipitates depends mainly on the [Mg]/[Ca] ratio, temperature and the carbonate accumulation rate. Preferentially aragonite was formed at least at [Mg]/[Ca] > 2, > 0.5, and > 0.2 at 6-10, 25, and 40°C, whereas pure aragonite was found at [Mg]/[Ca] > 3, > 1, and > 0.5 at 6-10, 25, and 40°C, respectively (Figs. 5-10a to c). However, limits of aragonite versus calcite formation strongly depend on the $(CO_3^{2-})_{fp}/(Ca^{2+})$ ratio or CO_3^{2-} accumulation rate (Figs. 5-10c and d for 40°C). The higher the $(CO_3^{2-})_{fp}/(Ca^{2+})$ ratio or CO_3^{2-} accumulation rate and the higher the temperature limit is, the lower are the [Mg]/[Ca] limits for aragonite formation (see Figs. 5-10a to d). The precipitation of aragonite at elevated CO_3^{2-} accumulation rates can also be observed in nature. E.g. rapid CO_2 degassing and evaporation of H_2O favours the aragonite formation according to Given and Wilkinson (1985). Moreover, the occurrence of aragonite at high saturation degrees of $CaCO_3$ polymorphs or $(CO_3^{2-})_{fp}/(Ca^{2+})$ ratio is in accordance with Fernández-Díaz et al. (1996) in the absence of Mg, but in contrast to De Choudens-Sanchez and Gonzalez (2009) and Lee and Morse (2010). Fernández-Díaz et al. (1996) has also used a diffusion technique, where CO_3^{2-} ions are accumulated, while De Choudens-Sanchez and Gonzalez (2009) and Lee and Morse (2010) have used CO_2 degassing experiments, where the pH has changed. This may indicate the significance of the reaction path until first precipitation of $CaCO_3$ occurs. Thus, - besides other parameters - the individual pathways for reaching the critical saturation degree may have a decisive impact on individual $CaCO_3$ polymorph formation.

As discussed above, nearly Mg free phases (aragonite) and sites grow faster than Mg incorporating phases (calcite and vaterite) and sites, due to the larger dehydration energy which have to be provided for Mg (Lippmann, 1973). According to Burton (1993) the solubility equivalent of aragonite is Mg-calcite with $MgCO_3$ content in the range from 7 to 18 mol%. The lower Mg value is valid at elevated structural defects, which can be caused by fast $CaCO_3$ precipitation in combination with foreign ions (e.g. Na^+; Burton, 1993). Thus, lower Mg concentrations are sufficient for aragonite in the case of high CO_3^{2-} concentration as our experiments have indicated it, especially at 40°C.

The isomorphic substitution of Ca^{2+} by Mg^{2+} in calcite increases at elevated temperature (see Oomori et al., 1987). These results in a stronger inhibition effect of Mg on calcite formation at elevated temperatures and a preferential aragonite formation at elevated temperature (see Fig. 5-10a for comparison of results from 6 to 40°C).

5.6.2   Vaterite versus calcite formation

Vaterite was mainly precipitated in association with calcite or aragonite + calcite at 25 and 40°C and in presence of Pasp (see Tab. A4; Fig. 5-10a to Fig. 5-10c). In our experiments the appearance of vaterite is limited to low [Mg]/[Ca] ratios (≤ 0.01) and high $(CO_3^{2-})_{fp}/(Ca^{2+})$ ratios ($> 10^{-2.8}$ in the absence of Pasp) (see Fig. 5-10b and Fig. 5-10c). In the absence of Pasp the R_{CO_3} value must exceed 50 µmol h^{-1} ($\log(D_{CO_2av}) > 2.9$ µmol h^{-1}), which is equivalent to a CO_3^{2-} accumulation rate of about $10^{1.7}$ µmol h^{-1} to reach the $\log((CO_3^{2-})_{fp}/(Ca^{2+}))$ ratio of -2.5 for both 25 and 40°C (Fig. 5-10b to Fig. 5-10d).

 In the presence of Pasp and in the absence of Mg the formation of vaterite occurs also at lower CO_3^{2-} accumulation rates compared to the experiments without Pasp. CO_3^{2-} accumulation rates of e.g. only $10^{1.2}$ µmol h^{-1} have to be exceeded (Tab. A4). The relative amount of vaterite versus the other $CaCO_3$ polymorphs increases generally with increasing CO_3^{2-} accumulation rate and increasing Pasp concentration. For instance, at a temperature of 25°C and Pasp concentration of 3.2 mg l^{-1} the vaterite content is 0 and 90 wt.% at a CO_3^{2-} accumulation rates of $R_{CO_3} = 10^{1.6}$ and $10^{2.3}$ µmol h^{-1}, respectively (see Tab. A4). According to our experiments vaterite formation occurs only at $\Omega_{vat\,fp} \geq 4$.

Preferential vaterite formation can be caused by disorientated CO_3^{2-} ions at the nuclei surface at elevated CO_3^{2-} concentrations (Lippmann, 1973). The open vaterite structure allows these slight "disordering" of the carbonate ions and larger O-O distances between the carbonates in its lattice (Lippmann, 1973, Wang and Becker, 2009).

At a CO_3^{2-} accumulation rate of $10^{1.5}$ µmol h^{-1} the vaterite content increases steadily with increasing Pasp content from 19 wt.% at 0.02 mg l^{-1} Pasp up to 90 wt.% at 0.24 mg l^{-1} Pasp at 25°C, when only experiments with [Mg]/[Ca] ratio below 0.01 were considered. At 40°C pure vaterite was formed at [Pasp] ≥ 1.6 mg l^{-1}, $R_{CO_3} > 10^{2.2}$ µmol h^{-1} and [Mg]/[Ca] ≤ 0.01. This can be explained by (1) elevated $(CO_3^{2-})_{fp}/(Ca^{2+})$ ratios, which are reached in presence of Pasp and (2) the inhibition of aragonite and calcite formation by Pasp. Pasp inhibits nucleation and growth of calcite and especially of aragonite, indicated by respective high t_{fp} values and $(CO_3^{2-})_{fp}/(Ca^{2+})$ ratios in the presence of Pasp. Pasp acts thereby as an inhibitor by adsorption onto the calcium carbonate surface, preferentially on active kinks and edges, where $CaCO_3$ growth takes place (Sikes et al., 1994). So that only small concentrations of Pasp are sufficient for inhibition of nucleation and crystal growth. The $CaCO_3$ nuclei remain small and dissolve easily, especially if they do not exceed a critical size for ongoing $CaCO_3$ growing. Pasp contains carboxyl-groups with the same atomic distances than calcite in the (001) direction. Thus, Pasp adsorbs preferentially on calcite parallel or perpendicular to (001) sites (Wierzbicki et al., 1994). This causes an inhibition of growth in the direction

perpendicular to (001) of calcite and thus a 2D growth. In consequence platy crystals are formed. Accordingly, vaterite formation can be stabilised versus calcite by Pasp. According to Meyer (1965) the stabilization of vaterite is reduced by lattice imperfections, temperature and the absence of nucleation and diffusion hindering substances. Incorporation of Mg into the vaterite lattice can favour such imperfections. This is in accordance with our experimental observation, at [Mg]/[Ca] ratios above 0.2 no vaterite is formed (without Pasp). Similar behaviour is found in experiments with Pasp. For instance, a concentration of 0.5 mmol l^{-1} Mg (experiment 89 in Tab. A4) results in an amount of vaterite of 30 wt.% compared to 70 wt.% without Mg (experiment 88) at analogous conditions ([Pasp]= 0.16 mg l^{-1}, $D_{CO_2av}=10^{2.7}$ μmol h^{-1}). In accordance with these results, Falini et al. (1994) found in their experiments no vaterite at a molar [Mg]/[Ca] ratio above 1 and [Pasp] of 4 mg l^{-1}.

5.6.3   Calcite versus vaterite and aragonite formation

Calcite is generally formed at low [Mg]/[Ca] ratios and in the absence of Pasp (Fig. 5-10). The individual limit of the [Mg]/[Ca] ratio for calcite formation depends on the temperature and $(CO_3^{2-})_{fp}/(Ca^{2+})$ ratio at the time of first precipitation (Figs. 5-10a to c). Thereby the $(CO_3^{2-})_{fp}/(Ca^{2+})$ ratio is directly proportional to the CO_3^{2-} accumulation rate and CO_2 diffusion rate. Pure calcite was formed up to [Mg]/[Ca] of 1 and 0.8 for 6 - 10°C and 25 - 40°C, respectively. Precipitation of pure calcite is related to low $(CO_3^{2-})_{fp}/(Ca^{2+})$ ratios, whereas at high ratios the formation of aragonite and vaterite may occur, e.g. $(CO_3^{2-})_{fp}/(Ca^{2+}) > 10^{-2.8}$ for 25 and 40°C.

Interestingly, calcite can also be formed when Pasp is present to inhibit aragonite formation and Mg is present to inhibit vaterite formation. E.g. at a [Mg]/[Ca] ratio of 1.13, 0.58 or 1.12 solely calcite was precipitated at Pasp concentrations of 3.3, 3.4 and 1.6 mg l^{-1}, respectively. Additionally calcite is also formed at high [Mg]/[Ca] ratios of 2.29 or 1.15 and high $(CO_3^{2-})/(Ca^{2+})_{fp}$ ratios of $10^{-1.9}$ and $10^{-2.3}$ at 25 and 40°C because of the presence of 3.2 and 0.25 mg l^{-1} Pasp, respectively. At these conditions pure aragonite is expected without Pasp (see also Tab. A4). Less aragonite at a [Mg]/[Ca] ratio above 5 and in the presence of 4 mg l^{-1} Pasp (poly-L-aspartate) was also found by Falini et al. (1994).

The formation of calcite at [Mg]/[Ca] ratios above 2 in the presence of Pasp might be highly important to understand calcite formation by organisms. Organisms like foraminifera, octacorals, echinoids, crinoids and asteroids form high magnesium calcite with up to 19 mol% $MgCO_3$ (Morse and Mackenzie, 1990). From our experimental results it is suggested, that calcite precipitates also in "aragonite seas" in the presence of macromolecules (like polyaspartic acid).

5.7 Morphologies and surfaces of the CaCO₃ crystals

5.7.1 Effect of magnesium

In absence of Mg the precipitation of calcite results in $\{10\bar{1}4\}$ rhombohedra with smooth surfaces (Fig. 5-11a to Fig. 5-11c). The side lengths of most crystals are below or equal to 30 µm in these experiments and decrease with increasing temperature. Crystal sizes up to 50 µm are reached at 6°C, whereas the side length is mostly below 30 µm at 25°C and smallest crystal sizes are observed in experiments at 40°C. Increasing Mg concentration in the solution initially causes rough and stepped edges and at elevated Mg concentration the morphology and size of calcite crystals is changing. The calcite morphology depends thereby mainly on the Mg concentration and temperature. At 6°C and [Mg]/[Ca] ratios from 0.3 to 0.5 dodecahedral crystal habits with a typical crystal size of 30 µm occur (Fig. 5-11d, Tab A5 a,b). Often bimodal size distributions with certain crystal sizes are found. At 6°C and [Mg]/[Ca] of ≥ 0.8 Mg-calcite occurs with elongated, steep rhombohedra shapes and rough surfaces with two different angles between the growth steps at about 110° and 28 to 45°, respectively (Fig. 5-11g). At 25°C the dodecahedral crystal habit occurred rarely. Usually crystals with stepped rounded edges (Fig. 5-11e), steep rhombic crystals (Fig. 5-11b) and other irregularly shaped crystals display a higher crystal surfaces roughness. The length of Mg-calcite crystals is usually between 20 and 30 µm with maximum sizes up to 50 µm. The calcite crystals at 40°C have typical side lengths from 2 to 10 µm with maximum sizes of 30 µm (Fig. 5-11). At 40°C the size distribution is rather unimodal and the shapes are irregular, often with rounded edges. Fig. 5-11f indicates the small but very well shaped crystals compared to other crystals at 40°C experiments. Generally elevated Mg concentration in the solution causes smaller crystal sizes, especially at 40°C.

The dodecahedral crystal habit (e.g. at 6°C) is caused by the stabilisation of the $\{01\bar{1}1\}$ face by the specific bond of Mg^{2+} ions to this surface site. In consequence, the calcite morphology is related to the smooth $\{10\bar{1}4\}$ faces and rough $\{01\bar{1}1\}$ faces. Both faces have thereby similar distances to the crystal centre. The steps at the $\{01\bar{1}1\}$ faces have an angle of about 110° (II in Figs. 5-11d and e) or 28 to 45° (I in Fig. 5-11g). Latter is caused when the $\{01\bar{1}1\}$ faces are dominating versus the $\{10\bar{1}4\}$ faces. However, an abutting face of $\{10\bar{1}4\}$ can persist and reveals the difference between the two different step angles (e.g. Fig. 5-11d versus g). The small angles occur usually at higher Mg concentrations and when calcite crystals are elongated (Fig. 5-11g), but few calcite habits are still dodecahedral like in experiment 8 (not shown here). A dodecahedral habit of calcite crystals in the presence of Mg is also reported by Albeck et al. (1993). Dodecahedral habit of calcite is also referred to further agents like cobald (Braybrook et al., 2002), phosphate and sulphates (Didymus et al., 1993), succinate (Mukkamala et al., 2006), and polymeric additives (Falini et al., 2009).

At temperatures between 25 and 40°C Mg^{2+} ions cause rounding of the edges (Fig. 5-11e), mainly at the opposite corner to a well-shaped corner of $\{10\bar{1}4\}$ planes (see Fig. 5-11e).

increasing temperature

6 - 10 °C   25 °C   40 °C

increasing Mg concentration
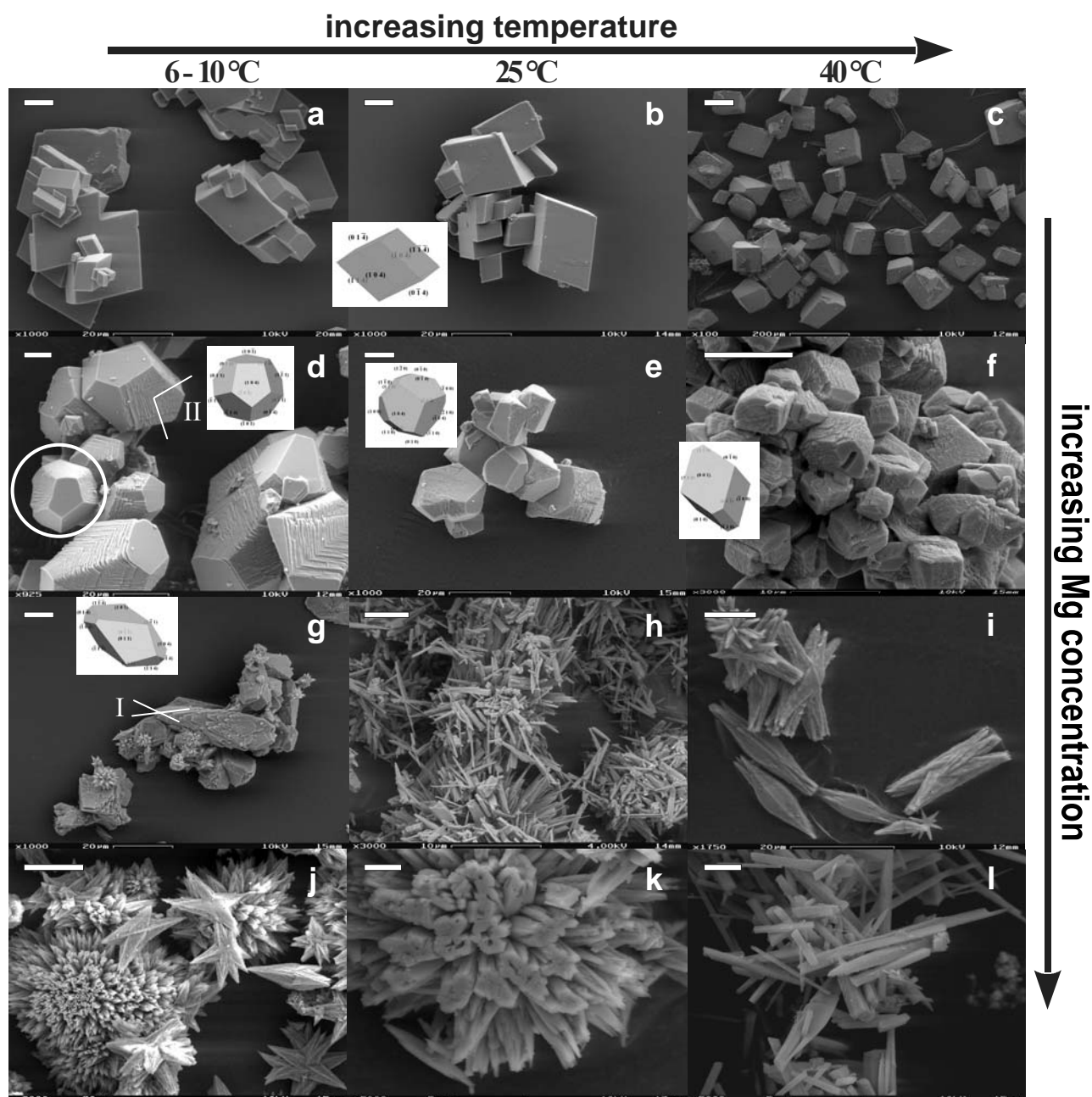
Fig. 5-11: Crystal morphology of calcium carbonates as a function of Mg concentrations and temperature in absence of Pasp in Secondary Electron (SE) images and face models displayed by WinXMorph software. The white scale bar has a length of 10 μm for all except of h, k and l where it is 2 μm and c where it is 100μm. The temperature increases from 6°C (left side) to 40°C (right side). (a), (b) and (c) have only {10$\bar{1}$4} faces with no Mg in the solution for the experiments 12, 23 and 65, respectively; the molar [Mg]/[Ca] ratios in the solutions are (d) 0.5, (e) 0.3, (f) 0.5, (g) 1.5, (h) 1, (i) 0.5, (j) 1.9, (k) 2 and (l) 4.5 for the experiments 5, 44, 74, 20, 58, 75, 9, 63 and 83, respectively. The pseudo dodecahedron (circle) is frequently found at moderate [Mg]/[Ca] ratios (0.3 to 0.5) especially at low temperature (e.g. at 6°C in (d)) and is caused by the stabilisation of {01$\bar{1}$1} faces with a similar influence on the calcite morphology than the most stabile {10$\bar{1}$4} faces. At elevated [Mg]/[Ca] ratios (g) the {01$\bar{1}$1} faces are dominating and elongated crystals are found at low temperature (mainly at 6 to 10°C). At 25°C rounding of crystal edges may be caused by additional stabilisation of the {11$\bar{2}$0} besides to {01$\bar{1}$0} and {10$\bar{1}$4} faces (see (e)). At 25°C and 40°C the {0001} and {01$\bar{1}$0} faces may be stabilised.

The round edges can be explained by stabilisation of the $\{01\bar{1}1\}$ face and the $\{10\bar{1}0\}$ face by Mg^{2+} ions or other inhibitors (e.g. by lysozyme in Jiménez-López, 2003). Another explanation for round edges is the limitation of the growth velocity in certain directions by Mg ions (Davis et al., 2004). This issue will be discussed more in detail in the AFM section (see below). Such round morphology were also observed in the presence of other additives like e.g. phenyl phosphate (Didymus et al., 1993), L- or D-aspartic acid (Teng et al., 1998; Orme et al., 2001), protein extracts isolated from sea urchins (Albeck et al., 1996, Mackenzie et al., 2004) or from aragonitic abalone cell nacre (Fu et al., 2005).

Elongated Mg-calcite crystals (Fig. 5-11g) are formed if the $\{01\bar{1}1\}$ faces are stabilized by Mg (or other additives). These faces become thereby more dominant because of the slower growth velocity perpendicular to these faces. Similar elongated calcite crystals were also found in the presence of other additives like e.g. Co^{2+} (Braybrook et al., 2002) and orthophosphate (Didymus et al., 1993).

At [Mg]/[Ca] ratios above 0.2 (40°C) and 1.5 (6°C) aragonite is formed additional to calcite, whereas at [Mg]/[Ca] > 0.8 (40°C) and > 3 (6°C) solely aragonite occurs (see Fig. 5-10 and sections 5.6.1 and 5.6.3). The aragonite crystals display needles formed in experiments at low CO_2 diffusion rates (thick PE membrane), low saturation degrees with respect to aragonite, $\Omega_{Ar\,fp}$, (e.g. $\Omega_{Ar\,fp} < 12$ for experiments with solely aragonite formation) and in consequence low $CaCO_3$ precipitation rates. Sometimes the aragonite needles aggregate to spherulites (hedgehog-like spheres). At 25°C the needles have typical diameters up to 1 μm and lengths of about 10 μm (Fig. 5-11h). However, diameters of the aragonite needles down to a few hundreds of nm appear. At 40°C the aragonite needles have a slightly larger diameter up to 3 μm but lengths mostly between 10 and 15 μm (Fig. 5-11l). These needles become significantly smaller with increasing [Mg]/[Ca] ratio in the solution. At a [Mg]/[Ca] ratio of 5 the needles are up to 15 μm in length and up to 0.8 μm in diameter at 40°C.

Dipyramidal shapes (Fig. 5-11i, Fig. 5-11j and Tab. A5a) with a high surface roughness are obtained at elevated saturation degrees with respect to aragonite at the time of first precipitation ($\Omega_{Ar\,fp} > 10$ (6°C), > 11 (25°C) and > 12 (40°C). These solids look like unidirectional oriented aggregates of aragonite needles (Fig. 5-11k) or like surface nucleation may have caused growth perpendicular to the c-axis. Furthermore these dipyramidal shaped aragonite aggregates may form spherulites (Fig. 5-11j) or star-like shapes (Fig. 5-11i and Fig. 5-11j). Often twins with the twin plane (024) are observed (Fig. 5-11i). The dipyramidal shaped aragonite aggregates have a diameter of up to 5 μm and a length of 25 μm at 25°C and 40°C, respectively. At 6°C and 10°C the aragonite aggregates are up to 5 μm in diameter and 15 μm in length (see also Fig. 5-11k). The Mg concentration influences the size of the dipyramidal aragonites besides to the temperatures. At [Mg]/[Ca] ratios > 3 the aragonite needles become smaller, especially at [Mg]/[Ca] ratios of 5 with needle length of up to 8 μm and a diameter of up to 2 μm (at 10°C). However single aragonite needles and dipyramidal aragonite precipitates show extinction at the same angle by observations with crossed polarisers under the light microscope. This indicates a homogenous structural orientation within a single crystal

or unidirectional well ordered crystals e.g by "self-assembly" crystallographically oriented attachment (e.g. Cölfen and Mann, 2003).

Several processes may have caused the spherulite formation (1-3: Gránásy et al., 2005 and references therein):

(1.) central multidirectional growth, e.g. through secondary nucleation at the growth front

(2.) unidirectional growth and low angle branching

(3.) quenching of orientated defects

(4.) preferential nucleation along edges and corners

(5.) aggregation

Besides to these processes cyclic twinning may cause star-like structures by the formation of new interfaces (Sunagawa, 2005). Twinned crystals were also observed in several experiments (e.g. 20, 21, 51, 53, 57, 61, 75 and 76 see Tab. A4). Secondary electron SEM images indicate that some aragonite spherulites and stars grow by penetration of dipyramidal crystals (Fig. 5-11j). In this case other dipyramidal crystals are attached to the centre of these penetration twins by their top (experiment 57, not shown here). In other cases new needles are formed at the top of the dipyramidal crystals (e.g. experiment 63). The first may indicate twinning, branching and quenching, the second indicates the central multidirectional growth.

The occurrence of dipyramidal compared to needle-like growth is in good agreement with the occurrence of elevated crystal growth rates (see Fig. 5-9). E.g. at 40°C dipyramidal growth occurred e.g. at saturation degree in respect of aragonite $\Omega_{Ar} > 12$ at a log $IAP_{fp} > -7.4$ and needles at log IAP < -7.4 or $\Omega_{Ar} < 12$. This indicates furthermore the secondary nucleation on the surface, which causes the rougher surface and thereby faster growth.

In the following part the effect of Mg^{2+} ions on the calcite surface will be discussed as it is displayed by Atomic Force Microscopy (AFM). AFM images indicate generally rounded edges (Figs. 5-12a and b, and Fig. 5-13a), disturbed growth (Fig. 5-13) and surface nucleation during polynuclear growth (Fig. 5-13c and e, see chapter 2.4) in the presence of Mg.
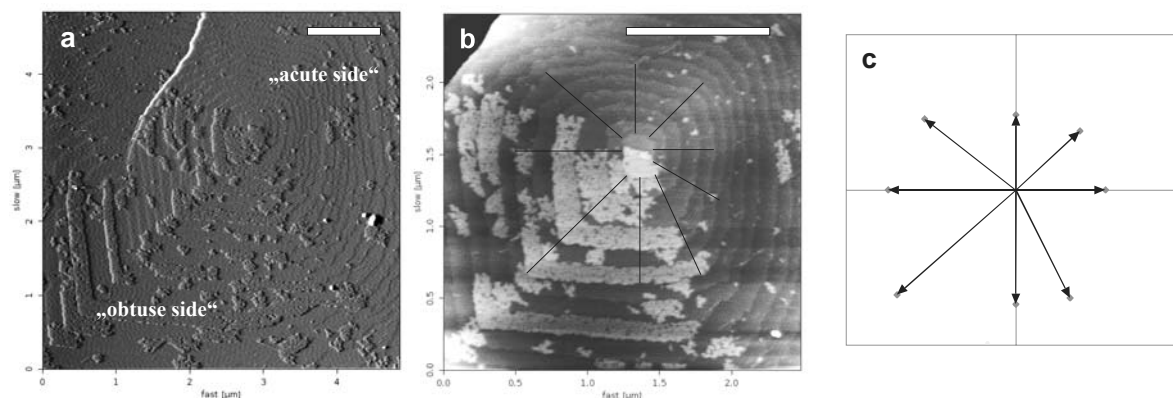
Fig. 5-12: AFM images of a Mg-calcite surface; (a) vertical deflection and (b) heigh image (see section 3.3.2) of experiment 41 at [Mg]/[Ca] of 0.2 and 25°C; (c) relative velocity in the different direction determined from the step size. The rough (a) and brighter (b) areas on the spiral terraces might be re-crystallised islands which are caused by adsorbed water (see also Stipp et al., 1996). All AFM images were carried out by Pablo Cubillas.

The corner between two sides is sharp (Figs. 5-12a and b) because of the higher growth rate in this direction (Fig. 5-12c). The relative growth rate and growth velocity v_i was determined from the average terrace width λ_i of 5 steps according to the equation

$$\lambda_1/\lambda_2 = v_1/v_2 \tag{5-13}$$

This calculation was also used by Davis et al. (2004), although in situ measurements of the step velocities in direction of crystallographic directions are necessary to obtain absolute values and to avoid errors by optical distortion.

The corner between the acute sides has the smallest growth rate (Fig. 5-12c) and is rounded, because of the elevated incorporation of Mg^{2+} ions at this side (acute) versus the opposite (obtuse) side. A higher Mg uptake in calcite causes retardation of the growth because it causes a disturbance of the lattice and therefore a higher solubility, which results into an increase of the backward reaction (dissolution) compared to the forward reaction (precipitation) (Paquette and Reeder, 1995; Davis et al., 2004).

Also the growth rate in direction of the edge between the acute and obtuse is small compared to the obtuse side (Fig. 5-12c) due to lattice mismatch of the highly Mg influenced acute side vs. less Mg influenced obtuse side (Davis et al., 2004). At a [Mg]/[Ca] ratio of 0.2 at 25°C (Figs. 5-13a and b) spiral growth was observed. At the displayed area the step size varied, whereas the previously discussed crystal (Fig. 5-12) has constant step sizes within at least 16 μm. The variation in the step size might be caused by the previous topology; the surface morphology indicates also a second slightly displaced spiral, which underlies the spiral (Fig. 5-12a). However, the upper corner was sharp compared to the left and lower corner, which were slightly rounded. Also the edges are not straight at the right side like they are at the left side in Fig. 5-12a. At a elevated [Mg]/[Ca] ratio of about 0.5 and low temperature of 6°C spiral (experiment 5) growth still occurred (Fig. 5-13d). Although the surface become significantly rougher and a larger angle was (>90°) observed. This angle is in accordance with the dodecahedral shape and was also found by secondary electron images of scanning electron microscopy (Fig. 5-11d). The step size of about 65 nm is relatively constant. At 25°C and a [Mg]/[Ca] of 0.4 a pretty rough surface occurred which indicates surface nucleation. In some cases also spiral like and terraced structures occur, but these structures are highly elongated and influenced by Mg (circle in Fig. 5-13c). A rough partly grained surface occurred also at [Mg]/[Ca] of 0.2 and 25°C, which may indicate surface nucleation (Fig. 5-13e). Incomplete planes were formed at [Mg]/[Ca] ratio of 0.1 and 25°C (Fig. 5-13f). The planes might indicate less nucleation events compared to calcite surfaces in Fig. 5-13e and Fig. 5-13c. However, some grainy objects (marked by arrows in Fig. 5-13) occur on the surface and surface nucleation has to take place to obtain such surface morphology. Further AFM images (not shown here) indicate that the whole surface of Mg-calcite crystals was covered by incomplete planes like in Fig. 5-13f.
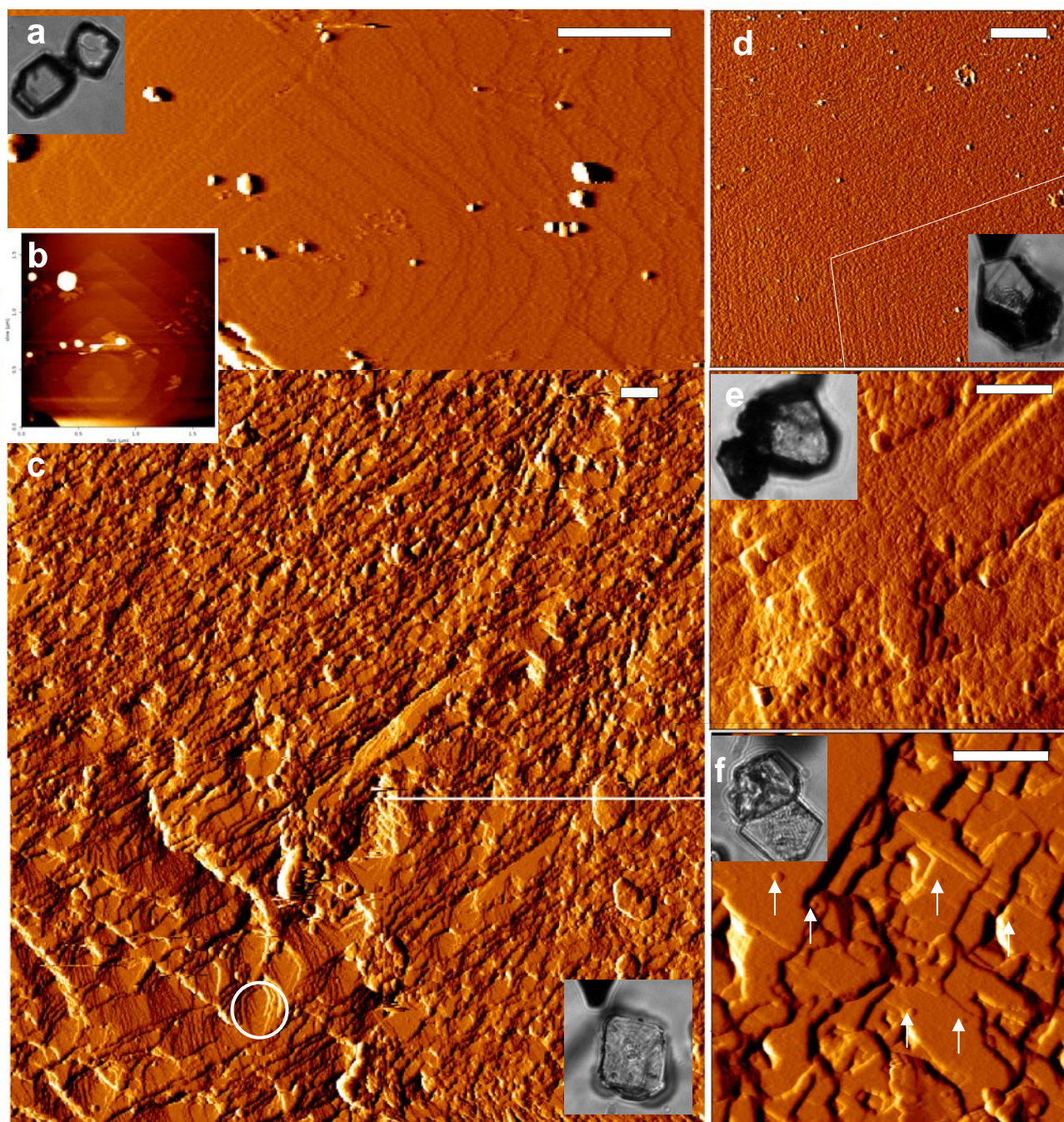
Fig. 5-13: AFM images of a Mg-calcite surface; (a) vertical deflection and (b) height image (see section 3.3.2) of experiment 41 at [Mg]/[Ca] of 0.2 and 25°C; (c) [Mg]/[Ca]of 0.4 and 25°C (experiment 45), the circle marks a terraced objects, (d) [Mg]/[Ca] of 0.49 and 6°C (experiment 5); (e) [Mg]/[Ca] of 0.2 and 6°C (experiment 4) (f) [Mg]/[Ca] of 0.1 and 25°C (experiment 38); Arrows mark small hills in (f). The scale bar has a length of 1 μm.

5.7.2   Effect of polyaspartic acid

Hexagonal platy vaterite (Fig. 5-14a, Tab. A6d) or desert rose like spherical aggregates of these hexagonal platy vaterite (Fig. 5-14b) are formed at relatively low supersaturation with respect to vaterite ($\Omega_{Vat\,fp}$ of below about 10) mostly in the presence of Pasp and absence of Mg^{2+} ions at 25°C and 40°C (Fig. 5-14a, b, d and g). The aggregates, which consist of few 100 nm thick plates, can reach diameters of several hundreds of μm (Fig. 5-14d and Fig. 5-14g). Above Ω_{vat} of 10 and at a

Pasp concentration > 0.4 mg l^{-1} irregularly rounded vaterite occurs with a rather smooth surface and without any single plates especially at 40°C (Figs. 5-14c, e, f, h and i). Some of these aggregates look like balls, corals or sponges and these aggregates reach sizes up to 200 μm (Figs. 5-14 c, e, f, h, i and o). Fig. 5-14o indicates a layer thickness of about 500 nm and a rough surface with partly hilly structures. The vaterite crystal in Fig. 5-14b and n might consist - according to the structure of vaterite - of (hexagonal) platy mesocrystals similar as proposed by Xu et al. (2006a). These authors have suggested the formation of hexagonal plates of vaterite from primary nanoparticles under the influence of hydroxyethyl cellulose. Polymers may play thereby an important role for the formation of hexagonal aggregates via oriented aggregation growth (Xu et al., 2006a).

With increasing Pasp concentration surface roughness decreases and the solids resemble amorphous material at a Pasp concentration of 1.6 mg l^{-1} (compare Fig. 5-14c and Fig. 5-14o with Fig. 5-14f and Fig. 5-14i), although there is still a roughness visible at a Pasp concentration of 3.2 mg l^{-1} at a magnification of 10000. However, generally the surfaces of the vaterite aggregates are very rough compared to typical smooth "pure" calcite crystals and have therefore a large specific surface area.

AFM images of the vaterite surface indicate a hilly surface with distances of down to 200 nm between the hills (Fig. 5-15). These hills may indicate surface nucleation, which is in accordance with the high saturation degrees with respect to vaterite ($\Omega_{Vat\ fp}$), which is reached in presence of Pasp (e.g. experiment 92; Fig. 5-15).

The diameter of the hills of few hundreds of nm and the morphology remind of ACC. Similar bumpy hills are also found for ACC under AFM (Xu et al., 2006b; Yeom and Char, 2010), although in their solids further smaller internal structures occur. Thus the hilly surface structure might indicate occurrence of surface nucleation and/or ACC or another grainy structured phase as precursor phase from which the surface morphology is preserved by Pasp. In some areas the hills are slightly elongated and larger, although an artificial apparent elongation by AFM measurement on the rounded surface cannot be excluded. However, this morphology is typical for vaterite, and it was also found in other studies for $CaCO_3$ precipitates in the presence of inhibitors like 2-phosphonobutane1,2,4-tricarboxylic acid (Yang et al., 2001) and polyacrylic acid (Yang et al., 2001; Kim et al., 2007).

In analogy to vaterite the morphology of calcite changes and its surface become rougher in the presence of Pasp (Fig. 5-14j to l). Moreover, intergrowth of calcite and vaterite crystals occurred (Fig. 5-14n). The edges of the calcite crystal become stepped and rounded in the presence of Pasp. At one corner single stepped edges with a step size of about 400 to 700 nm occur, whereas the opposite corner is rounded and contains several steps (Fig. 5-14j to m). This morphology looks similar to the morphology in the presence of Mg ions (Fig. 5-11e) - except of the single steps between $\{10\bar{1}4\}$ faces - and may also be formed by stabilisation of the "smooth" $\{10\bar{1}4\}$ face at the first corner and the rougher $\{11\bar{2}0\}$ and $\{01\bar{1}0\}$ faces or more generally $\{hki0\}$ (with $h+k=\bar{i}$) face on the opposite crystal side. This morphology is in accordance with the observation of Teng et al. (1998) and Orme et al. (2001) in the presence of L- or D-aspartic acid.

Fig. 5-14: SEM-SE images of crystal morphologies and surfaces of calcium carbonates displaying the effect of Pasp. The white scale bar is 10 μm, except in (h) and (j) to (o), where it is 2 μm.

(a) to (i), (n) and (o) vaterite, (j) to (n) calcite: (a) vaterite plates formed at 25°C, without Pasp, D_{CO_2} av = 103.5 μmol h^{-1}, experiment 31; (b) aggregate of vaterite plates (desert rose like morphology) at 25°C, 0.40 mg l^{-1} Pasp, experiment 92 ; (c) coral-like shape at 40°C, 0.39 mg l^{-1} Pasp, experiment 101; (d) 25°C, 0.24 mg l^{-1} Pasp, experiment 90; (e) 25°C, 0.32 mg l^{-1} Pasp, experiment 91; (f) 25°C, 1.6 mg l^{-1} Pasp, experiment 104; (g), (h) and (i) are images of samples shown in (d), (e) and (f), respectively, at higher magnification; (j), (k) and (l) porous calcite with single steps at the {10$\bar{1}$4} edges at 25°C, 3.2 mg l^{-1} Pasp, experiment 97; (m) 6°C, 1.6 mg l^{-1} Pasp, experiment 85; (n) 25°C, 0.16 mg l^{-1} Pasp, experiment 88; (o) 40°C, 0.39 mg l^{-1} Pasp, experiment 101.

Fig. 5-15: AFM (a) deflection image and (b) height image of vaterite surface for 0.4 mg l^{-1} Pasp and 25°C (experiment 92) and at a saturation degree with respect to vaterite of $\Omega_{vat\ fp} \approx 11$. The scale bar is 10µm.
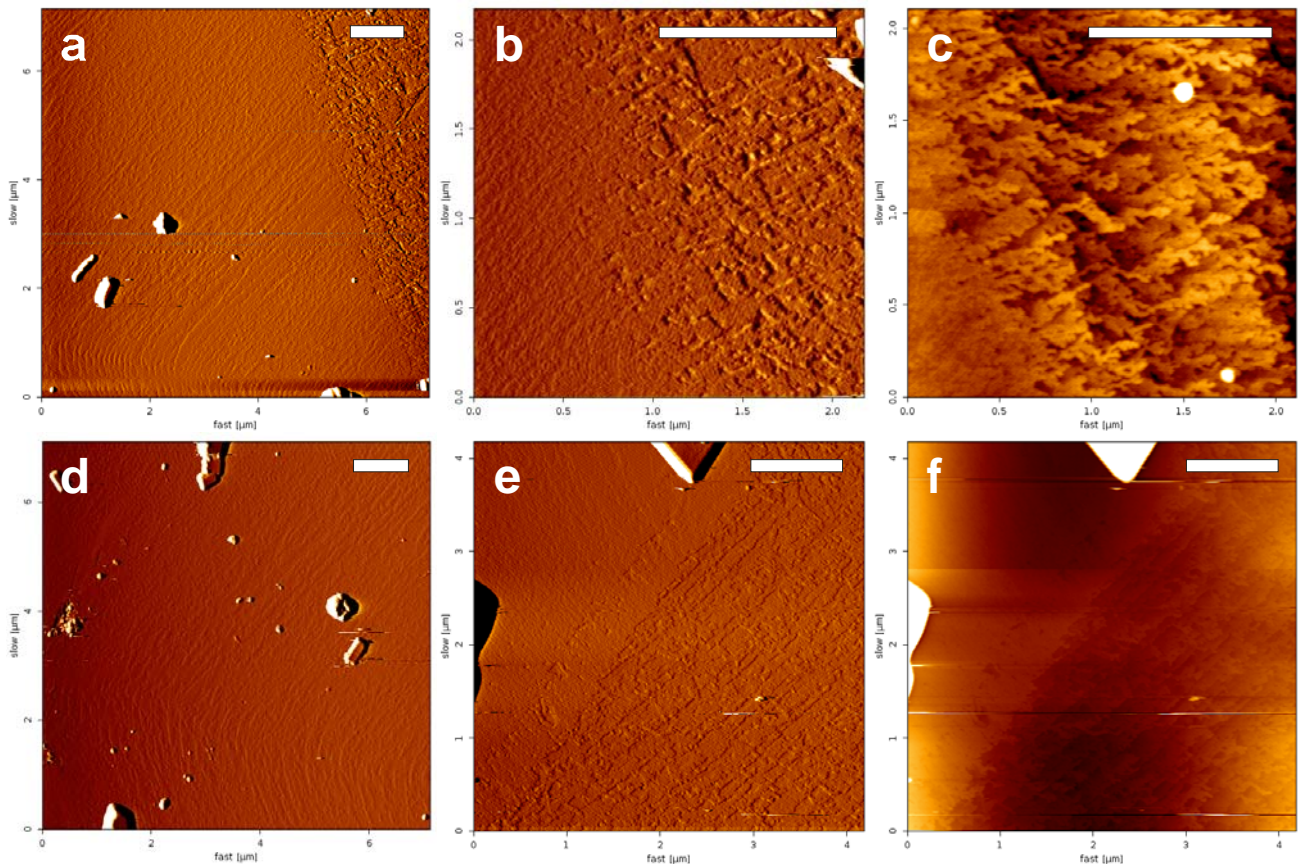
Fig. 5-16: AFM images of calcite surface for 0.4 mg l^{-1} Pasp at 25°C and at a saturation degree of $\Omega_{Vat\ fp} \approx 11$. (a),(b), (d) and (e) are vertical deflection images and (c) and (f) are height images (see section 3.3.2). The white scale bar is 1 µm.

Edges with such regular step like in Fig. 5-14k and Fig. 5-14l where also found at the seeded experiments of DeOliveria and Laursen (1997) in the presence of α-helical peptides. In this study fluorescence measurements indicate strong bond or overgrowth of peptides by CaCO$_3$. Thus the steps might be caused by the growth of calcite, which was partly (e.g. at the edges) covered by Pasp

and a further epitaxial overgrowth of $CaCO_3$. Thereby selective binding of Pasp to the non $\{10\overline{1}4\}$ planes at the edges occur and blocks the growth at these edges, whereas the growth within the $\{10\overline{1}4\}$ faces is not affected.

In general the steps display incomplete growing of the surface, which might be caused by selective blocking the growth at edges by Pasp either in the same plane or the plane below. This is in accordance with the selective binding of Pasp on $\{0001\}$ sites, whereas the bonding strength to $\{10\overline{1}4\}$ faces is significantly smaller (Wierzbicki et al., 1994). Such steps were also found in the presence of globular proteins (Hernandez-Hernandez et al., 2008) and copolymers (Kulak et al., 2007).

The calcite crystals are partly porous at Pasp concentrations above 3 mg l^{-1} (see Fig. 5-14j, Fig. 5-14k and Fig. 5-14l). Different crystal faces have a different porosity and roughness (see Fig. 5-14k). Fig. 5-14l indicates holes over the whole step. Cracks occur on the surface in the presence of Pasp (Fig. 5-14j, Fig. 5-14k and Fig. 5-14m). In some samples a fibrous structure occurs on the calcite surface (Fig. 5-14j).

AFM images indicate that especially the calcite surface is strongly affected by Pasp. The "acute" sides are highly disturbed (Fig. 5-16a, b and e) and appear fibrous in 2D view (Fig. 5-16c and f), but also the other ("obtuse") sides are influenced as it can be observed in the AFM amplitude image especially at the corner (Fig. 5-16a, b, d and e), although the edges remain more or less straight at the obtuse side. Thus a high roughness occurs mainly on the "acute" side.

5.7.3   Combined effect of polyaspartic acid and magnesium

At a temperature of 25°C calcite was formed if both Mg and Pasp are present in the outer solution, e.g. experiment 93 with 1.6 mg l^{-1} Pasp and a [Mg]/[Ca] ratio of 1. The surface of these calcite crystals is rough and sharp angled steps and rounded areas occur (Fig. 5-17a) under the influence of both additives. No typical $\{10\overline{1}4\}$ rhombohedra occurred; the morphology looks more like an intergrowth of several highly inhibited grown $CaCO_3$ crystals. Similar stepped calcite crystals were found at high saturation degrees with respect to calcite ($\Omega_{Cc} > 16$; Beck and Andreassen, 2010). Such high saturation degrees are in good agreement with e.g. the experiment 93 with $\Omega_{Cc,fp} = 64$.

Concerning 40°C aragonite-calcite mixtures occur at [Mg]/[Ca] of about 1.1 and at Pasp concentrations of 0.25 and 1.58 mg l^{-1} (Fig. 5-17b and c) in experiments 100 and 103, respectively. The aragonites needles form spherulite. The (Mg-) calcite crystals look similar to the previous described ones (see section 5.7.1), although several of them have rounded areas. At 40°C and [Mg]/[Ca] ratios of 0.3 and 0.5 only calcite was identified in the XRD pattern. However, SEM-SE images indicate the presence of very small spheroids, typically related to ACC (Fig. 5-17f).
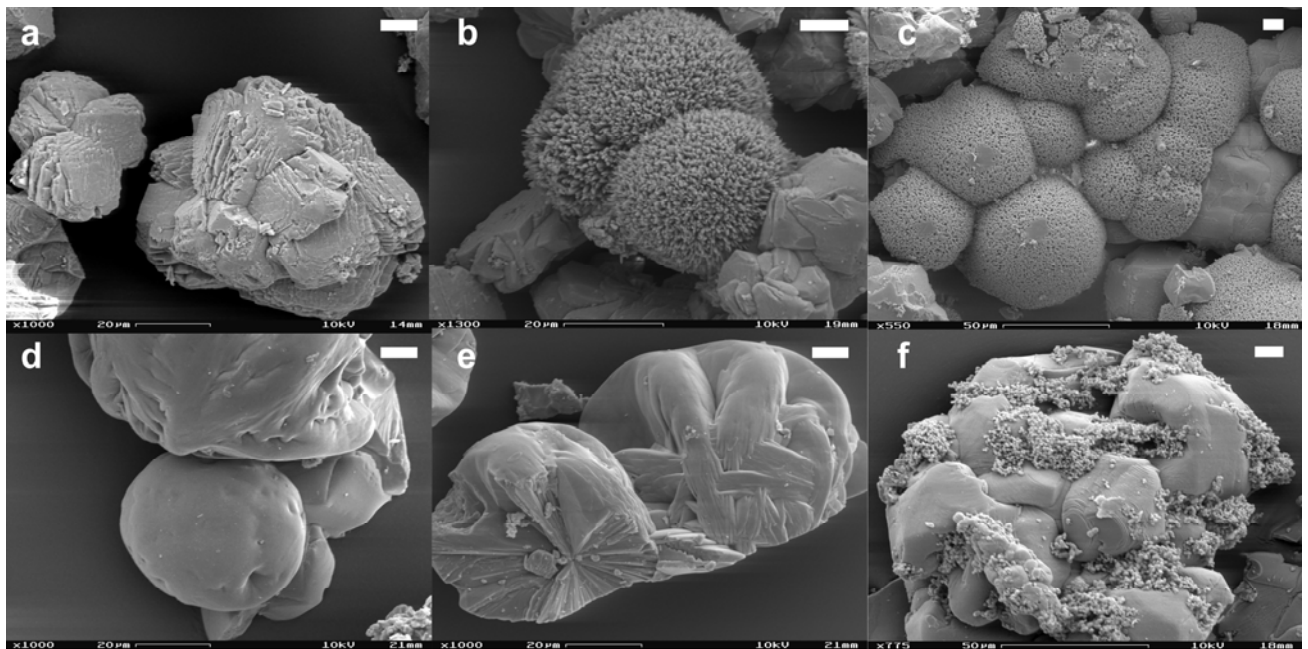
Fig. 5-17: SEM-SE images of crystal morphologies and surfaces of calcium carbonates in the presence of Pasp and Mg. The white scale bar is 10 μm. (a) [Mg]/[Ca] = 0.98 and 1.6 mg l^{-1} Pasp at 25°C, experiment 93; (b) [Mg]/[Ca] = 1.15 and 0.25 mg l^{-1} Pasp at 40°C, experiment 100; (c) [Mg]/[Ca] = 1.12 and 1.6 mg l^{-1} Pasp at 40°C, experiment 103; (d) and (e) [Mg]/[Ca] = 0.35 and 3.3 mg l^{-1} Pasp at 40°C, experiment 107; (f) [Mg]/[Ca] = 0.58 and 3.4 mg l^{-1} Pasp at 40°C, experiment 108.
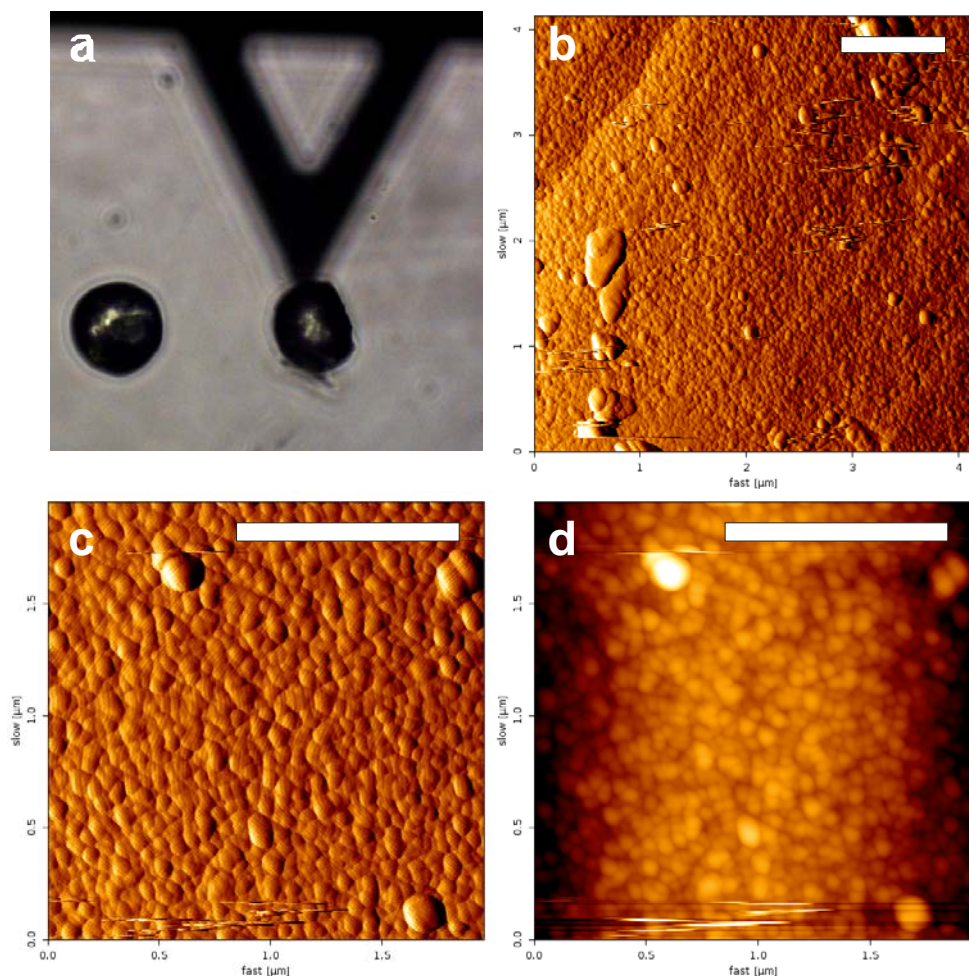
Fig. 5-18: AFM images of a vaterite surface in the presence of 3.3 mg l^{-1} Pasp and magnesium ([Mg]/[Ca] = 0.35) at 40°C; experiment 107. The white scale bar is 1 μm. Hills with a diameter of 40 to 200 nm are visible. (a) microscopic image, (b) and (c) is vertical deflection image and (d) height image.

At a [Mg]/[Ca] ratio of 1.13 vaterite was additionally formed besides calcite (Fig. 5-17d and e). The radial structures are still preserved in the crystals, although the plates are grown to massive balls (Fig. 5-17d and e). The surfaces of the crystals are rounded and "smooth", but vaterite plates are still sometimes visible (Fig. 5-17e). The AFM image in Fig. 5-18 indicates again hilly surfaces for vaterite with hill diameters down to 40 nm, similar to the morphology of vaterite in absence of Mg (see Fig. 5-15).

5.8   Magnesium incorporation

5.8.1 Spatial magnesium distribution and structural effects

The Mg^{2+} ions are differently incorporated at distinct crystallographic sides (see section 5.7.1) as it was verified by microprobe analyses. Within one experiment different crystals possess partly distinct shapes like e.g. experiment 4 at a $[Mg]/[Ca]_{aq}$ ratio of 0.2 at 6°C (Fig. 5-19a). Some crystal shapes are influenced by Mg^{2+} ions and exhibit morphologies with e.g. rounded shapes (sites 4 and 5 in Fig. 5-19a and Fig. 5-20a), while others are not affected (sites 1 and 2 in Fig. 5-19). Higher Mg and lower Sr content were found in the samples with modified morphologies by microprobe analyses (Fig. 5-19 and Fig. 5-20a). Element distribution within a single crystal can be explained by the different incorporation behaviour of Mg^{2+} and Sr^{2+} ions at the distinct sides (acute and obtuse side). Latter was also analysed by e.g. Paquette and Reeder (1995) and Davis et al. (2004). According to these authors more Mg^{2+} ions are incorporated into the acute step, while the larger Sr ions are preferentially incorporated at the obtuse side (Fig. 5-19c).
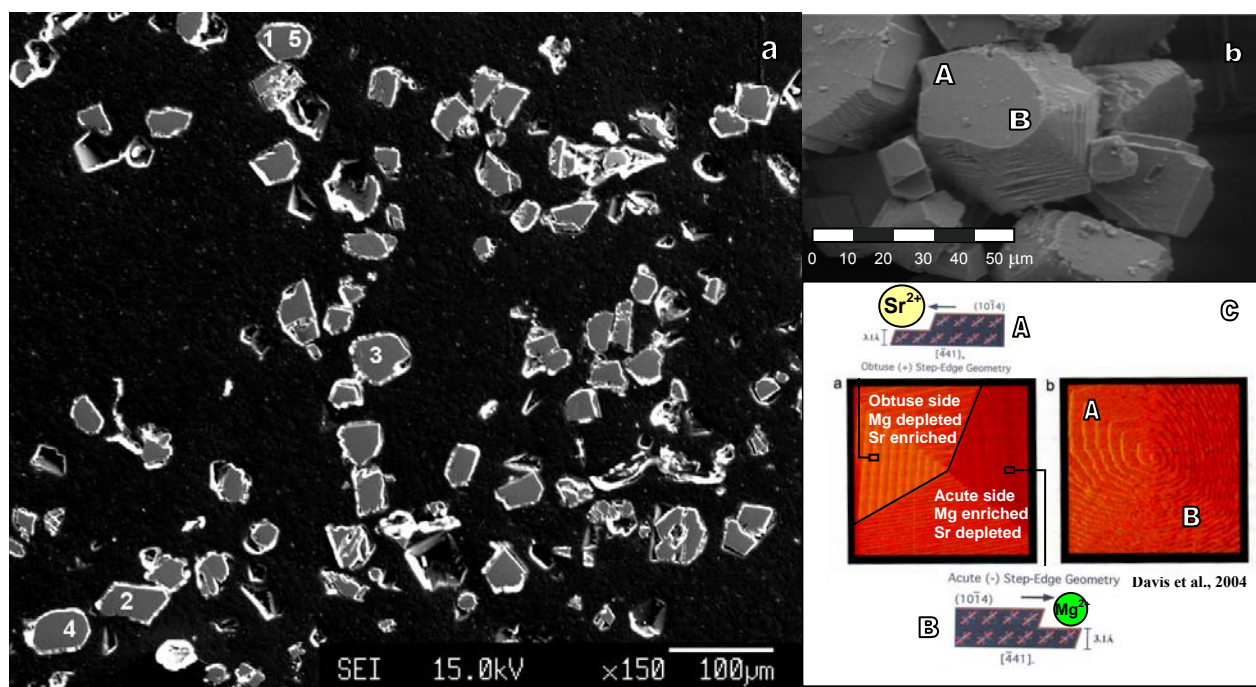
Fig. 5-19: (a) Secondary electron image with sites 1 to 5 (see Fig. 5-20) for microprobe analyses in experiment 4, (b) secondary electron images of the morphology of Mg-calcite. (c) results of Davis et al. (2004) for comparison and interpretation.

A similar behaviour was also found for the crystals from our experiments. The more Mg^{2+} ions are incorporated the more the edges are rounded and the morphology changed (compare e.g. Fig. 5-20 a, b and d). On the one hand Mg enrichment is correlated with Sr depletion within a single crystal due to the different incorporation at different sides (acute vs. obtuse); on the other hand a direct correlation between Mg and Sr concentrations was found when the compositions of different experiments or different crystals (with the same mineralogical composition) are compared to each other (Fig. 5-20a, b vs. d). A larger amount of defects which occurs in these Mg influenced crystals might promote Sr incorporation into the crystal and therefore the positive correlation between Mg and Sr ions in the bulk of these crystals. The large Sr ion might also compensate the lattice distortion by the small Mg^{2+} ion. This issue needs to be verified by high resolution TEM measurements.
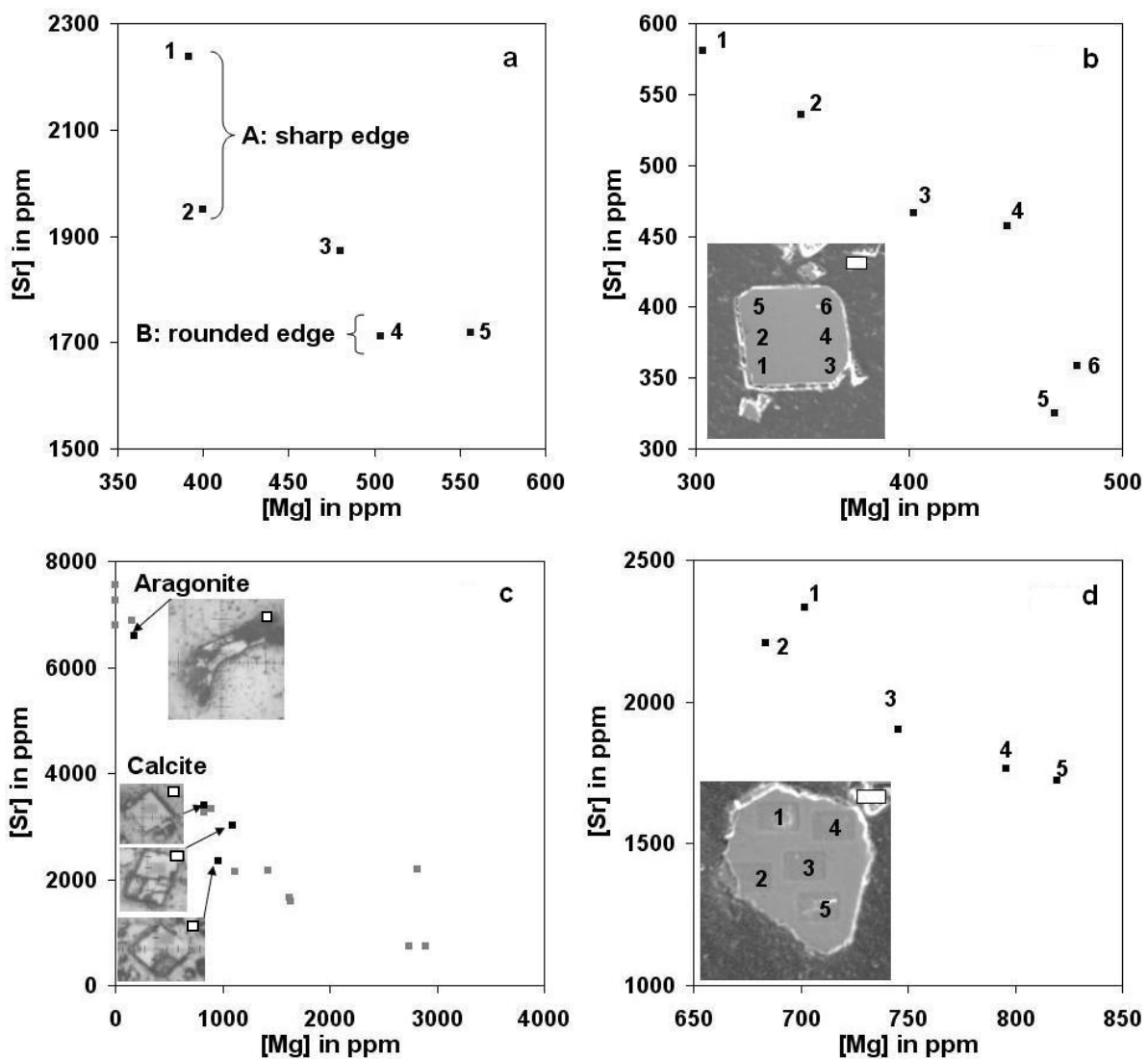
Fig. 5-20: Micro probe data for Sr versus Mg content showing inhomogeneous Sr and Mg incorporation due to crystallographic effects and mineralogy. The sampling areas are marked by dark shades in (c) and (d). Scale bars are 10 μm. (a) Relation between the shape of crystals and elemental incorporation in calcite crystals of experiment 4, (b) elemental distribution in a calcite crystal of experiment 39, (c) impact of the mineralogy (aragonite and calcite) on the elemental distribution from experiment 40, (d) elemental distribution in a Mg-calcite crystal of the experiment 39. The crystal in (d) indicates a larger Mg and Sr incorporation than in (b).

Furthermore incorporation of Mg^{2+} ions causes lower step velocities of the (acute) faces, whereas the step velocity of the highly Sr incorporating obtuse side is less affected at constant Sr concentrations (see Fig. 5-12 and discussion in section 5.7.1 and Davis et al., 2004). The relative velocity of the Sr enriched obtuse step increases in comparison to the Mg enriched acute step. More calcium carbonate is formed at these obtuse sides and therefore more Sr is incorporated in Mg enriched solutions compared to Mg free solution. On the other hand the growth velocity may depend on the $(CO_3^{2-})/(Ca^{2+})$ ratio in the solution. The step velocity of the acute steps becomes higher with increasing $(CO_3^{2-})/(Ca^{2+})$ ratio (Larsen et al., 2010). Latter means for our experiments that the retardation of the precipitation rate by Mg and therefore the higher $(CO_3^{2-})_{fp}/(Ca^{2+})$ ratio at the beginning of the precipitation compensate partly the retardation of the growth of the acute crystal face. In consequence still a lot of calcium carbonate is formed at the acute side and the effect of Mg^{2+} ions at the distinct sides is partly compensated by the higher $(CO_3^{2-})_{fp}/(Ca^{2+})$ ratio in the solution.

Inhomogeneous structures (defects like e.g. incorporated trace elements, twinning planes and grain boundaries) of vaterite and Mg-calcite crystals were discovered in CL-images (Fig. 5-21). Reflected light microscope images indicate that the internal structures of vaterite are most probably related to the radial textures (Fig. 5-21a; Fig. 5-22a and b).
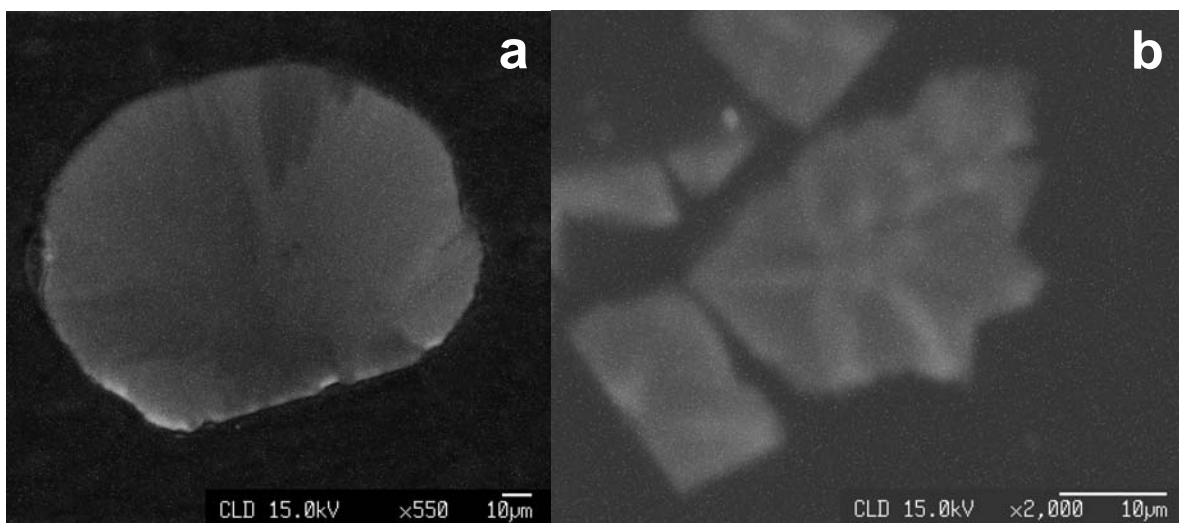
Fig. 5-21: Cathodoluminescence (CL) images displaying crystal defects and inhomogeneities like incorporated trace element, dislocations, twinning planes and grain boundaries (a) vaterite (experiment 92) and (b) Mg calcite (experiment 5). Homogeneous CL images are analysed for pure calcite (not shown).
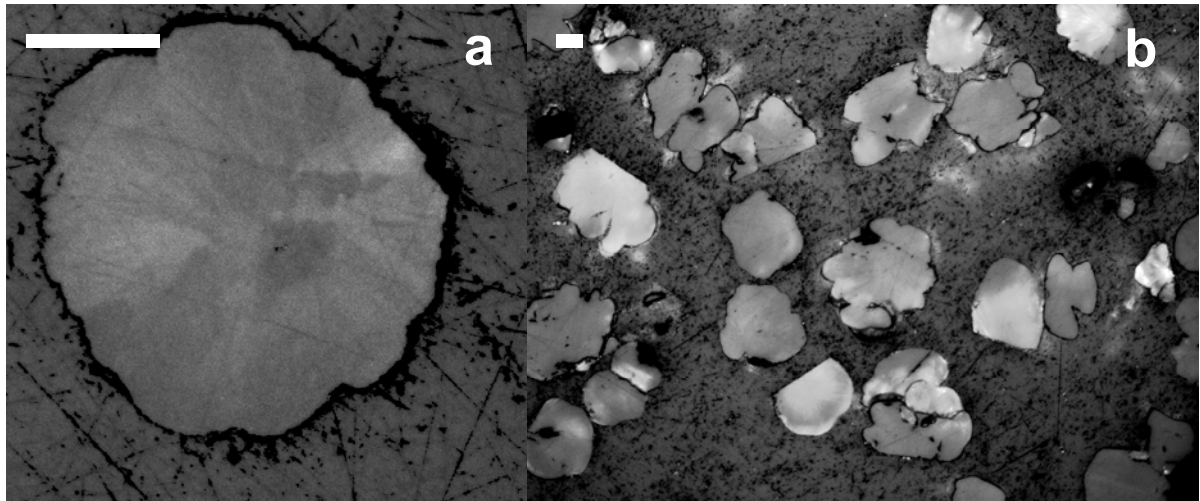
Fig. 5-22a and b: Carbon coated samples under the reflected light microscope indicate radial structures as a reason for the radial pattern at the CL images. White scale bar is 50 μm.

5.8.2 Crystal cell parameters

Spatial variations in the Mg^{2+} ion incorporation into calcite cause an increase of the full width at half maximum (FWHM) of the XRD peaks. The FWHM increases significantly from 0.06 to 0.15 with increasing $([Mg]/[Ca])_{Cc}$ ratio from 0.07 to 50 in calcite (Fig. 5-23a, Tab A6b and c in appendix) according to the following equation:

$$FWHM\ (°) = 0.0019\ ([Mg]/[Ca])_{Cc} + 0.073 \qquad (n=32, R^2 = 0.66) \qquad (\ 5\text{-}14\ )$$

$[Mg]/[Ca]_{Cc}$ was calculated from $[Mg]/[Ca]$ for a pure calcite sample under the assumption of a negligible incorporation of Mg into aragonite and an equal incorporation behaviour between calcite and vaterite.
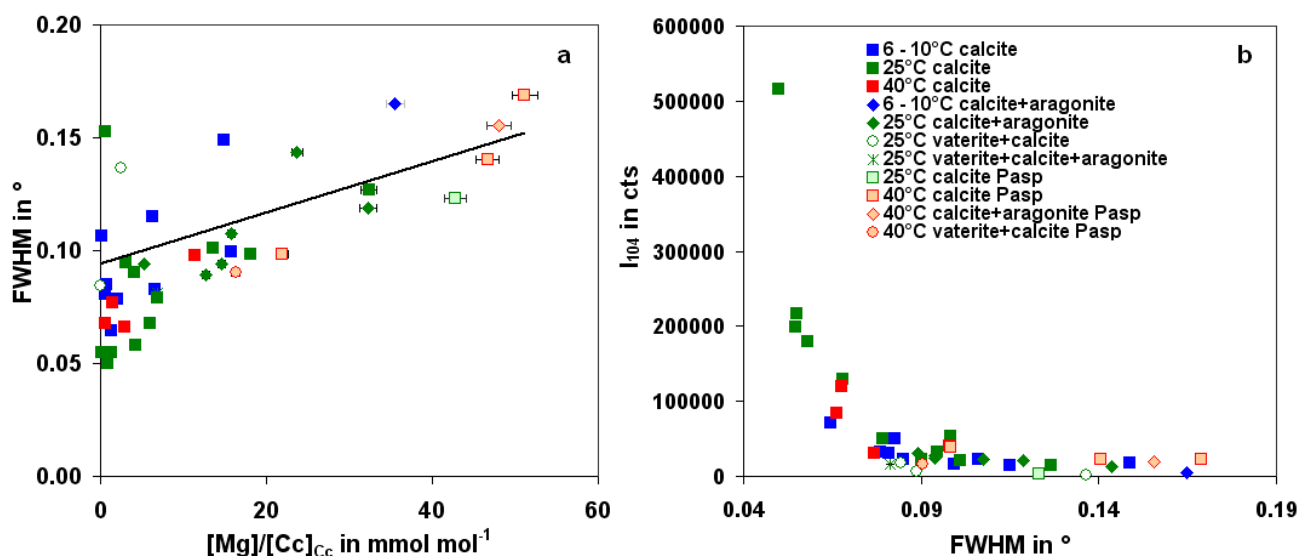
Fig. 5-23: (a) Full width at half maximum of the main calcite peak (FWHM) in XRD pattern vs. incorporated $[Mg]/[Ca]_{Cc}$ ratio. (b) Intensity vs. FWHM. Different symbols indicate different compositions of the samples with and without the influence of Pasp (legend see b) formed at 6 to 10°C (blue), 25°C (green) or 40°C (red).

Furthermore the peak intensity correlates inversely with the FWHM (Fig. 5-23b, Tab A6b and c in appendix). At low $[Mg]/[Ca]_{Cc}$ ratio the FWHM is small and the intensity of the $(10\overline{1}4)$ peak is high (Fig. 5-23b). This reveals the preferential growth and occurrences of these faces and is in well agreement with the morphology displayed in the last section (5.7.1).

Incorporation of the smaller Mg^{2+} ion causes a decrease in the average unit cell axes dimension according to following equations:

$$a = -0.392\ [Mg]/[Ca]_{Cc} + 4.991 \qquad (n=32,\ R^2 = 0.94) \qquad\qquad (\ 5\text{-}15\ )$$

$$c = -1.828\ [Mg]/[Ca]_{Cc} + 17.067 \qquad (n=26,\ R = 0.95) \qquad\qquad (\ 5\text{-}16\ )$$

as it was quantified by Rietveld analyses of the XRD pattern. Results are plotted also in Fig. 5-24.
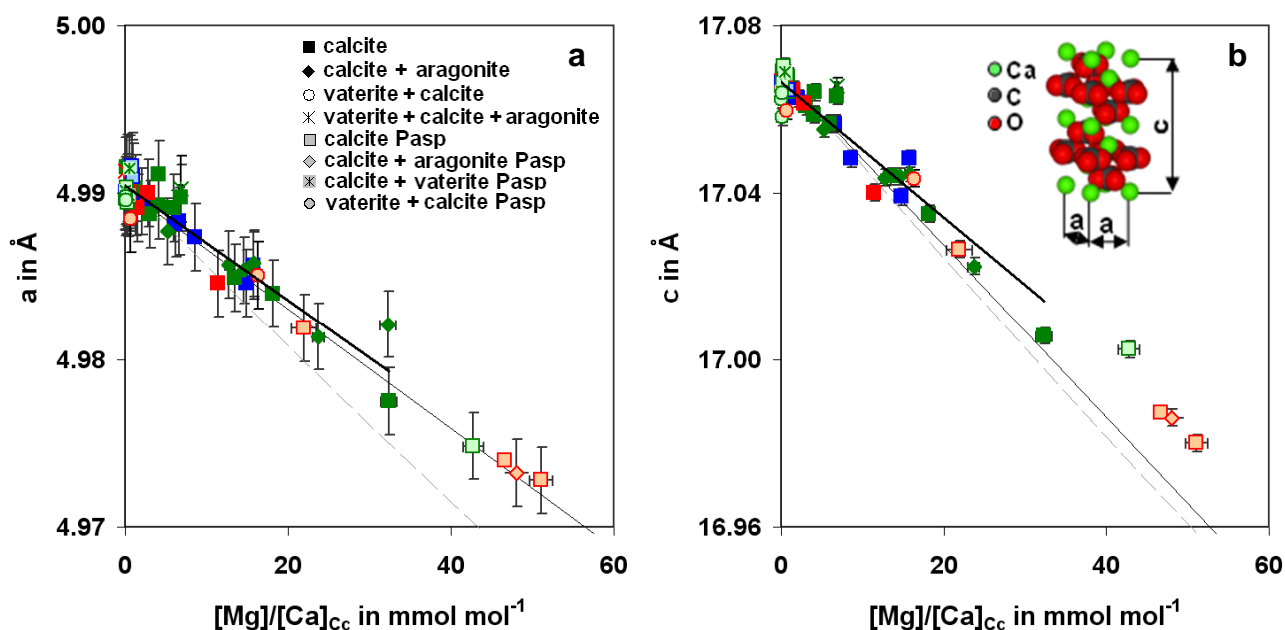
Fig. 5-24: Reduction of the cell parameters a and c of calcite vs. $[Mg]/[Ca]_{Cc}$ ratio at 6 to 10°C (blue), 25°C (green) and 40°C (red). The calcite structure of Maslen et al. (1993) was used as initial structure for Rietveld analyses. The legend give the mixtures from which the calcites were analyzed.

Rietveld analyses of vaterite display a lower agreement with the published structures as it was indicated by the weighted profile parameter R_{wp} (see Tab. A6d in appendix) which was seldom below 10. The best fits were obtained by the structures of Kamhi (1963) and Wang and Becker (2009). The theoretical structure of vaterite given by Wang and Becker (2009) had too many peaks in comparison to the observed XRD pattern of the vaterite samples in the present study. In the structure of Kamhi (1963) some peaks are missing which occur in observed XRD pattern in the present study, but are covered by the structure of vaterite given by Wang and Becker (2009). At low and high 2Θ angles the vaterite structure from Kamhi (1963) and Wang and Becker (2009), respectively, fits best. The overall best fit was obtained by combination of both structures so that the vaterite crystals may contain domains of the structure given by Kamhi (1963) and Wang and Becker (2009). In the following discussion the structure of Kamhi (1963) was used due to the better fit at the

low angle patterns, but further studies on the structure of vaterite are required to solve this discrepancies between the theoretical structure and the obtained XRD pattern.

Investigations of the Mg^{2+} ion effect on vaterite indicate that a similar reduction of the cell size of vaterite than it was found for calcite (Fig. 5-26). More analyses are required to verify this, because in this set of experiments only once vaterite was formed in presence of a significant amount of Mg. As discussed in section 5.6.2 the vaterite formation is only possible in presence of few mg l^{-1} of Pasp when Mg^{2+} ions are present.
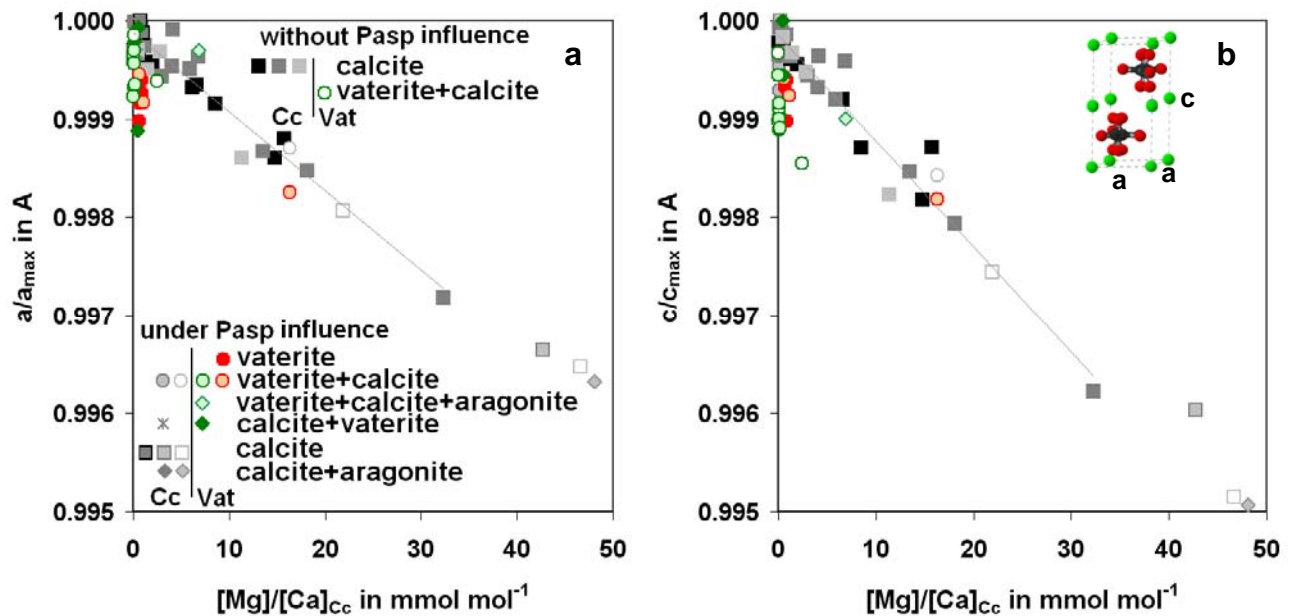
Fig. 5-25: Reduction of the cell parameters a and c related to the max. value of vaterite (structure of Kamhi, 1963) and calcite (Maslen et al., 1993) vs. calculated [Mg]/[Ca]$_{Cc}$ ratio calcite (squares) and/or vaterite (circles), at 25°C (green) and 40°C (red) under the assumption that calcite and vaterite incorporate similar Mg amounts ([Mg]/[Ca]$_{Cc}$=[Mg]/[Ca]$_{Vat}$). The cell sizes were related to the maximal cell size of the individual CaCO$_3$ polymorph for a better comparison. Calcite is marked at 6 – 10°C (black), 25°C (grey) and 40°C (slight grey), with a margin marked symbols indicated experiments which are done in the presence of Pasp. The used vaterite structure according to Kamhi (1963) was plotted in b.

Pasp itself has only a small effect on the cell size of vaterite and calcite if there is any (Fig. 5-26). The cell size a in vaterite may decrease slightly with increasing Pasp concentration in the solution while c increases in both vaterite and calcite (Fig. 5-26). But this effect has to be verified more in detail by e.g. single crystal XRD analyses. The FWHM of the vaterite in XRD measurements increases by 0.084 (R^2=0.9994, n=5) per mg l^{-1} Pasp for samples which are formed at 25°C. The increase of FWHM at 40°C in XRD pattern is 0.024 (R^2=0.65, n=6) per mg l^{-1} Pasp. Also the cell size in c direction might be slightly influenced by Pasp (see Tab. A6d in appendix).

In comparison to vaterite the ideal aragonite crystal structure (Devilliers, 1971) can be fitted with a higher agreement to the measured XRD pattern. Best fits (R_p and R_{wp}-value) were obtained at low temperature (see Tab. A6a in appendix). The R_p values of the Rietveld analyses are 5-6, 5-8 and 7-14 for 6 - 10°C, 25°C and 40°C, respectively. Similar behaviour is valid for the R_{wp} value with 7, 7 to 11 and 10 to 19 at 6 - 10°C, 25°C and 40°C, respectively (Tab. A6a in Appendix).
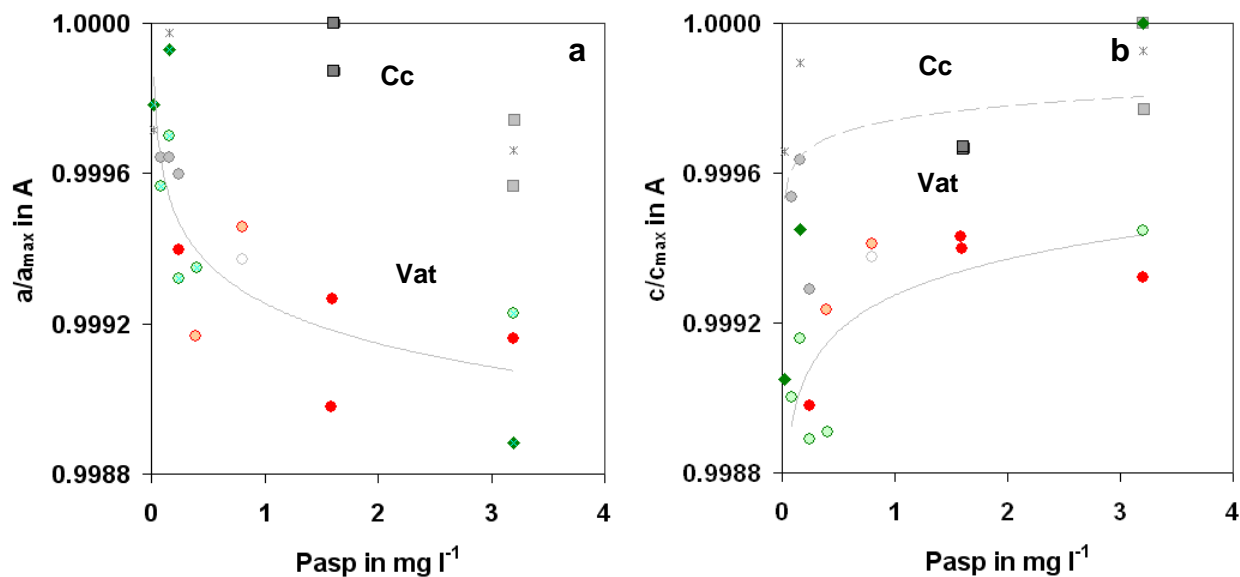
Fig. 5-26: Cell parameters a and c for vaterite (colour) and calcite (grey shades) vs. Pasp concentration in the solution at 25°C (green) and 40°C (red) experiments. The different symbols indicate the CaCO₃ polymorph composition. Full red circle indicate "pure" vaterite samples (<5 wt. % calcite), half field circles indicate vaterite-calcite mixtures with mainly vaterite, squares indicate calcite samples and rhombs indicate calcite-vaterite mixtures with mainly calcite. Calcites are displayed as grey symbols, bright grey is 40°C and grey is 25°C.

The cell parameter a of aragonite is not influenced by the [Mg]/[Ca] ratio in the solution, even at [Mg]/[Ca] ratios up to 5 (Fig. 5-27, Tab. A6a in appendix) due to the small amount of incorporated Mg. At 40°C the parameter c of aragonite might be slightly affected by the [Mg]/[Ca] ratio of the solution. A similar behaviour is valid for the parameter b, although in this case the temperature effect was not observed. The dipyramidal shaped aragonite crystals have a significant larger cell size c, which might be caused by a different growing mechanism or by the higher saturation degrees in respect to aragonite (Tab. A5 and A6 in appendix), at which it was growing. Fig. 5-27c indicates a tendency to smaller cell sizes with increasing temperature, especially if the sample which is grown at low Sr concentration (marked by an arrow) is excluded. This indicates that the temperature dependency of Sr incorporation is responsible for the variation in the cell parameter c and it might explain the variation of c (normal to the carbonate planes) in the literature, whereas the variation of the published parameter a is smaller (e.g. Dalnegro and Ungaretti, 1971; Devilliers, 1971; Lucas et al., 1999; Antao and Hassan, 2009). The decrease in the cell size at elevated temperature is reverse to the extension of the aragonite crystals which was obtained by heating up aragonite to several hundred °C under high pressure conditions (Antao and Hassan, 2010) or as it was calculated by Lucas et al. (1999) for pure systems. This is a further indication that Sr incorporation is responsible for the extention of the cell size parameter *c*, this issue will be discussed more in detail in section 5.9.3.
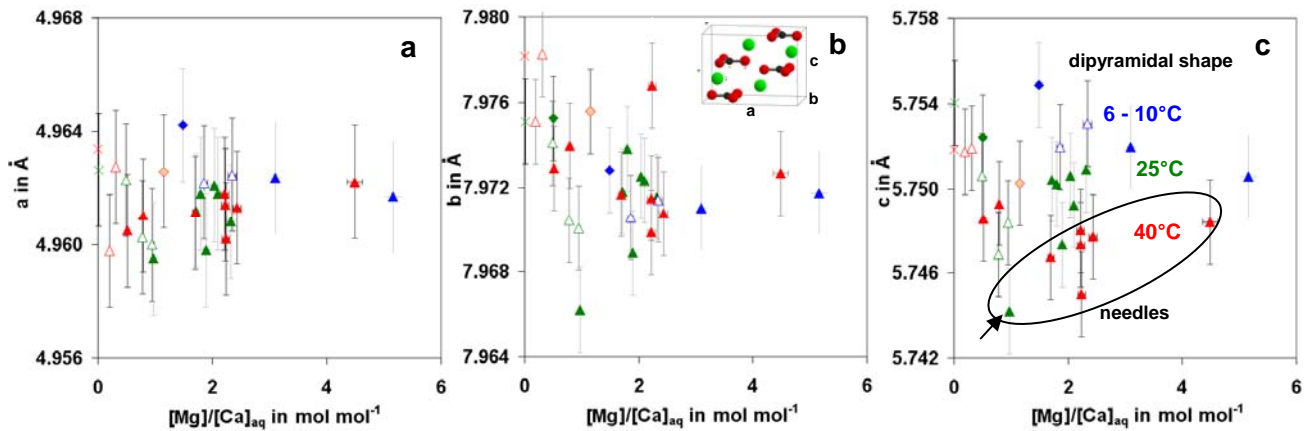
Fig. 5-27: Cell parameters a, b and c of aragonite crystals (Rietveld analyses according to the structure given by De Villiers, 1971), which were produced in solutions with [Mg]/[Ca]$_{aq}$ of 0 to 5 mol mol^{-1} at 6 to 10°C (blue), 25°C (green) and 40°C (red) experiments. Different symbols indicate CaCO$_3$ polymorphs which are formed additionally to aragonite (full triangle: pure aragonite, open triangle: mainly aragonite and some calcite, rhombs: mainly calcite and some aragonite). The needle like shaped crystals in c are within the ellipse, all other crystals have a dipyramidal shape. With arrow marked sample has no Sr in the solution.

Furthermore the aragonite samples display a positive correlation between the cell parameters a and c especially at 40°C and a positive correlation between a and b (values see Tab. A6a in appendix), especially at 25°C (not shown). The FWHM of the main peak (221) of the needle shaped aragonite decreases from 0.28 to 0.13 with increasing [Mg]/[Ca] ratio up to 4 at 40°, it is smaller for 25°C experiments. Whereas the half width of the main peak (221) of the dipyramidal shaped is more or less constant between 0.2 and 0.3 for [Mg]/[Ca] ratios from 0 to 5. There is no correlation between the FWHM and intensity for aragonite. This verifies the small effect of Mg ions on aragonite structure due to its low Mg incorporation during aragonite crystallization.

5.8.3 Temperature, precipitation rate and polymorph effect

The distribution coefficient of Mg^{2+} ions between dissolved Mg and aragonite, D$_{Mg}$, is about 0.001 (see Fig. 5-28b, Fig. 5-29 and Tab. A7a in appendix) and therefore about 2 orders of magnitude lower than that of calcite (Fig. 5-28b and Tab. A7b and c in appendix). This low value for the distribution coefficient of Mg is caused by the nine fold coordination of the cation in aragonite. More space is available for the cation in this nine fold coordination in which the small Mg fit worse compared to six fold coordination of the cation in calcite. The analysed variability in Mg content in aragonite might be also caused – besides incorporation - by adsorption of Mg ion at the aragonite surface or MgCl$_2$ impurities and should be evaluated in further studies e.g. by x-ray photoelectron spectroscopy (XPS) analyses.

During the formation of vaterite similar amounts of Mg^{2+} ions are incorporated in calcite and also an analogue rate dependency of the Mg incorporation is obtained (Fig. 5-29, Tab. A7d in appendix). The incorporation of Mg^{2+} ions into calcite depends mainly on the temperature, [Mg]/[Ca] ratio in the solution and precipitation rate (Fig. 5-28 and Fig. 5-29). Generally less Mg is found in both vaterite and calcite at low temperatures (Fig. 5-28a) and elevated precipitation rates (Fig. 5-29). The

D_{Mg} value of calcite increases e.g. from 0.01 at 6°C to 0.1 at 40°C or in vaterite from 0.009 at 25°C to 0.16 at 40°C.
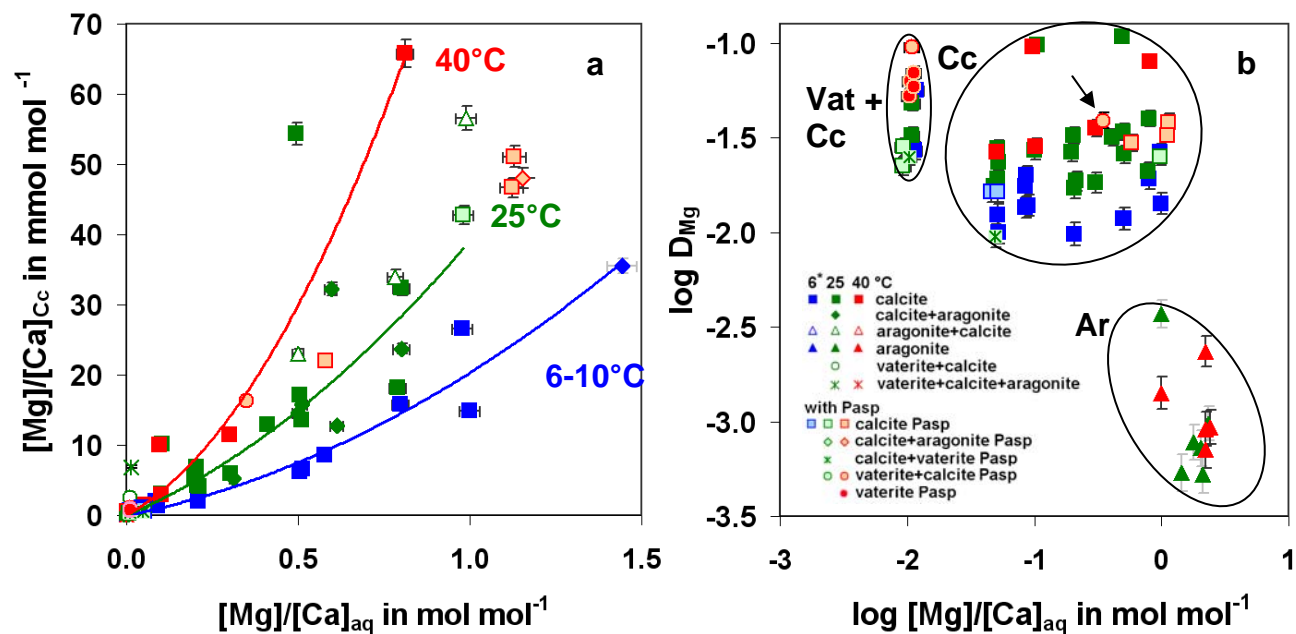
Fig. 5-28: (a) Incorporation of Mg ions in the calcite crystals. (b) Distribution coefficient of Mg, D_{Mg}, vs. [Mg]/[Ca] ratio in the solution. The [Mg]/[Ca] ratio was calculated for pure calcite under the assumption that the Mg incorporation into aragonite is negligible and vaterite incorporates similar amounts compared to calcite. The circles indicate dominant areas of the individual $CaCO_3$ polymorph in these experiments; although mixtures occur also in all fields and vaterite can occur in the calcite field if sufficient concentrations of Pasp are present (see the vaterite sample marked by the black arrow).
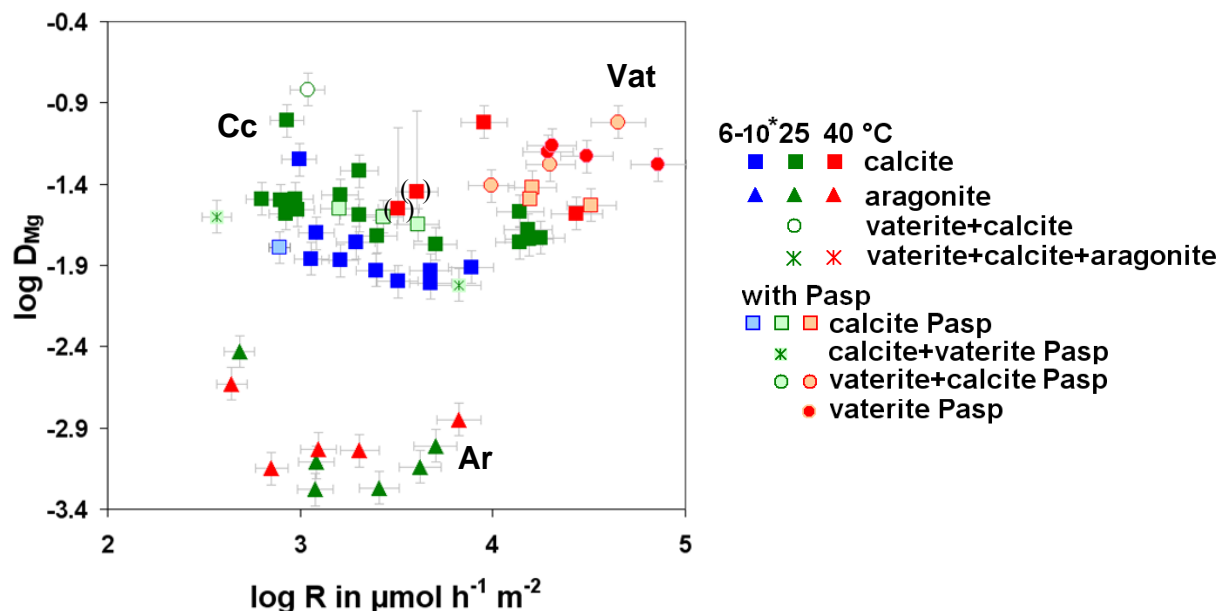
Fig. 5-29: Distribution coefficient of Mg, D_{Mg}, between precipitated $CaCO_3$ and the solution versus precipitation rate R of the $CaCO_3$ polymorphs. The D_{Mg} of calcite and vaterite are inversely proportional to their precipitation rates at 6 to 10 and 25°C. The D_{Mg} values for calcite and vaterite are 2 orders of magnitudes higher than those of aragonite. Data marked with brackets show a large variation in the analysed Mg concentration at repeated measurements by ICP-OES.

The nonlinear relationship between $[Mg]/[Ca]_{Cc}$ and $[Mg]/[Ca]_{aq}$ (Fig. 5-28a) indicates furthermore a rise of Mg ion incorporation during (Mg-)calcite formation with increasing $[Mg]/[Ca]$ ratio in the solution. This increase in D_{Mg} with increasing $[Mg]/[Ca]$ ratio for unseeded experiments is in contrast to Mucci and Morse (1983) for seeded experiments. The discrepancy might be explained by the change in the size and structure of the crystals which nucleate at the investigated $[Mg]/[Ca]$ composition compared to the seeds. As Mg influenced crystals incorporate more easily Mg.

On the other hand at elevated $[Mg]/[Ca]$ ratios in the solution nearly "Mg-free" aragonite can be formed. So that the apparent Mg "distribution coefficient" between calcium carbonate and solution decreases at elevated Mg ($[Mg]/[Ca]>2$ depending on the temperature, CO_3^{2-} accumulation rate and other additives see chapter 5.6). However all experiments plot above a certain D_{Mg} - log $[Mg]/[Ca]$ line which is related to the minimal Mg ion incorporation of calcite on the one side and by Mg ions required for the formation of aragonite for spontaneous formation in homogeneous solutions on the other side (Fig. 5-28b).

5.9   Strontium incorporation

5.9.1 Calcite and Mg-calcite

Strontium incorporation into calcite rises with decreasing temperature and increasing precipitation rate (Fig. 5-30) as it was also observed e.g. by Tang et al. (2008b), Nehrke et al. (2007), Tesoriero and Pankow (1996) and Lorens (1981) (see also section 2.7). Tesoriero and Pankow (1996), Lorens (1981) and Nehrke et al. (2007) have carried out their experiments at pH of 6.2, 7.4 and 10.2, respectively. Different pH values result in different strontium incorporation behaviour into calcite due to a change in precipitation rates and surface complexation (see also Tang et al., 2008b). At pH 8.3 the surface densities of the species $>CO_3^-$, $>CaCO_3^-$ and $>CaOH^0$ are higher and those of $>CO_3Ca^+$ and $>CO_3H^0$ are lower compared to the surface densities of these species at lower pH of e.g. 7.4 (Van Cappellen et al., 1993). The pH dependency of the surface densities of $>MeHCO_3^0$ and $>CaOH_2^+$ is related to the type of pH adjustment, e.g. adjusted by CO_2 or by the addition of acids and bases (see Van Cappellen et al., 1993). Different Sr and Ca complexes have different stability constants (Pokrovsky and Schott, 2002 and references therein) and therefore different formation conditions.

However, in this study the Mg, Pasp, T and carbonate accumulation rate effects can be directly compared to Tang et al. (2008b) at the same pH and ionic strength. For the pH effect on Sr incorporation the reader is referred to Tang et al. (2008b) and for the ionic strength effect to Pingitore and Eastman (1986), Holland et al. (1964) and Tang et al., (subm.). The range of precipitation rates for determining D_{Sr} values given by Tang et al. (2008b) was extended in the present study to higher precipitation rates especially at 6°C (Fig. 5-30). The distribution coefficient between calcite and solution increases with decreasing temperature and is therefore inversely related to the behaviour at thermodynamic equilibrium as it was found by phase transformation (aragonite-

calcite and dolomite-calcite) methods (Katz et al., 1972; Humphrey and Howell, 1999). The precipitation rate and temperature dependency of Sr incorporation into calcite can be explained by the "surface entrapment model". According to this model, Sr is enriched at a $CaCO_3$ surface layer compared to Sr incorporation at equilibrium in the crystal lattice. The idea of this model was introduced by Noyes and Whitney (1897), and is used in one of the latest version e.g. by Watson (2009) and Tang (2008b) (see also chapter 2.4). High temperatures cause faster ion diffusion in the $CaCO_3$ surface layer resulting in a smaller surface entrapment factor (Tang et al., 2008b). Strontium can more easily re-equilibrate by escaping from the surface layer into the aqueous solution due to larger vibration energy, higher mobility and diffusion rates at elevated temperature. On the other side, elevated $CaCO_3$ precipitation rates result in less time for ion diffusion and for Sr exchange between the surface layer and the aqueous solution. More strontium remains in the surface layer and in the crystal. The samples fit to the data of Tang et al. (2008) as long as ideal rhombohedral shaped crystals without attached small particles occur. The blue sample in Fig. 5-30a which lies significantly above the log D_{Sr} - log R line consists of rounded and partly very tiny crystals (partly <1μm) (not included into the least square fit). This immature crystal shapes and small crystal size might be caused by the relative "short" precipitation time (141 h) in comparison to the long time until first precipitation occurs (933 h). The precipitation time is only 13% of the total experimental time, whereas it is usually around 50% at the other experiments. Similar is valid for the 40°C experiments where tiny particles were found at the secondary electron microscopy image.

The fit of the experimental data of Tang et al. (2008) and this study result into the following regression lines:

$$\log D_{Sr} = 0.27 \log R - 1.69 \qquad \text{at 5 to 6°C for } 2.2 \le \log R \le 3.9 \ \ n=14, R^2=0.98 \qquad (5\text{-}18)$$

$$\log D_{Sr} = 0.26 \log R - 1.79 \qquad \text{at 25°C for } 2.2 \le \log R \le 4.4 \ \ n=14, R^2=0.88 \qquad (5\text{-}19)$$

No significant nonlinearity was found in these experiments, even if the precipitation rates were about 10^4 μmol $h^{-1}m^{-2}$. For 40°C the data of the new experiments scatter too much (because of the tiny particles) to extent the range and to calculate new equations.

Elevated Mg concentrations in the solution cause a slightly larger Sr incorporation as without Mg (compare Figs. 5-30a and b, see also section 5.8.1) as it was also found by Morse and Bender (1990). Besides to the discussed structural and crystallographic effect, more Sr is incorporated because higher saturation degrees and higher precipitation rates are reached at elevated Mg concentrations in this kind of experiments due to the retardation of the precipitation (see section 5.3.2). However, the effect of Mg on the Sr incorporation is relatively small at the investigated concentration range compared to the effect of the temperature and precipitation rate (comp. Figs. 5-30a and b).

Pasp causes a significant increase of the Sr incorporation into calcite. Log D_{Sr} values of at least -0.5 were found in experiments where calcite was formed in the presence of Pasp and Mg (Fig. 5-30). The large Sr incorporation into calcite in presence of Pasp might be caused by the large rise of the saturation degree and therefore of the precipitation rate when Pasp is present (see also section 5.3.4

and chapter 5.5). A high precipitation rate causes a high Sr uptake in calcite. The surface related precipitation rate does not indicate the higher precipitation rate as the total geometric surface area increases significantly due to the higher surface roughness and alteration of the crystal morphology under the influence of Pasp (see section 5.7.2 and 5.7.3). However, adsorption of Pasp on the calcite surface (section 5.7.2) inhibits partly the calcium carbonate precipitation and the total surface area exceeds therefore the reactive surface area.
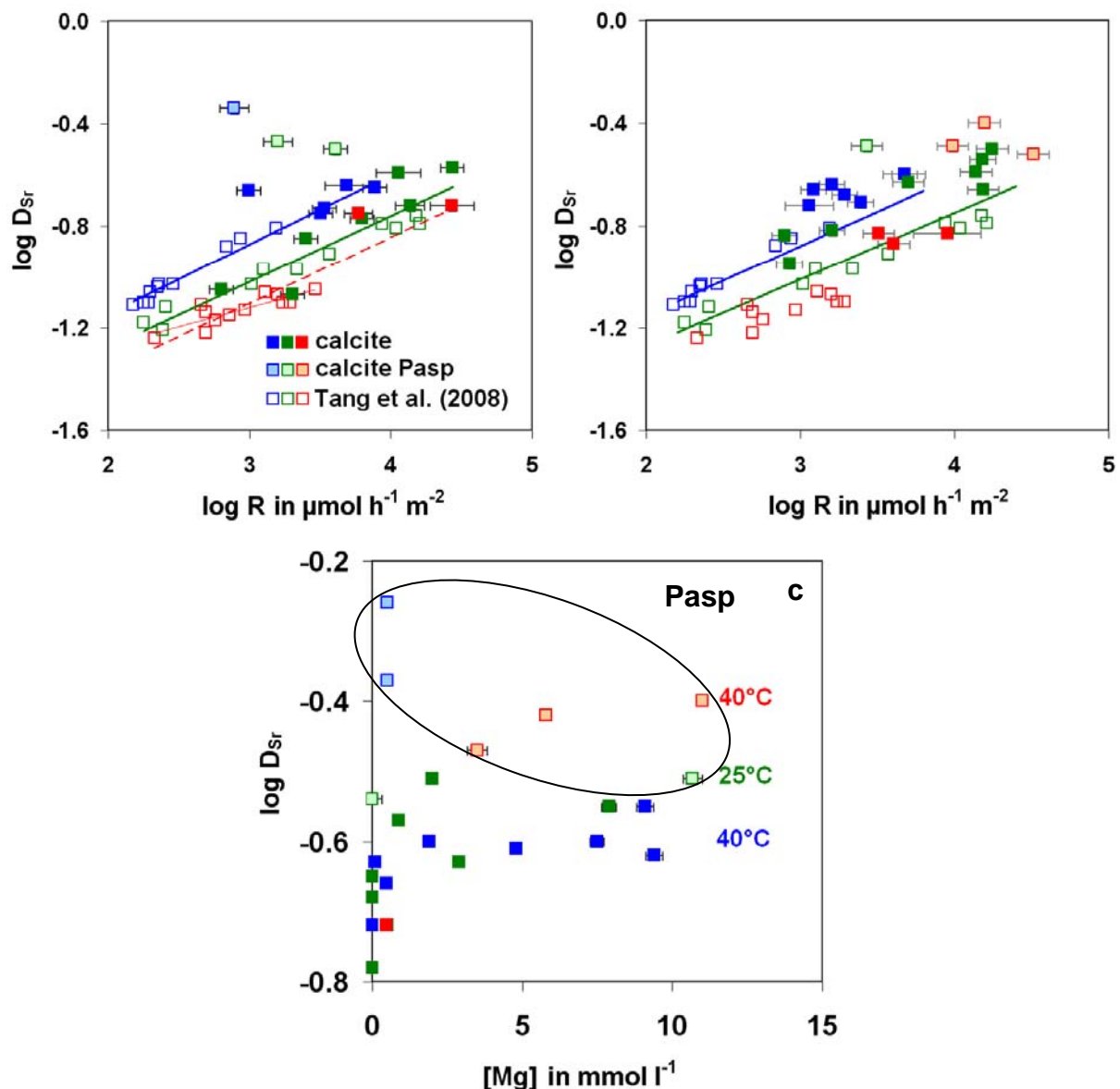
Fig. 5-30: Distribution coefficient of strontium (D_{Sr}) between calcite and aqueous solution versus surface related precipitation rate R of calcite displaying (a) experiments without and with low [Mg] up to [Mg]/[Ca] of 0.05 and (b) in presence of Mg (0.05 < [Mg]/[Ca] ≤ 1.1). (c) D_{Sr} against the initial Mg concentration in the solution for experiments with a thin membrane 0.2 mm. In all diagrams the experiments with Pasp are given by light-coloured symbols (see legend in a). Red coloured symbols are for experiments at 40°C, green for experiments at 25°C and blue for experiments at 6 to 10°C and 5°C, this study and Tang et al. (2008), respectively.

In the log Sr - log R' plot (R` is not surface related, not shown) the Pasp influenced samples are closer to the extrapolated log Sr - log R relation of inhibitor free experiments, but still do not fit on the given lines. This means that either a direct influence of Pasp on Sr incorporation or a nonlinear

relation between log Sr and log R at higher R of about 10^4 µmol h^{-1} may occur. On the other hand the surface area and roughness is affected by Pasp (section 5.7.2) and this may enhance also the Sr uptake. Furthermore at pH 8.3 the negatively charged Pasp (see Fig. 2.6, Wu and Grant, 2002) may interact with the positively charged ions. Aspartarte anions are known to form aqua complexes with Mg^{2+}, Ca^{2+} and Sr^{2+} ions. Water molecules can compete thereby with the Me-Aspartarte complexes to favour of Mg-, Ca- and Sr-complexation (Schmidbaur et al., 1990). These metal ions have distinct values for their related aqua complex formation constants, e.g. the smaller Mg has a 1.5 stronger bound to aspartic acid compared to Ca (Wang et al., 2009). In analogy to aspartic acid, the larger Sr ion might have also less affinity to Pasp compared to Ca and Mg, although Pasp may only influence the Sr concentrations at the crystal surface because of its low concentrations in the solution and the enrichment at the reactive crystal sites. Furthermore the surface properties like the surface charge are locally modified by Pasp. Pasp may act in consequence directly (by surface complexation) or indirectly (by changing the morphology of the surface and complexation in the water) for elevated Sr uptake. In order to deceiver if Pasp acts directly or indirectly for Sr uptake the spatial distribution of the two substances on the surface should be investigated by TEM or fluorescence microscopy in combination with microprobe analyses at future studies.

5.9.2 Vaterite

Sr is incorporated into vaterite and calcite at a similar range (Fig. 5-31a and b). The specific surface area of the vaterite samples and especially of the Pasp influenced calcite samples is very high (see the with the arrow marked sample in Figs. 5-31a and b, section 5.7.2 and Tab. A7d). This causes a shift to lower surface related precipitation rates as it is indicated by comparison of the marked samples in Fig. 5-31a with Fig. 5-31b. The Sr incorporation into vaterite is slightly lower than that for calcite at 25°C, when it is referred to the "total" precipitation rate R' (not surface related - Fig. 5-31b).

The variations of log D_{Sr} at 40°C for vaterite formation are mainly caused by the presence of Pasp (Fig. 5-31c). The following equation is found for the Pasp influenced "pure" vaterite samples in experiments 99, 104, 105 and 106 at an almost constant precipitation rate of about $10^{4.3}$ µmol h^{-1} m^{-2}:

$$\log D_{Sr\ Vat} = 0.087\ [Pasp] - 1.05 \qquad (n=4,\ R^2=0.89) \qquad (5 - 20)$$

The concentration of [Pasp] is given in mg l^{-1}. This equation indicates a distribution coefficient of $10^{-1.05}$ for vaterite in the absence of Pasp at 40°C at a precipitation rate R of about $10^{4.3}$ µmol h^{-1} m^{-2}. This value is very close to the log D_{Sr} value of $10^{-1.05}$ for calcite calculated by the equations of Tang et al. (2008b) at the given temperature and precipitation rate. The distribution coefficient for vaterite is therefore suggested to be similar as that of calcite.

Significantly more Sr is incorporated into the Mg influenced vaterite than into "Mg-free" vaterite, as also the structural influence of Mg on vaterite is similar to that on calcite like indicated in section 5.8.2. The effects of the surface related precipitation rate and the temperature on Sr incorporation are similar for both calcite and vaterite (Fig. 5-31a and b).
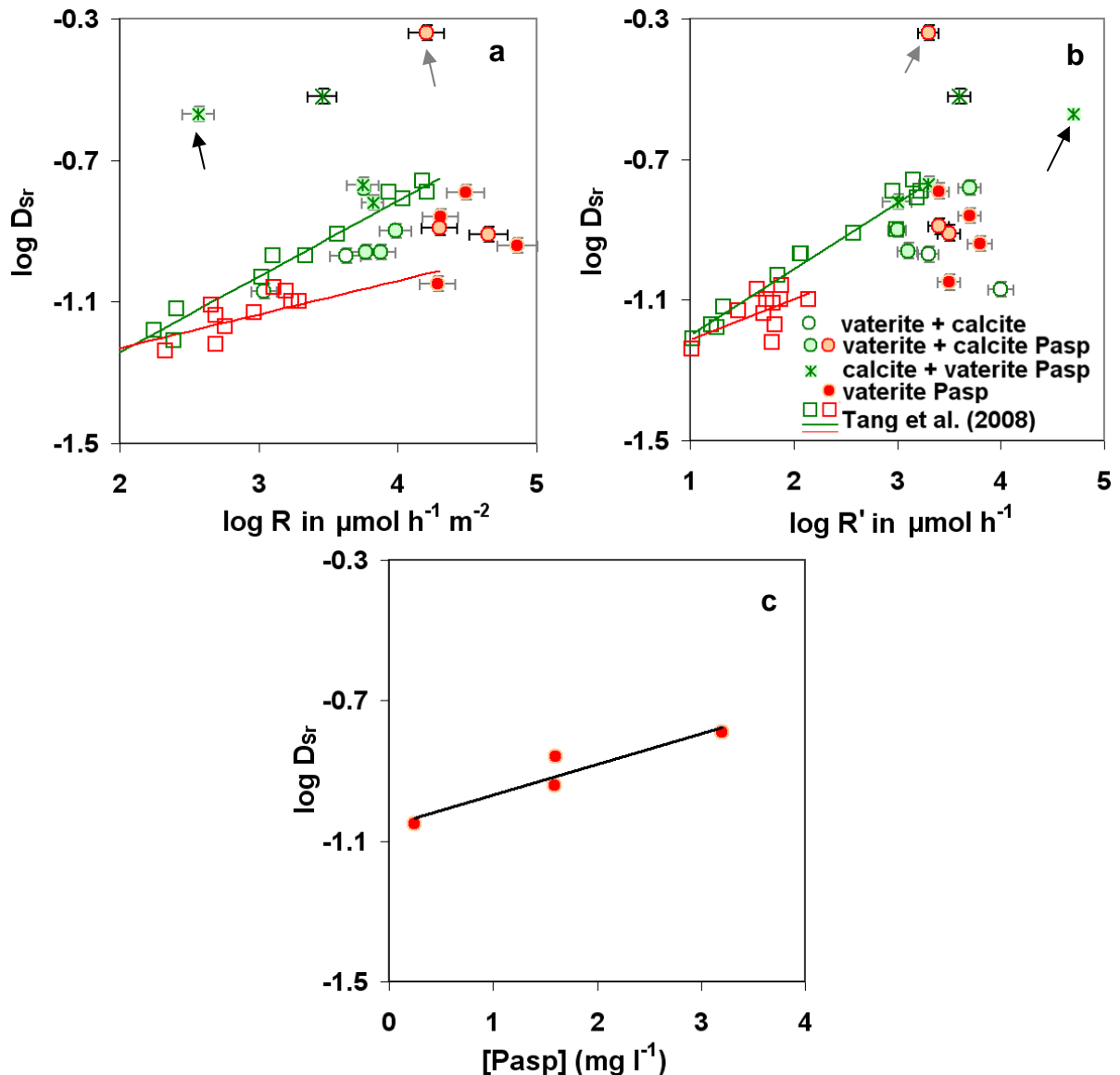
Fig. 5-31: Distribution coefficient of strontium (D_{Sr}) for vaterite containing $CaCO_3$ samples versus the solution (a) surface related precipitation rate R, (b) "total" precipitation rate of experiment (5l) R' and (c) pure vaterite under the influence of Pasp at a temperature of 40°C. Vaterite containing samples (sample composition see legend) were plotted in comparison with calcite samples from Tang et al. (2008b). The black arrow indicates a sample with a very large surface area due to a high roughness (see therefore also section 5.7.2). The grey arrow marks a vaterite-calcite mixture with a significant incorporation of Mg into the vaterite structure (see Fig. 5-26). The colour determines the temperature: experiments at 25 and 40°C are given in green and red, respectively.

Published data on Sr incorporation in vaterite are limited and often related to the Sr incorporation in further polymorph. Tzeng et al. (2007) found e.g. a 7.1 to 7.4 fold lower Sr/Ca ratio in vateritic otolith parts compared to the aragonitic otolith parts. Assuming a D_{Sr} value of about 1 for aragonite (see e.g. D_{Sr} values of aragonite formed at 40°C in Fig. 5-32 next section) this would result into a log D_{Sr} value of -0.87 between water and vaterite. It is therefore similar to the values of this study (Fig. 5-31, Tab. A7d). Melancon (2005) found a Sr content in vaterite from trout otoliths, which was 10 (otolith core) to 17 (otolith edge) fold lower than that in simultaneously grown aragonite, whereas the Sr distribution between aragonite and vaterite was only 2.4 in cultured freshwater pearls (Soldati

et al., 2008). The large Sr incorporation in the freshwater pearls might be related to the organic components of the mussels as typically more Sr is incorporated in presence of e.g. Pasp (Fig. 5-31c).

5.9.3 Aragonite

The strontium incorporation into aragonite is 1 to 1.5 orders of magnitude higher than that into calcite and vaterite and decreases at high precipitation rates and elevated temperatures (Fig. 5-32). This inverse correlation between Sr incorporation and temperature is in agreement with aragonite data from inorganic experiments (Kinsman and Holland, 1969; Dietzel et al., 2004; Gaetani and Cohen, 2006; Holcomb et al., 2009) and from corals (Cohen and Gaetani, 2010 and references therein). While the D_{Sr} values at 40°C of Dietzel et al. (2004) agree well with the D_{Sr} values for aragonite in this study, the Sr incorporation into their precipitated aragonite was lower at 10°C. Reasons for this might be in the different reactants (e.g. an ammonia buffer was used instead of NaOH for the titration). The results of the experiments carried out at 10°C in the present study are in good agreement with the extrapolated line of Gaetani and Cohen (2006).
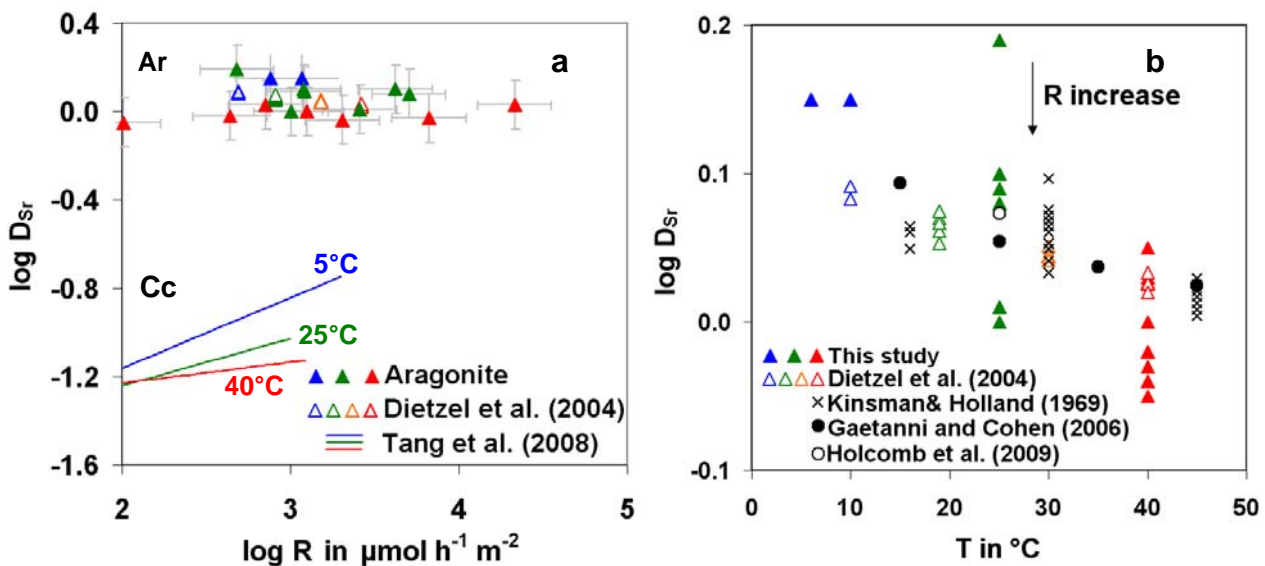
Fig. 5-32: Distribution coefficient of strontium (D_{Sr}) between CaCO$_3$ and the solution versus (a) precipitation rate R and (b) temperature. (a) For comparison the results of aragonite from Dietzel et al. (2004) and for calcite from Tang et al. (2008b) are shown. (b) Data from the present study in comparison with Dietzel et al. (2004) and Gaetani and Cohen (2006) . Colour of specific temperatures in (a) is also displayed in (b).

The precipitation rate – Sr incorporation (D_{Sr}) relationship of the present study is in accordance with the proposed precipitation rate by Cohen and Gaetani (2010) who have compared the Sr incorporation at fast (black dots in Fig. 5-32; Gaetani and Cohen, 2006) and slow growth rates (black open circle in Fig. 5-32; Holcomb et al., 2009).

The incorporation of Sr into the aragonite lattice causes a significant rise of the cell size c, whereas b might become slightly lower in dipyramidal shaped aragonite. It is obvious that the needles have smaller elementary cell parameters c than the dipyramidal aragonite crystals (Abb.5-33).
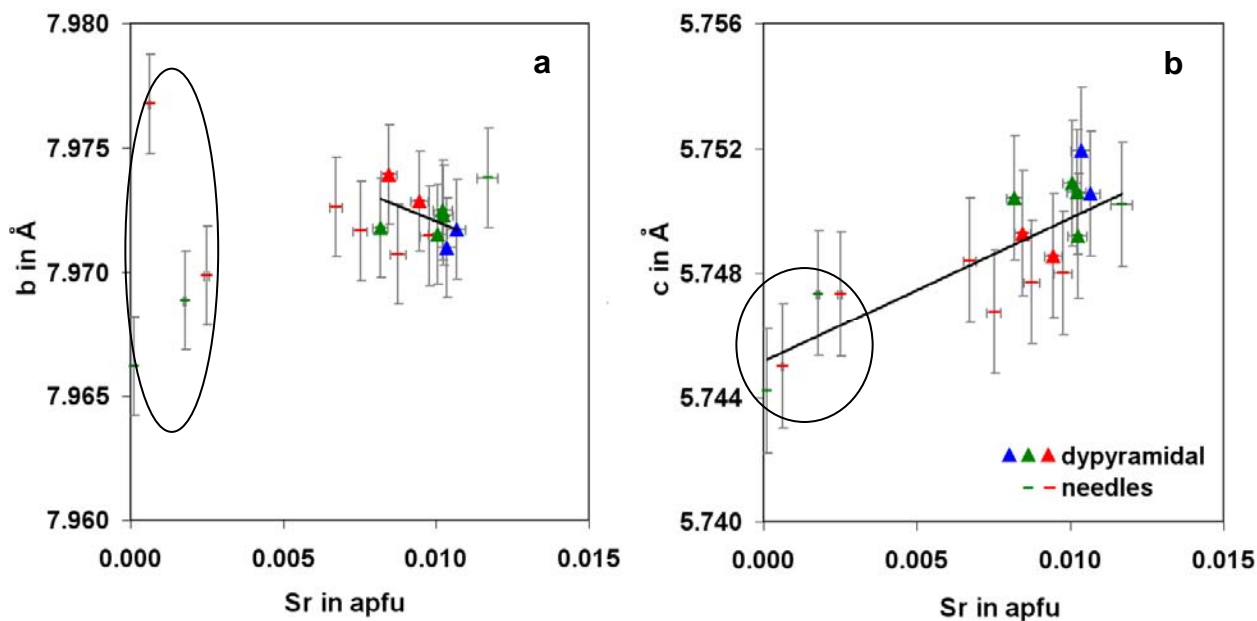
Fig. 5-33: Cell parameter b and c of aragonite vs. incorporated Sr. Circles mark samples with smaller Sr concentrations of the experimental solution. The cell size is larger for aragonite crystals which are formed at 6 to 10°C (blue) compared to that at 25°C (green) or 40°C (red), in case of a similar concentration of Sr in the initial solution. The unit apfu means atom per formula unit. Spicular aragonite crystals are marked by lines and dipyramidal aragonite crystals are marked by triangles.

5.9.4 Comparison of the polymorphs

The apparent "D_{Sr} values" of aragonite-calcite mixtures plot between the calcite and aragonite samples in the right upper corner (Fig. 5-34). Pasp influenced calcite precipitates display log D_{Sr} - values of about -0.4. Pasp affected calcite has a large surface area and therefore a lower precipitation rate especially at 6°C. A similar behaviour is observed for the other samples at the other temperatures although especially at 40°C the increase of the specific surface area alone does not explain the shift to higher Sr incorporation. Thus a specific rise of the D_{Sr} value in the presence of Pasp has to be considered, besides to the increase of Sr incorporation due to the higher precipitation rate, which is caused by the Pasp.

The occurrence of small aragonite proportions of a few percent in calcite samples can increase the apparent D_{Sr}-value significantly (Fig. 5-34). At low precipitation rates the difference in the Sr incorporation between calcite and aragonite is higher than at high precipitation rates. In consequence the distribution coefficient of Sr between aragonite and calcite might be referred to the average precipitation rate. Therefore proportions of simultaneously grown calcite and aragonite with their individual Sr content are highly relevant for the reconstruction of the individual precipitation rates at known temperature. Large differences in the Sr incorporation indicate a slower growth than small differences.

The increase in the Mg concentration in the solution causes a slight increase of Sr in calcite, although the effect of Pasp on the Sr incorporation is much higher (Fig. 5-34). Calcite and vaterite have a similar Mg (Fig. 5-29) and Sr incorporation (Fig. 5-34), although the log D_{Sr} – log R range in Fig. 5-35 is slightly shifted to higher Mg incorporation.
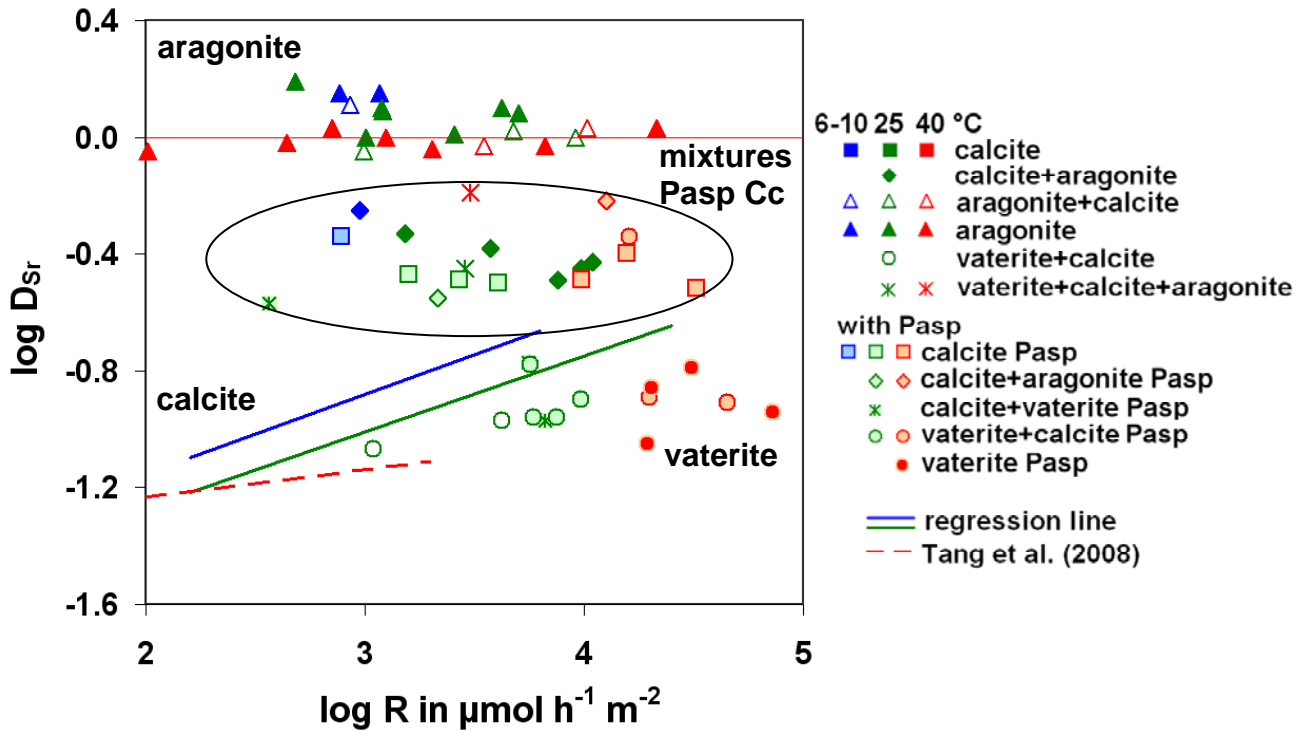
Fig. 5-34: Distribution coefficient of strontium (D_{Sr}) between CaCO$_3$ and the solution versus precipitation rate R for all precipitation experiments excluding pure calcite which is given by blue and green solid line (regression incl. data of Tang et al. (2008b) and the present study) and by the red dashed line from Tang et al. (2008b).

The apparent "distribution coefficient" of Sr and Mg between calcite-aragonite mixtures and the solution is referred to the Sr incorporated into aragonite and the Mg incorporated into calcite. Since either a high amount of Sr (log D_{Sr}>0) is incorporated in aragonite or "high" amounts of Mg (log D_{Mg}>-2) are incorporated in calcite and vaterite, no calcium carbonate polymorph is formed at low D_{Mg} and simultaneously low D_{Sr} values (Fig. 5-35). Also neither the apparent "distribution coefficient" between aragonite-calcite mixtures and the solution nor the D_{Sr}-D_{Mg} values at Pasp influenced samples have simultaneously low log D_{Sr} and low log D_{Mg} values. In consequence, calcium carbonates plotting in this field have vital effect and might be formed by selective ion uptake. The internal CaCO$_3$ growth solution is modifidied, so that the sea water is not any longer the valid growing solution. Depletion of Mg in the calcium carbonate shell or skeleton might also be caused by preferential complexation of Mg by organic substances like Pasp compared to the complexation of Ca, as the bonding strength of Asp to Mg is much larger than that to Ca (Wang et al., 2009). Organisms whose shells and skeletons are characterized by low log D_{Sr} and low log D_{Mg} like mussels (Klein et al., 1996), gastropods, pelecypods, bryozoa, cephalopods, echinoids, crinoids, calcareous algae, calcareous brachiopods, annelid worms (all: Morse and Mackenzie, 1990 and references therein), coccolithophores (Müller et al., in press) and foraminifera (Morse and Mackenzie, 1990; Rosenheim et al., 2005 and references therein) (Fig. 5-36). Most of these organism have shells or skeletons made of calcite, but in several cases are depleted in Mg compared to the expected Mg content from inorganic calcite precipitates (see inserted rectangular in Fig. 5-36). Others like the cephalopods, whose skeleton is made of aragonite, have therefore depletions in Sr.

Furthermore bryozoa, pelecypods, gastropods and calcerous algues consist of a calcite and aragonite mixture.

Other organism like asteroids, crustaceans, ophiuroids, calcitic sponges (Morse and Mackenzie, 1990 and references therein) plot in the same area as inorganic calcium carbonates like e.g. from the present study and stalagmites and stalactites (Huang et al., 2001). These organisms show no or a smaller depletion of Mg and may have smaller vital effects. Aragonitic sclerosponges, aragonite corals (both: Rosenheim et al., 2005 and references therein) and scleractinian corals (Mackenzie et al., 1983 and references therein) have a similar Mg and Sr incorporation into their aragonitic skeletons as it was observed by inorganic precipitates of e.g. inorganic aragonite (Dietzel et al. 2004 and Gahetani and Cohen, 2006).
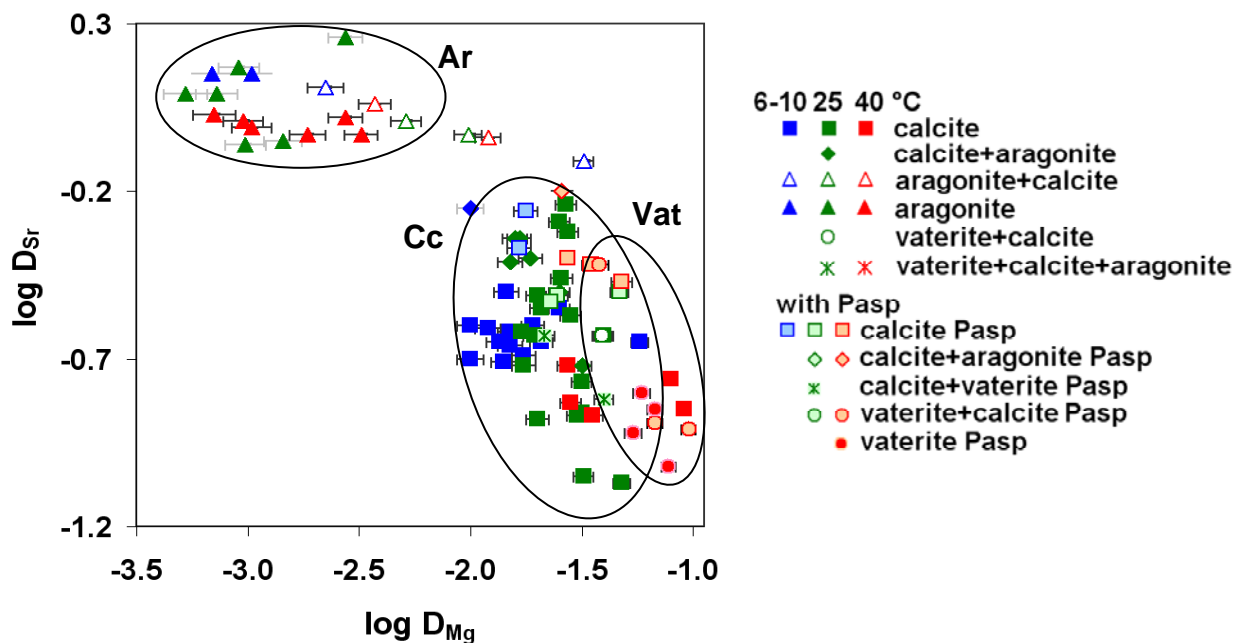
Fig. 5-35: Distribution coefficient of strontium (D_{Sr}) vs. distribution coefficient of magnesium (D_{Mg}) between CaCO$_3$ and solution.
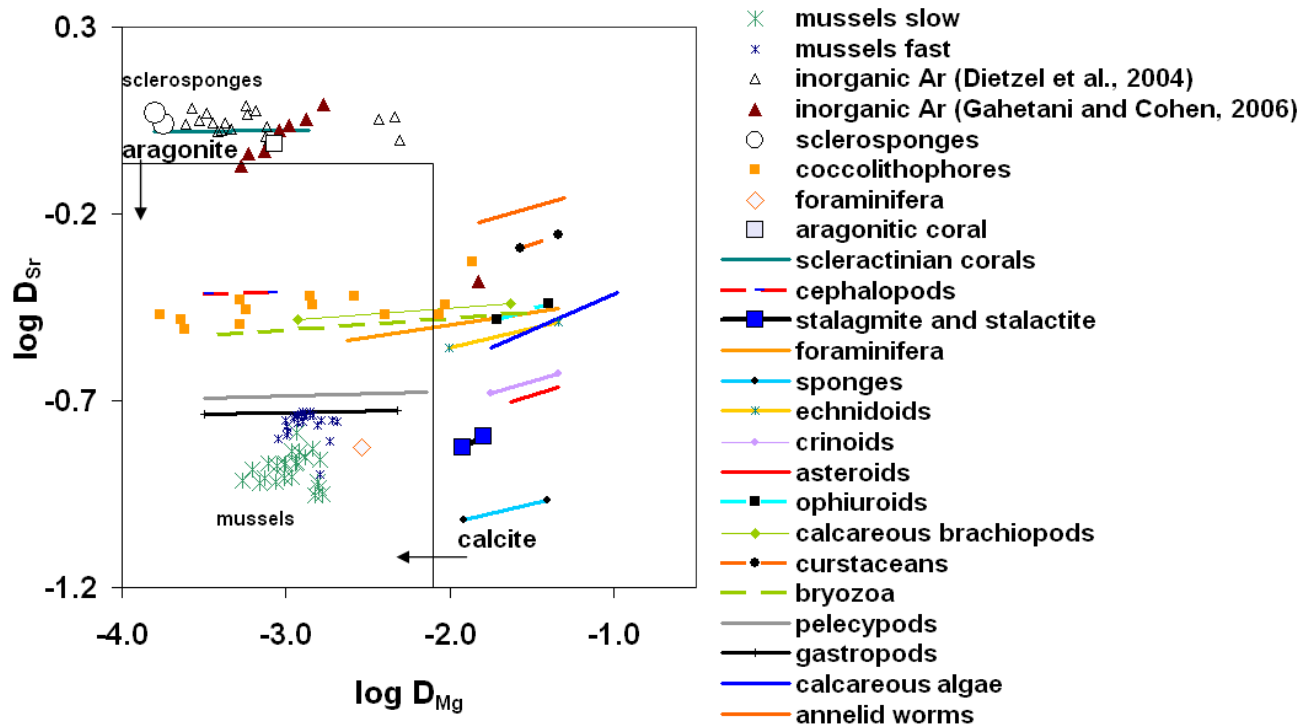
Fig. 5-36: Distribution coefficient of strontium (D_{Sr}) vs. distribution coefficient of magnesium (D_{Mg}) between CaCO$_3$ and solution. No inorganic precipitated CaCO$_3$ of these study (see Fig 5-35) plots in the area below the inserted rectangle as well as published data of e.g. stalagmites and stalactites (Huang et al., 2001), inorganic aragonite (Dietzel et al. 2004 & Gahetani and Cohen, 2006). Several organisms plot in the aragonite zone (upper left corner) like aragonitic sclerosponges, aragonite corals (both: Rosenheim et al., 2005 and references therein), scleractinian corals (Mackenzie et al., 1983 and references therein). Other organisms plot into the calcite field (lower right corner) at higher Mg concentrations like asteroids, crustaceans, ophiuroids, calcitic sponges (Morse and Mackenzie, 1990 and references therein). But further organisms plot in the range where no inorganic calcium carbonate was precipitated: mussels (Klein et al., 1996), gastropods, pelecypods, bryozoa, cephalopods, echinoids, crinoids, calcareous algae, calcareous brachiopods, annelid worms (all: Morse and Mackenzie, 1990 and references therein), coccolithophores (Müller et al., in press) and foraminifera (Morse and Mackenzie, 1990; Rosenheim et al., 2005 and references therein). Latter organisms may have a selective cation uptake or vital effects to explain either the low Mg content of calcite or low Sr uptake of aragonite (see text). In case of the data of Morse and Mackenzie (Morse and Mackenzie, 1990) the sea water (Millero, 2004) composition was used for aqueous Sr, Mg and Ca.

5.10 Calcium isotopic fractionation

5.10.1 Calcite and Mg-calcite

The calcium isotopic fractionation between calcite and aqueous Ca ions $\Delta^{44/40}Ca_{Cc\text{-}aq}$ (definition see section 2.8.4) increases with decreasing temperature and increasing precipitation rate (Fig. 5-37) which is in accordance with the data and model of Tang et al. (2008a) and model of DePaolo (2011). Tang et al. (2008a) have used the surface entrapment model from Watson (2004) to explain the isotopic fractionation behaviour during calcite formation. This model is based on an enrichment of ^{40}Ca in the surface layer compared to the solution and solid phase and ion diffusion processes. Faster dehydration and diffusion of ^{40}Ca cause an enrichment of ^{40}Ca in the surface layer due to weaker bonds between ^{40}Ca and the oxygen ions in its hydration sphere compared to ^{44}Ca-O$_{water}$ (see also Gussone et al., 2003). The water molecules remain for a shorter residence time in the hydration sphere of ^{40}Ca (for H$_2$O-Ca residence time see Bruneval et al., 2007; Raiteri et al., 2010). But ^{40}Ca

has also weaker bonds to the crystal lattice and it can be easier removed from the surface layer. At low temperature the residence time of H_2O in the hydration sphere of Ca is larger (e.g. 122 ps at 27°C) compared to that at high temperate (e.g. 40 ps at 92°C; Bruneval et al., 2007). Additonally the diffusion rates of Ca and hydrated Ca are slower at low temperature compared to that at high temperature. In consequence the difference in the uptake of ^{44}Ca and ^{40}Ca will be even higher at low temperature. ^{40}Ca remains also longer at the surface layer of the calcite at low temperature due to smaller vibration energies, so that ^{40}Ca removes slowlier and the balancing in ^{40}Ca and ^{44}Ca is smaller. Both processes cause a larger fractionation at low temperature as it was observed in this study (see Fig.5-37a) and by Tang et al. (2008a). Latter authors have assumed that the $^{44/40}$Ca fractionation between the solid and the aqueous solution becomes 0 ‰ at equilibrium. As ^{40}Ca is faster entrapped at the surface layer, it is also faster removed from the surface layer than ^{44}Ca due to the weaker bonds. As long as enough time is available to reach nearly isotopic equilibrium the isotopic fractionation remains small. The faster ^{40}Ca uptake compared to the ^{44}Ca uptake becomes dominant and larger Ca isotopic fractionation occurs at fast precipitation rates. At higher temperature the precipitation rate effect is smaller due to faster diffusion and removal processes of ^{40}Ca in and from the surface layer.

By comparison of Figs. 5.37a and b, a slight shift to smaller precipitation rates at a given Ca isotope fractionation in presence of Mg is observed. This may be caused by high specific surface areas of Mg-calcite, although not the whole surface area is reactive. Some areas are inhibited or grow more slowly (see section 5.7.1 and references therein). The plot of the Ca isotopic fractionation vs. Mg (Fig. 5-38a and b) indicates an elevated fractionation between ^{44}Ca and ^{40}Ca in the latter formed calcite at higher Mg concentrations in the solution (Fig. 5-38a and b). This might be partly caused by the higher supersaturation and higher total precipitation rate in the presence of Mg. The effects of precipitation rate and temperature are much larger than the effect of Mg under the investigated conditions.
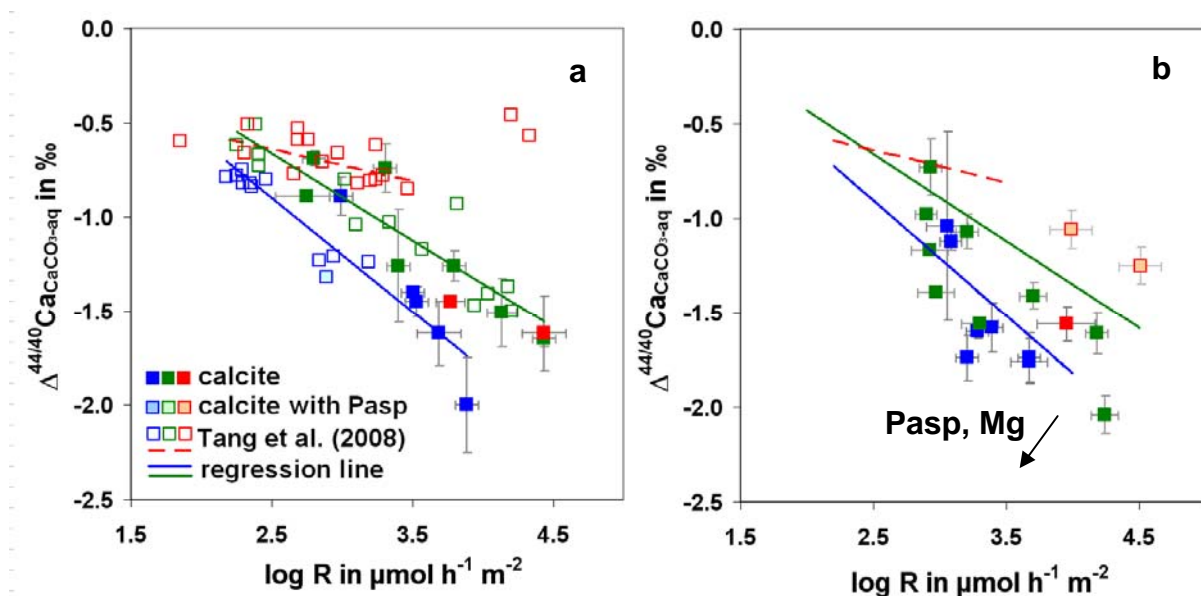
Fig. 5-37: Calcium isotopic fractionation of ^{44}Ca/^{40}Ca between calcite and aqueous Ca vs. precipitation rate in (a) at [Mg]/[Ca] ≤ 0.05 mM and (b) at [Mg]/[Ca] > 0.05 mM in the solution. Pasp influenced CaCO$_3$ precipitation is given by a brighter interior in both diagrams. For the legend see in (a), different colours indicate experiments at different temperatures (5 – 10°C blue, 25°C green and 40°C red).

In contrast, the $^{44/40}$Ca isotopic fractionation is slightly smaller in presence of Pasp (Fig. 5-38b) under similar growing conditions. The reason may be (i) the larger surface area, although also supersaturation with respect to calcite is higher if Pasp is present.

But the larger surface area is more dominant and the samples are shifted to the right at the $\Delta^{44/40}$Ca$_{Cc-aq}$-log R plot. The reactive surface area is again lower than the determined surface area. Thus the Pasp influenced solids plot on the left side of the $\Delta^{44/40}$Ca$_{Cc-aq}$-log R line. Adsorbed Pasp on calcite surface may also influence the complexation and dehydration of ^{40}Ca and ^{44}Ca on the surface. Furthermore as indicated in section 5.8.1 distinct faces incorporate different concentrations of trace elements and most probably fractionate also Ca isotopes in a different way. Dickson (1991) found e.g. also a different $^{13/12}$C- and $^{18/16}$O- isotopic composition at distinct faces of calcite. The stronger interaction of Pasp with specific faces like (0001) and ($1\overline{1}00$) (see section 2.6.1) may result in a slightly different $^{44/40}$Ca fractionation compared to Pasp free calcite.
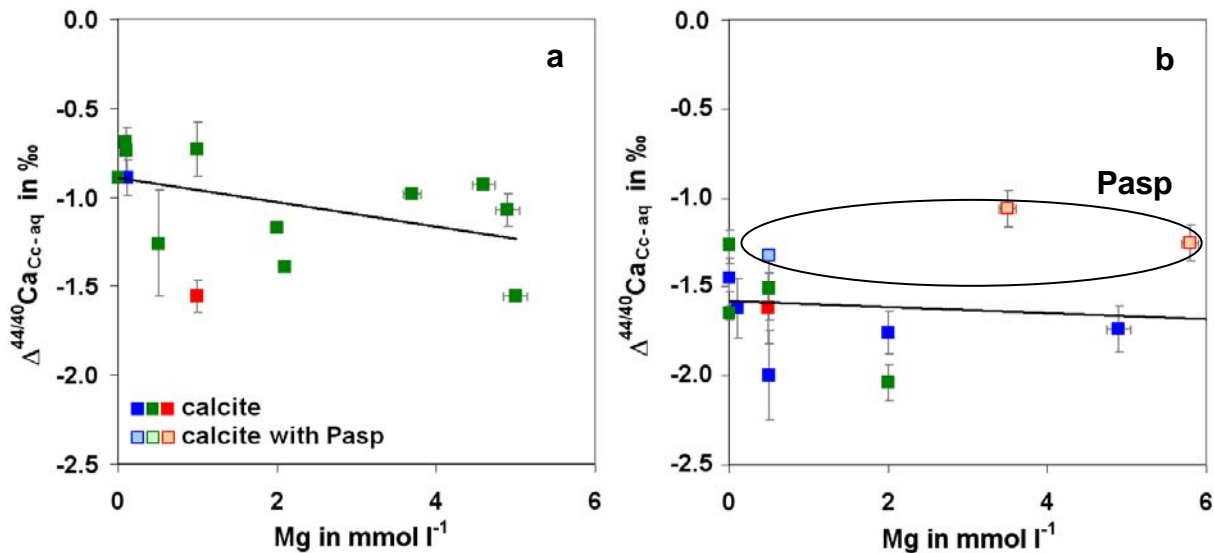
Fig. 5-38: Calcium isotopic fractionation between calcite and aqueous Ca ($\Delta^{44/40}$Ca$_{Cc-aq}$) vs. Mg concentration in the solution at (a) low precipitation rates (for 2mm PE membrane thickness) and (b) high precipitation rates (for 0.2 mm PE membrane thickness).

Moreover, Mg and Pasp influence the different steps (acute, obtuse side) differently and therefore one of the isotopes might be promoted by the lower inhibition of its preferred face/step. The variation in the saturation degrees (Wasylenki et al., 2005) and $[Ca^{2+}]/[CO_3^{2-}]$ ratios (Larsen et al., 2010) influence also the individual growing velocity of different steps. Different steps may have different $^{44/40}$Ca uptake rates as they have also different Sr and Mg incorporation (see section 5.8.1) so that the change in the growing velocity by e.g. $[Ca^{2+}]/[CO_3^{2-}]$ ratios, [Mg] and [Pasp] may also alter the $^{44/40}$Ca fractionation between calcite and solution indirectly.

Analyses of the spatial distributions of the Ca-isotopic on the surface by e.g. Tof-SIMS or similar methods are therefore of large interest for further studies.

However the effect of Pasp on the isotopic fractionation is small compared to the effect of precipitation rate and temperature and also Mg. Ca isotopic fractionation is therefore less influenced than Sr incorporation in calcite.

5.10.2 Aragonite

In general, the calcium isotopic fractionation between aragonite and aqueous Ca ions is significantly larger at low precipitation rates than the isotopic fractionation between calcite and Ca^{2+} ions (Fig. 5-39). Gussone et al. (2005) found also an enrichment in ^{44}Ca in calcite compared to aragonite and argued by a 60% stronger bond strength between Ca and O in calcite compared to aragonite (Zheng, 1999), because the vibration behaviour is different in the nine fold coordinated aragonite vs. six fold coordinated calcite (Gussone et al., 2005; Marriott et al., 2004 and Zhang et al., 1988). These two polymorphs might have also different surface characteristics which results into distinct Ca isotopic fractionations (Gussone et al., 2005).

The difference between the calcium isotopic fractionation during aragonite and calcite formation becomes smaller with increasing precipitation rate and insignificant in the precipitation rate range from $10^{3.5}$ to 10^5 μmol m^{-2} s^{-1} (Fig. 5-39). This is mainly caused by the precipitation rate dependency of the calcium isotopic fractionation between calcite and solution. In contrast, Ca isotope fractionation during aragonite formation have a reverse dependency on the precipitation rate and depend rather not on the precipitation rate at 40°C in the range from 10^2 to 10^4 μmol m^{-2} s^{-1}. A slightly positive correlation between $\delta^{44}Ca$ of aragonite and log R is obtained at 25°C. The two samples at R of up to 10^5 μmol m^{-2} s^{-1} and 40°C with the dipyramidal shape might be influenced by calcite growth due to the low Mg concentration in the solution. Furthermore the sample marked by brackets has larger inhomogeneities within the sample as it was observed by larger variations of its $\Delta^{44/40}Ca_{Ar-aq}$ values by repeated measurements.

The tendency to lower Ca isotopic fractionation during aragonite formation with increasing precipitation rates at 25°C might be caused by a change of the surface characteristics and lattice parameter.

Spicular aragonite samples had a lower Ca isotopic fractionation than the dipyramidal shaped aragonite (Fig. 5-39) and this spicular aragonite were grown at lower precipitation rates. Although the spicular aragonites are very small and have therefore a similar specific surface area (about 1.5 m^2 g^{-1} at 25°C and 0.5 to 16 m^2 g^{-1} at 40°C) compared to the dipyramidal shaped aragonite as latter have a high surface roughness (0.5 to 5 g m^{-2} at 25°C and 0.9 at 40°C), but a different reactive surface area can be observed between spicular and dipyramidal shaped aragonite. Spicular crystals grow mainly linearly in direction of the length axis on the small bottom and top side of the crystal and have therefore a small reactive surface area, while dipyramidal crystals grow also perpendicular to the length axis. The small reactive surface area of the spicular aragonite might result into a smaller isotopic exchange rate between solution and the surface layer of aragonite. Thus the light ^{40}Ca can not escape sufficiently fast before it is bound in the crystal according to the surface entrapment model (Tang et al., 2008a) or kinetic surface reaction model (Depaolo, 2011).
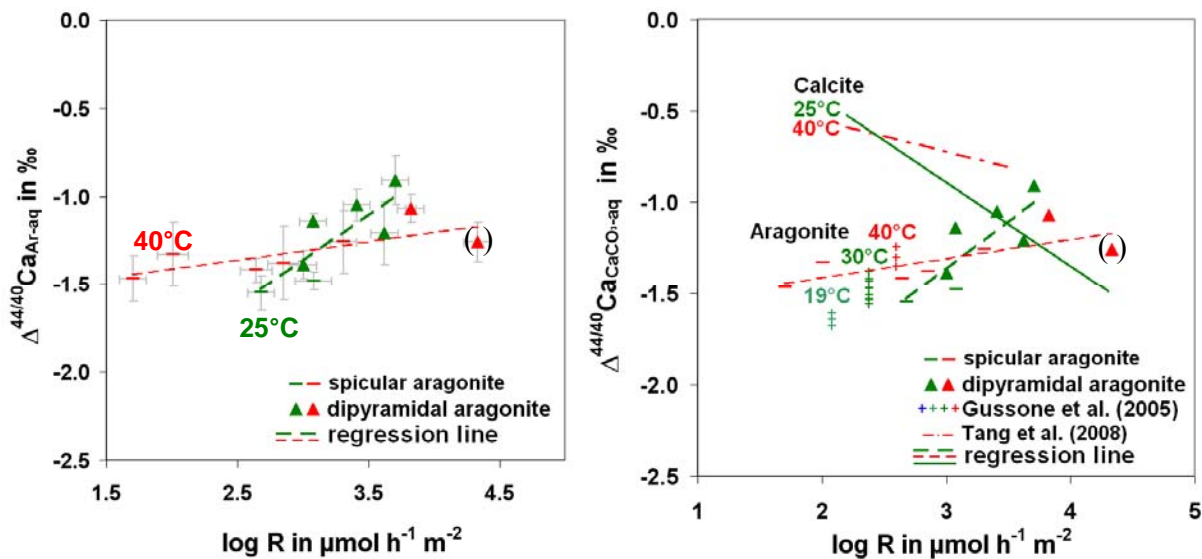
Fig. 5-39: Fractionation of $^{44/40}$Ca between aragonite and aqueous Ca ions vs. precipitation rate R at 25°C (green) and 40°C (red). (a) Error bars give the standard deviation of 3 replicates (experiment 23, 24 and 27) and 2 σ of the Ca isotopic measurements, respectively (b) Related equations from calcite precipitation experiments by Tang et al. (2008) are plotted as solid lines for comparison and + are aragonites from Dietzel et al. (2008) with precipitation rates from Gussone et al. (2005) for the same experiments. This precipitation rates might be slightly overestimated due to small surface area which was used by Gussone et all. (2005). The sample in brackets might be inhomogeneous due to large variations in the measured Ca isotopic composition at different sample parts and measurements.

The growth mechanisms as well as the cell size (see section 5.8.2) of these two types of aragonite are most probably different. Faster escape of ^{40}Ca from the aragonite crystals with larger cell sizes would also be in accordance with the results. Larger cell sizes combined with more Sr distortions at the dipyramidal aragonite crystals result into smaller bound energies which makes ^{40}Ca escape from the surface more easily. The inverse rate effect of aragonite might be caused in consequence by a change in the growth mechanisms, which is in accordance with the significant higher precipitation rate, change in the morphology and larger cell size (sections 5.5, 5.7.1, 5.8.2) at elevated saturation degrees with respect to aragonite. At elevated saturation degrees and therefore elevated precipitation rates additionally nucleation on the surface or aggregation of very small particles may cause less ^{40}Ca enrichment, when these small particles are already in Ca isotopic equilibrium before they are attached to the surface (see Fig. 5-11k). This Ca isotopic equilibrium of the small particles might be caused by their large surface area to volume ratio. Furthermore other processes are responsible for the calcium isotopic fractionation between small CaCO$_3$ particles and solution as polynuclear growth with surface nucleation may be the dominant process instead of regular crystal growth.

Precipitation rate influences the temperature dependency of Ca isotopic fractionation between aragonite and solution slightly (Fig. 5-39 and Fig. 5-40). However the temperature can be reconstructed (but with a small resolution) by Ca isotopic fractionation between aragonite and the solution as long as the biologic species (Fig. 5-40) are considered and/or the same physicochemical conditions (e.g. membrane thickness and chemical composition, Gussone et al., 2003 in Fig. 5-40) are used. Each species has to be investigated and treated separately due to their different precipitation mechanism and physicochemical conditions, as temperature dependent parameters like

the precipitation rate are involved. Within one species this temperature dependent parameters just amplify or attenuate the temperature effect due to the depency of e.g. the precipitation rate on the temperature. The effect of the temperature on the Ca isotopic fractionation is therefore amplified indirectly over the precipitation rate like e.g. in Gussone et al. (2003). Elevated temperature causes also a higher precipitation rate, because carbonate is faster accumulated if all other physiochemical parameters (chemical composition and membrane thickness in the experiments, see Fig. 5-5 and Tab. A4) are constant. At elevated temperature as well as at elevated precipitation rates a smaller calcium isotopic fractionation between aragonite and solution was observed (see Fig. 5-39). Organisms of one species have often similar formation conditions (e.g. carbonate accumulation mechanism) and temperature effect on various parameters like e.g. precipitation rate might simply amplify or attenuate the direct temperature effect on calcium isotopic fractionation. Such organisms within one species should plot on one line. The $\Delta^{44/40}Ca_{CaCO_3-aq}$ -T slopes and positions of different species may vary with the amplification and attenuation of the temperature effect by additional temperature dependent parameters (e.g. R) which influence also the Ca isotopic composition besides to the vital effects.
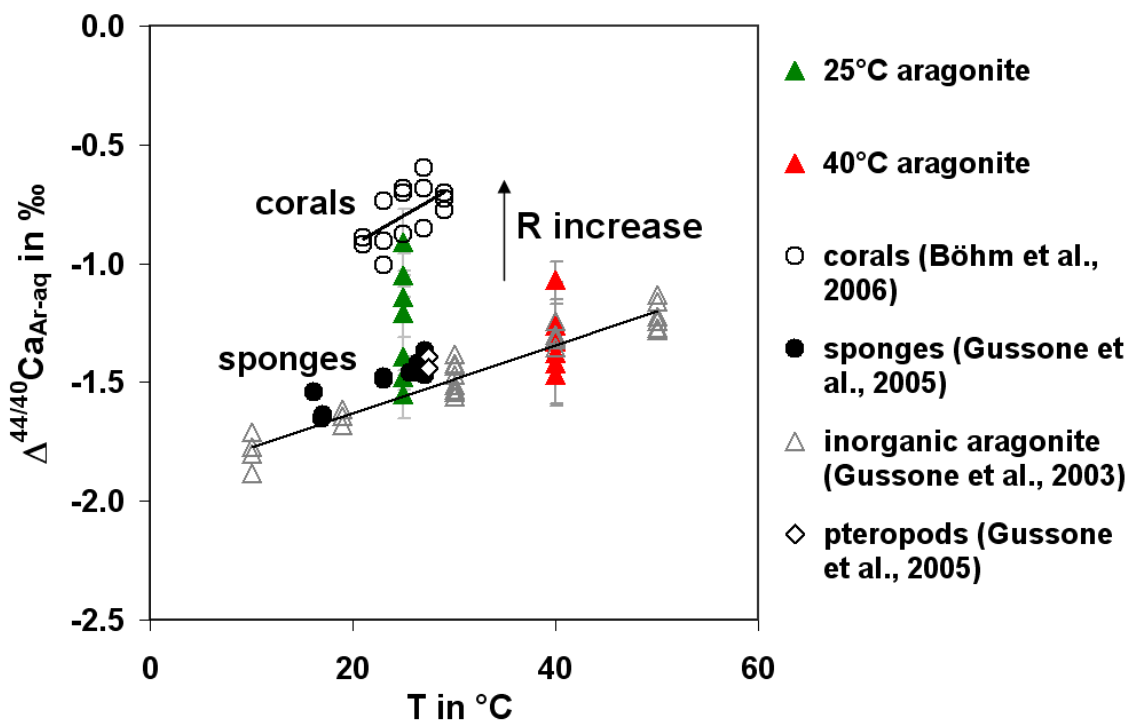
Fig. 5-40: Fractionation of $^{44/40}$Ca between aragonite and aqueous Ca ions vs. temperature in comparison with inorganic aragonite data from Gussone et al. (2003) and biogenic aragonite formed by corals (Böhm et al., 2006) sponges and pteropods (Gussone et al., 2005). Fig. 5-39 indicates a decrease in the Ca isotopic fractionation with increasing precipitation rate (R) in inorganic aragonite samples.

5.10.3 Vaterite

Precipitation of vaterite results in a significantly smaller Ca-isotopic fractionation ($\Delta^{44/40}Ca_{vat-aq}$ = -0.10 to -0.55 ‰) compared to the calcite ($\Delta^{44/40}Ca_{Cc-aq}$ = -0.69 to -2.04 ‰) and aragonite ($\Delta^{44/40}Ca_{Ar-aq}$ = -0.91 to -1.55 ‰) (Fig. 5-41). Ca isotopic fractionation for vaterite formation increases slightly with increasing precipitation rate, although further experiments are required to verify this correlation. Moreover, it has to be pointed out that precipitation of vaterite is obtained by the addition of Pasp, except the experiment with the smallest isotopic fractionation and smallest precipitation rate. However, the proposed precipitation rate effect on the Ca isotopic fractionation is similar to that for calcite.
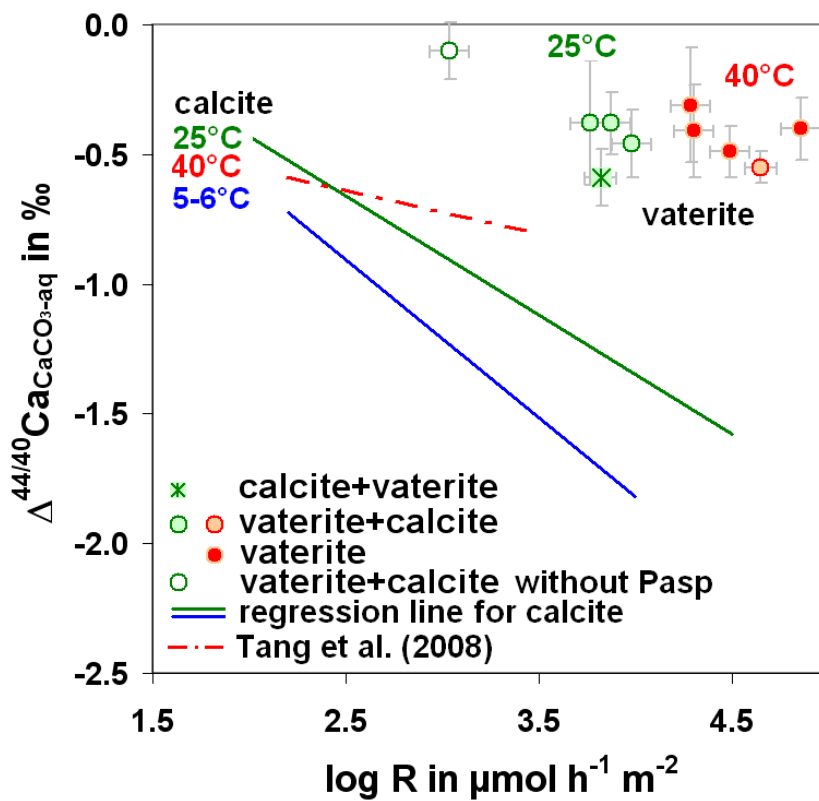
Fig. 5-41: Fractionation of $^{44}Ca/^{40}Ca$ between vaterite and aqueous Ca ions vs. precipitation rate R at 25°C (green) and 40°C (red). Related equations from calcite precipitation experiments by Tang et al. (2008) are plotted as solid lines for comparison.

The low Ca isotopic fractionation during vaterite formation may be due to the "open" structure of vaterite with slight disordering and larger O-O distances between the carbonate ions (Lippmann, 1973, Wang and Becker, 2009; see also discussion in 5.6.2). Consequently, elevated ion diffusion rates in the boundary surface layer may be valid. Thus according to the surface entrapment model of Watson (2004) and Tang (2008) less Ca isotopic fractionation can found for vaterite compared to calcite at a certain precipitation rate. Weaker bonds of Ca in the vaterite lattice (Gopinath et al., 2002, see also section 2.5.4) and most probably also in the surface facilitate the removal of ^{40}Ca from the surface and cause therefore also the smaller Ca isotopic fractionation and a faster equilibration of ^{44}Ca and ^{40}Ca between the solid and the solution.

Another possibility would be the explanation by the growth mechanism as followed:

As discussed in section 5.7.2 the vaterite crystals might be formed by oriented aggregation of very tiny plates like it is indicated by the morphology (see e.g. Fig. 5-14b and o) and proposed by Xu et al.(2006a) for vaterite growth with such morphology. These small particles have a large surface to volume ratio and are therefore most probably in isotopic equilibrium with the solution. In consequence a small or no Ca isotopic fractionation should occur. This is in accordance with the measured Ca isotopic fractionation of the vaterite samples and can occur even at high precipitation rates because the small particles need a very short equilibration time, especially when the open structure of vaterite is considered.

The effect of Pasp, temperature and precipitation rate on Ca isotope fractionation between vaterite and aqueous Ca can only be proposed due to the lack of data. As discussed above (section 5.5) an elevated temperature cause a shift to higher saturation degrees and in consequence to higher precipitation rates while the measured Ca isotopic fractionation was similar. In case of the suggested precipitation rate effect on Ca isotopic fractionation this would mean a smaller ^{44}Ca-^{40}Ca isotopic fractionation at 40°C in accordance with the ^{44}Ca-^{40}Ca isotopic fractionation in calcite.

5.10.4 Polymorphs in comparison

Comparison of all polymorphs indicates clearly smaller ^{40}Ca depletion during formation of vaterite compared to that during formation of calcite and aragonite (Fig. 5-42). Vaterite has a calcium isotopic fractionation $\Delta^{44/40}$Ca value between -0.1 and -0.5 ‰. However, the precipitation rate and temperature effects on the calcium isotopic fractionation for vaterite seem to be similar to that of calcite, whereas the signatures of aragonite react different in regard to the temperature and precipitation rate effect. The difference between aragonite vs. calcite and vaterite is in accordance with the different surface composition of these minerals as it was analysed with X-ray photoelectron spectroscopy by Gopinath et al. (2002). Aragonite has a significant smaller Ca content (15.5 instead of 18.2 and 18.1%) and higher O content (65.8 instead of 63.4 and 62.2%) on the surface than calcite and vaterite, while the Ca concentration at the surface of calcite and vaterite are nearly similar (Gopinath et al., 2002). The higher Ca content may increase the possibility for ^{40}Ca exchange in the surface layer. Furthermore the different speciation will influence the Ca isotopic fractionation behaviour in regard to the precipitation rate effect most probably differently, as different surface species composition allow the dissolution and escape of ^{40}Ca from the surface more easily than other species compositions.

All three polymorphs indicate furthermore a smaller dependency of the calcium isotopic fractionation on the precipitation rate at 40°C compared to 25°C. Although for vaterite more experiments are necessary to evaluate this behaviour (Fig. 5-42).

The significant different Ca isotopic fractionations between the solution and the polymorphs indicate the importance of the calcium carbonate surface layer and growth mechanism besides to dehydration processes.
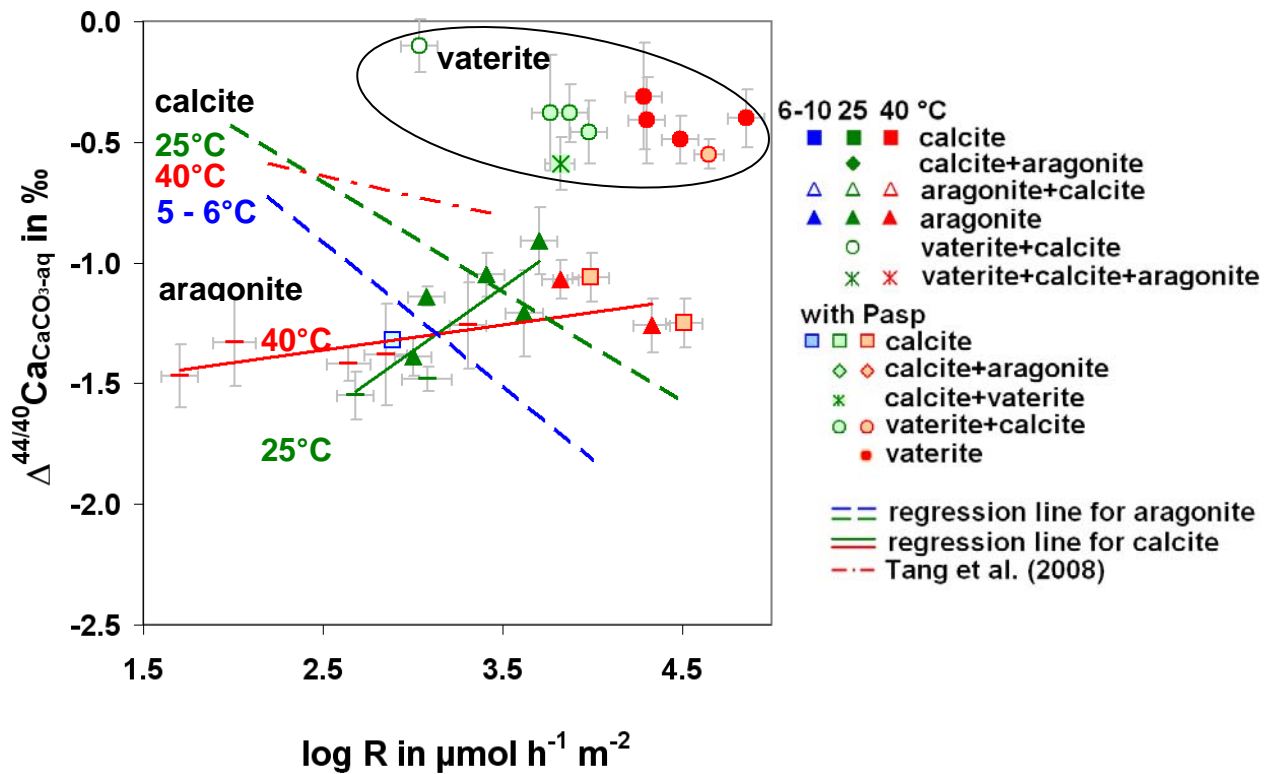
Fig. 5-42: $^{44}Ca/^{40}Ca$ **fractionation between CaCO$_3$ and aqueous Ca ions vs. precipitation rate. Symbols indicate the different CaCO$_3$ phases in the solid samples and the presence of Pasp in the solution (see legend). Colours indicate experiments at different temperatures (5 – 10°C blue, 25°C green and 40°C red).**

Interestingly, calcium carbonate polymorphs can be well distinguished in the $\Delta^{44/40}Ca$ - log D_{Sr} diagram (Fig. 5-43). Moreover, Pasp affected calcite precipitates has a distinct range in Fig. 5-45. These findings may be used to decipher polymorph transformation and alteration processes and to evaluate so-called "vital effects" during biomineralization.

The Sr incorporation and Ca isotopic fractionation during CaCO$_3$ formation for several organisms (foraminifera) may be affected by the organic molecules such as Pasp. Organisms like foraminifera, brachiopods, blue mussels and coccolithophores plot with their Sr concentration and Ca isotopic fractionation in the range of Pasp affected calcites in Fig. 5-44. This indicates that organic substances like Pasp might be involved during CaCO$_3$ formation of these organisms.

The $\Delta^{44/40}Ca$ - log D_{Sr} values of aragonitic sponges are similar to the values of synthetic aragonites of the present study and that of Dietzel et al. (2004) combined with Gussone (2005) (Fig. 5-44). This may indicate the dominance of the inorganic precipitation in the aragonitic sponges. The $\Delta^{44/40}Ca$ - log D_{Sr} values of aragonitic mussels plot in the field of the Pasp affected calcites or aragonite- calcite mixtures and may indicate vital effects in the aragonitic mussels or phase transformations. The $\Delta^{44/40}Ca$ - log D_{Sr} composition of aragonitic mussels is therefore not only influenced by the growth of aragonite.
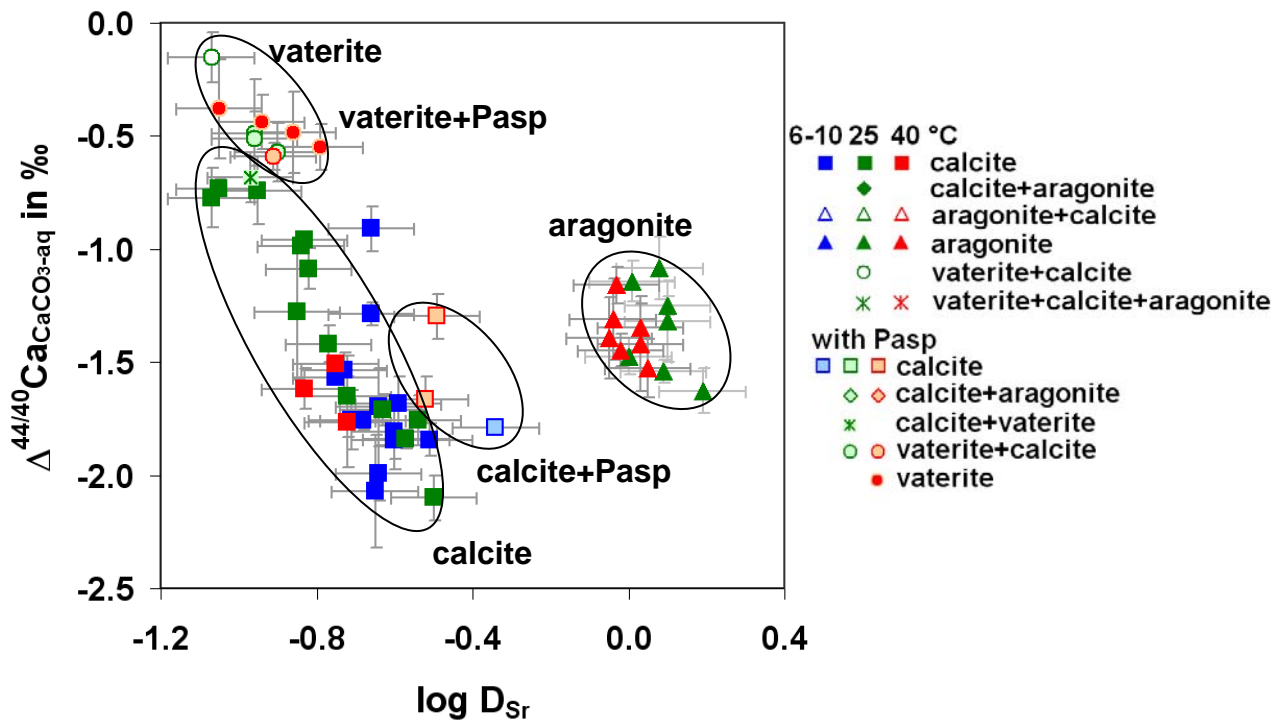
Fig. 5-43 Calcium isotopic fractionation between CaCO₃ and aqueous Ca ions vs. Sr distribution coefficient for CaCO₃ polymorphs with and without Pasp. Different symbols indicate the different phases and the presence of Pasp (see legend). Colours indicate experiments at different temperatures (6 – 10°C blue, 25°C green and 40°C red).
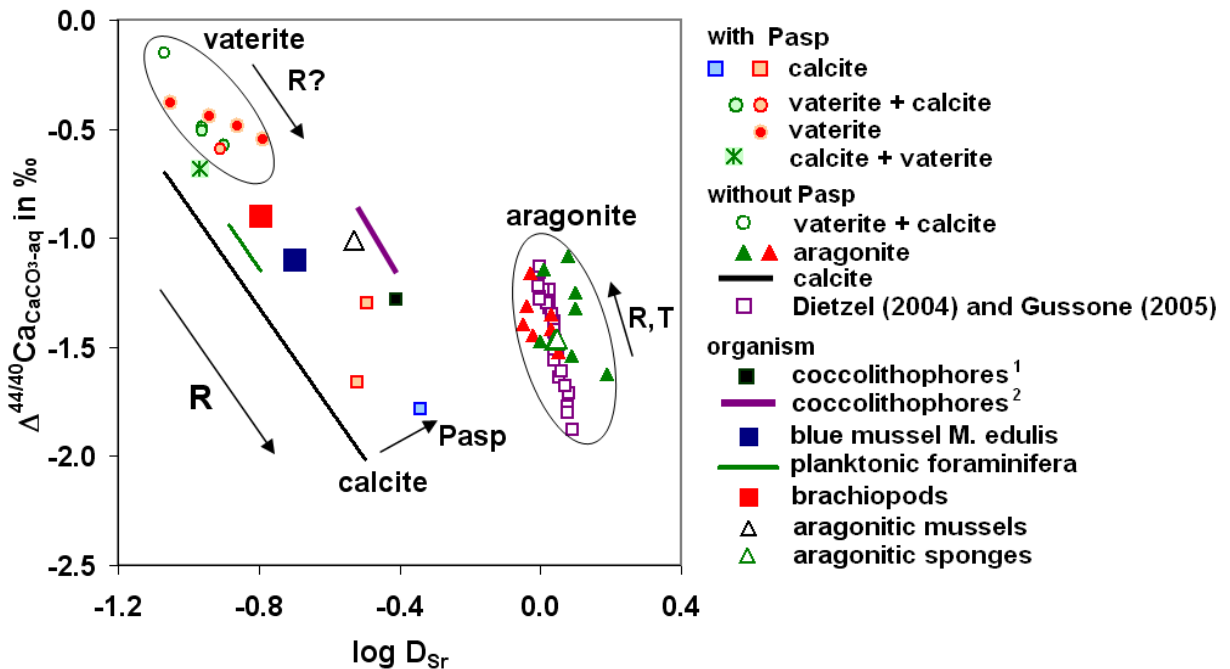
Fig. 5-44: Calcium isotopic fractionation between CaCO₃ and aqueous Ca ions vs. Sr distribution coefficient in comparison with literature data: synthetic aragonite (Gussone et al., 2003; Dietzel et al., 2004), planktonic foraminifera (Kisakürek et al., 2011), coccolithophores[1] (Langer et al., 2006, Langer et al., 2007), coccolithophores[2] (Müller et al., in press), blue mussels (Heinemann et al., 2008), brachiopods (Farkaš et al., 2007a), aragonitic sponges (Haase-Schramm et al., 2003 and Gussone et al., 2005) and aragonitic mussels (Heinemann et al., 2008).

5.11 Comparison of the field and laboratory study

Investigations of a spring in Wolfsgraben indicate calcite precipitation at a [Mg]/[Ca] ratio of 0.76, a temperature of 8.6 to 9.6°C and a saturation degree with respect to calcite, Ω_{Cc}, of about 5. This calcite formation at the Wolfsgraben under the given physicochemical condition is in good accordance with laboratory experiments under similar conditions (see Tab.A1 vs. A4). The variation of the Ω_{Cc} is about ±0.1 along the flow path of 45 m, so that the effect of CO_2 degassing and $CaCO_3$ precipitation compensate each other. According to the evolution of the chemical data no measureable $CaCO_3$ precipitation occurred at $\Omega_{Cc} \leq 2.5$ at the Wolfsgraben spring. This Ω_{Cc} limit for calcite precipitation is nearly similar or slightly lower than Ω_{Cc} obtained in the laboratory experiments for spontaneous calcite precipitation. In the field solid calcium carbonate is already present which allows heterogeneous $CaCO_3$ formation at lower Ω_{Cc} values.

The [Mg]/[Ca] ratio of 0.8, temperature of 10.4°C and saturation degree in respect to calcite Ω_{Cc} of 35.5 in the drainage system of the Spital tunnel results in a high precipitation rate, R of about $10^{3.5}$ μmol h^{-1} l^{-1}. A similar range (3 to 3.5) was estimated from the laboratory data in Fig. 5.8. The high saturation degree and especially the high $[CO_3^{2-}]/[Ca^{2+}]$ concentration and presence of Mg should have caused aragonite formation according to extrapolation of the data of the laboratory experiments (Fig. 5-10). Accordingly, XRD analyses of the precipitated solids from this drainage indicate also small proportions of aragonite. The Ω_{Cc} value decreases along the flow path by 0.5 in contrast to the spring in Wolfsgraben where it was constant along the flow path. The drop is caused by the precipitation of $CaCO_3$ which is not compensated by degassing of CO_2 and results into a pH change of 1 along the flow path.

5.12 Implication for natural environments and technical applications

The experimental results of the present study can be directly applied to systems, where the CO_3^{2-} concentration is low compared to that of [Ca] and where carbonate ions are continuously accumulated to reach a critical saturation degree with respect to $CaCO_3$ phases in a homogeneous solution. Obviously, in most common natural systems the CO_3^{2-} concentration is low and that of Ca is relatively high, like for seawater ($[CO_3^{2-}]$ = 0.27 mmol l^{-1}, [Ca] = 10.4 mmol l^{-1}; Garrels and Thompson, 1962). Similar CO_3^{2-} concentrations at the time of first $CaCO_3$ precipitation were reached in our experiments in the presence of Mg and Pasp. Furthermore, in experiments with Pasp or moderate to high CO_2 diffusion rates (log (D_{CO_2av}) > $10^{1.5}$ μmol h^{-1}) similar physicochemical conditions at the time of first $CaCO_3$ precipitation are valid as estimated in cells of corals ($\Omega_{Ar\ coral}$ = 3 (dark) to 25 (light); Al-Horani et al., 2003) and foraminifera vacuoles ($\Omega_{Ar\ Foram.}$= 9 to 14; Erez, 2003).

Our CO_2 diffusion technique at pH stat. conditions can be used to simulate CO_3^{2-} accumulation e.g. in coral coelenterons, where H^+ is actively pumped out of the cell by using ATPase enzymes. Consequently, CO_2 diffuses into the calcifying fluid and reacts with OH^- to form CO_3^{2-} (Al-Horani et al., 2003). The reaction of incoming CO_2 with OH^- continues until the critical IAP_{fp} for $CaCO_3$ formation is reached. The composition of the calcifying fluid of the corals can range from [Ca] = 10.6 to 10.2 mmol l^{-1} and pH from 8.13 to 9.28 with and without light exposure, respectively (Al-Horani et al., 2003). Considering our experimental results, it is suggested that such organisms may control the individual $CaCO_3$ polymorph formation by variation of the carbonate accumulation rates besides using macromolecules like Pasp. It has to be pointed out that Pasp triggers the formation of Mg-calcite even at elevated [Mg]/[Ca] ratios like in sea water.

Pasp is used as an inhibitor for $CaCO_3$ formation in man-made environments. $CaCO_3$ inhibition effects of Pasp can be applied to carbonate sinter formation e.g. in drainage systems of tunnels, where CO_3^{2-} is accumulated by the uptake of gaseous CO_2 into an alkaline solution to reach a critical IAP_{fp}. Our experiments can be used to estimate the dosage of inhibitors and especially to estimate the inhibition time. Mg ions which might be dissolved from dolomitic host rock in subsurface waters causes a slightly larger inhibition effect of Pasp as it was demonstrated in the experiments. The study further more indicates the problematic of systems where the solution is not removed and precipitation takes place by accumulation, because the inhibition causes higher saturation degrees, where finally vaterite is formed. This $CaCO_3$ polymorph is on the one hand more soluble, but on the other hand missing cleavages of calcite result into a harder mechanical removal.

Spherical or coral like morphologies as they occur in nature were obtained in the presence of Pasp at 40°C in case of vaterite formation. It was shown that Pasp (or similar acting organic acid) provoke the formation of massive spherical $CaCO_3$ particles at 40°C. Also the higher Sr incorporation into calcite in presence of Pasp is in accordance with the relatively high Sr concentrations of some organisms (see log D_{Sr}-$\Delta^{44/40}Ca$ plot in Fig. 5-44). These signatures may reveal the importance of Pasp or similar acting macromolecules in the formation of $CaCO_3$ by organisms.

The knowledge how to modify the morphology and shape of aragonite crystals by variation of the saturation degree, Mg and temperature can be applied e.g. for paper coating issues to design $CaCO_3$ products with distinct properties. Furthermore the variation in the lattice parameter *c* of aragonite by Sr incorporation might be important for its mechanical "strength" due to defects, distortions and extension of the lattice. The log D_{Mg}-log D_{Sr} diagram is suggested to distinguish between aragonite and calcite samples easily and to decipher "vital" effects on the elemental incorporation. Aragonite samples plot into the upper left corner of the D_{Mg}-D_{Sr} diagram, whereas calcite and vaterite samples in the lower right corner and mixtures in the upper right corner. No inorganic precipitated calcium carbonate plots in the lower left corner at simultaneously low D_{Mg} and low D_{Sr} values. Mg depletion occurs in several organisms as they are made of calcite and plot into the lower left side of this diagram.

The $^{44/40}$Ca fractionation during $CaCO_3$ formation is suggested to be controlled by the ion diffusion and dehydration of ions on the one hand (forward reactions) and on solid surface processes coupled with growth rates on the other hand (e.g. Depaolo, 2011). Latter is dominated e.g. by how fast the ^{40}Ca isotope can escape from the surface layer vs. how fast it is sealed into the solid structure by overgrowth. Ca isotopes may provide therefore information about the kinetics of surface reactions of the individual polymorphs. Ca isotopic data suggest that the "open structure" of vaterite (e.g. Lippmann, 1973, Wang and Becker, 2009) extends to its surface. The stability of ^{40}Ca on the surface seems to be significantly lower than that of calcite and the removal of ^{40}Ca seems to be faster as the fractionation of $^{44/40}$Ca during vaterite formation is much smaller compared to calcite formation.

6   Summary and conclusions

In the comprehensive experimental part of this thesis the CO_2 diffusion technique was applied to nucleate and precipitate calcium carbonates at a constant pH of 8.3 and calcium concentration of mostly 10 mmol l^{-1} to study the effects of temperature, carbonate accumulation rate (R_{CO_3}), Mg and polyaspartic acid (Pasp) content on the $CaCO_3$ polymorph formation as well as their isotopic and elemental composition. This technique allows the precise determination of ongoing reactions like CO_2 diffusion and $CaCO_3$ precipitation as well as the evolution of the solution chemistry. The detection of the first precipitation is highly accurate down to Ca concentration changes of about only 1 ‰.

The kinetic and chemical evolution of the aqueous solution was followed by the consumption of NaOH (pH stat.) and by chemical analyses of the solution by ICP-OES. Furthermore extensive solid phase characterisation of the precipitates were carried out by spectroscopic (FTIR, Raman, ICP-OES), diffraction (XRD), microscopic methods (SEM, AFM, optical microscope) and mass spectroscopic methods (TIMS, IR-MS). The effect of temperature between 6 and 40°C, carbonate accumulation rate between 0.15 and 320 µmol h^{-1}, Mg up to a [Mg]/[Ca] ratio of 5.2 and Pasp concentration, [Pasp], up to 3.4 mg l^{-1} on the kinetics of calcium carbonate formation and the properties of the resulting polymorphs was tested. Many of these parameters are not independent in their effects and were therefore also investigated in various combinations. (Mg)calcite is formed in the case when Mg and Pasp are simultaneously present, although in the absence of Pasp elevated [Mg] induces aragonite formation, while in the presence of Pasp vaterite precipitates at very low Mg concentrations (≤ 0.01 mmol l^{-1}).

The time of the first $CaCO_3$ precipitation (t_{fp}) is negatively correlated with the temperature and the CO_3^{2-} accumulation rate. In this kind of experiments the CO_3^{2-} accumulation rate is caused by the accumulation and conversion of CO_2 into CO_3^{2-}. The t_{fp} value is strongly increased up to several hundred hours by the presence of Pasp and/or Mg. Interestingly, the t_{fp} value is independent of the formation of distinct $CaCO_3$ polymorphs. This suggests a similar $CaCO_3$ precursor or a similar nucleation mechanism for all $CaCO_3$ polymorphs in our experiments.

The degree of supersaturation with respect to calcite at t_{fp} increases at elevated CO_3^{2-} accumulation rates. In the presence of Pasp supersaturation with respect to monohydrocalcite was required for $CaCO_3$ formation in all experiments, whereas without Pasp the solution was undersaturated with respect to monohydrocalcite at the time of first $CaCO_3$ precipitation in nearly all experiments. First precipitation of vaterite, aragonite and calcite was observed at nearly similar respective saturation degrees $\Omega_{fp} \geq 3$. Similar observations are also obtained in field studies where no significant precipitations occur at Ω_{fp} values below 2.5.

The relation between $CaCO_3$ precipitation rate and ion activity product of Ca^{2+} and CO_3^{2-} at the time of the first $CaCO_3$ precipitation (IAP_{fp}) is independent whether calcite or aragonite was formed. The precipitation rate of $CaCO_3$ from homogeneous solution is determined by the temperature and the IAP_{fp}-value and not by the saturation degree of the individual $CaCO_3$ phases.

The formation of a distinct $CaCO_3$ polymorph was controlled by the CO_3^{2-} accumulation rate (R_{CO_3}) or the $(CO_3^{2-})_{fp}/(Ca^{2+})$-ratio at the time of first precipitation of $CaCO_3$, besides temperature, Mg and Pasp concentration. All four parameters (R_{CO_3}, T, [Mg], [Pasp]) must be considered for the formation of distinct $CaCO_3$ polymorphs. Aragonite is preferentially formed in the absence of Pasp at high [Mg]/[Ca] ratios above 0.2 (40°C) to 2 (6°C), at high R_{CO_3} rates and elevated temperature (40°C). Calcite precipitates preferentially at low carbonate accumulation rates, low [Mg]/[Ca] ratios, low temperature or if both Pasp and Mg are present. Vaterite formation is favoured at R_{CO_3} values above 50 µmol h^{-1}, high [Pasp] and elevated temperature (25-40°C), if Mg is absent. No vaterite was detected in our experiments at a temperature of 6°C. Transformation of precipitated $CaCO_3$ was not found in our experiments within the time periods between the beginnings of the observation (several hours after the first precipitation of $CaCO_3$ occurs) until the end of the experiments.

The crystal habit of calcite is mainly dominated by [Mg], [Pasp] and temperature. Mg inhibits the growth of typically fast growing faces like the $\{01\overline{1}1\}$ faces and stabilise them. Dodecahedrons with rough $\{01\overline{1}1\}$ faces were formed at 6 to 10°C at [Mg]/[Ca] between 0.3 and 0.5 and seldom at 25°C. Furthermore rounded or elongated crystals occur. At 6 to 10°C and [Mg]/[Ca]>0.8 this elongation was caused by the dominance of the $\{01\overline{1}1\}$ faces.

The solid surface becomes generally rougher and stepped in the presence of Mg and Pasp by inhibition or deceleration of the crystal growth (velocity) in mainly two directions (e.g. acute under Mg influence), whereas the deceleration of the other two steps at the surface is small. Rhombohedra crystals with a single step at each edge between the $\{10\overline{1}4\}$ surfaces were formed in the presence of Pasp. The surface of calcite becomes rough and porous under the influence of Pasp, especially on two sides, where also fibrous structures were discovered by AFM. In the presence of both Pasp and Mg and/or at high temperature the typical $\{10\overline{1}4\}$ planes disappear and rounded shaped crystals or crystals with a high number of edges appear.

The morphology and shape of aragonite precipitates is mainly determined by the carbonate accumulation rate or saturation degree. Dipyramidal shaped aragonite crystals with relatively small elementary cell sizes are formed at $\Omega_{Ar\,fp} > 10$ (6°C) to 12 (40°), instead of the formation of spicular aragonite crystals.

The morphology of vaterite varies as a function of temperature and saturation degree mainly due to elevated Pasp concentrations. Platy hexagonal or desert rose like vaterite crystals occur in case of small saturation degrees with respect to vaterite at t_{fp}, $\Omega_{vat\,fp} \leq 10$ at 25°C and at 40°C. Spherical or coral-shaped massive crystals occur at $\Omega_{vat\,fp} > 10$ and at a [Pasp] > 0.4 mg l^{-1} at 40°C. AFM analyses of these vaterite crystals indicate a hilly surface similar to published ACC structures.

Mg incorporation in calcite is not homogenous within a single crystal. Different sides incorporate different levels of Mg. High Mg concentrations correlate with rounded edges and crystals. The Mg incorporation into calcite or vaterite increases at elevated temperatures, higher Mg concentrations and lower precipitation rates. Vaterite and calcite incorporate Mg at a similar level (log D_{Mg}= -1.9 to -0.9), whereas the distribution coefficient of Mg (D_{Mg}) between aragonite and aqueous Mg is up to about two orders of magnitude lower (log $D_{Mg} \approx$ -3).

The elementary cell sizes of calcite and vaterite decreases with increasing Mg concentration. The cell parameters a and c of calcite and those of vaterite decrease both at a similar level as it was verified by Riedveld analyses of XRD pattern. The cell parameter c of aragonite (Pmcn) is (i) positively correlated with Sr, and (ii) inversely correlated with temperature due to the increase in Sr incorporation from log D_{Sr} < 0.05 at 40°C to log D_{Sr} = 0.15 at 6°C. Calcite displays a 1 to 2 orders of magnitude lower Sr incorporation (log D_{Sr} = -1.3 to -0.4) compared to aragonite. Vaterite indicates a slightly higher Sr uptake than calcite (log $D_{Sr} \geq$ -1.1) due to the elevated precipitation rates during vaterite formation. Similar to aragonite, the Sr incorporation into calcite and vaterite is higher at lower temperatures and higher precipitation rates. The presence of Pasp and Mg increases the Sr incorporation into calcite significantly: log D_{Sr} = -0.34 at [Pasp] = 1.6 mg l^{-1}, log D_{Sr} = -0.5 at [Mg]/[Ca] = 1 compared to log D_{Sr} = -0.65 at 6°C at [Mg]/[Ca] = 0.05 in absence of Pasp and all at 6°C. The D_{Mg}-D_{Sr} plot is a useful tool to decipher vital effects during $CaCO_3$ precipitation of organism.

The present study indicates furthermore the importance of the polymorphic composition for the interpretation of the calcium isotopic signatures in calcium carbonates. A significantly lower isotopic fractionation occurs between vaterite and aqueous Ca ions ($\Delta^{44/40}$Ca = -0.10 to -0.55 ‰) than between calcite and aqueous Ca ions (-0.69 to -2.04 ‰) or aragonite and aqueous Ca ions (-0.91 to -1.55 ‰). The difference in the Ca isotopic composition of calcite and vaterite might be caused by the different growth mechanisms of these polymorphs and/or the slightly disordered structure with large O-O distances in vaterite which allows a faster removal of the lighter ^{40}Ca from the vaterite surface.

The large variations in the Ca isotopic composition of calcite are caused by the dominance of the kinetic fractionation during calcite precipitation. Relatively high $^{44/40}$Ca fractionations between calcite and the solution were obtained at high precipitation rates in accordance with Tang et al. (2008). The calcium isotopic fractionation between calcite and aqueous Ca ions is smaller at elevated temperatures and in the presence of Pasp. The effect of the precipitation rate on calcium isotopic fractionation during aragonite is lower than that for calcite. Various carbonate accumulation rates induce different saturation degrees. This may change the Ca isotopic fractionation by structural and surface related effects.

Ca isotopic signatures and Sr concentration of calcites are very useful for the reconstruction of the precipitation rate during formation, especially when the difference in the Sr incorporation between aragonite and calcite are measured and compared. The log D_{Sr} - $\Delta^{44/40}$Ca diagram is useful to decipher the existence and primary formation of $CaCO_3$ polymorphs or the effects of organics like

Pasp. The Mg content e.g in calcite is important to estimate possible effects on Sr incorporation. Furthermore crystallographic effects on Mg and Sr incorporation into $CaCO_3$ (calcite) have to be considered at very high spatial resolved sedimentary climate archives. This may limit the spatial resolution as the zoning and different incorporations of Mg and Sr at different sides have to be accounted. Less Ca isotopic fractionation between $CaCO_3$ and aqueous Ca ions reveal the presence of vaterite, or very slow precipitation rates. Unusual high Sr concentrations in the $CaCO_3$ solids are a hint for an occurrence of aragonite. The log D_{Sr} - $\Delta^{44/40}Ca$ diagram is also very useful for the identification of effects caused by organics like Pasp besides $CaCO_3$ polymorphism. A similar shift to higher Sr incorporation like in foraminifers, brachiopods and other $CaCO_3$ precipitating organisms was found in our experiments in the presence of Pasp. In conclusion, the combination of such parameters within a multiproxy approach might be useful for advanced reconstructions of the paleoenvironmental conditions during $CaCO_3$ formation.

The experimental results of the present study can be applied to natural and man-made systems, e.g. $CaCO_3$ precipitating marine organisms, in a further way. $CaCO_3$ polymorphous type selection can simply happen by the presence of Pasp or by adjusting the rate of CO_3^{2-} accumulation. The former allows the formation of high Mg-calcite, whereas without Pasp aragonite is formed in the absence of seeds. In man-made environments, the inhibition effect of Pasp can be enhanced by Mg. The temperature and the accumulation rate of CO_3^{2-} have to be accounted for the adjustment of Pasp addition as inhibitor for scaling. Respective inhibition times for $CaCO_3$ formation are given by the experimental results. Moreover, tailored $CaCO_3$ polymorphs can be formed under well defined kinetic conditions, which can be applied to conduct further experiments e.g. for the investigation of the REE incorporation behaviour or to crystallize $CaCO_3$ with distinct properties for paper coating industry.

In the field part of this study the kinetics and ongoing reactions were studied at a spring in Wolfsgraben, in the Spital and Koralm tunnel. The precipitation of $CaCO_3$ in the spring was caused by CO_2 degassing and a subsequently increase in pH. In contrast, the precipitation of $CaCO_3$ from highly alkaline solutions of the tunnel drainage is mainly caused by adsorption of gaseous CO_2 as it was also verified by the isotopic and chemical evolution of these solutions. Interestingly the $\delta^{13}C$ signatures of the spring in Wolfsgraben are similar to the published data of the spring in Köttmannsdorf, as well as the isotopic composition after CO_2 degassing. This indicates the similarity in the host rock and the bioactivity in the soil (climate zone) of both springs. In the present study, the reaction kinetics and polymorph formation conditions found in the field are comparable to the experimental results in the laboratory.

7   References

Abdel-Aal N., Satoh K., and Sawada K. (2002) Study of the adhesion mechanism of $CaCO_3$ using a combined bulk chemistry/QCM technique. *Journal of Crystal Growth* **245**, 87-100.

Aizenberg J., Addadi L., Weiner S., and Lambert G. (1996) Stabilization of amorphous calcium carbonate by specialized macromolecules in biological and synthetic precipitates. *Advanced Materials* **8**, 222-226.

Al-Horani F. A., Al-Moghrabi S. M., and de Beer D. (2003) The mechanism of calcification and its relation to photosynthesis and respiration in the scleractinian coral Galaxea fascicularis. *Marine Biology* **142**, 419-426.

Albeck S., Aizenberg J., Addadi L., and Weiner S. (1993) Interactions of various skeletal intracrystalline components with calcite crystals. *Journal of the American Chemical Society* **115**, 11691-11697.

Albeck S., Weiner S., and Addadi L. (1996) Polysaccharides of Intracrystalline Glycoproteins Modulate Calcite Crystal Growth In Vitro. *Chemistry – A European Journal* **2**, 278-284.

Alia J. M., de Mera Y. D., Edwards H. G. M., Martin P. G., and Andres S. L. (1997) FT-Raman and infrared spectroscopic study of aragonite-strontianite ($Ca_xSr_{1-x}CO_3$) solid solution. *Spectrochimica Acta Part A: Molecular and Biomolecular Spectroscopy* **53**, 2347-2362.

Allmann R. (2003) *Röntgenpulverdiffraktometrie*. Springer-Verlag, Heidelberg.

Andersen F. A. and Brecevic L. (1991) Infrared Spectra of Amorphous and Crystalline Calcium Carbonate. *Acta Chemica Scandinavica* **45**, 1018-1024.

Antao S. M. and Hassan I. (2009) The orthorhombic structure of $CaCO_3$, $SrCO_3$, $PbCO_3$ and $BaCO_3$: linear structural trends. *The Canadian Mineralogist* **47**, 1245-1255.

Antao S. M. and Hassan I. (2010) Temperature dependence of the structural parameters in the transformation of aragonite to calcite, as determined from in situ synchrotron powder x-ray-diffraction data. *The Canadian Mineralogist* **48**, 1225-1236.

Appelo C. A. J. and Postma D. (2006) *Geochemistry, groundwater and pollution*. Balkema, Rotterdam.

Arvidson R. S. and Mackenzie F. T. (2000) Temperature Dependence of Mineral Precipitation Rates Along the $CaCO_3$–$MgCO_3$ Join. *Aquatic Geochemistry* **6**, 249–256.

Aschauer U., Spagnoli D., Bowen P., and Parker S. C. (2010) Growth modification of seeded calcite using carboxylic acids: Atomistic simulations. *Journal of Colloid and Interface Science* **346**, 226-231.

Astilleros J. M., Pina C. M., Fernández-Díaz L., Prieto M., and Putnis A. (2006) Nanoscale phenomena during the growth of solid solutions on calcite $\{10\bar{1}4\}$ surfaces. *Chemical Geology* **225**, 322-335.

Ball J. W. and Nordstrom D. K. (2001) User's manual for WATEQ4F, with revised thermodynamic data base and test cases for calculating speciation of major, trace, and redox elements in natural waters. U.S. geological survey, California.

Beck-Mannagetta P. (1980) Wolfsberg (188)*Geologische Karte der Republik Österreich 1 :50000*. Geologische Bundesanstalt Wien.

Beck R. and Andreassen J.-P. (2010) The onset of spherulitic growth in crystallization of calcium carbonate. *Journal of Crystal Growth* **312**, 2226-2238.

Becker A., Bismayer U., Epple M., Fabritius H., Hasse B., Shi J., and Ziegler A. (2003) Structural characterisation of X-ray amorphous calcium carbonate (ACC) in sternal deposits of the crustacea Porcellio scaber. *Dalton Trans.*, 551-555.

Bentov S., Weil S., Glazer L., Sagi A., and Berman A. (2010) Stabilization of amorphous calcium carbonate by phosphate rich organic matrix proteins and by single phosphoamino acids. *J Struct Biol.* **171**, 207-215.

Berner R. A. (1975) The role of magnesium in the crystal growth of calcite and aragonite from sea water. *Geochimica et Cosmochimica Acta* **39**, 489-504.

Bethke C. M. (2008) *Geochemical and Biogeochemical Reaction Modeling*. Cambridge University Press, New York.

Bigeleisen J. and Mayer M. G. (1947) Calculation of Equilibrium Constants for Isotopic Exchange Reaction. *J. Chem. Phys.* **15**, 261-267.

Billinge S. J. L. (2009) Condensed matter: How do your crystals grow? *Nat Phys* **5**, 13-14.

Bischoff W. D., Bishop F. C., and Mackenzie F. T. (1983) Biogenically produced magnesian calcite: inhomogeneities in chemical and physical properties: comparison with synthetic phases *American Mineralogist* **68**, 1183-1188.

Bischoff W. D., Sharma S. K., and Mackenzie F. T. (1985) Carbonate ion disorder in synethetic and biogenic magnesian calcites: a Raman spectral study. *American Mineralogist* **70**, 581-589.

Böhm F., Gussone N., Eisenhauer A., Dullo W.-C., Reynaud S., and Paytan A. (2006) Calcium isotope fractionation in modern scleractinian corals. *Geochimica et Cosmochimica Acta* **70**, 4452-4462.

Böttcher M. E. and Dietzel M. (2010) Metal-ion partitioning during low temperature precipitation and dissolution of anhydrous carbonates and sulphates. In: Stoll, M. P. a. H. (Ed.), *Ion Partitioning in Ambient-Temperature Aqueous Systems*. European mineralogical union, Twickenham, UK.

Böttcher M. E., Gehlken P.-L., and Steele D. F. (1997) Characterization of inorganic and biogenic magnesian calcites by Fourier Transform infrared spectroscopy. *Solid State Ionics* **101-103**, 1379-1385.

Bottinga Y. and Craig H. (1968) Oxygen isotope fractionation between CO_2 and water, and the isotopic composition of marine atmospheric CO_2. *Earth and Planetary Science Letters* **5**, 285-295.

Braybrook A. L., Heywood B. R., Jackson R. A., and Pitt K. (2002) Parallel computational and experimental studies of the morphological modification of calcium carbonate by cobalt. *Journal of Crystal Growth* **243**, 336-344.

Brečević L., Nöthig-Laslo V., Kralj D., and Popović S. (1996) Effect of divalent cations on the formation and structure of calcium carbonate polyrnorphs. *Faraday Trans.* **92**, 1017-1022.

Broughton P. L. (1972) Monohydrocalcite in Speleothems: An Alternative Interpretation. *Contr. Mineral. and Petrol.* **36**, 171-174.

Brunauer S., Emmett P. H., and Teller E. (1938) Adsorption of Gases in Multimolecular Layers. *Journal of the American Chemical Society* **60**, 309-319.

Bruneval F., Donadio D., and Parrinello M. (2007) Molecular Dynamics Study of the Solvation of Calcium Carbonate in Water. *The Journal of Physical Chemistry B* **111**, 12219-12227.

Burton E. A. (1993) Controls on marine carbonate cement mineralogy: review and reassessment. *Chemical Geology* **105**, 163-179.

Burton E. A. and Walter L. M. (1987) Relative precipitation rates of aragonite and Mg calcite from seawater: Temperature or carbonate ion control? *Geology* **15**, 111-114.

Busenberg E. and Plummer N. L. (1989) Thermodynamics of magnesian calcite solid-solutions at 25°C and 1 atm total pressure. *Geochimica et Cosmochimica Acta* **53**, 1189-1208.

Butt H.-J., Cappella B., and Kappl M. (2005) Force measurements with the atomic force microscope: Technique, interpretation and applications. *Surface Science Reports* **59**, 1-152.

Carlström D. (1963) A crystallographic study of vertebrate otoliths. *Biol Bull* **125**, 441-463.

Chacko T. and Deines P. (2008) Theoretical calculation of oxygen isotope fractionation factors in carbonate systems. *Geochimica et Cosmochimica Acta* **72**, 3642-3660.

Chen T. (2005) New insights into the mechanisms of calcium carbonate mineral scale formation and inhibition. PhD Thesis, Heriot-Watt University.

Clark I. and Fritz P. (1997) *Environmental Isotopes in Hydrogeology*. CRC Press LLC, Lewis Publishers, Boca Raton/ Florida.

Clarke F. W. and Wheeler W. C. (1922) *The inorganic constituents of marine invertebrates*. Government printing office, Washington.

Clarkson J. R., Price T. J., and Adams C. J. (1992) Role of metastable phases in the spontaneous precipitation of calcium carbonate. *J. Chem. Soc., Faraday Trans.* **88**, 243-249.

Cohen A. L. and Gaetani G. A. (2010) Ion partioning and the geochemistry of coral skeletons: solving the mystery of the vital effect. In: Stoll, M. P. a. H. (Ed.), *Ion partioning in ambient-temperature aqueous systems*. European mineralogical union, London.

Cohen A. L. and McConnaughey T. A. (2003) Geochemical Perspectives on Coral Mineralization. In: Dove, P. M., Yoreo, J. J. D., and Weiner, S. Eds.), *Biomineralization*. Mineralogical Society of America and The Geochemistry Society, Washington.

Cohen A. L., Owens K. E., Layne G. D., and Shimizu N. (2002) The effect of algal symbionts on the accuracy of Sr/Ca paleotemperatures from coral. *Science* **296**, 331-333.

Coleyshaw E. E., Crump G., and Griffith W. P. (2003) Vibrational spectra of the hydrated carbonate minerals ikaite, monohydrocalcite, lansfordite and nesquehonite. *Spectrochimica Acta Part A* **59**, 2231-2239.

Cölfen H. and Mann S. (2003) Higher-Order Organization by Mesoscale Self-Assembly and Transformation of Hybrid Nanostructures. *Angewandte Chemie International Edition* **42**, 2350-2365.

Cölfen H. and Völkel A. (2006) Application of the Density Variation Method on Calciumcarbonate Nanoparticles. *Progr Colloid Polm Sci* **131**, 126-128.

Compton R. G. and Brown C. A. (1994) The Inhibition of Calcite Dissolution/Precipitation: Mg^{2+} Cations. *Journal of Colloid and Interface Science* **165**, 445-449.

DalNegro A. and Ungaretti L. (1971) Refinement of the crystal structure of aragonite. *American Mineralogist* **56**, 768-772.

Davis K. J., Dove P. M., and Yoreo J. J. D. (2000) The Role of Mg^{2+} as an Impurity in Calcite Growth. *Science* **290**, 1134-1137.

Davis K. J., Dove P. M., and Yoreo J. J. D. (2004) Morphological consequences differential Mg^{2+} incorporation at structurally distinct steps on calcite. *American Mineralogist* **89**, 714 - 720.

De Choudens-Sanchez V. and Gonzalez L. A. (2009) Calcite and Aragonite Precipitation Under Controlled Instantaneous Supersaturation: Elucidating the Role of $CaCO_3$ Saturation State and Mg/Ca Ratio on Calcium Carbonate Polymorphism. *Journal of Sedimentary Research* **79**, 363-376.

De Leeuw N. H. and Parker S. C. (1998) Surface Structure and Morphology of Calcium Carbonate Polymorphs Calcite, Aragonite, and Vaterite: An Atomistic Approach. *The Journal of Physical Chemistry B* **102**, 2914-2922.

De Villiers J. P. R. (1971) Crystal structures of aragonite, strontianite, and witherite. *American Mineralogist* **56**, 758-767.

DeOliveira D. B. and Laursen R. A. (1997) Control of Calcite Crystal Morphology by a Peptide Designed To Bind to a Specific Surface. *Journal of the American Chemical Society* **119**, 10627-10631.

DePaolo D. J. (2011) Surface kinetic model for isotopic and trace element fractionation during precipitation of calcite from aqueous solutions. *Geochimica et Cosmochimica Acta* **75**, 1039-1056.

DeVilliers J. P. R. (1971) Crystal structures of aragonite, strontianite, and witherite. *American Mineralogist* **56**, 758-767.

DeYoreo J. J. and Vekilov P. G. (2003) Principles of Crystal Nucleation and Growth. In: Dove, P. M., Yoreo, J. J. D., and Weiner, S. Eds.), *Biomineralization*. Mineralogical Society of America and The Geochemistry Society, Washington.

Dickson J. A. D. (1991) Disequilibrium carbon and oxygen isotope variations in natural calcite. *Nature* **353**, 842-844.

Didymus J. M., Oliver P., Mann S., DeVries A. L., Hauschka P. V., and Westbroek P. (1993) Influence of low-molecular-weight and macromolecular organic additives on the morphology of calcium carbonate. *Journal of the Chemical Society, Faraday Transactions* **89**, 2891-2900.

Dietzel M., Gussone N., and Eisenhauer A. (2004) Co-precipitation of Sr^{2+} and Ba^{2+} with aragonite by membrane diffusion of CO_2 between 10 and 50 °C. *Chemical Geology* **203**, 139-151.

Dietzel M. and Kirchhoff T. (2003) Stable Isotope Ratio and the Evolution of Acidulous Ground Water. *Aquatic Geochemistry* **8**, 229.

Dietzel M., Tang J., Leis A., and Köhler S. J. (2009) Oxygen isotopic fractionation during inorganic calcite precipitation — Effects of temperature, precipitation rate and pH. *Chemical Geology* **268**, 107-115.

Dietzel M., Usdowski E., and Hoefs J. (1992) Chemical and $^{13}C/^{12}C$- and $^{18}O/^{16}O$-isotope evolution of alkaline drainage waters and the precipitation of calcite. *Applied Geochemistry* **7**, 177-184.

Donald S. (2004) Introduction to Solid State Chemistry. Massachusetts Institute of Technology: MIT OpenCourseWare.

Drever J. I. (2002) *The Geochemistry of Natural Waters: Surface and Groundwater Environments*. Prentice-Hall, New Jersey.

Drever J. I. (2004) *Surface and Ground Water, Weathering, and Soils*. Elsevier – Pergamon, Oxford.

Dudley L. Y. and Baker J. S. (2007) The Role of Antiscalants and Cleaning Chemicals to Control Membrane Fouling.

Edwards H. G. M., Villar S. E. J., Jehlicka J., and Munshi T. (2005) FT-Raman spectroscopic study of calcium-rich and magnesium-rich carbonate minerals. *Spectrochimica Acta Part A: Molecular and Biomolecular Spectroscopy* **61**, 2273-2280.

Elderfield H. (2010) Seawater Chemistry and Climate. *Science* **327**, 1092-1093.

Elderfield H., Yu J., Anand P., Kiefer T., and Nyland B. (2006) Calibrations for benthic foraminiferal Mg/Ca paleothermometry and the carbonate ion hypothesis. *Earth and Planetary Science Letters* **250**, 633-649.

Elhadj S., Salter E. A., Wierzbicki A., De Yoreo J. J., Han N., and Dove P. M. (2005) Peptide Controls on Calcite Mineralization: Polyaspartate Chain Length Affects Growth Kinetics and Acts as a Stereochemical Switch on Morphology. *Crystal Growth & Design* **6**, 197-201.

Engstrom D. R. and Nelson S. R. (1991) Paleosalinity from trace metals in fossil ostracodes compared with observational records at Devils Lake, North Dakota, USA. *Palaeogeography, Palaeoclimatology, Palaeoecology* **83**, 295-312.

Epstein S., Buchsbaum R., Lowenstam H. A., and Urey H. C. (1953) Revised carbonate-water isotopic temperature scale. *Geological Society of America Bulletin* **64**, 1315-1326.

Epstein S. and Mayeda T. (1953) Variation of O^{18} content of waters from natural sources. *Geochimica et Cosmochimica Acta* **4**, 213-224.

Erez J. (2003) The Source of Ions for Biomineralization in Foraminifera and Their Implications for Paleoceanographic Proxies. In: Dove, P. M., Yoreo, J. J. D., and Weiner, S. Eds.),

Biomineralization. Mineralogical Society of America and The Geochemistry Society, Washington.

Fairchild I. J. and Treble P. C. (2009) Trace elements in speleothems as recorders of environmental change. *Quaternary Science Reviews* **28**, 449-468.

Falini G., Fermani S., Goisis M., and Manganelli G. (2009) Calcite Morphology and Aggregation in the Presence of Comb-like Polymers Adsorbed on Cement Particles. *Crystal Growth & Design* **9**, 2240-2247.

Falini G., Gazzano M., and Ripamonti A. (1994) Crystallization of calcium carbonate in presence of magnesium and polyelectrolytes. *Journal of Crystal Growth* **137**, 577-584.

Fantle M. S. and DePaolo D. J. (2007a) Ca isotopes in carbonate sediment and pore fluid from ODP Site 807A: The Ca^{2+}(aq)-calcite equilibrium fractionation factor and calcite recrystallization rates in Pleistocene sediments. *Geochimica et Cosmochimica Acta* **71**, 2524-2546.

Fantle M. S. and DePaolo D. J. (2007b) Ca isotopes in carbonate sediment and pore fluid from ODP Site 807A: The Ca^{2+}(aq)–calcite equilibrium fractionation factor and calcite recrystallization rates in Pleistocene sediments. *Geochimica et Cosmochimica Acta* **71**, 2524 - 2546

Farkaš J., Böhm F., Wallmann K., Blenkinsop J., Eisenhauer A., van Geldern R., Munnecke A., Voigt S., and Veizer J. (2007a) Calcium isotope record of Phanerozoic oceans: Implications for chemical evolution of seawater and its causative mechanisms. *Geochimica et Cosmochimica Acta* **71**, 5117-5134.

Farkaš J., Buhl D., Blenkinsop J., and Veizer J. (2007b) Evolution of the oceanic calcium cycle during the late Mesozoic: Evidence from $\delta^{44/40}$Ca of marine skeletal carbonates. *Earth and Planetary Science Letters* **253**, 96-111.

Faure G. and Mensing T. M. (2005) *Isotopes: principles and applications*. John Wiley & Sons, New Jersey.

Fenter P., Geissbühler P., DiMasi E., Srajer G., Sorensen L. B., and Sturchio N. C. (2000) Surface speciation of calcite observed in situ by high-resolution X-ray reflectivity. *Geochimica et Cosmochimica Acta* **64**, 1221-1228.

Fernández-Díaz L., Putnis A., Prieto M., and Putnis C. V. (1996) The role of magnesium in the crystallization of calcite and aragonite in a porous medium. *Journal of Sedimentary Research* **66**, 482-481.

Finch A. A. and Allison N. (2008) Coordination of Sr and Mg in calcite and aragonite. *Mineral. Mag.* **71**, 539-552.

Fischbeck R. and Müller G. (1971) Monohydrocalcite, Hydromagnesite, Nesquehonite, Dolomite, Aragonite, and Calcite in Speleothems of the Fränkische Schweiz, Western Germany. *Contr. Mineral. and Petrol.* **33**, 87-92.

Fleitmann D., Burns S. J., Mudelsee M., Neff U., Kramers J., Mangini A., and Matter A. (2003) Holocene forcing of the Indian monsoon recorded in a stalagmite from Southern Oman. *Science* **300**, 1737-1739.

Frisia S., Borsato A., Fairchild I. J., McDermott F., and Selmo E. M. (2002) Aragonite-Calcite Relationships in Speleothems (Grotte De Clamouse, France): Environment, Fabrics, and Carbonate Geochemistry. *Journal of Sedimentary Research* **72**, 687-699.

Fu G., Valiyaveettil S., Wopenka B., and Morse D. E. (2005) CaCO3 Biomineralization:â€‰ Acidic 8-kDa Proteins Isolated from Aragonitic Abalone Shell Nacre Can Specifically Modify Calcite Crystal Morphology. *Biomacromolecules* **6**, 1289-1298.

Gabitov R. I., Gaetani G. A., Watson E. B., Cohen A. L., and Ehrlich H. L. (2008) Experimental determination of growth rate effect on U^{6+} and Mg^{2+} partitioning between aragonite and fluid at elevated U^{6+} concentration. *Geochimica et Cosmochimica Acta* **72**, 4058-4068.

Gaetani G. A. and Cohen A. L. (2006) Element partitioning during precipitation of aragonite from seawater: A framework for understanding paleoproxies. *Geochimica et Cosmochimica Acta* **70**, 4617-4634.

Gagnon A. C., Adkins J. F., Fernandez D. P., and Robinson L. F. (2007) Sr/Ca and Mg/Ca vital effects correlated with skeletal architecture in a scleractinian deep-sea coral and the role of Rayleigh fractionation. *Earth and Planetary Science Letters* **261**, 280-295.

Gamisch T. and Girmscheid G. (2007) *Versinterungsprobleme in Bauwerksentwässerungen*. Bauwerk, Berlin.

Garrels R. M. and Thompson M. E. (1962) A chemical model for sea water at 25 °C and one atmosphere total pressure. *American Journal of Science* **260**, 57-66.

Gauldie R. W. (1993) Polymorphic crystalline structure of fish otoliths. *Journal of Morphology* **218**, 1-28.

Gebauer D. (2008) A Novel View on the Early Stage of Crystallization. PhD Thesis, Universität Potsdam.

Gebauer D., Gunawidjaja P. N., Ko J. Y. P., Bacsik Z., Aziz B., Liu L., Hu Y., Bergström L., Tai C.-W., Sham T.-K., Edén M., and Hedin N. (2010) Proto-Calcite and Proto-Vaterite in Amorphous Calcium Carbonates. *Angewandte Chemie International Edition* **49**, 8889-8891.

Gebauer D., Volkel A., and Cölfen H. (2008) Stable Prenucleation Calcium Carbonate Clusters. *Science* **322**, 1819-1822.

Gills T. E. (1995) Certificate of Analysis - Standard Reference Material 915a*National Institute of Standards & Technology*.

Given R. K. and Wilkinson B. H. (1985) Kinetic control of morphology, composition, and mineralogy of abiotic sedimentary carbonates. *Journal of Sedimentary Petrology* **55**, 109-119.

Goldsmith J. R., Graf D. L., chodos A. A., Joensuu O. I., and McVicker L. D. (1958) Relation between lattice constants and composition of Ca-Mg carbonates *American Mineralogist* **43**, 84-101.

Goldsmith J. R., Graf D. L., and Heard H. C. (1961) Lattice constants of the calcium-magnesium carbonates *American Mineralogist* **46**, 453-457.

Gonfiantini R., Panichi C., and Tongiorgi E. (1968) Isotopic disequilibrium in travertine deposition. *Earth and Planetary Science Letters* **5**, 55-58.

Gopinath C. S., Hegde S. G., Ramaswamy A. V., and Mahapatra S. (2002) Photoemission studies of polymorphic $CaCO_3$ materials. *Materials Research Bulletin* **37**, 1323-1332.

Gránásy L., Pusztai T., Tegze G., Warren J. A., and Douglas J. F. (2005) Growth and form of spherulites. *Physical Review E* **72**, 011605-1 - 011605-15.

Griesshaber E., Kelm K., Sehrbrock A., Mader W., Mutterlose J., Brand U., and Schmahl W. (2009) Amorphous calcium carbonate in the shell material of the brachiopod Megerlia truncata *Eur. J. Mineral.* **21**, 715-723.

Gussone N., Böhm F., Eisenhauer A., Dietzel M., Heuser A., Teichert B. M. A., Reitner J., Worheide G., and Dullo W.-C. (2005) Calcium isotope fractionation in calcite and aragonite. *Geochimica et Cosmochimica Acta* **69**, 4485-4494.

Gussone N., Eisenhauer A., Heuser A., Dietzel M., Bock B., Böhm F., Spero H. J., Lea D. W., Bijma J., and Nägler T. F. (2003) Model for kinetic effects on calcium isotope fractionation ($\delta^{44}Ca$) in inorganic aragonite and cultured planktonic foraminifera. *Geochimica et Cosmochimica Acta* **67**, 1375-1382.

Gussone N., Eisenhauer A., Tiedemann R., Haug G. H., Heuser A., Bock B., Th.F. N., and A. M. (2004) Reconstruction of Caribbean Sea surface temperature and salinity fluctuations in response to the Pliocene closure of the Central American Gateway and radiative forcing, using $\delta^{44/40}Ca$, $\delta^{18}O$ and Mg/Ca ratios. *Earth and Planetary Science Letters* **227**, 201.

Gussone N., Langer G., Geisen M., Steel B. A., and Riebesell U. (2007) Calcium isotope fractionation in coccoliths of cultured Calcidiscus leptoporus, Helicosphaera carteri, Syracosphaera pulchra and Umbilicosphaera foliosa. *Earth and Planetary Science Letters* **260**, 505-515.

Gutjahr A., Dabringhaus H., and Lacmann R. (1996) Studies of the growth and dissolution kinetics of the $CaCO_3$ polymorphs calcite and aragonite II. The influence of divalent cation additives on the growth and dissolution rates. *Journal of Crystal Growth* **158**, 310-315.

Haase-Schramm A., Böhm F., Eisenhauer A., Dullo W.-C., Joachimski M. M., Hansen B., and Reitner J. (2003) Sr/Ca ratios and oxygen isotopes from sclerosponges: Temperature history of the Caribbean mixed layer and thermocline during the Little Ice Age. *Paleoceanography* **18**, 1073-1088.

Heberling F., Trainor T. P., Lützenkirchen J., Eng P., Denecke M. A., and Bosbach D. (2011) Structure and reactivity of the calcite-water interface. *Journal of Colloid and Interface Science* **354**, 843-857.

Heinemann A., Fietzke J., Eisenhauer A., and Zumholz K. (2008) Modification of Ca isotope and trace metal composition of the major matrices involved in shell formation of Mytilus edulis. *Geochemistry, Geophysics, Geosystems* **9**.

Henderson L. M. and Kracek F. C. (1927) The Fractional Precipitation of Barium and Radium Chronmates. *Journal of the American Chemical Society* **49**, 738-749.

Hendy C. H. (1971) The isotopic geochemistry of speleothems-I. The calculation of the effects of different modes of formation on the isotopic composition of speleothems and their applicability as palaeoclimatic indicators. *Geochimica et Cosmochimica Acta* **35**, 801-824.

Hernandez-Hernandez A., Rodriguez-Navarro A. B., Gomez-Morales J., Jimanez-Lopez C., Nys Y., and Garcia-Ruiz J. M. (2008) Influence of Model Globular Proteins with Different Isoelectric Points on the Precipitation of Calcium Carbonate. *Crystal Growth & Design* **8**, 1495-1502.

Hesse K.-F., Küppers H., and Suess E. (1983) Refinement of the structure of Ikaite, $CaCO_3 \cdot 6H_2O$. *Zeitschrift für Kristallographie* **163**, 227-231.

Heuser A., Eisenhauer A., Gussone N., Bock B., Hansen B. T., and Nägler T. F. (2002) Measurement of calcium isotopes ($\delta^{44}Ca$) using a multicollector TIMS technique. *International Journal of Mass Spectrometry* **220**, 385-397.

Hoch A. R., Reddy M. M., and Aiken G. R. (2000) Calcite crystal growth inhibition by humic substances with emphasis on hydrophobic acids from the Florida Everglades. *Geochimica et Cosmochimica Acta* **64**, 61-72.

Hoefs J. (2009) *Stable isotope geochemistry*. Springer, Heidelberg.

Holcomb M., Cohen A. L., Gabitov R. I., and Hutter J. L. (2009) Compositional and morphological features of aragonite precipitated experimentally from seawater and biogenically by corals. *Geochimica et Cosmochimica Acta* **73**, 4166-4179.

Holland H. D., Holland H. J., and Munoz J. L. (1964) The coprecipitation of cations with $CaCO_3$ - II. The coprecipitation of Sr^{2+} with calcite between 90° and 100°C. *Geochimica et Cosmochimica Acta* **28**, 1287-1301.

Horn D. and Rieger J. (2001) Organic Nanoparticles in the Aqueous Phase–Theory, Experiment, and Use. *Angew. Chem. Int. Ed.* **40**, 4330-4361.

Huang Y., Fairchild I. J., Borsato A., Frisia S., Cassidy N. J., McDermott F., and Hawkesworth C. J. (2001) Seasonal variations in Sr, Mg and P in modern speleothems (Grotta di Ernesto, Italy). *Chemical Geology* **175**, 429-448.

Hubmann B., Winkler G., and Masser E. (2008) Der (hydro)geologische Rahmen von Sinterquellen im Raum St. Pankrazen/Weststeiermark. *Mitt. naturwiss. Ver. Steiermark* **137**, 51-62.

Humphrey J. D. and Howell R. P. (1999) Effect of differential stress on strontium partitioning in calcite. *Journal of Sedimentary Research* **69**, 208-215.

Jiménez-López C., Caballero E., Huertas F. J., and Romanek C. S. (2001) Chemical, mineralogical and isotope behavior, and phase transformation during the precipitation of calcium carbonate minerals from intermediate ionic solution at 25°C. *Geochimica et Cosmochimica Acta* **65**, 3219-3231.

Jiménez-López C., Rodriguez-Navarro A., Dominguez-Vera J. M., and Garcia-Ruiz J. M. (2003) Influence of lysozyme on the precipitation of calcium carbonate: A kinetic and morphologic study. *Geochimica et Cosmochimica Acta* **67**, 1667-1676.

Joentgen W., Müller N., Mitschker A., and Schmidt H. (2002) Polyaspartic acids. In: Fahnestock, S. and Steinbüchel, A. Eds.), *Polyamides and Complex Proteinaceous Materials I*. WILEY-VCH, Weinheim.

Kamhi S. R. (1963) On Structure of Vaterite, $CaCO_3$. *Acta Crystallographica* **16**, 770-772.

Kanakis J., Malkaj P., Petroheilos J., and Dalas E. (2001) The crystallization of calcium carbonate on porcine and human cardiac valves and the antimineralization effect of sodium alginate. *Journal of Crystal Growth* **223**, 557-564.

Katz A., Sass E., Starinsky A., and Holland H. D. (1972) Strontium behavior in the aragonite-calcite transformation: An experimental study at 40-98°C. *Geochimica et Cosmochimica Acta* **36**, 481-496.

Kendall C. and Doctor D. H. (2004) Stable Isotope Applications in Hydrologic Studies. In: I.Drever, J. (Ed.), *Surface and Ground Water, Weathering, and Soils*. Elsevier-Pergamon, Oxford.

Kim S. T. and O'Neil J. R. (1997) Equilibrium and nonequilibrium oxygen isotope effects in synthetic carbonates. *Geochimica et Cosmochimica Acta* **61**, 3461-3475.

Kim Y.-Y., Douglas E. P., and Gower L. B. (2007) Patterning Inorganic (CaCO3) Thin Films via a Polymer-Induced Liquid-Precursor Process. *Langmuir* **23**, 4862-4870.

Kinsman D. J. J. and Holland H. D. (1969) The co-precipitation of cations with $CaCO_3$-IV. The co-precipitation of Sr^{2+} with aragonite between 16° and 96°C. *Geochimica et Cosmochimica Acta* **33**, 1-17.

Kisakürek B., Eisenhauer A., Böhm F., Hathorne E. C., and Erez J. (2011) Controls on calcium isotope fractionation in cultured planktic foraminifera, Globigerinoides ruber and Globigerinella siphonifera. *Geochimica et Cosmochimica Acta* **75**, 427-443.

Klein R. T., Lohmann K. C., and Thayer C. W. (1996) Sr/Ca and 13C/12C ratios in skeletal calcite of Mytilus trossulus: Covariation with metabolic rate, salinity, and carbon isotopic composition of seawater. *Geochimica et Cosmochimica Acta* **60**, 4207-4221.

Knapp H. (2010) Aminosäuren. In: Deckwer, W.-D., Dill, B., Eisenbrand, G., Fugmann, B., Heiker, F. R., Hulpke, H., Kirschning, A., Pohnert, G., Pühler, A., Schmid, R. D., and Schreier, P. Eds.), *RÖMPP Online*. Thieme.

Kontoyannis C. G. and Vagenas N. V. (2000) Calcium carbonate phase analysis using XRD and FT-Raman spectroscopy. *Analyst* **125**, 251-255.

Kossel W. (1934) Zur Energetik von Oberflächenvorgängen. *Annalen der Physik* **21**, 457-480.

Koutsoukos P. G. and Kontoyannis C. G. (1984) Precipitation of calcium carbonate in aqueous solutions. *Journal of the Chemical Society, Faraday Transactions 1: Physical Chemistry in Condensed Phases* **80**, 1181-1192.

Kralj D. and Brecevic L. (1995) Dissolution kinetics and solubility of calcium carbonate monohydrate. *Colloids and Surfaces A: Physicochemical and Engineering Aspects* **96**, 287-293.

Kulak A. N., Iddon P., Li Y., Armes S. P., Cölfen H., Paris O., Wilson R. M., and Meldrum F. C. (2007) Continuous Structural Evolution of Calcium Carbonate Particles: A Unifying Model

of Copolymer-Mediated Crystallization. *Journal of the American Chemical Society* **129**, 3729-3736.

Lam R. S. K., Charnock J. M., Lennie A., and Meldrum F. C. (2007) Synthesis-dependant structural variations in amorphous calcium carbonate. *CrystEngComm* **9**, 1226-1236.

Langer G., Gussone N., Nehrke G., Riebesell U., Eisenhauer A., Kuhnert H., Rost B., Trimborn S., and Thoms S. (2006) Coccolith strontium to calcium ratios in Emiliania huxleyi: The dependence on seawater strontium and calcium concentrations. *Limnol. Oceanogr.* **51**, 310-320.

Langer G., Gussone N., Nehrke G., Riebesell U., Eisenhauer A., and Thoms S. (2007) Calcium isotope fractionation during coccolith formation in Emiliania huxleyi: Independence of growth and calcification rate. *Geochem. Geophys. Geosyst.* **8**, Q05007.

Larsen K., Bechgaard K., and Stipp S. L. S. (2010) The Effect of the Ca^{2+} to CO_3^{2-} Activity Ratio on Spiral Growth at the Calcite Surface. *Geochimica et Cosmochimica Acta* **74**, 2099-2109.

Lasaga A. C. (1984) Chemical kinetics of water-rock interactions. *Journal of Geophysical Research* **89**, 4009-4025.

Lea D. W., Mashiotta T. A., and Spero H. J. (1999) Controls on magnesium and strontium uptake in planktonic foraminifera determined by live culturing. *Geochimica et Cosmochimica Acta* **63**, 2369-2379.

Lea D. W., Pak D. K., and Spero H. J. (2000) Climate Impact of Late Quaternary Equatorial Pacific Sea Surface Temperature Variations. *Science* **289**, 1719-1724.

Lebron I. and Suarez D. L. (1998) Kinetics and mechanisms of precipitation of calcite as affected by PCO_2 and organic ligands at 25°C. *Geochimica et Cosmochimica Acta* **62**, 405-416.

Lee J. and Morse J. W. (2010) Influences of alkalinity and pCO_2 on $CaCO_3$ nucleation from estimated Cretaceous composition seawater representative of "calcite seas". *Geology* **38**, 115-118.

Lemarchand D., Wasserburg G. J., and Papanastassiou D. A. (2004) Rate-controlled calcium isotope fractionation in synthetic calcite. *Geochimica et Cosmochimica Acta* **68**, 4665-4678.

Lill R. E., King G. A., and O'Donoghue E. M. (1990) Physiological changes in asparagus spears immediately after harvest. *Scientia Horticulturae* **44**, 191-199.

Lippmann F. (1973) *Sedimentary Carbonate Minerals*. Springer Verlag, Gießen.

Lorens R. B. (1981) Sr, Cd, Mn and Co distribution coefficients in calcite as a function of calcite precipitation rate. *Geochimica et Cosmochimica Acta* **45**, 553-561.

Loste E., Wilson R. M., Seshadri R., and Meldrum F. C. (2003) The role of magnesium in stabilising amorphous calcium carbonate and controlling calcite morphologies. *Journal of Crystal Growth* **254**, 206-218.

Lucas A., Mouallem-Bahout M., Carel C., Gaudé J., and Matecki M. (1999) Thermal Expansion of Synthetic Aragonite Condensed Review of Elastic Properties. *Journal of Solid State Chemistry* **146**, 73-78.

MacKenzie C. R., Wilbanks S. M., and McGrath K. M. (2004) Superimposed effect of kinetics and echinoderm glycoproteins on hierarchical growth of calcium carbonate. *Journal of Materials Chemistry* **14**, 1238-1244.

MacKenzie F. T., Bischoff W. D., and Bishop F. C. (1983) Magnesian calcites: low-temperature occurence solubility and solid-solution behavior. In: Reeder, R. J. (Ed.), *Carbonates: mineralogy and chemistry*. Mineralogical society of America.

Mandl G. W., Mowotny A., Rockenschaub M., Berka R., Brosch F. J., Fasching A., Klima K., Magiera J., Mandl G. W., Matura A., Mello J., Nievoll J., Nowotny A., Pölser P., Schweighofer B., Riedmüller G., and Rockenschaub M. (2001) Mürzzuschlag (104) *Geologische Karte der Republik Österreich 1:50000*. Geologische Bundesanstalt, Wien.

Marriott C. S., Henderson G. M., Belshaw N. S., and Tudhope A. W. (2004) Temperature dependence of δ^7Li, δ^{44}Ca and Li/Ca during growth of calcium carbonate. *Earth and Planetary Science Letters* **222**, 615-624.

Maslen E. N., Streltsov V. A., and Streltsova N. R. (1993) X-ray study of the electron density in calcite, $CaCO_3$. *Acta Crystallographica Section B* **49**, 636-641.

Melancon S., Fryer B. J., Ludsin S. A., Gagnon J. E., and Yang Z. (2005) Effects of crystal structure on the uptake of metals by lake trout (Salvelinus namaycush) otoliths. *Canadian Journal of Fisheries & Aquatic Sciences* **62**, 2609-2619.

Meyer H. J. (1965) Bildung und Morphologie des Vaterits. *Zeitschrift für Kristallographie* **121**, 220-242.

Meyer H. J. (1969) Struktur und Fehlordnung des Vaterits. *Zeitschrift für Kristallographie* **128**, 183-212.

Michaelis J., Usdowski E., and Menschel G. (1985) Partitioning of ^{13}C and ^{12}C on the degassing of CO_2 and the precipitation of calcite; Rayleigh-type fractionation and a kinetic model. *American Journal of Science* **285**, 318-327.

Michel F. M., MacDonald J., Feng J., Phillips B. L., Ehm L., Tarabrella C., Parise J. B., and Reeder R. J. (2008) Structural Characteristics of Synthetic Amorphous Calcium Carbonate. *Chemistry of Materials* **20**, 4720-4728.

Millero F. J. (2004) Physicochemical Controls on Seawater. In: Elderfield, H. (Ed.), *The Ocean and Marine Geochemistry*. Elsevier Pergamon, Oxford.

Mook W. G., Bommerson J. C., and Staverman W. H. (1974) Carbon isotope fractionation between dissolved bicarbonate and gaseous carbon dioxide. *Earth and Planetary Science Letters* **22**, 169-176.

Morse J. W. (1978) Dissolution kinetics of calcium carbonate in sea water: VI. The near-equilibrium dissolution kinetics of calcium carbonate-rich deep sea sediments. *American Journal of Science* **278**, 344-358.

Morse J. W. (1983) The kinetics of calcium carbonate dissolution and precipitation. In: Reeder, R. J. (Ed.), *Carbonates: Mineralogy and chemistry*. Mineralogical Society of America, Virginia.

Morse J. W. and Bender M. L. (1990) Partition coefficients in calcite: Examination of factors influencing the validity of experimental results and their application to natural systems. *Chem. Geol.* **82**, 265-277.

Morse J. W. and MacKenzie F. T. (1990) *Geochemistry of Sedimentary Carbonates* Elsevier, Amsterdam.

Mucci A. (1987) Influence of temperature on the composition of magnesian calcite overgrowths precipitated from seawater. *Geochimica et Cosmochimica Acta* **51**, 1977-1984.

Mucci A. and Morse J. W. (1983) The incorporation of Mg^{2+} and Sr^{2+} into calcite overgrowths: influences of growth rate and solution composition. *Geochimica et Cosmochimica Acta* **47**, 217-233.

Mucci A. and Morse J. W. (1984) The solubility of calcite in seawater solutions of various magnesium concentration, I_t = 0.697 m at 25 °C and one atmosphere total pressure. *Geochimica et Cosmochimica Acta* **48**, 815-822.

Mukkamala S. B., Anson C. E., and Powell A. K. (2006) Modelling calcium carbonate biomineralisation processes. *Journal of Inorganic Biochemistry* **100**, 1128-1138.

Müller M. N., Kisakürek B., Buhl D., Gutperlet R., Kolevica A., Riebesell U., Stoll H., and Eisenhauer A. Response of the coccolithophores Emiliania huxleyi and Coccolithus braarudii to changing seawater Mg^{2+} and Ca^{2+} concentrations: Mg/Ca, Sr/Ca ratios and $\delta^{44/40}Ca$, $\delta^{26/24}Mg$ of coccolith calcite. *Geochimica et Cosmochimica Acta* **In Press, Accepted Manuscript**.

Mullin J. W. (2001) *Crystallization*. Butterworth Heinemann Oxford.

Myers-Beaghton A. K. and Vvedensky D. D. (1991) Generalized Burton-Cabrera-Frank theory for growth and equilibration on stepped surfaces. *Physical Review A* **44**, 2457.

Nancollas G. H. and Reddy V. (1971) The Crystallization of Calcium Carbonate - II. Calcite Growth Mechanism. *Journal of Colloid and Interface Science* **37**, 824-830.

Nehrke G., Reichart G. J., Van Cappellen P., Meile C., and Bijma J. (2007) Dependence of calcite growth rate and Sr partitioning on solution stoichiometry: Non-Kossel crystal growth. *Geochimica et Cosmochimica Acta* **71**, 2240-2249.

Nernst W. (1904) Theorie der Reaktionsgeschwindigkeit in htereogenen Systemen. *Z. phys. Chem.* **47**, 52-55.

Nielsen A. E. and Toft J. M. (1984) Electrolyte crystal growth kinetics. *Journal of Crystal Growth* **67**, 278-288.

Nilsson O. and Sternbeck J. (1999) A mechanistic model for calcite crystal growth using surface speciation. *Geochimica et Cosmochimica Acta* **63**, 217-225.

Noethig-Laslo V. and Brečević L. (1998) Mode and sites of incorporation of divalent cations in vaterite. *J. Chem. Soc. Faraday Trans.* **94**, 2005-2009.

Noguera C., Fritz B., Clément A., and Baronnet A. (2006) Nucleation, growth and ageing scenarios in closed systems I: A unified mathematical framework for precipitation, condensation and crystallization. *Journal of Crystal Growth* **297**, 180-186.

Noyes A. A. and Whitney W. R. (1897) The rate of solution of solid substances in their own solutions. *Journal of American Chemical Society* **19**, 930-934.

Ogino T., Suzuki T., and Sawada K. (1987) The formation and transformation mechanism of calcium carbonate in water. *Geochimica et Cosmochimica Acta* **51**, 2757-2767.

Olshausen S. v. (1925) Strukturuntersuchungen nach der Debye-Scherrer-Methode. *Zeitschrift für Kristallographie* **61**, 463-514.

Oomori T., Kaneshima H., Maezato Y., and Kitano Y. (1987) Distribution coefficient of Mg^{2+} ions between calcite and solution at 10-50°C. *Marine Chemistry* **20**, 327-336.

Orme C. A., Noy A., Wierzbicki A., McBride M. T., Grantham M., Teng H. H., Dove P. M., and DeYoreo J. J. (2001) Formation of chiral morphologies through selective binding of amino acids to calcite surface steps. *Nature* **411**, 775-779.

Ostwald W. (1897) Studien über die Bildung und Umwandlung fester Körper. *Zeitschrift für Physikalische Chemie* **22**, 289.

Palchik N. A. and Moroz T. N. (2005) Polymorph modifications of calcium carbonate in gallstones. *Journal of Crystal Growth* **283**, 450-456.

Paquette J. and Reeder R. J. (1995) Relationship between surface structure, growth mechanism, and trace element incorporation in calcite. *Geochimica et Cosmochimica Acta* **59**, 735-749.

Pingitore Jr N. E. and Eastman M. P. (1986) The coprecipitation of Sr^{2+} with calcite at 25°C and 1 atm. *Geochimica et Cosmochimica Acta* **50**, 2195-2203.

Plummer L. N. and Busenberg E. (1982) The solubilities of calcite, aragonite and vaterite in CO_2-H_2O solutions between 0 and 90°C, and an evaluation of the aqueous model for the system $CaCO_3$-CO_2-H_2O. *Geochimica et Cosmochimica Acta* **46**, 1011-1040.

Pokrovsky O. S. (1998) Precipitation of calcium and magnesium carbonates from homogeneous supersaturated solutions. *Journal of Crystal Growth* **186**, 233-239.

Pokrovsky O. S., Mielczarski J. A., Barres O., and Schott J. (2000) Surface Speciation Models of Calcite and Dolomite/Aqueous Solution Interfaces and Their Spectroscopic Evaluation. *Langmuir* **16**, 2677-2688.

Pokrovsky O. S. and Schott J. (2002) Surface Chemistry and Dissolution Kinetics of Divalent Metal Carbonates. *Environmental Science & Technology* **36**, 426-432.

Pokrovsky O. S., Schott J., and Thomas F. (1999a) Dolomite surface speciation and reactivity in aquatic systems. *Geochimica et Cosmochimica Acta* **63**, 3133-3143.

Pokrovsky O. S., Schott J., and Thomas F. (1999b) Processes at the magnesium-bearing carbonates/solution interface. I. A surface speciation model for magnesite. *Geochimica et Cosmochimica Acta* **63**, 863-880.

Politi Y., Arad T., Klein E., Weiner S., and Addadi L. (2004) Sea urchin spine calcite forms via a transient amorphous calcium carbonate phase. *Science* **306**, 1161-1164.

Porter S. M. (2007) Seawater Chemistry and Early Carbonate Biomineralization. *Science* **316**, 1302.

Pouget E. M., Bomans P. H. H., Goos J. A. C. M., Frederik P. M., With G. d., and Sommerdijk N. A. J. M. (2009) The Initial Stages of Template-Controlled CaCO$_3$ Formation Revealed by Cryo-TEM. *Science* **323**, 1455-1458.

Raiteri P., Gale J. D., Quigley D., and Rodger P. M. (2010) Derivation of an Accurate Force-Field for Simulating the Growth of Calcium Carbonate from Aqueous Solution: A New Model for the Calcite-Water Interface. *J. Phys. Chem. C* **114**, 5997-6010.

Reeder R. J. (1983) *Carbonates: Mineralogy and chemistry.* Mineralogical Society of America, Virginia.

Rieger J., Frechen T., Cox G., Heckmann W., Schmidt C., and Thieme J. (2007) Precursor structures in the crystallization/precipitation processes of CaCO$_3$ and control of particle formation by polyelectrolytes. *Faraday Discussions* **136**, 265-277.

Rodriguez-Blanco J. D., Shaw S., and Benning L. G. (2008) How to make 'stable' ACC: protocol and preliminary structural characterization. *Mineralogical Magazine* **72**, 283-286.

Romanek C. S., Grossman E. L., and Morse J. W. (1992) Carbon isotopic fractionation in synthetic aragonite and calcite: Effects of temperature and precipitation rate. *Geochimica et Cosmochimica Acta* **56**, 419-430.

Rosenheim B. E., Swart P. K., and Thorrold S. R. (2005) Minor and trace elements in sclerosponge Ceratoporella nicholsoni: Biogenic aragonite near the inorganic endmember? *Palaeogeography, Palaeoclimatology, Palaeoecology* **228**, 109-129.

Rowlands D. L. G. and Webster R. K. (1971) Precipitation of Vaterite in Lake Water. *Nature Phys. Sci.* **229**, 158.

Sawada K., Ogino T., and Suzuki T. (1990) The distribution coefficients of Mg^{2+} ion between CaCO$_3$ polymorphs and solution and the effects on the formation and transformation of CaCO$_3$ in water. *Journal of Crystal Growth* **106**, 393-399.

Schauble E. A., Méheut M., and Hill P. S. (2009) Combining Metal Stable Isotope Fractionation Theory with Experiments. *Elements* **5**, 369–374.

Schmelzer J. W. P., Schmelzer J., and Gutzow I. S. (2000) Reconciling Gibbs and van der Waals: A new approach to nucleation theory. *J. Chem. Phys.* **112**, 3820-3831.

Schmidbaur H., Classen H. G., and Helbig J. (1990) Aspartic and Glutamic Acid as Ligands to Alkali and Alkaline-Earth Metals: Structural Chemistry as Related to Magnesium Therapy. *Angewandte Chemie International Edition in English* **29**, 1090-1103.

Schmidt M., Stumpf T., Walther C., Geckeis H., and Fanghänel T. (2010) Phase transformation in CaCO$_3$ polymorphs: A spectroscopic, microscopic and diffraction study. *Journal of Colloid and Interface Science* **351**, 50-56.

Schwister K., Aust E., Dure G., Groteklaes M., Stephan R., and Volgnandt P. (1999) *Taschenbuch der Chemie.* Carl-Hanser-Verlag, München.

Selleck B. W., Carr P. F., and Jones B. G. (2007) A review and synthesis of glendonites (pseudomorphs after ikaite) with new data: assessing applicability as recorders of ancient coldwater conditions. *Journal of Sedimentary Research* **77**, 980-991.

Sethmann I., Wang J., Becker U., and Putnis A. (2010) Strain-Induced Segmentation of Magnesian Calcite Thin Films Growing on a Calcite Substrate. *Crystal Growth & Design* **10**, 4319-4326.

Shannon R. D. (1976) Revised effective ionic radii and systematic studies of interatomic distances in halides and chalcogenides. *Acta Crystallographica Section A* **32**, 751-767.

Sikes C. S., Wierzbicki A., and Fabry V. J. (1994) From atomic to global scales in biomineralization. *Bulletin de l'Institut océanographique, Monaco* **14**, 1-47.

Soldati A. L., Jacob D. E., Wehrmeister U., and Hofmeister W. (2008) Structural characterization and chemical composition of aragonite and vaterite in freshwater cultured pearls. *Mineral. Mag.* **72**, 579-592.

Spanos N. and Koutsoukos P. G. (1998) Kinetics of Precipitation of Calcium Carbonate in Alkaline pH at Constant Supersaturation. Spontaneous and Seeded Growth. *The Journal of Physical Chemistry B* **102**, 6679-6684.

Spero H. J., Bijma J., Lea D. W., and Bemis B. E. (1997) Effect of seawater carbonate concentration on foraminiferal carbon and oxygen isotopes. *Nature* **390**, 497-500.

Spötl C. and Mangini A. (2002) Stalagmite from the Austrian Alps reveals Dansgaard - Oeschger events during isotope stage 3: Implications for the absolute chronology of Greenland ice cores. *Earth and Planetary Science Letters* **203**, 507-518.

Stipp S. L. and Hochella M. F. (1991) Structure and bonding environments at the calcite surface as observed with X-ray photoelectron spectroscopy (XPS) and low energy electron diffraction (LEED). *Geochimica et Cosmochimica Acta* **55**, 1723-1736.

Stipp S. L. S., Gutmannsbauer W., and Lehmann T. (1996) The dynamic nature of calcite surfaces in air. *American Mineralogist* **81**, 1-8.

Stoll H. M., Klaas C. M., Probert I., Ruiz Encinar J., and Garcia Alonso J. I. (2002) Calcification rate and temperature effects on Sr partitioning in coccoliths of multiple species of coccolithophorids in culture. *Global and Planetary Change* **34**, 153-171.

Strasser A. (1989) *Die Minerale Salzburgs*. Eigenverlag, Salzburg.

Stumm W. and Morgan J. J. (1996) *Aquatic Chemistry : chemical equilibria and rates in natural waters*. Wiley-Interscience, New York.

Sunagawa I. (2005) *Crystals: Growth, Morphology and Perfection*. Cambridge University Press, Cambridge, UK.

Swainson I. P. (2008) The structure of monohydrocalcite and the phase composition of the beachrock deposits of Lake Butler and Lake Fellmongery, South Australia. *American Mineralogist* **93**, 1014-1018.

Tang J., Dietzel M., Böhm F., Köhler S. J., and Eisenhauer A. (2008a) Sr^{2+}/Ca^{2+} and $^{44}Ca/^{40}Ca$ fractionation during inorganic calcite formation: II. Ca isotopes. *Geochimica et Cosmochimica Acta* **72**, 3733-3745.

Tang J., Köhler S. J., and Dietzel M. (2008b) Sr^{2+}/Ca^{2+} and $^{44}Ca/^{40}Ca$ fractionation during inorganic calcite formation: I. Sr incorporation. *Geochimica et Cosmochimica Acta* **72**, 3718-3732.

Tang J., Niedermayr A., Köhler S. J., Böhm F., Kısakürek B., Eisenhauer A., and Dietzel M. Sr^{2+}/Ca^{2+} and $^{44}Ca/^{40}Ca$ fractionation during inorganic calcite formation: III. Impact of salinity/ionic strength *Geochimica et Cosmochimica Acta* **submitted**.

Tarutani T., Clayton R. N., and Mayeda T. K. (1969) The effect of polymorphism and magnesium substitution on oxygen isotope fractionation between calcium carbonate and water. *Geochimica et Cosmochimica Acta* **33**, 987-996.

Taylor G. (1975) The Occurrence of Monohydrocalcitein Two Small Lakes in the South-East of South Australia. *American Mineralogist* **60**, 690-697.

Teng H. H., Dove P. M., Orme C. A., and De Yoreo J. J. (1998) Thermodynamics of Calcite Growth: Baseline for Understanding Biomineral Formation. *Science* **282**, 724-727.

Tesoriero A. J. and Pankow J. F. (1996) Solid solution partitioning of Sr^{2+}, Ba^{2+}, and Cd^{2+} to calcite. *Geochimica et Cosmochimica Acta* **60**, 1053-1063.

Tipper E. T., Galy A., and Bickle M. J. (2008) Calcium and magnesium isotope systematics in rivers draining the Himalaya-Tibetan-Plateau region: Lithological or fractionation control? *Geochimica et Cosmochimica Acta* **72**, 1057-1075.

Todt W. (2000) Isotopenmassenspektrometrie. In: Pavićević, M. K. and Amthauer, G. Eds.), *Physikalisch-chemische Untersuchungsmethoden in den Geowissenschaften*. E. Schweizbart'sche Verlagsbuchhandlung, Mörlenbach.

Tommaso D. D. and Leeuw N. H. d. (2008) The Onset of Calcium Carbonate Nucleation: A Density Functional Theory Molecular Dynamics and Hybrid Microsolvation/Continuum Study. *J. Phys. Chem. B* **112**, 6965.

Tong H., Ma W., Wang L., Wan P., Hu J., and Cao L. (2004) Control over the crystal phase, shape, size and aggregation of calcium carbonate via a l-aspartic acid inducing process. *Biomaterials* **25**, 3923-3929.

Tzeng W.-N., Chang C.-W., Wang C.-H., Shiao J.-C., Iizuka Y., Yang Y.-J., You C.-F., and Ložys L. (2007) Misidentification of the migratory history of anguillid eels by Sr/Ca ratios of vaterite otoliths. *Marine ecology progress series* **348**, 285-295.

Ungaretti A. D. N. a. L. (1971) Refinement of the crystal structure of aragonite *American Mineralogist* **56**, 768-772.

Urey H. C. (1947) The thermodynamic properties of isotopic substances. *J. Chem. Soc.*, 562.

Usdowski E., Hoefs J., and Menschel G. (1979) Relationship between ^{13}C and ^{18}O fractionation and changes in major element composition in a recent calcite-depositing spring - A model of chemical variations with inorganic $CaCO_3$ precipitation. *Earth and Planetary Science Letters* **42**, 267-276.

Usdowski H. E. (1975) *Fraktionierung der Spurenelemente bei der Kristallisation* Springer-Verlag, Berlin Heidelberg New York.

Van Cappellen P., Charlet L., Stumm W., and Wersin P. (1993) A surface complexation model of the carbonate mineral-aqueous solution interface. *Geochimica et Cosmochimica Acta* **57**, 3505-3518.

Veizer J., Demovic R., and Turan J. (1971) Possible use of strontium in sedimentary carbonate rocks as a paleoenvironmental indicator. *Sedimentary Geology* **5**, 5-22.

Veizer J. and Mackenzie F. T. (2003) Evolution of sedimentary rocks. In: Mackenzie, F. T. (Ed.), *Sediments, Diagenesis and Sedimentary Rocks*. Elsevier.

Villegas-Jimenez A., Mucci A., and Paquette J. (2009) Proton/calcium ion exchange behavior of calcite. *Physical Chemistry Chemical Physics* **11**, 8895-8912.

Vogel J. C., Grootes P. M., and Mook W. G. (1970) Isotopic fractionation between gaseous and dissolved carbon dioxide. *Z. Phys.* **230**, 225.

Wada N., Yamashita K., and Umegaki T. (1995) Effects of divalent cations upon nucleation, growth and transformation of calcium carbonate polymorphs under conditions of double diffusion. *Journal of Crystal Growth* **148**, 297-304.

Wagenknecht H. A. and Knapp H. (2010) L-Asparinsäure. In: Deckwer, W.-D., Dill, B., Eisenbrand, G., Fugmann, B., Heiker, F. R., Hulpke, H., Kirschning, A., Pohnert, G., Pühler, A., Schmid, R. D., and Schreier, P. Eds.), *RÖMPP Online*. Thieme.

Wang D., Wallace A. F., De Yoreo J. J., and Dove P. M. (2009) Carboxylated molecules regulate magnesium content of amorphous calcium carbonates during calcification. *PNAS* **106**, 21511-21516.

Wang J. and Becker U. (2009) Structure and carbonate orientation of vaterite ($CaCO_3$). *American Mineralogist* **94**, 380-386.

Wasylenki L. E., Dove P. M., Wilson D. S., and De Yoreo J. J. (2005) Nanoscale effects of strontium on calcite growth: An in situ AFM study in the absence of vital effects. *Geochimica et Cosmochimica Acta* **69**, 3017-3027.

Watson E. B. (1996) Surface enrichment and trace-element uptake during crystal growth. *Geochimica et Cosmochimica Acta* **60**, 5013-5020.

Watson E. B. (2004) A conceptual model for near-surface kinetic controls on the trace-element and stable isotope composition of abiogenic calcite crystals. *Geochimica et Cosmochimica Acta* **68**, 1473-1488.

Watson E. B. and Müller T. (2009) Non-equilibrium isotopic and elemental fractionation during diffusion-controlled crystal growth under static and dynamic conditions. *Chemical Geology* **267**, 111-124.

Wiegand B., Dietzel M., Leis A., Benischke R., and Hänsel S. (2004) Precipitation of calcite from spring water (Carinthia, austria) and the evolution of $^{13}C/^{12}C$- and $^{44}Ca/^{40}Ca$-signatures. In: Hubmann, B. P., W. E. (Ed.),*Pangeo Austria 2004*. Karl-Franzens-Universität Graz, Graz.

Wierzbicki A., Sikes C., Madura J., and Drake B. (1994) Atomic force microscopy and molecular modeling of protein and peptide binding to calcite. *Calcif Tissue Int.* **54**, 133-141.

Wu Y.-T. and Grant C. (2002) Effect of Chelation Chemistry of Sodium Polyaspartate on the Dissolution of Calcite. *Langmuir* **18**, 6813-6820.

Xu A. W., Antonietti M., Cölfen H., and Fang Y. P. (2006a) Uniform Hexagonal Plates of Vaterite CaCO$_3$ Mesocrystals Formed by Biomimetic Mineralization. *Advanced Functional Materials* **16**, 903-908.

Xu X., Han J. T., Kim D. H., and Cho K. (2006b) Two Modes of Transformation of Amorphous Calcium Carbonate Films in Air. *The Journal of Physical Chemistry B* **110**, 2764-2770.

Yang Q., Liu Y., Gu A., Ding J., and Shen Z. (2001) Investigation of calcium carbonate scaling inhibition and scale morphology by AFM. *Journal of Colloid and Interface Science* **240**, 608-621.

Yeom B. and Char K. (2010) Nanostructured CaCO3 Thin Films Formed on the Urease Multilayers Prepared by the Layer-by-Layer Deposition. *Chem. Mater.* **22**, 101-107.

Zhang R.-S., Nash C. P., and Rock P. A. (1988) Thermodynamics of Calcium- Isotope-Exchange Reactions. 1. Exchange between Isotopic Calcium Carbonates and Aqueous Calcium Ions. *J . Phys. Chem.* **92**, 3989-3993.

Zhang T. H. and Liu X. Y. (2009) Nucleation: What happens at the initial stage? *Angewandte Chemie* **48**, 1308.

Zhang Y., Shaw H., Farquhar R., and Dawe R. (2001) The kinetics of carbonate scaling - application for the prediction of downhole carbonate scaling. *Journal of Petroleum Science and Engineering* **29**, 85-95.

Zheng Y.-F. (1999) Oxygen isotope fractionation in carbonate and sulfate minerals. *Geochemical Journal* **33**, 109-126.

Zhong C. and Chu C. C. (2009) Acid Polysaccharide-Induced Amorphous Calcium Carbonate (ACC) Films: Colloidal Nanoparticle Self-Organization Process. *Langmuir* **25**, 3045-3049.

Zhong S. and Mucci A. (1989) Calcite and aragonite precipitation from seawater solutions of various salinities: Precipitation rates and overgrowth compositions. *Chemical Geology* **78**, 283-299.

Zuddas P. and Mucci A. (1998) Kinetics of calcite precipitation from seawater: II. The Influence of the ionic strength. *Geochimica et Cosmochimica Acta* **62**, 757-766.

8   Appendix

A1 Figure
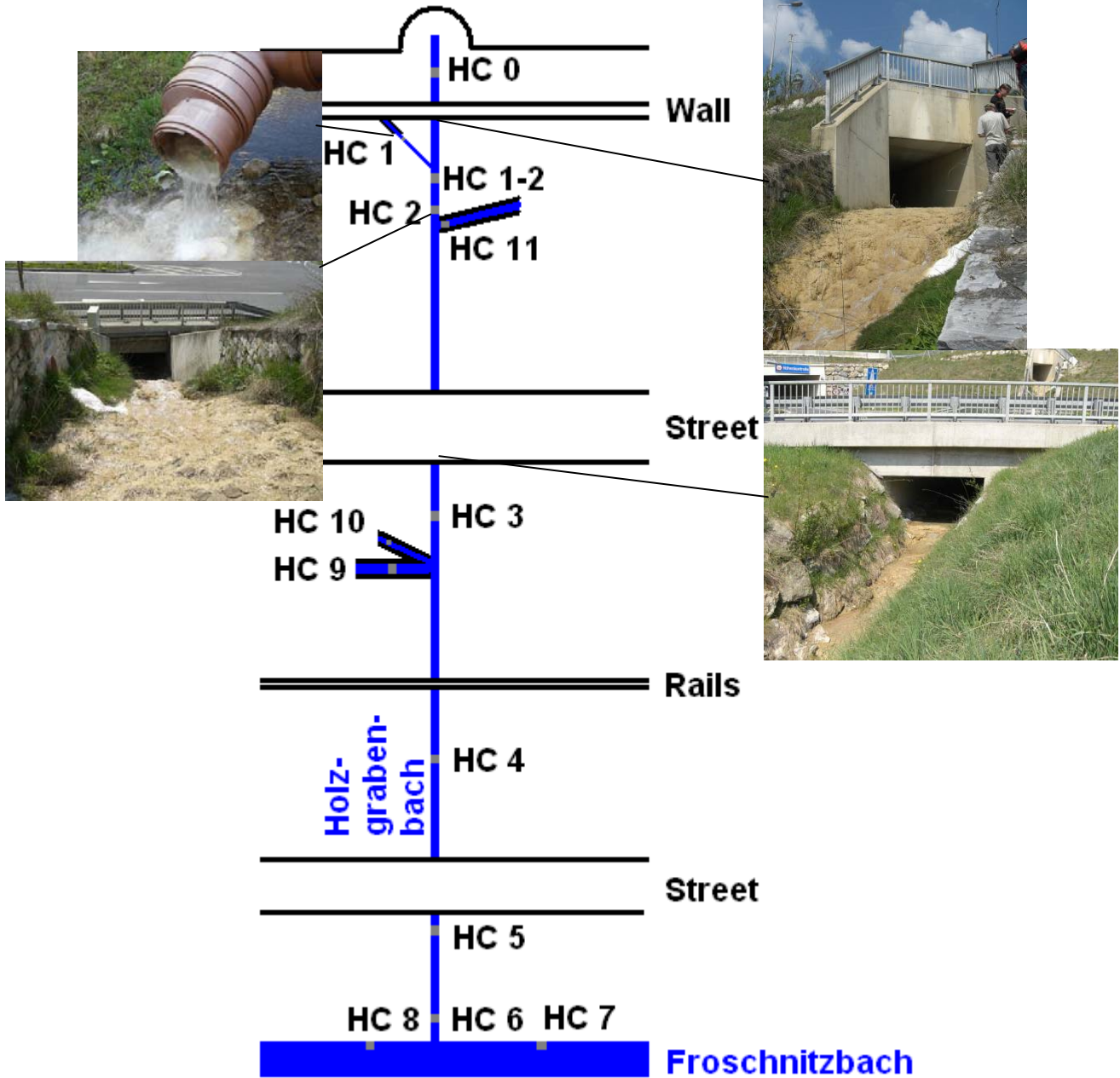
Fig. A1: Sampling sites at Spital tunnel (marked with grey squares)

Tab. A1: Field parameters from 20.11.2007, dist. denotes the distance from reference point Mitterpichling (site: M) or Paierdorf (site: P) in meter, T is the temperature, and SpC is the Specific Conductivity.

Nr.	dist. m	site	T °C	SpC µS/cm	pH
M1	135	(M)	11.0	250	7.7
M2	240	(M)	11.4	249	7.8
M3	540	(M)	11.2	246	7.6
M4	1740	(M)	12.1	184	7.6
M5	1848	(M)	9.9	136	7.1
M6	2293	(M)	12.2	211	7.1
M7	2414	(M)	9.4	1030	12.1
M8	593	(P)	9.0	2330	12.5
M9	593	(P)	10.6	186	10.4
M9-2	590	(P)	9.7	174	9.8
M9-2	595	(P)	7.9	159	8.3
M7-2	2412	(P)	8.8	559	11.4
M6-2	2360	(M)	11.5	144	7.3
M6-2	2358	(M)	12.0	179	7.1

Tab. A2: Concentrations [ ] of the cations and anions in the water samples from 20.11.2007

Nr.	[Ca]	[Mg]	[Na]	[Si]	[Al]	[B]	[Ba]	[Fe]	[K]	[Li]	[Mn]	[Sr]	[Cl⁻]	[NO₃⁻]	[SO₄²⁻]
		mmol l⁻¹						µmol l⁻¹						µmol l⁻¹	
M1	0.73	0.31	0.41	0.65	0.65		0.23	0.80	0.07	3.5	1.29	1.6	65	54.1	128.9
M2	0.73	0.32	0.44	0.65	0.65	2.96	0.23	0.89	0.07	3.6	1.22	1.6	67	54.8	130.8
M3	0.72	0.31	0.43	0.66	0.59	1.47	0.23	1.04	0.07	3.5	1.31	1.6	65	54.4	130.3
M4	0.50	0.19	0.50	0.81	0.76	1.07	0.27	1.57	0.07	4.6	2.15	1.7	20	8.5	86.4
M5	0.38	0.19	0.27	0.50	0.81	0.63	0.13	0.06	0.05	1.3	0.02	0.9	23	25.8	17.1
M6	0.57	0.23	0.50	0.81	-	0.65	0.39	6.76	0.05	6.2	7.68	2.2	19	1.0	258.5
M7	1.60	0.02	0.84	0.39	2.31	-	0.56	0.11	0.54	6.5	-	3.9	35	2.4	28.3
M8	3.77	0.01	1.13	0.05	28	-	1.02	0.14	1.16	8.3	-	12.6	22	8.9	22.8
M9	0.56	0.11	0.56	0.59	2.94	-	0.08	0.74	0.17	4.7	0.88	1.8	18	6.0	47.1
M9-2	0.44	0.11	0.53	0.61	1.58	-	0.04	1.35	141	4.77	1.48	1.7	24	18	43.28
M9-2	0.29	0.13	0.56	0.61	10.08	-	0.07	0.25	250	5.05	0.08	1.8	58	8.9	92.43
M7-2	1.36	0.05	0.69	0.44	1.26	-	0.29	0.02	400	5.73	0.00	3.9	36	31	23.43
M6-2	0.35	0.18	0.46	0.84	-	-	0.32	1.49	43	5.69	4.45	1.4	16	1.7	31.12
M6-2	0.46	0.22	0.50	-	-	32.0	0.38	15.76	45	5.32	2.67	-	19	0.7	90.15

Tab. A3: Calculated dissolved inorganic carbon (DIC) concentration, bicarbonate concentration [HCO₃⁻] carbonate concentration [CO₃²⁻], carbonic acid concentration [H₂CO₃], supersaturation index SI with respect to calcite (Cc), aragonite (Ar), vaterite (Vat) and brucite (Br), partial pressure of CO₂ (pCO₂₍g₎) and carbon isotopes δ¹³C at the sample sites (sampling: 20.11.2007).

Nr.	[DIC]	[HCO₃⁻]	[CO₃²⁻]	[H₂CO₃]	SI$_{cc}$	SI$_{Ar}$	SI$_{Vat}$	SI$_{Br}$	pCO₂₍g₎	δ¹³C in‰
M1	2.41	2.28	0.008	0.114	-0.26	-0.42	-0.87	-6.00	-2.7	-14.9
M2	2.39	2.27	0.009	0.107	-0.24	-0.39	-0.84	-5.91	-2.7	-14.7
M3	2.33	2.25	0.015	0.061	-0.01	-0.16	-0.61	-5.45	-2.9	-14.6
M4	1.91	1.78	0.004	0.127	-0.65	-0.81	-1.25	-6.43	-2.6	-17.0
M5	1.68	1.38	0.001	0.303	-1.37	-1.52	-1.98	-7.51	-2.3	-18.0
M6	2.05	1.69	0.001	0.359	-1.12	-1.27	-1.72	-7.30	-2.1	-18.8
M7	0.27	0.003	0.261	0.001	1.38	1.22	0.77	1.00	-9.9	-19.6
M8	0.04	0.000	0.037	0.0001	0.63	0.48	0.02	1.25	-11.7	-25.2
M9	0.68	0.30	0.381	0.002	1.24	1.08	0.63	-1.23	-6.3	-18.5
M9-2	1.42	1.09	0.33	0.003	1.16	1.007	0.55	-2.46	-5.0	
M9-2	1.34	1.31	0.011	0.021	-0.39	-0.55	-1.01	-5.51	-3.4	
M7-2	1.24	0.08	1.16	0.003	1.94	1.788	1.33	0.13	-7.8	
M6-2	1.69	1.51	0.002	0.185	-1.1	-1.26	-1.71	-6.95	-2.4	
M6-2	2.11	1.73	0.001	0.388	-1.21	-1.36	-1.81	-7.37	-2.1	

Tab. A4a: Physicochemical conditions and individual parameters of the experiments (see Fig. 3-1). T: temperature; [i]: individual concentration of Mg^{2+}, Ca^{2+} and polyaspartic acid (Pasp); mt: PE membrane thickness; add: added amount of 0.5 M HCl (+) or NaOH (–) in the inner solution; pCO_{2in}: initial partial pressure of CO_2 (atm) of the inner solution; D_{CO2av}: average diffusion rate of CO_2; R_{CO3}: CO_3^{2-} accumulation rate; t_{fp}: time of first $CaCO_3$ precipitation; Ω: saturation degree with respect to calcite (Cc), aragonite (Ar), vaterite (Vat) and monohydrocalcite (Mhc) at t_{fp}; IAP_{fp}: ion activity product at t_{fp}; $(CO_3^{2-})_{fp}/(Ca^{2+})$: activity ratio of dissolved free carbonate and calcium ion at t_{fp}; t_{prec}: total time of $CaCO_3$ precipitation; R: $CaCO_3$ precipitation rate; R': $CaCO_3$ precipitation rate; M_{prec}: total amount of the precipitated $CaCO_3$; Cc, Ar, and Vat denote the fraction of calcite, aragonite and vaterite of the precipitates in wt.%. The term Min indicates the following composition, where the sequence of mineral abbreviations reflects their abundance. The first named mineral is > 95 wt.% in the "mono" mineralic system, > 50 wt.% in binary and > 35 wt.% in ternary mixtures. Replicate measurements (experiments 22, 23, 24, 25 and 27) indicate a standard deviation of ±0.11 for $\log D_{CO2av}$, ±0.15 for $\log R_{CO3}$, ±0.09 for $\log t_{fp}$ and ±0.11 for $\log IAP_{fp}$. The standard deviation of $\log R'$ is ±0.06, when only pure calcite precipitation experiments are considered (experiments 23, 24 and 27).

No.	T (°C)	$\frac{[Mg^{2+}]}{[Ca^{2+}]}$ (mol mol⁻¹)	[Pasp] (mg l⁻¹)	mt (mm)	add (ml)	pCO_{2in}	$\log D_{CO2av}$ (μmol h⁻¹)	$\log R_{CO3}$ (μmol h⁻¹)	t_{fp} (h)	$\log IAP_{fp}$	$\log\frac{(CO_3^{2-})_{fp}}{(Ca^{2+})}$	t_{prec} (h)	$\Omega_{Cc\,fp}$	$\Omega_{Ar\,fp}$	$\Omega_{Vat\,fp}$	$\Omega_{Mhc\,fp}$	M_{prec} (mmol)	$\log R'$ (μmol h⁻¹)	Cc (wt.%)	Ar (wt.%)	Vat (wt.%)	Min
1	–	0.00	–	0.2	–	-0.6	2.1	0.7	72	-7.39	-2.8	30	7	5	2.5	0.5	5.5	2.2	100	–	–	Cc
2	–	0.05	–	0.2	–	-0.6	2.0	0.6	106	-7.27	-2.6	30	10	7	3.2	0.6	2.9	1.9	100	–	–	Cc
3[a]	–	0.05	–	0.2	26	0.0	2.5	1.1	51	-7.14	-2.5	18	13	9	4.3	0.8	9.3	2.5	100	–	–	Cc
4	–	0.20	–	0.2	–	-0.6	2.1	0.6	107	-7.29	-2.6	28	13	9	3.1	0.6	2.1	1.6	100	–	–	Cc
5	6.0	0.49	–	0.2	–	-0.6	2.0	0.6	145	-7.22	-2.6	45	15	10	3.6	0.7	4.9	2.1	100	–	–	Cc
6	±1.1	0.79	–	0.2	–	-0.6	2.0	0.7	98	-7.36	-2.6	18	11	8	2.6	0.5	3.5	2.3	100	–	–	Cc
7	–	0.97	–	0.2	–	-0.6	2.0	0.7	106	-7.38	-2.6	26	10	7	2.5	0.5	2.0	1.9	100	–	–	Cc
8	–	1.00	–	0.2	–	-0.6	2.4	1.0	(215)	(-6.78)	(-2.0)	(47)	(41)	(29)	(9.9)	(0.6)	5.4	2.6	100	–	–	Cc
9	–	1.86	–	0.2	–	-0.6	1.9	0.6	322	-7.06	-2.2	76	21	15	5.2	1.0	7.4	2.2	5	95	–	Ar+Cc
10	–	2.34	–	0.2	–	-0.6	2.0	0.7	185	-7.24	-2.4	51	15	10	3.5	0.7	2.8	2.4	10	90	–	Ar+Cc
11	–	3.10	–	0.2	–	-0.6	1.9	0.6	520	-6.99	-2.1	55	26	18	6.2	1.3	10.1	2.5	–	100	–	Ar
12	–	0.01	–	0.2	–	-0.5	2.3	0.9	50	-7.32	-2.7	34	12	9	3.0	0.6	4.0	2.3	100	–	–	Cc
13	–	0.01	–	0.2	–	-0.5	0.6	-0.8	933	-7.71	-3.1	142	5	3	1.2	0.2	1.4	1.6	100	–	–	Cc
14[a]	–	0.09	–	0.2	-31	-0.8	1.7	0.3	47[e]	-7.62	-3.0	55	6	4	1.5	0.3	4.2	2.1	100	–	–	Cc
15[a]	–	0.09	–	2.0	17	0.0	1.2	-0.2	66[e]	-7.61	-3.0	76	6	4	1.6	0.3	8.0	1.8	100[d]	–	–	Cc
16[a]	–	0.09	–	0.2	20	0.0	2.6	1.2	34	-7.19	-2.6	34	17	12	4.1	0.8	11.2	2.6	100	–	–	Cc
17[a,b]	10.0	0.09	–	0.2	20	0.0	2.7	1.5	16	-7.20	-3.0	53	16	11	4.0	0.7	22.3	2.9	100	–	–	Cc
18[a,b]	±0.5	0.41	–	0.2	25	0.1	2.4	1.2	64	-7.03	-2.6	43	24	17	5.9	1.1	13.4	2.5	100	–	–	Cc
19[b]	–	0.58	–	2.0	40	0.3	1.5	0.4	293	-7.17	-3.0	113	17	12	4.3	0.8	0.8	2.0	100	–	–	Cc
20	–	1.49	–	0.2	–	-0.5	1.8	0.6	340	-7.09	-2.3	59	21	15	5.2	1.0	16.2	2.3	50	50	–	Cc/Ar
21	–	5.16	–	0.2	–	-0.5	1.6	0.5	1130	-6.92	-2.0	55	31	22	7.7	1.4	3.5	2.3	–	100	–	Ar
22	–	0.00	–	0.2	–	-0.2	3.0	1.9	11	-7.34	-2.7	14	10	7	3.7	0.6	11.6	3.3	40	–	60	Vat+Cc
23	–	0.00	–	0.2	–	-0.2	2.8	1.6	16	-7.19	-2.6	20	14	10	5.3	0.9	9.9	2.8	100	–	–	Cc
24	–	0.00	–	0.2	–	-0.2	2.7	1.6	10	-7.34	-2.8	17	10	7	3.7	0.6	10.6	2.7	100	–	–	Cc
25	–	0.00	–	0.2	–	-0.2	2.9	1.7	13	-7.15	-2.5	20	15	11	5.8	1.0	14.6	3.4	15	–	85	Vat+Cc
26	–	0.00	–	2.0[c]	–	-0.2	1.5	0.4	81	-7.71	-3.2	92	6	4	1.6	0.3	7.4	1.9	100	–	–	Cc
27	–	0.00	–	0.2	–	-0.2	2.8	1.9	9	-7.48	-2.8	10	10	7	2.7	0.6	2.8	2.8	100	–	–	Cc
28	25.0	0.01	–	0.2	50	0.6	3.6	2.4	5	-6.92	-2.3	8	37	26	10.0	1.7	15.4	3.6	30	45	25	Ar+Cc+Vat
29	±1.3	0.01	–	0.2	–	0.6	1.3	0.1	83	(-7.98)	(-3.3)	(169)	(3)	(2)	(0.9)	(0.1)	5.1	1.8	100	–	–	Cc
30	–	0.01	–	2.0	–	-0.2	1.7	0.6	75	-7.44	-2.9	183	11	8	2.9	0.9	4.2	2.9	100	–	–	Cc
31[b]	–	0.01	–	0.2	39	0.5	3.5	2.4	3	-7.17	-2.8	15	21	15	5.6	1.0	37.5	4.0	10	–	90	Vat+Cc
32	–	0.05	–	2.0[c]	–	-0.2	1.3	0.2	100	-7.81	-3.2	109	5	3	1.3	0.2	3.1	2.0	100	–	–	Cc
33	–	0.05	–	0.2	–	-0.2	2.8	1.7	12	-7.25	-2.7	9	17	12	4.6	0.7	8.4	3.0	100	–	–	Cc
34	–	0.05	–	2.0[c]	–	-0.2	1.3	0.2	141	-7.68	-3.1	95	6	4.5	1.7	0.3	4.2	2.0	100	–	–	Cc
35	–	0.05	–	2.0	–	-0.2	1.1	0.0	222	-7.70	-3.1	70	6	4	1.6	0.3	2.4	1.7	100[d]	–	–	Cc
36	–	0.10	–	0.2	–	-0.2	2.8	1.7	12	-7.33	-2.6	10	14	10	3.9	0.7	6.8	2.8	100	–	–	Cc
37[a]	–	0.10	–	0.2	24	0.3	3.2	2.1	5	-7.26	-2.6	14	16	12	4.5	0.8	15.5	3.1	65	35	–	Cc+Ar

Tab. A4b: (continue of Tab. A4a)

No.	T °C	[Mg²⁺]/[Ca²⁺] mol mol⁻¹	[Pasp] mg l⁻¹	mt mm	add ml	pCO₂in	log D_{CO2av} µmol h⁻¹	log R_{CO3} µmol h⁻¹	t_{fp} h	log IAP_{fp}	log $(CO_3^{2-})_{fp}/(Ca^{2+})$	t_{prec} h	$\Omega_{Cc\,fp}$	$\Omega_{Ar\,fp}$	$\Omega_{Vat\,fp}$	$\Omega_{Mhc\,fp}$	M_{prec} mmol	log R µmol h⁻¹	Cc wt.%	Ar wt.%	Vat wt.%	Min
38		0.10	-	2.0	-	-0.2	1.2	0.0	190	-7.67	-3.1	90	6	5	1.8	0.3	3.7	2.0	100[d]	-	-	Cc
39		0.19	-	2.0[c]	-	-0.2	1.5	0.4	72	-7.79	-3.2	100	5	3	1.3	0.2	3.6	2.0	100[d]	-	-	Cc
40		0.20	-	2.0[c]	-	-0.2	1.5	0.4	110	-7.76	-3.2	150	5	4	1.4	0.2	5.1	2.0	100	-	-	Cc
41[a]		0.21	-	0.2	28	0.3	3.3	2.1	5	-7.17	-2.5	14	21	15	5.6	1.0	16.0	3.5	100	-	-	Cc
42		0.20	-	0.2	-	-0.2	2.8	1.7	17	-7.17	-2.5	8	21	15	5.6	1.0	4.2	2.9	100	-	-	Cc
43		0.30	-	0.2	-	-0.2	2.8	1.7	12	-7.31	-2.6	11	15	11	4.1	0.7	5.5	3.4	90	10	-	Cc+Ar
44		0.29	-	0.2	-	-0.2	2.9	1.8	7	-7.41	-2.8	10	12	9	3.2	0.6	5.5	2.8	100	-	-	Cc
45		0.40	-	2.0	-	-0.2	1.2	0.0	292	-7.69	-3.0	139	6	4	1.7	0.3	2.9	1.6	100[d]	-	-	Cc
46		0.49	-	2.0	-	-0.2	0.7	-0.5	390	-7.94	-3.3	69	3	2	0.9	0.2	2.0	2.2	100[d]	-	-	Cc
47		0.50	-	2.0[c]	-	-0.2	1.5	0.4	144	-7.57	-2.9	74	8	6	2.2	0.4	2.7	2.0	100	-	-	Cc
48		0.49	-	0.2	-	-0.2	2.9	1.8	14	-7.22	-2.5	7	18	13	4.9	0.9	8.8	3.3	25	75	-	Ar+Cc
49	25	0.51	-	2.0[c]	-	-0.2	1.1	0.0	331	-7.61	-2.9	64	7	5	2.0	0.3	1.5	1.8	100[d]	-	-	Cc
50	±1.3	0.49	-	0.2	-	-0.2	2.9	1.8	8	-7.63	-3.0	33	7	5	1.9	0.3	16.4	3.0	70	30	-	Cc+Ar
51		0.59	-	0.2	-	-0.2	2.8	1.6	17	-7.22	-2.5	9	18	13	4.9	0.8	6.4	3.5	90	10	-	Cc+Ar
52		0.59	-	2.0	-	-0.2	1.1	0.0	533	-7.41	-2.8	41	12	8	3.2	0.5	1.7	3.1	90	10	-	Cc+Ar
53		0.77	-	0.2	-	-0.2	2.8	1.7	14	-7.26	-2.5	20	17	12	4.5	0.8	10.8	2.9	25	75	-	Ar+Cc
54		0.78	-	0.2	-	-0.2	2.7	1.5	11	-7.38	-2.6	15	13	7	3.4	0.5	6.6	2.2	90	10	-	Cc+Ar
55		0.78	-	2.0[c]	-	-0.2	1.4	0.3	103	-7.66	-2.9	89	7	5	1.8	0.3	1.5	1.8	100	-	-	Cc
56		0.79	-	0.2	-	-0.2	2.8	1.8	14	-7.23	-2.5	9	18	13	4.8	0.8	7.9	2.8	100	-	-	Cc
57		0.95	-	0.2	-	-0.2	2.8	1.8	11	-7.30	-2.6	4	15	11	4.1	0.7	12.0	3.2	10	90	-	Ar+Cc
58		0.97	-	2.0[c]	-	-0.2	1.5	0.4	165	-7.53	-2.8	52	9	7	2.4	0.4	3.8	2.4	-	100	-	Ar
59[b]		1.72	-	0.2	-	-0.2	3.0	1.9	14	-7.06	-2.6	10	26	19	7.1	1.1	12.9	3.4	-	100	-	Ar
60		1.80	-	2.0	-	-0.2	1.0	-0.1	705	-7.52	-2.7	132	9	7	2.5	0.4	3.7	2.6	-	100	-	Ar
61		1.90	-	0.2	-	-0.2	2.9	1.8	19	-7.20	-2.4	6	19	14	5.2	0.9	4.2	2.7	5	95	-	Ar+Cc
62		2.04	-	0.2	-108	-1.1	2.2	1.2	78	-7.23	-2.4	19	18	13	4.9	0.8	7.7	2.9	-	100	-	Ar
63		2.09	-	0.2	-227	-1.5	1.6	0.9	323	-7.23	-2.4	81	18	13	4.8	0.8	8.7	2.9	-	100	-	Ar
64		2.32	-	0.2	43	0.5	3.5	2.5	8	-6.94	-2.1	7	35	25	9.5	1.6	14.9	3.5	-	100	-	Ar
65		0.00	-	2.0	4	0.2	1.9	1.0	49	-7.45	-2.8	31	13	10	4.0	0.6	3.7	2.4	100	-	-	Cc
66		0.00	-	0.2	-	0.1	3.4	2.5	2	-7.31	-2.7	10	19	14	5.5	0.9	15.5	3.7	50	45	5	Cc+Ar+Vat
67		0.05	-	0.2	-	0.1	3.4	2.4	3	-7.36	-2.7	5	17	12	4.9	0.8	7.2	3.2	100	-	-	Cc
68		0.10	-	2.0	40	0.6	2.3	1.3	21	-7.56	-2.9	12	10	8	3.1	0.6	2.5	2.5	100	-	-	Cc
69		0.11	-	2.0	-	0.1	1.7	0.8	26	-7.83	-3.2	22	6	4	1.7	0.3	4.0	2.3	100[d]	-	-	Cc
70		0.20	-	0.2	-	0.1	3.3	2.4	2	-7.37	-2.7	6	16	12	4.8	1.0	11.1	3.4	5	95	-	Ar+Cc
71		0.30	-	2.0	40	0.6	2.9	1.9	3	-7.59	-2.9	15	10	7	2.9	0.4	7.5	3.1	100	-	-	Cc
72		0.30	-	0.2	-	0.1	1.6	0.7	40	-7.71	-3.1	27	7	5	2.2	0.4	1.4	2.0	100[d]	-	-	Cc
73	40	0.30	-	2.0	-	0.1	3.1	2.2	4	-7.31	-2.6	7	19	14	5.5	1.0	9.4	3.6	25	75	-	Ar+Cc
74	±1.5	0.52	-	2.0	-	0.1	1.7	0.8	39	-7.62	-2.9	27	9	7	2.7	0.5	2.0	2.4	100[d]	-	-	Cc
75		0.52	-	0.2	-	0.1	3.2	2.3	3	-7.36	-2.7	2	17	12	4.9	0.9	6.2	3.8	-	100	-	Ar
76		0.79	-	0.2	-	0.1	3.3	2.4	3	-7.37	-2.6	4	16	12	4.8	0.9	3.1	3.7	-	100	-	Ar
77		0.80	-	2.0	-	0.1	1.7	0.8	(25)	(-8.24)	(-3.5)	(44)	(2)	(2)	(0.7)	(0.1)	2.5	1.9	100[d]	-	-	Cc
78		1.69	-	2.0	-	0.1	1.9	1.1	78	-7.74	-2.9	41	7	5	2.0	0.4	4.2	2.4	-	100	-	Ar
79		2.21	-	2.0	-	0.1	1.6	0.8	86	-7.70	-2.8	30	7	6	2.3	0.4	2.5	2.3	-	100	-	Ar
80		2.24	-	2.0	101	1.0	2.7	1.8	17	-7.39	-2.5	54	16	12	4.6	0.8	18.4	3.1	100[d]	-	-	Cc
81		2.23	-	2.0	-	0.1	1.6	0.8	96	-7.70	-2.8	22	8	6	2.3	0.4	3.7	2.4	-	100	-	Ar
82		2.43	-	2.0	-	0.1	1.6	0.8	75	-7.73	-2.9	44	7	5	2.1	0.3	3.0	2.2	-	100	-	Ar
83		4.49	-	2.0	-	0.1	2.0	1.2	107	-7.44	-2.4	35	14	10	4.1	0.7	3.2	3.0	-	100	-	Ar

Tab. A4c: (continue of Tab. A4b)

No.	T °C	$[Mg^{2+}]/[Ca^{2+}]$ mol mol⁻¹	[Pasp] mg l⁻¹	mt mm	add ml	pCO₂in log	D_{CO_2av} log μmol h⁻¹	R_{CO_3} log μmol h⁻¹	tp h	log IAPtp	log $(CO_3^{2-})_{tp}/(Ca^{2+})$	tprec h	ΩCc tp	ΩAr tp	ΩVat tp	ΩMhc tp	Mprec mmol	log R μmol h⁻¹	Cc wt.%	Ar wt.%	Vat wt.%	Min
84	6.0	0.05	1.61	0.2	-	-0.6	1.2	-0.3	1082	-6.36	-1.5	424	109	76	26	1.1	5.3	0.8	100	-	-	Cc
85	±0.3	0.05	1.61	0.2	-	-0.6	2.1	0.7	114	-7.14	-2.6	155	18	13	4	0.9	23.7	2.9	100	-	-	Cc
86		0.00	0.02	0.2	-	-0.2	2.8	1.7	14	-7.15	-2.5	10	22	15	6	1.0	11.4	3.3	80	-	20	Cc+Vat
87		0.00	0.08	0.2	-	-0.2	2.7	1.5	35	-6.97	-2.3	14	32	23	9	1.5	15.6	3.1	40	-	60	Vat+Cc
88		0.05	0.16	0.2	-	-0.2	2.7	1.5	37	-7.01	-2.4	19	29	21	8	1.4	16.5	3.0	30	-	70	Vat+Cc
89		0.05	0.16	0.2	-	-0.2	1.6	1.6	33	-6.92	-2.4	10	37	26	10	1.7	13.5	3.0	70	-	30	Cc+Vat
90		0.00	0.24	0.2	-	-0.2	1.5	1.5	32	-6.97	-2.3	26	33	23	9	1.5	18.5	3.1	10	-	90	Vat+Cc
91	25	0.00	0.32	0.2	-	-0.2	2.6	1.5	44	-6.89	-2.2	12	39	28	11	1.8	1.4	3.7	100d	-	-	Cc
92	±1	0.00	0.40	0.2	-	-0.2	2.7	1.5	43	-6.87	-2.2	28	40	29	11	1.9	20.6	3.1	10	-	90	Vat+Cc
93		0.98	1.60	0.2	-	-0.2	1.3	1.3	160	-6.67	-1.9	52	64	46	17	3.0	39.5	3.5	100	-	-	Cc
94		0.01	3.20	0.2	-	-0.2	1.2	1.2	135	-6.65	-2.0	79	67	48	18	3.1	33.1	4.7	95	-	5	Cc+Vat
95		0.01	3.20	2.0	41	0.5	0.5	0.5	508	-6.78	-2.2	26	50	36	14	2.3	12.4	3.3	100	-	-	Cc
96b		0.00	3.20	2.0	-	-0.2	2.7	1.8	48	-6.48	-2.8	24	100	72	27	4.6	24.4	3.7	10	-	90	Vat+Cc
97		0.01	3.21	2.0	29	0.3	1.6	0.4	654	-6.79	-2.2	42	49	35	13	2.3	21.2	4.3	100	-	-	Cc
98		2.29	3.22	0.2	-	-0.2	2.1	1.1	276	-6.79	-1.9	35	49	35	13	2.5	27.7	3.8	90	10	-	Cc+Ar
99		0.01	0.24	0.2	-	0.1	3.3	2.4	5	-7.13	-2.5	8	28	21	8	1.5	15.4	3.5	-	-	100	Vat
100		1.15	0.25	0.2	-	0.1	3.1	2.3	10	-7.06	-2.3	11	33	24	10	1.7	1.6	3.4	60	40	-	Cc+Ar
101		0.01	0.39	0.2	-	0.1	3.2	2.2	7	-7.03	-2.3	4	35	26	10	1.9	5.8	3.5	5	-	95	Vat+Cc
102		0.01	0.80	0.2	-	0.1	3.2	2.3	6	-7.02	-2.4	7	36	26	11	2.0	13.0	3.4	15	-	85	Vat+Cc
103	40	1.12	1.58	0.2	-	0.1	3.2	2.3	15	-6.87	-2.1	12	51	38	15	2.7	16.2	3.4	95	5	-	Cc
104	±1.5	0.01	1.59	0.2	-	0.1	3.2	2.2	9	-6.96	-2.3	5	42	31	12	2.3	8.0	3.8	-	-	100	Vat
105		0.01	1.60	0.2	-	0.1	3.2	2.3	8	-6.95	-2.3	9	43	31	13	2.4	13.9	3.7	-	-	100	Vat
106		0.01	3.20	0.2	-	0.1	3.0	2.1	23	-6.72	-2.0	6	72	53	21	3.8	9.7	3.4	-	-	100	Vat
107		0.35	3.27	0.2	-	0.1	3.1	2.1	25	-6.70	-2.0	13	75	55	22	4.3	16.3	3.4	45	-	55	Vat+Cc
108		0.58	3.37	0.2	-	0.1	3.1	2.2	22	-6.70	-1.9	9	75	55	22	4.0	21.2	3.6	100	-	-	Cc
109		1.13	3.26	0.2	-	0.1	3.1	2.2	25	-6.75	-1.9	12	67	49	20	3.5	15.6	3.3	100	-	-	Cc

(a) Experiment where 40 g NaHCO₃ was used for the inner solution instead of 35 g

(b) [Ca] ≠ 10 mmol l⁻¹; [Ca] = 14, 14, 17, 19, 20 and 42 mmol l⁻¹ for experiments 31, 18, 59, 17, 19 and 96, respectively

(c) Different type of 2 mm membrane compared to the other experiments

(d) Mineralogical composition quantified by FTIR instead of XRD pattern

(e) Initial addition of 1 mmol l⁻¹ NaHCO₃ in the outer solution in these experiments caused less time for first CaCO₃ precipitation

Parentheses denote values with elevated uncertainties due to e.g. poor titration data

Tab. A5a: Ω_{Ar} saturation degree in respect to aragonite, shape

No.	Temp.	[Mg]/[Ca]$_{aq}$	[Pasp] mg l^{-1}	Ω_{Ar}	shape Cc	Ar
11	6	3.1	-	18		dipyramidal
21	10	5.2	-	22		dipyramidal
58	25	1.0	-	6		needle
59	25	1.4	-	19		dipyramidal
60	25	1.8	-	7		needle
61	25	1.9	-	14		dipyramidal
62	25	2.0	-	13		dipyramidal
63	25	2.1	-	13		dipyramidal
64	25	2.3	-	25		dipyramidal
75	40	0.5	-	12		dipyramidal
76	40	1.0	-	12		dipyramidal
78	40	1.7	-	5		needle
79	40	2.2	-	6		needle
80	40	2.2	-	11		needle
81	40	2.2	-	6		needle
82	40	2.4	-	5		needle
83	40	4.5	-	10		needle
9	6	1.8	-	15	steep rhombic shape	dipyramidal
10	6	2.3	-	10	stepped Mg-Cc	dipyramidal
48	25	0.5	-	13	dodecahedra	dipyramidal
53	25	0.8	-	12	stepped Mg-Cc	dipyramidal
57	25	1.0	-	11	stepped Mg-Cc	dipyramidal
70	40	0.2	-	12	rounded rhombohedra	dipyramidal
73	40	0.3	-	14	stepped Mg-Cc	dipyramidal + needle

Tab. A5b: continue of Tab. A5a for Ω_{Cc} saturation degree in respect to calcite

No.	Temp.	[Mg]/[Ca]$_{aq}$	[Pasp] mg l^{-1}	Ω_{Cc}	shape Cc	Ar
1	6	0.0	-	10	rhombohedra	
2	6	0.1	-	13	rhombohedra	
3	6	0.1	-	18	rhombohedra	
4	6	0.2	-	13	rounded rhombohedra	
5	6	0.5	-	15	dodecahedra	
6	6	0.8	-	11	dodecahedra	
7	6	1.0	-	10	dodecahedra	
8	6	1.0	-	41	steep rhombic shape	
12	10	0.0	-	12	rhombohedra	
13	10	0.0	-	5	stepped Mg-Cc	
14	10	0.1	-	6	stepped Mg-Cc	
15	10	0.1	-	6	stepped Mg-Cc	
16	10	0.1	-	17	rhombohedra	
17*	10	0.1	-	16	rhombohedra	
18*	10	0.5	-	24	stepped Mg-Cc	
19*	10	0.6	-	17	stepped Mg-Cc	
23	25	0.0	-	20	rhombohedra	
24	25	0.0	-	14	rhombohedra	
26	25	0.0	-	6	rhombohedra	
27	25	0.0	-	10	rhombohedra	
29	25	0.0	-	3	rounded rhombohedra	
30	25	0.0	-	11	rounded rhombohedra	
32	25	0.1	-	5	rhombohedra	
33	25	0.0	-	17	rhombohedra	
34	25	0.1	-	6		
35	25	0.1	-	6	rounded rhombohedra	
36	25	0.1	-	14	rhombohedra	
38	25	0.1	-	6	stepped Mg-Cc	
39	25	0.2	-	5	stepped Mg-Cc	
40	25	0.2	-	5	steep rhombic shape	
41	25	0.2	-	21	rhombohedra	
42	25	0.2	-	21	rhombohedra	
44	25	0.3	-	12	rounded Mg-Cc	
45	25	0.4	-	6	stepped Mg-Cc	
46	25	0.5	-	3	stepped Mg-Cc	
47	25	0.5	-	8	stepped Mg-Cc	
49	25	0.5	-	7	rounded rhombohedra	dipyramidal
55	25	0.8	-	7	stepped Mg-Cc	needle
56	25	0.8	-	18	stepped Mg-Cc	dipyramidal
65	40	0.0	-	13	rhombohedra	

Tab. A5c: continue of Tab. A5b for Ω_{Cc} saturation degree in respect to calcite

No.	Temp.	[Mg]/[Ca]$_{aq}$	[Pasp] mg l^{-1}	Ω_{Cc}	shape Cc	Ar
67	40	0.05	-	17	rhombohedra	
68	40	0.10	-	10	rounded rhombohedra	
69	40	0.10	-	6	rounded rhombohedra	
72	40	0.31	-	7	stepped Mg-Cc	
74	40	0.52	-	9	stepped Mg-Cc	
77	40	0.81	-	2	rounded rhombohedra	
71	40	0.30	-	10	stepped Mg-Cc	
85	6	0.05	1.6	18	single step rhombohedra	
84	6	0.05	1.6	109	single step rhombohedra	
91	25	0.00	0.3	39		
93	25	0.98	1.6	64	steep rhombic shape	
95	25	0.01	3.2	50	rhombohedra	
97	25	0.01	3.2	49	single step rhombohedra	
108	40	0.58	3.4	75	rounded	
103	40	1.12	1.6	51	rounded	porous balls
109	40	1.13	3.3	67		rounded
20	10	1.44	-	21	steep rhombic shape	dipyramidal
37	25	0.51	-	16	dodecahedra	dipyramidal
43	25	0.31	-	15	rounded Mg-Cc	
50	25	0.50	-	7	stepped Mg-Cc	dipyramidal
51	25	0.61	-	18	dodecahedra	dipyramidal
52	25	0.60	-	12	rounded Mg-Cc	
54	25	0.80	-	12	stepped Mg-Cc	dipyramidal
98	25	2.29	3.2	49	steep rhombic shape	
100	40	1.15	0.3	33	rounded	needle

Tab. A5d: continue of Tab. A5c for Ω_{Vat} saturation degree in respect to vaterite

No.	Temp.	[Mg]/[Ca]$_{aq}$	[Pasp] mg l^{-1}	Ω_{vat}	shape Vat	Cc	Ar
99	40	0.01	0.2	8	spheres out of plates		
104	40	0.01	1.6	12	coral like shape		
105	40	0.01	1.6	13	coral like shape		
106	40	0.01	3.2	22	coral like shape		
86	25	0.00	0.0	6	spheres out of plates	rhombohedra	
89	25	0.05	0.2	10	spheres out of plates	rhombohedra	
94	25	0.01	3.2	18	very tiny	single step rhombohedra	
22	25	0.00	-	4	plates	rhombohedra	
25	25	0.00	-	6	plates	rhombohedra	
31	25	0.01	-	6	flat plates		
87	25	0.00	0.1	9	spheres out of plates	rhombohedra	
88	25	0.00	0.2	8	coral shape out of plates	rhombohedra	
90	25	0.00	0.2	9		cattle rhomohedra + cone plates	
92	25	0.00	0.4	11	spheres out of plates	rhombohedra	
96	25	0.00	3.2	27	spheres out of plates		
107	40	0.35	3.3	22	rounded		
101	40	0.01	0.4	10	coral like shape		
102	40	0.01	0.8	11		rounded (corals)	
28	25	0.01	-	10	plates	rhombohedra	dipyramidal
66	40	0.00	-	6	spheres out of plates	rhombohedra	dipyramidal

Tab. A6a: Mineralogical parameter of Rietveld analysis of aragonite (index: Ar): cell parameter a, b, c; R_p and R_{wp} are the profil agreement index and the weighted profil agreement index, FWHM is the full width at half maximum, A and Int are the area under and the intensity of the (221) peak.

No.	T °C	([Mg]/[Ca])aq mol mol⁻¹	[Pasp] mg l⁻¹	Min	a_{Ar} Å	b_{Ar} Å	c_{Ar} Å	R_p	R_{wp}	c_{Ar}/a_{Ar}	a_{Ar}/a_{Ar0}	b_{Ar}/b_{Ar0}	c_{Ar}/c_{Ar0}	$FWHM_{Ar}$ °2θ	A_{Ar} cts. °2θ	Int_{Ar} cts.
11	6	3.10	-	a	4.9624	7.971	5.7519	5.4	6.9	1.3858	0.9996	0.9991	0.9995	0.2501	850.2	3316
21	10	5.16	-	a	4.9617	7.9717	5.7506	5.7	7.5	1.3862	0.9995	0.9992	0.9993	0.3047	790.0	2631
58	25	0.99	-	a	4.9595	7.9662	5.7442	5.2	7.1	1.3868	0.9990	0.9985	0.9981	0.2572	526.9	2010
59	25	1.45	-	a	4.9612	7.9718	5.7504	6.5	8.4	1.3863	0.9994	0.9992	0.9992	0.2433	984.4	3923
60	25	1.79	-	a	4.9618	7.9738	5.7502	7.4	10.8	1.3867	0.9995	0.9994	0.9992	0.1972	673.1	3256
61	25	1.94	-	a	4.9598	7.9689	5.7473	7.3	9.6	1.3865	0.9991	0.9988	0.9987	0.2355	518.4	2112
62	25	2.04	-	a	4.9621	7.9725	5.7506	7.9	10.3	1.3864	0.9996	0.9993	0.9993	0.2609	916.3	3456
63	25	2.10	-	a	4.9618	7.9723	5.7492	8.1	10.7	1.3867	0.9995	0.9993	0.9990	0.2241	1037.6	4410
64	25	2.32	-	a	4.9608	7.9715	5.7509	7.2	9.6	1.3861	0.9993	0.9992	0.9993	0.2560	1099.4	4209
75	40	0.53	-	a	4.9605	7.9729	5.7486	11.4	14.9	1.3869	0.9993	0.9993	0.9989	0.2632	626.0	2374
76	40	1.00	-	a	4.9610	7.9739	5.7493	13.5	19.0	1.3869	0.9994	0.9995	0.9990	0.2531	1044.0	4033
78	40	1.70	-	a	4.9611	7.9717	5.7468	10.3	14.6	1.3872	0.9994	0.9992	0.9986	0.2262	682.8	2882
79	40	2.22	-	a	4.9618	7.9715	5.7480	7.2	10.2	1.3868	0.9995	0.9992	0.9988	0.2250	510.2	2163
80	40	2.23	-	a	4.9602	7.9768	5.7450	7.8	10.9	1.3885	0.9992	0.9998	0.9983	0.2317	777.7	3218
81	40	2.22	-	a	4.9614	7.9699	5.7473	7.4	10.2	1.3867	0.9994	0.9990	0.9987	0.2810	550.5	1957
82	40	2.43	-	a	4.9613	7.9707	5.7477	7.5	10.5	1.3868	0.9994	0.9991	0.9988	0.2190	911.2	3943
83	40	4.49	-	a	4.9622	7.9726	5.7484	12.7	17.4	1.3869	0.9996	0.9993	0.9989	0.1310	1057.0	6848

Tab. A6b: Continue of Tab. A6a for calcite (Cc)

No.	T °C	([Mg]/[Ca])aq mol mol⁻¹	[Pasp] mg l⁻¹	Min	a_{Cc} Å	c_{Cc} Å	R_p	R_{wp}	c_{Cc}/a_{Cc}	a_{Cc}/a_{Cc0}	c_{Cc}/c_{Cc0}	$FMWH_{Cc}$ °2θ	A_{Cc} cts. °2θ	Int_{Cc} cts.
1	6	0.00	-	c	4.9900	17.0663	9.3	11.6	3.4201	0.9997	0.9998	0.106	2681	22727
3	6	0.05	-	c	4.9897	17.0652			3.4201	0.9996	0.9997	0.081	2879	30264
5	6	0.51	-	c	4.9882	17.0565	11.9	14.6	3.4194	0.9993	0.9992	0.115	1902	15161
6	6	0.80	-	c	4.9856	17.0482	7.8	10.0	3.4195	0.9988	0.9987	0.099	1849	16389
8	6	1.00	-	c	4.9846	17.0391	8.4	10.7	3.4184	0.9986	0.9982	0.149	2816	18347
16	10	0.09	-	c	4.9895	17.0635			3.4199	0.9996	0.9996	0.065	5704	71439
17*	10	0.09	-	c	4.9895	17.0626	9.1	11.4	3.4197	0.9996	0.9996	0.079	2934	31668
18*	10	0.51	-	c	4.9883	17.0566	15.3	18.2	3.4193	0.9993	0.9992	0.083	4819	49788
19*	10	0.58	-	c	4.9874	17.0482	12.6	15.3	3.4183	0.9992	0.9987	0.283	1139	5198
23	25	0.00	-	c	4.9898	17.0633	8.5	11.4	3.4196	0.9997	0.9996	0.293	2284	11920
24	25	0.00	-	c	4.9915	17.0690	36.3	43.2	3.4196	1.0000	0.9999	0.055	14788	216338
27	25	0.00	-	c	4.9900	17.0643	8.5	10.7	3.4197	0.9997	0.9996	0.081	3685	38929
30	25	0.01	-	c	4.9899	17.0645	10.1	13.0	3.4198	0.9997	0.9997	0.153	1379	8816
33	25	0.05	-	c	4.9912	17.0678	62.6	77.1	3.4196	0.9999	0.9999	0.050	32035	515332
34	25	0.05	-	c	4.9903	17.0641	38.1	45.6	3.4195	0.9997	0.9996	0.055	13528	198617
36	25	0.10	-	c	4.9887	17.0607			3.4198	0.9994	0.9994	0.095	3637	32595
40	25	0.20	-	c	4.9897	17.0631	12.4	15.3	3.4197	0.9996	0.9996	0.079	4757	50872
41	25	0.21	-	c	4.9911	17.0641	37.1	45.1	3.4189	0.9999	0.9996	0.058	12844	179094
42	25	0.21	-	c	4.9893	17.0587	12.1	15.0	3.4191	0.9995	0.9993	0.090	2370	22930
44	25	0.30	-	c	4.9891	17.0565	26.1	35.7	3.4188	0.9995	0.9992	0.068	10567	128775
47	25	0.51	-	c	4.9849	17.0440	15.2	18.9	3.4191	0.9987	0.9985	0.101	2389	21090
55	25	0.80	-	c	4.9775	17.0057	10.1	12.7	3.4165	0.9972	0.9962	0.127	1915	14151
56	25	0.79	-	c	4.9840	17.0350	20.2	24.0	3.4180	0.9985	0.9979	0.098	5955	53559
65	40	0.00	-	c	4.9901	17.0673	23.1	28.9	3.4203	0.9997	0.9998	0.068	9838	120364
67	40	0.05	-	c	4.9891	17.0646			3.4204	0.9995	0.9997	0.077	2839	30727
68	40	0.10	-	c	4.9900	17.0613	25.2	31.1	3.4191	0.9997	0.9995	0.066	6699	83582
71	40	0.30	-	c	4.9846	17.0400	6.4	8.2	3.4185	0.9986	0.9982	0.098	4495	40782
85	6	0.05	1.6	c	4.9910	17.0645	7.5	9.4	3.4191	0.9999	0.9997	0.086	3408	34164
84	6	0.05	1.6	c	4.9916	17.0646	8.5	11.0	3.4187	1.0000	0.9997	0.14	2912	20012
93	25	0.98	1.6	c	4.9748	17.0025	6.4	8.4	3.4177	0.9966	0.9960	0.123	288	3112
95	25	0.01	3.2	c	4.9894	17.0703	6.5	8.5	3.4213	0.9996	1.0000	0.054	2284	22153
97	25	0.01	3.2	c	4.9903	17.0663	6.7	8.6	3.4199	0.9997	0.9998	0.093	4181	39347
108	40	0.58	3.4	c	4.9819	17.0265	11.4	14.1	3.4177	0.9981	0.9974	0.098	4274	38487
103	40	1.12	1.6	c	4.9740	16.9874	6.4	8.1	3.4152	0.9965	0.9951	0.141	3209	21875
109	40	1.13	3.3	c	4.9728	16.9801	6.9	8.7	3.4146	0.9962	0.9947	0.169	3812	22453

A6c: Continue of Tab. A6b for calcite and aragonite mixtures (ac... dominantly aragonite, ca... dominantly calcite)

T	$([Mg]/[Ca])_{aq}$	[Pasp]	Min	a_{Co}	c_{Co}	a_{Ar}	b_{Ar}	c_{Ar}	R_p	R_{wp}	c_{Co}/a_{Co}	c_{Ar}/a_{Ar}	a_{Co}/a_{Co0}	c_{Co}/c_{Co0}	a_{Ar}/a_{Ar0}	b_{Ar}/b_{Ar0}	c_{Ar}/c_{Ar0}	$FMWH_{Co}$	A_{Co}	Int_{Co}	$FMWH_{Ar}$	A_{Ar}	Int_{Ar}
°C	mol mol^{-1}	mg l^{-1}		Å	Å	Å	Å	Å										°2θ	cts. °2θ	cts.	°2θ	cts. °2θ	cts.
6	1.80	0.24	ac	4.9762	16.9973	4.9622	7.9706	5.7520	4.9	6.3	3.4157	1.3857	0.997	0.996	0.9996	0.9990	0.9995	0.148	398	2618	0.2435	833.6	3320
6	2.34	-	ac	4.9767	16.9933	4.9625	7.9714	5.7531	5.9	7.7	3.4146	1.3856	0.997	0.995	0.9997	0.9991	0.9997	0.194	483	2549	0.2562	499.1	1910
25	0.50	-	ac	4.9872	17.0431	4.9623	7.9741	5.7506	12.4	18.4	3.4173	1.3867	0.999	0.998	0.9996	0.9995	0.9993	0.067	1576	19408	0.2518	786.0	3048
25	0.78	-	ac	4.9816	17.0248	4.9603	7.9704	5.7469	8.0	10.6	3.4176	1.3869	0.998	0.997	0.9992	0.9990	0.9986	0.109	725	5950	0.2335	389.0	1594
25	0.99	-	ac	4.9801	17.0138	4.9600	7.9701	5.7484	8.4	11.1	3.4164	1.3865	0.998	0.998	0.9992	0.9990	0.9989	0.110	285	2312	0.2390	488.8	1971
40	0.21	-	ac	4.9863	17.0433	4.9598	7.9751	5.7517	13.2	17.7	3.4180	1.3866	0.999	0.998	0.9991	0.9996	0.9994	0.083	116	1164	0.2476	542.7	2154
40	0.31	-	ac	4.9865	17.0480	4.9627	7.9783	5.7519	16.4	27.7	3.4188	1.3871	0.999	0.999	0.9997	1.0000	0.9995	0.071	2031	23697	0.2648	938.0	3496
10	1.44	-	ca	4.9815	17.0241	4.964	7.973	5.755	6.6	9.0	3.4175	1.3854	0.998	0.9973	1.0000	0.9993	1.0000	0.165	841	5055	0.2809	132.3	472
25	0.51	-	ca	4.9858	17.0447	4.963	7.975	5.752	6.3	8.3	3.4186	1.3864	0.9988	0.9985	0.9998	0.9996	0.9996	0.108	2676	22573	0.2487	229.0	897
25	0.31	-	ca	4.9877	17.0553	4.959	7.978	5.748	13.0	17.1	3.4195	1.3880	0.999	0.9991	0.9989	1.0000	0.9987	0.094	3026	27769	0.2174	47.1	205
25	0.50	-	ca	4.9854	17.0439	4.962	7.975	5.748	11.0	14.3	3.4188	1.3875	0.998	0.9985	0.9995	0.9996	0.9987	0.094	2589	23651	0.2503	168.9	658
25	0.61	-	ca	4.9857	17.0437	4.962	7.967	5.751	7.3	9.7	3.4185	1.3854	0.998	0.9984	0.9995	0.9986	0.9993	0.089	3181	30957	0.2217	50.6	217
25	0.60	-	ca	4.9821	17.0274	4.962	7.973	5.753	7.7	9.8	3.4177	1.3860	0.999	0.9975	0.9996	0.9993	0.9996	0.119	2667	20719	0.3991	47.3	126
25	0.80	-	ca	4.9814	17.0225	4.960	7.953	5.752	6.3	9.1	3.4172	1.3827	0.998	0.9972	0.9992	0.9968	0.9994	0.144	1870	12402	0.2688	31.2	115
25	2.29	3.2	ca	4.9647	16.9455	4.963	7.983	5.751	5.7	7.2	3.4132	1.3881	0.9946	0.9927	0.9998	1.0006	0.9993	0.238	3625	16137	0.3558	78.9	231
40	1.15	0.3	ca	4.9732	16.9861	4.963	7.976	5.750	9.1	11.3	3.4155	1.3871	0.9963	0.9951	0.9997	0.9997	0.9992	0.155	3139	19776	0.2048	300.3	1369

Tab. A6d: Continue of Tab. A6c for vaterite and vaterite mixtures (v... vaterite, vc and vca... dominantly vaterite, cv anc cav ... dominantly calcite, three letters indicate all polymorphs)

No.	T	$([Mg]/[Ca])_{aq}$	[Pasp]	Min	a_{Co}	c_{Co}	a_{Ar}	b_{Ar}	c_{Ar}	a_{vat}	c_{vat}	R_p	R_{wp}	c_{Co}/a_{Co}	c_{Ar}/a_{Ar}	c_{vat}/a_{vat}	a_{Co}/a_{Co0}	c_{Co}/c_{Co0}	a_{Ar}/a_{Ar0}	b_{Ar}/b_{Ar0}	c_{Ar}/c_{Ar0}	a_{vat}/a_{vat0}	c_{vat}/c_{vat0}
	°C	mol mol^{-1}	mg l^{-1}		Å	Å	Å	Å	Å	Å	Å												
99	40	0.01	0.24	v						4.129	8.466	13.56	18.78			2.050						0.9994	0.999
104	40	0.01	1.59	v						4.127	8.469	13.42	16.53			2.052						0.999	0.9994
105	40	0.01	1.60	v						4.128	8.469	16.54	20.01			2.051						0.9993	0.9994
106	40	0.01	3.20	v						4.128	8.469	14.58	18.08			2.051						0.9992	0.9993
86	25	0.00	0.02	cv	4.9902	17.0644				4.131	8.466	8.05	10.14	3.420		2.050	0.9997	0.9997				0.9998	0.9991
89	25	0.05	0.16	cv	4.9915	17.0685				4.131	8.470	26.78	40.23	3.420		2.050	1.0000	0.9999				0.9999	0.9994
94	25	0.01	3.20	cv	4.9899	17.0690				4.127	8.474	10.77	14.48	3.421		2.053	0.9997	0.9999				0.9989	1
22	25	0.00	-	vc	4.9899	17.0652				4.131	8.467	18.71	24.11	3.420		2.050	0.9997	0.9997				0.9999	0.9991
31	25	0.01	-	vc	4.9895	17.0647				4.130	8.466	19.86	24.77	3.420		2.050	0.9996	0.9997				0.9997	0.999
87	25	0.00	0.08	vc	4.9882	17.0580				4.129	8.462	13.09	18.38	3.420		2.049	0.9993	0.9993				0.9994	0.9986
88	25	0.00	0.16	vc	4.9898	17.0623				4.130	8.466	14.43	19.07	3.419		2.050	0.9996	0.9995				0.9996	0.999
90	25	0.00	0.24	vc	4.9898	17.0640				4.129	8.467	11.37	14.62	3.420		2.050	0.9996	0.9996				0.9997	0.9992
92	25	0.00	0.40	vc	4.9896	17.0581				4.129	8.465	11.53	14.62	3.419		2.050	0.9994	0.9993				0.9993	0.9989
96	25	0.00	3.20	vc	4.9887	17.0514				4.128	8.470	14.96	19.13	3.418		2.052	0.9996	0.9989				0.9993	0.9989
107	40	0.35	3.27	vc	4.9897	17.0644				4.124	8.459	12.14	15.36	3.420		2.051	0.9987	0.9997				0.9992	0.9994
101	40	0.01	0.39	vc	4.9851	17.0434				4.128	8.468	10.99	13.84	3.419		2.051	0.9581	0.9984				0.9983	0.9982
102	40	0.01	0.80	vc	4.7823	16.4544				4.129	8.469	14.32	17.86	3.441		2.051	0.9994	0.9639				0.9992	0.9992
28	25	0.01	-	vca	4.9885	17.0596	4.9626	7.9750	5.7540	4.130	8.466	14.85	19.05	3.420	1.159	2.050	0.9997	0.9997	0.9996	0.9996	0.9997	0.9995	0.9994
66	40	0.00	-	cav	4.9913	17.0670	4.9634	7.9780	5.7518	4.132	8.464	15.12	24.69	3.419	1.159	2.049	0.9999	0.9998	0.9998	1	0.9995	1.0000	0.9988

Tab. A7a: Chemical and Isotopic composition of aragonite: T: temperature, $[Mg^{2+}]/[Ca^{2+}]$: $[Mg^{2+}]/[Ca^{2+}]$ ratio in the initial solution, R precipitation rate, $[Me^{2+}]/[Ca^{2+}]$: $[Me^{2+}]/[Ca^{2+}]$ ratio in the CaCO3 with $Me^{2+} = Mg^{2+}$ or Sr^{2+}, D_{Mg}, D_{Sr}: distribution coefficient between $CaCO_3$ and solution of Mg^{2+} and Sr^{2+}, respectively by using equation (2-37), $\Delta^{44/40}Ca$: $^{44/40}Ca$ isotopic fractionation, $\pm\Delta Ca$: 2 σ of $\Delta^{44/40}Ca$, n amount of repetitions of the Ca isotopic measurements

No.	T °C	$[Mg^{2+}]/[Ca^{2+}]$ mol mol-1	log R µmol h-1 m-2	$[Mg^{2+}]/[Ca^{2+}]_{CaCO_3}$ mmol mol-1	log D_{Mg}	$[Sr^{2+}]/[Ca^{2+}]_{CaCO_3}$ mmol mol-1	log D_{Sr}	ΔCa (‰)	±ΔCa (‰)	n
11	6	3.10	2.9	3.6	-2.98	10.5	0.15	d	d	d
21	10	5.16	3.1	3.7	-3.16	10.8	0.15	d	d	d
58	25	0.99	2.7	3.9	-2.43	0.1	0.19	-1.55	0.10	3
59	25	1.45	3.4	0.8	-3.27	8.3	0.01	-1.05	0.09	4
60	25	1.79	3.1	1.4	-3.11	11.8	0.09	-1.48	0.05	2
61	25	1.94	3.0	b	b	1.9	0.00	-1.39	0.08	3
62	25	2.04	3.6	1.6	-3.14	10.3	0.10	-1.21	0.18	4
63	25	2.10	3.1	1.2	-3.28	10.4	0.10	-1.14	0.04	2
64	25	2.32	3.7	2.7	-3.01	10.2	0.08	-0.91	0.14	5
75	40	0.53	4.3	5.8		9.6	0.03	-1.26	0.11	4
76	40	1.00	3.8	1.5	-2.85	8.5	-0.03	-1.07	0.08	3
78	40	1.70	2.0	b	b	8.2	-0.05	-1.33	0.18	6
79	40	2.22	2.9	1.6	-3.15	9.9	0.03	-1.38	0.21	4
80	40	2.23	2.6	5.4	-2.63	0.6	-0.02	-1.42	0.07	2
81	40	2.22	3.3	2.1	-3.04	2.5	-0.04	-1.26	0.18	5
82	40	2.43	3.1	2.3	-3.03	8.8	0.00	d	d	d
83	40	4.49	1.7	b	b	9.2	0.05	-1.47	0.13	2

Tab. A7b: continue of Tab. A7a for calcite

No.	T °C	$[Mg^{2+}]/[Ca^{2+}]$ mol mol-1	log R µmol h-1 m-2	$[Mg^{2+}]/[Ca^{2+}]_{CaCO_3}$ mmol mol-1	log $D_{Mg\ rel}$	$[Sr^{2+}]/[Ca^{2+}]_{CaCO_3}$ mmol mol-1	log $D_{Sr\ rel}$	ΔCa (‰)	±ΔCa (‰)	n
1	6	0.00	3.5	0.1	-0.48	0.3	-0.73	-1.5	0.08	0
2	6	0.05	3.9	0.7	-1.91	2.0	-0.65	-2	0.25	4
3	6	0.05	3.5	0.6	-2.00	1.8	-0.75	-1.4	0.03	2
4	6	0.21	3.7	2.0	-2.01	2.2	-0.6	-1.8	0.12	4
5	6	0.51	3.7	6.2	-1.93	2.2	-0.6	-1.7	0.13	4
6	6	0.80	a	15.8	-1.72	2.3	-0.59	-1.6	0.12	4
7	6	0.98	a	26.6	-1.58	2.7	-0.51	-1.8	0.07	2
8	6	1.00	3.5	14.8	-1.85	2.1	-0.64	d	d	d
12	10	0.01	3.7	0.3	-1.57	0.0	-0.64	-1.6	0.17	5
13	10	0.01	3.0	0.7	-1.25	0.0	-0.66	-0.9	0.10	2
14	10	0.09	3.1	1.3	-1.86	0.1	-0.72	-1	0.50	1
15	10	0.09	3.3	1.6	-1.76	0.1	-0.68	-1.6	0.04	3
16	10	0.09	3.2	1.3	-1.87	0.1	-0.64	-1.7	0.12	3
17*	10	0.09	3.1	2.0	-1.70	0.1	-0.66	-1.1	0.05	3
18*	10	0.51	3.4	6.6	-1.93	2.2	-0.71	-1.6	0.13	5
19*	10	0.58	3.0	8.6	-1.83	1.0	-0.69	d	d	d
23	25	0.00	4.4	c	c	0.5	-0.57	-1.7	0.04	0
24	25	0.00	3.8	c	c	0.3	-0.77	-1.3	0.08	0
26	25	0.00	2.7	c	c	c	c	-0.9	d	d
27	25	0.00	4.1	c	c	0.5	-0.59	d	d	d

Tab. A7c: continue of Tab. A7b for calcite

No.	T °C	$[Mg^{2+}]/[Ca^{2+}]$ mol mol^{-1}	log R μmol h^{-1} m^{-2}	$[Mg^{2+}]/[Ca^{2+}]_{CaCO_3}$ mmol mol^{-1}	log $D_{Mg\,rel}$	$[Sr^{2+}]/[Ca^{2+}]_{CaCO_3}$ mmol mol^{-1}	log $D_{Sr\,rel}$	ΔCa (‰)	±ΔCa (‰)	n
29	25	0.01	2.8	0.4	-1.49	0.8	-1.05	-0.7	0.04	2
30	25	0.01	3.3	0.5	-1.32	0.7	-1.07	-0.7	0.13	6
32	25	0.05	3.0	1.5	-1.56	c	c	d	d	d
33	25	0.05	4.1	0.9	-1.76	1.9	-0.72	-1.5	0.18	5
34	25	0.05	a	1.3	-1.63	c	c	d	d	d
35	25	0.05	3.4	1.0	-1.72	1.2	-0.85	-1.3	0.30	4
36	25	0.10	4.1	3.0	-1.57	0.5	-0.59		d	d
38	25	0.11	2.9	10.2	-1.01	1.0	-0.95	-0.7	0.15	3
39	25	0.20	2.9	5.4	-1.58	c	c	-1.2	d	d
40	25	0.20	3.0	6.9	-1.49	c	c	-1.4	d	d
41	25	0.21	3.7	4.2	-1.77	2.4	-0.63	-1.4	0.07	3
42	25	0.21	4.2	4.1	-1.73	0.6	-0.50	-2.0	0.10	4
44	25	0.30	4.2	5.9	-1.74	0.4	-0.66		d	d
45	25	0.41	2.9	12.8	-1.50	1.3	-0.84	-1.0	0.03	2
46	25	0.49	a	54.3	-0.97	1.3	-0.83	-0.9	0.03	2
47	25	0.51	3.3	13.5	-1.59	c	c	-1.6	d	d
49	25	0.51	3.2	17.1	-1.47	1.3	-0.82	-1.1	0.09	2
55	25	0.80	a	32.3	-1.40	c	c	d	d	d
56	25	0.79	4.2	18.2	-1.68	2.6	-0.54	-1.6	0.11	3
65	40	0.00	3.8	0.6	c	1.6	-0.75	-1.5	0.03	2
67	40	0.05	4.4	1.5	-1.58	1.8	-0.72	-1.6	0.20	4
68	40	0.10	3.5	2.9	-1.55	1.3	-0.83		d	d
69	40	0.10	4	10.0	-1.02	1.3	-0.83	-1.6	0.09	3
77	40	0.81	a	65.7	-1.10	1.6	-0.74	d	d	d
71	40	0.30	3.6	11.4	-1.45	1.3	-0.87	d	d	d
85	6	0.05	2.9	1.0	-1.79	4.0	-0.34	-1.3	d	d
84	6	0.05	1.8	0.8	-1.79	3.4	-0.41	d	d	d
91	25	0.00	a	0.0	-0.17	c	c	d	d	d
93	25	0.98	3.4	42.8	-1.60	3.6	-0.49	d	d	d
95	25	0.01	3.2	0.3	-1.55	2.8	-0.47	d	d	d
97	25	0.01	3.6	0.3	-1.65	2.8	-0.50	d	d	d
108	40	0.58	4.5	21.9	-1.53	2.9	-0.52	-1.3	0.12	5
103	40	1.12	4.2	44.3	-1.49	3.7	-0.40	d	d	d
109	40		4.2	51.1	-1.42	4.1	-0.34	d	d	d
20	10	1.44	3	17.8	-2.00	5.1	-0.25	d	d	d
37	25	0.51	3.6	10.2	-1.77	4.1	-0.38	d	d	d
43	25	0.31	4	4.7	-1.87	0.9	-0.45	d	d	d
50	25	0.50	3.2	10.2	-1.77	0.8	-0.33	d	d	d
51	25	0.61	4	11.4	-1.76	0.7	-0.43	-2.1	0.02	3
52	25	0.60	3.2	29.0	-1.34	2.6	-0.56	-1.0	0.30	3
54	25	0.80	3.9	21.4	-1.61	0.6	-0.49	d	d	d
98	25	2.29	3.3	132.6	-1.39	4.2	-0.55	d	d	d
100	40	1.15	4.1	28.8	-1.61	5.1	-0.22	d	d	d

Tab. A7d: continue of Tab. A7c for vaterite

No.	T	$[Mg^{2+}]/[Ca^{2+}]$	log R	$[Mg^{2+}]/[Ca^{2+}]_{CaCO_3}$	log $D_{Mg\ rel}$	$[Sr^{2+}]/[Ca^{2+}]_{CaCO_3}$	log $D_{Sr\ rel}$	ΔCa	±ΔCa	n
	°C	mol mol^{-1}	µmol h^{-1} m^{-2}	mmol mol^{-1}		mmol mol^{-1}		(‰)	(‰)	
99	40	0.01	4.3	0.9	-1.20	0.9	-1.05	-0.3	0.22	3
104	40	0.01	4.9	0.6	-1.28	1.0	-0.94	-0.4	0.12	5
105	40	0.01	4.3	0.9	-1.16	1.2	-0.86	-0.4	0.18	4
106	40	0.01	4.5	0.7	-1.23	1.4	-0.79	-0.5	0.10	3
86	25	0.00	3.7	c	c	0.0	-0.77	d	d	d
89	25	0.05	3.8	0.5	-2.02	1.0	-0.97	-0.6	0.11	3
94	25	0.01	2.6	0.5	-1.60	3.3	-0.57	d	d	d
22	25	0.00	3.6	c	c	0.2	-0.97	d	d	d
31	25	0.01	3.0	2.5	-0.82	1.3	-1.07	-0.1	0.11	4
88	25	0.00	4.0	c	c	0.0	-0.90	-0.5	0.13	5
90	25	0.00	3.8	c	c	0.0	-0.96	-0.4	0.24	6
92	25	0.00	3.9	c	c	0.0	-0.96	-0.4	0.12	3
96	25	0.00	3.8	c	c	1.5	-0.78	d	d	d
107	40	0.35	4.0	16.3	-1.41	3.0	-0.49	-1.1	0.10	3
101	40	0.01	4.7	1.1	-1.02	1.1	-0.91	-0.6	0.06	3
102	40	0.01	4.3	0.6	-1.28	1.2	-0.89	d	d	d
28	25	0.01	3.5	3.8	-0.59	4.3	-0.45	d	d	d
66	40	0.00	3.5	c	c	5.8	-0.19	d	d	d

A3 Publication list (related to this thesis)

A3.1 Articles in Journals

Niedermayr A., Köhler S.J. & Dietzel M.: Effects of Mg^{2+}, polyaspartic acid, CO_3^{2-} accumulation rate and temperature on the nucleation and crystallization of calcite, aragonite and vaterite, submitted to *Geochim. Cosmochim. Acta*

Tang J., Niedermayr A., Dietzel M., Köhler S.J., Böhm F., Kisakürek B. & Eisenhauer A.: Sr^{2+}/Ca^{2+} and $^{44}Ca/^{40}Ca$ fractionation during inorganic calcite formation: III. Impact of salinity/ionic strength, submitted to *Geochim. Cosmochim. Acta*

Immenhauser A., Buhl D., Richter D., Niedermayr A., Riechelmann S., Dietzel M. & Schulte U. (2010): Magnesium-isotope fractionation during low-Mg calcite precipitation in a limestone cave – field study and experiments, *Geochim. Cosmochim. Acta*, **74**, 4346-4364.

Dietzel M., Harer G., Klammer D., Köhler S. J., Leis A., Mittermayr F., Niedermayr A., Reichl P. & Rinder T. (2010): Karbonatabscheidungen in Drainagesystemen von Tunnelbauten, *Beiträge zur Hydrogeologie*, **57**, 143-153.

Dietzel M., Rinder T., Niedermayr A., Mittermayr F., Leis A., Klammer D., Köhler S.J. & Reichl P. (2008): Ursachen und Mechanismen der Versinterung von Tunneldrainagen, *Berg- und Hüttenmännische Monatshefte*, **153**, Springer Verlag, 369-372.

Dietzel M., Rinder T., Niedermayr A., Köhler S. J. & Leis A. (2008): Versinterungen in Drainagesystemen von Tunnelbauten - Mechanismen, Monitoring und Prognosen, *Geotechnik*, **34**, 89-100.

Niedermayr A., Köhler S.J., Cubillias P. & Dietzel M.: Impact of magnesium and polyaspartic acid on solid $CaCO_3$ phases, in prep.

Niedermayr A., Kisakürek B., Böhm F., Köhler S.J., Eisenhauer A. & Dietzel M.: Incorporation of Sr and Ca isotopic fractionation during $CaCO_3$ polymorph formation, in prep.

Rongemaille E., Niedermayr A., Dietzel M., Bollinger C., Liebetrau V., Pierre C. & Bayon G.: Experimental determination of REE partition coefficients in cold seep carbonate phases, in prep.

A3.2 Short articles and abstracts

Niedermayr A., Dietzel M., Kisakürek B., Böhm F., Köhler S. J., Leis A. & Eisenhauer A. (2010): Calcium isotopic fractionation during precipitation of calcium carbonate polymorphs and ACC at low temperatures, *Geophysical Research Abstracts*, **12**, A-12448.

Niedermayr A., Dietzel M., Köhler S. J. & Petautschnig S. (2010): Magnesium and strontium incorporation into calcium carbonate polymorphs and ACC – Experimental Study, *Geophysical Research Abstracts*, **12**, A-12633.

Niedermayr, A.; Köhler, S. J.; Petautschnig, S.; Dietzel, M. (2010): Magnesium and Strontium Incorporation into Calcite, Aragonite, Vaterite and ACC – Impact of Polyaspartic acid and Mg. - in: Ion-partitioning in ambient temperature aqueous systems, EMU summer school Abstracts.

Boehm F., Eisenhauer A., Horn Ch., Kisakurek B., Krabbenhoeft A., Tang J., Niedermayr A.& Dietzel M. (2010): Kinetic Strontium Isotope Fractionation of Planktic Foraminifera and Inorganic Calcite, PP11A-1419, *AGU Fall Meeting 2010*, USA.

Immenhauser, A.; Buhl, D.; Richter, D. K.; Niedermayr, A.; Riechelmann, D.; Dietzel, M.; Schulte, U.: Towards a new proxy for Holocene climate change: Magnesium-isotope fractionation during low-Mg calcite precipitation in a limestone cave. - in: *Geochim. Cosmochim. Acta Spec. Suppl.*, **74**, A445.

Rongemaille E., Niedermayr A., Dietzel M., Bollinger C., Liebetrau V., Pierre C. & Bayon G. (2010): Experimental determination of REE partition coefficients in cold seep carbonate phases, *Geophysical Research Abstracts*, **12**, A-10977.

Niedermayr A., Dietzel M., Köhler S. J., Kisakürek B., Böhm F. & Eisenhauer A. (2009): Magnesium and strontium incorporation and calcium isotopic fractionation during calcium carbonate formation at low temperature (5 to 40°C), *Mitteilungen der Österreichischen Mineralogischen Gesellschaft.*, **155**, 116.

Niedermayr A., Dietzel M., Köhler S.J., Kisakürek B., Böhm F. & Eisenhauer A. (2009) Mg-, Sr-incorporation and Ca isotopic fractionation during calcium carbonate precipitation, *Geochim. Cosmochim. Acta Spec. Suppl.,* **73**, A-941.

Niedermayr A.; Dietzel M.; Köhler S. J. (2009): Mg and Sr Incorporation during Calcium Carbonate Precipitation, *Geophysical Research Abstracts*, **11**, A-10867.

Niedermayr A.; Dietzel M.; Köhler S. J.; Böhm F.; Kisakürek B.; Eisenhauer, A. (2009): Sr Incorporation and Calcium Isotopic Fractionation during Calcium Carbonate Precipitation, *Geophysical Research Abstracts*, **11**, A-10842.

Kisakürek B., <u>Niedermayr</u> A., Müller M., Taubner I., Eisenhauer A., Dietzel M., Buhl D., Fietzke J. & Erez J. (2009): Magnesium isotope fractionation in inorganic and biogenic calcite, *Geochim. Cosmochim. Acta* Spec. Suppl.*,* **73**, A-663.

Buhl D., Immenhauser A., Richter D., Schulte U., Dietzel M., Richelman D. & <u>Niedermayr</u> A. (2009): Magnesium-isotope fractionation in a monitored limestone cave, *Geochim. Cosmochim. Acta Spec. Suppl.*, **73**, A-171.

Tang J.; <u>Niedermayr</u> A.; Köhler S. J.; Dietzel M.; Böhm F.; Kisakürek B.; Eisenhauer A.: No impact of ionic strength/salinity on divalent cation fractionation during inorganic calcite precipitation, *Geophysical Research Abstracts*, **11**, A- 9927.

<u>Niedermayr</u> A., Dietzel M. & Köhler S. J. (2008): Effects of magnesium and polyaspartic acid on calcium carbonate formation, *DMG*, S16-353.

<u>Niedermayr</u> A., Dietzel M. & Köhler S. J. (2008): Inhibition of $CaCO_3$ precipitation – experimental study, *Geophysical Research Abstracts*, **10**, A-09466.

Tang J., <u>Niedermayr</u> A., Dietzel M., Köhler S.J., Böhm F., Kisakürek B. & Eisenhauer A. (2008): No impact of ionic strength/salinity on divalent cation fractionation during inorganic calcite precipitation, *Eos Transactions-American Geophysical Union*, **89**, B11C-0386.

Dietzel M.; Rinder T.; <u>Niedermayr</u> A.; Köhler S. J.; Leis A. (2008): Versinterungen in Drainagesystemen von Tunnelbauten - Mechanismen, Monitoring und Prognosen, *Beiträge zum Symposium "Drainagesysteme im Tunnelbau - Design, Versinterung und Instandhaltung*, S. 89 - 100.

Dietzel M.; Draschitz C.; Harer G.; Klammer D.; Köhler, S. J.; Leis A.; Mittermayr F.; <u>Niedermayr</u> A.; Reichl P.; Rinder T.; Sellner P. (2008): Versinterungen von Tunneldrainagen - Ursachen, Risikoabschätzung, Gegenmaßnahmen, *Tagungsband "Wasserressourchen und deren Bewirtschaftung- Die Bedeutung von Netzwerken.*, S. 236 - 243.

A3.3 Talks at international conferences, workshops and meetings

30. Juni 2010	Magnesium and strontium incorporation into calcite, aragonite, vaterite and ACC, EMU summer school, Oviedo (Spain) (short talk)
05. April 2010	Calcium isotopic fractionations during precipitation of calcium carbonate polymorphs and ACC at low temperatures, European Geosciences Union General Assembly, Wien (Austria)
08. Feb. 2010	Formation of different $CaCO_3$ phases – Chemical and Isotopic Signatures, FB1-Seminar, IFM-Geomar, Kiel (Germany).
26. Juni 2009	Mg-, Sr- incorporation and Ca isotopic fractionation during calcium carbonate precipitation, Goldschmidt Konferenz, Davos (Switzerland).
24. April 2009	Mg- and Sr- incorporation during calcium carbonate precipitation, European Geosciences Union General Assembly, Wien (Austria).
17. Okt. 2008	Effects of magnesium and polyaspartic acid on calcium carbonate formation, DMG, Berlin (Germany).
03. Juli 2007	Bildung und Inhibition von Sinter in Tunneldrainagen – experimentelle Ansätze, Int. Workshop für Versinterungen in Tunneldrainagen, Graz (Österreich).